Title

Phenolic-enabled nanoparticle engineering for biomedical applications

Author

Yim, Wonjun

Publication Date

2023

UNIVERSITY OF CALIFORNIA SAN DIEGO

Phenolic-enabled nanoparticle engineering for biomedical applications

A Dissertation submitted in partial satisfaction of the requirements
for the degree Doctor of Philosophy

in

Materials Science & Engineering

by

Wonjun Yim

Committee in charge:

Professor Jesse V. Jokerst, Chair
Professor Marc A. Meyers
Professor Jeffrey Rinehart
Professor Michael J. Sailor
Professor Donald J. Sirbuly
Professor Liangfang Zhang

2023

The Dissertation of Wonjun Yim is approved, and it is acceptable in quality and form for publication on microfilm and electronically.

University of California San Diego

2023

DEDICATION

To Mr. Mangyu Yim, Ms. Shinhee Kang,

and Dr. Heawon Kim

For their endless love and support

TABLE OF CONTENTS

DISSERTATION APPROVAL PAGE iii

DEDICATION iv

TABLE OF CONTENTS v

LIST OF FIGURES xi

LIST OF TABLES xvii

ACKNOWLEDGEMENTS xviii

VITA xxi

ABSTRACT OF THE DISSERTATION xxv

CHAPTER 1. Gold nanorod-melanin hybrids for enhanced and prolonged photoacoustic imaging in the near-infrared-II window 1

1.1. Abstract 1

1.2. Introduction 2

1.3. Materials and methods 4

1.3.1. Synthesis of GNR Particles 4

1.3.2. Synthesis of PEGylated GNR Particles 5

1.3.3. Synthesis of PDA Coated GNR Particles 5

1.3.4. Synthesis of Rod-Shaped PDA Capsules 5

1.3.5. Stability test of PDA coated GNR Particles 6

1.3.6. In vivo Subcutaneous Injection 6

1.3.7. Instrumentation 6

1.3.8. Photothermal conversion efficiency of GNR and GNR@PDA 7

1.3.9. Data Analysis 7

1.4. Results and discussion 8

1.4.1. Synthesis and Characterization 8

1.4.2. Photoacoustic performance of GNR@PDAs 14

1.4.3. Thermal and structural stability of GNR@PDAs 20

1.4.4. Photoacoustic performance of rod-shaped PDA Capsules 25

1.4.5. In vivo stability of GNR@PDA 29

1.5. Conclusion 32

1.6. Acknowledgement 32

CHAPTER 2. Ultrasmall gold nanorod-polydopamine hybrids for enhanced photoacoustic imaging and photothermal therapy in second near-infrared window 34

2.1. Abstract 34

2.2. Introduction 35

2.3. Materials and methods 38

2.3.1. Synthesis of large GNR 38

2.3.2. Synthesis of ultrasmall GNR 39

2.3.3. Surface modification of large and ultrasmall GNRs 39

2.3.4. Synthesis of PDA coated GNRs 40

2.3.5. Cell culture and preparation 40

2.3.6. Cytotoxicity assay 40

2.3.7. In vitro PTT in NIR-II Window 41

2.3.8. Cell staining with Calcein AM and Propidium Iodide Dyes 41

2.3.9. Instrumentations 42

2.3.10. Photoacoustic imaging of LGNR, SGNR, and SGNR@PDA 42

2.3.11. Photothermal conversion efficiency of LGNR, SGNR, SGNR@PDA 43

2.4. Results and discussion 43

2.4.1. Synthesis and characterization of SGNR@PDA 43

2.4.2. Photoacoustic performance of SGNR@PDAs 47

2.4.3. Photothermal performance of SGNR@PDAs 53
2.4.4. Photothermal treatment of SGNR@PDA *in vitro* 58
2.5. Conclusion 62
2.6. Acknowledgement 63
CHAPTER 3. Enhanced photoacoustic detection of heparin in whole blood via melanin nanocapsules carrying molecular agents. 64
3.1. Abstract 64
3.2. Introduction 65
3.3. Materials and methods 70
3.3.1. Synthesis of PBDT–TA nanoparticles 70
3.3.2. Synthesis of PBDT–TA@PDA nanoparticles 70
3.3.3. Synthesis of PEGylated PNCs 70
3.3.4. Synthesis of dye-loaded PNCs 71
3.3.5. Stability test of dye-loaded PNCs 71
3.3.6. Computational methodology 71
3.3.7. Decomposition analysis of Gibbs free energy 72
3.3.8. Human blood sample preparation, aPTT assay, hemolysis, and specificity test with different biological samples 73
3.3.9. Clinical sample collection 73
3.3.10. Surface area calculation 74
3.3.11. Limit of detection calibration 74
3.3.12. Loading capacity calculation 75
3.3.13. Data analysis 75
3.3.14. General characterizations 75
3.4. Results and Discussion 77
3.4.1. Synthesis of dye-loaded PNC 77

3.4.2. Multiple interactions in the dye-PNC assemblies 85

3.4.3. Release of the loaded dye in negatively charged PNC 90

3.4.4. PA enhancement of positively charged PNC 95

3.5. Conclusions 106

3.6. Acknowledgements 106

CHAPTER 4. 3D bioprinted phantom with human skin phototypes for biomedical optics 108

4.1. Abstract 108

4.2. Introduction 109

4.3. Materials and method 112

4.3.1. Synthesis of GelMA hydrogel 112

4.3.2. Synthesis of synthetic melanin 113

4.3.3. Bio-ink preparation and bio-printing procedure 114

4.3.4. Human skin preparation 114

4.3.5. Multi-laser nanoparticle tracking analysis 115

4.3.6. Reversibility of (Ca^{2+}–EDTA) test 115

4.3.7. PDMS synthesis 116

4.3.8. Synthesis of gold nanorods (GNRs) 116

4.3.9. PA measurement 117

4.3.10. Data analysis 117

4.3.11. General characterization 118

4.4. Results and discussion 119

4.4.1. Design of synthetic melanin 119

4.4.2. Cluster-dependent PA performance 125

4.4.3. PA characterization of real and mimicked human skin 134

4.4.4. Impact of skin phototype on biomedical optic modalities 139

4.5. Conclusions 148

4.6. Acknowledgement 149

CHAPTER 5. A goldilocks energy minimum: peptide-based reversible aggregation and biosensing 150

5.1. Abstract 150

5.2. Introduction 151

5.3. Materials and method 153

5.3.1. Preparation of AuNPs and AuNP aggregates 153

5.3.2. Dissociation of AuNP aggregates using proteolysis of peptides 153

5.3.3. Dissociation of AuNP aggregates using proteolysis of peptides 154

5.3.4. Peptide synthesis 155

5.3.5. Limit of detection 156

5.3.6. Inhibitor test 157

5.3.7. Colloidal stability test 158

5.3.8. Dissociation strategy using AgNPs 158

5.3.9. Investigation of RRK interaction on a citrate coated AuNP using MD simulation 159

5.3.10. Determining free energies as a function of nanoparticle distance using steered molecular dynamics simulation 159

5.3.11. Investigation of RRK/Au and citrate/Au interactions using quantum mechanics 160

5.3.12. Free energy investigation using Metadynamics approach 161

5.3.13. General characterizations 162

5.3.14. DLVO theory 163

5.4. Results and discussion 164

5.4.1. Short cationic peptides for reversible aggregation 164

5.4.2. Peptide-based dissociation of AuNP aggregates 168

5.4.3. Impact of hydrophilicity and steric bulk on particle dissociation. 175

5.4.4. Protease detection with dissociation peptide 179
5.4.5. Matrix-insensitive M^{pro} detection 183
5.5. Conclusions 191
5.6. Acknowledgement 192
REFERENCES 193

LIST OF FIGURES

Figure 1.1 Schematic of synthesis and PA imaging of GNR@PDAs 4

Figure 1.2 Controllable size of GNR@PDAs 11

Figure 1.3 Mushroom and brush confirmation. 12

Figure 1.4 SEM images of GNR@PDAs 13

Figure 1.5 GNR@PDA150 13

Figure 1.6 ICP-MS data 17

Figure 1.7 PA peformance of GNR@PDA. 18

Figure 1.8 Absorption cross-sectional area of GNR@PDAs 19

Figure 1.9 PA signal of GNR 19

Figure 1.10 Shape transition of GNR under the laser illumination 22

Figure 1.11 GNR@PDA stability test 23

Figure 1.12 Changes of UV-vis-NIR spectra 24

Figure 1.13 Shape transition of GNR@PDAs 24

Figure 1.14 Shape transition of PDA@GNR50 25

Figure 1.15 PA performance of rod-shape PDA capsules. 27

Figure 1.16 TEM images of single PDA capsule particle 28

Figure 1.17 PDA coated gold nanospheres (GNSs) 28

Figure 1.18 Photothermal conversion efficiency of GNR and GNR@PDA. 29

Figure 1.19 PA imaging of GNR@PDA *in vivo* 31

Figure 2.1 Schematic of synthesis SGNR@PDA 38

Figure 2.2 PDA-coated large and ultrasmall GNRs 45

Figure 2.3 TEM images with different PDA shell thicknesses 46

Figure 2.4 HAADF and bright field image of SGNR@PDA 46

Figure 2.5 Size and charge of PEGylated SGNRs 47

Figure 2.6 PA imaging of GNR@PDAs 51

Figure 2.7 UV-vis-NIR spectra of LGNR and SGNR 52

Figure 2.8 ICP-MS data 52

Figure 2.9 Photothermal performance of SGNR, LGNR, and SGNR@PDA 55

Figure 2.10 Temperature curve and UV-vis-NIR of PDA 56

Figure 2.11 Temperature curves of LGNR and LGNR@PDA 56

Figure 2.12 Robust SGNR@PDA before and after four cycles of 1064 nm laser irradiation . 57

Figure 2.13 Temperature curves of SGNR and LGNR 57

Figure 2.14 Photothermal performance of SGNR@PDA on SKOV3 cancer cell. 60

Figure 2.15 Colloidal stability of SGNR@PDA in different conditions 61

Figure 2.16 Photobleaching of SKOV3 cancer cells 61

Figure 3.1 Synthetic pathway and charge-dependent behaviors of functionalized PNC 69

Figure 3.2 PBDT–TA core nanoparticles 79

Figure 3.3 Dye-loaded PNC 80

Figure 3.4 Characterization of core–shell nanoparticles 81

Figure 3.5 PBDT–TA@PDAs with different PDA thicknesses 82

Figure 3.6 Monodisperse PNC 83

Figure 3.7 Michael addition and Schiff base reactions of PDA 83

Figure 3.8 Colloidal stability of PEGylated PNC 84

Figure 3.9 Fluorescence of dye-loaded PNC 84

Figure 3.10 Nanoparticle tracking analysis of PNC 85

Figure 3.11 Dye–PNC assemblies 87

Figure 3.12 PNC modified with different concentrations of HS-mPEG 88

Figure 3.13 Surface charge of PEGylated PNC 88

Figure 3.14 Loading free dyes in PNC in a basic condition 89

Figure 3.15 Absorbance of dye-loaded PNC and PDA nanoparticles 89

Figure 3.16 Ruling out the interference of free dye in heparin-dye interactions 91

Figure 3.17 Disassembly of the loaded dyes in negatively charged PNC 92

Figure 3.18 Optical changes of dye-loaded PNC 93

Figure 3.19 Release of the loaded MB dye in PNC 93

Figure 3.20 No interaction between PNC alone and heparin 94

Figure 3.21 PA intensity comparison 94

Figure 3.22 Aggregation-induced PA enhancement of positively charged PNC 98

Figure 3.23 Surface charge-dependent PA signal 99

Figure 3.24 PA spectra of PNC@NB 99

Figure 3.25 Concentration-dependent PA signal 100

Figure 3.26 PA intensity comparison in whole human blood 100

Figure 3.27 Photograph of PNC@NB-heparin interaction 101

Figure 3.28 Decreased absorbance and fluorescence of PNC@NB 101

Figure 3.29 PA signal stability of PNC@NB 101

Figure 3.30 PA response of PNC@NB with/without protamine 102

Figure 3.31 Linear correlation between ACT and cumulative heparin 102

Figure 3.32 Colloidal stability of PNC@NB 103

Figure 3.33 Hemolysis analysis of PNC, PNC@MB, PNC@AA, and PNC@NB 103

Figure 3.34 Correlation of aPTT and PA response of PNC@NB. 104

Figure 3.35 Proposed functional optic fiber for heparin detection 104

Figure 3.36 PDA–heparin interactions with NB dye 105

Figure 3.37 PDA–heparin interactions without NB dye 105

Figure 4.1 Mimicking human skin phototype for biomedical optics 111

Figure 4.2 PA image of human skin specimens 112

Figure 4.3 NMR spectra of gelatin and gelatin methacrylate 113

Figure 4.4 Material characterization of synthetic melanin 122

Figure 4.5 SEM image of PDA nanoparticles 123

Figure 4.6 Size-controllable PDA nanoparticles 123

Figure 4.7 PA spectrum of PDA at the same O.D. 124

Figure 4.8 M-NTA data of PDA_{120} and PDA_{500} at the same O.D. 124

Figure 4.9 TEM images of PDA clusters 128

Figure 4.10 Clusters of synthetic melanin 129

Figure 4.11 PA signal of PDA clusters 130

Figure 4.12 M-NTA data of PDA_{120} in 0, 20, and 200 mM Ca^{2+} 130

Figure 4.13 Disassembly of PDA clusters 131

Figure 4.14 Assembly-disassembly of PDA clusters 131

Figure 4.15 M-NTA image of PDA mixtures 132

Figure 4.16 Particle distribution of PDA_{120} and PDA_{300} 132

Figure 4.17 Bio-ink preparation and 3D-bioprinting process 133

Figure 4.18 Bio-inks including PDA clusters 133

Figure 4.19 Histogram of variable sized melanosomes in human skin 135

Figure 4.20 PA comparison between real and mimicked skin 136

Figure 4.21 Cross-sectional image of human skin specimens 137

Figure 4.22 Mimicking skin phototypes using PDA mixtures 137

Figure 4.23 Randomly distributed PA signal of melanosomes in epidermis 138

Figure 4.24 Light scattering in the dermis 138

Figure 4.25 Photograph of mimicked skin phototypes 142

Figure 4.26 CIE coordinates of mimicked skin-tone phantoms 142

Figure 4.27 Impact of skin phototypes on biomedical optics 143

Figure 4.28 Optical spectra of MB, ICG, and Cy 5.5 143

Figure 4.29 Skin tone impacts on PA imaging 144

Figure 4.30 PA spectrum of the MB and ICG dyes under the mimicked skin phototypes 145

Figure 4.31 Imaging depths under mimicked skin phototypes 145

Figure 4.32 Blood vessel scaffold 146

Figure 4.33 808 and 1064 nm gold nanorods 146

Figure 5.1 Short cationic peptides for reversible aggregation. 166

Figure 5.2 RRK-induced AuNP aggregates 167

Figure 5.3 Interactions between RRK and citrate molecules 167

Figure 5.4 Free energy investigation as a function of AuNP distance 168

Figure 5.5 Peptide-enabled dissociation of AuNP aggregates 171

Figure 5.6 TEM images of AuNP aggregates and particle dissociations 172

Figure 5.7 ESI-MS data of eight peptide sequences (A1–A8) to define the role of amino acid in dissociation peptide 173

Figure 5.8 The role of cysteine and acetylation in the particle dissociation 174

Figure 5.9 Free amine at N terminus prevents particle dissociation 174

Figure 5.10 Impact of hydrophilicity and steric bulk on particle dissociation. 177

Figure 5.11 ESI-MS data A9–A13 peptides 178

Figure 5.12 Photographs of the dissociated AuNPs by A1, A9, A10, A11 peptides 178

Figure 5.13 Impact of spacer lengths on the particle dissociation 179

Figure 5.14 M^{pro} detection using dissociation strategy 181

Figure 5.15 ESI-MS data of A14–A17 peptides 182

Figure 5.16 Impact of the fragment sequence, length, and the location of cysteine on the particle dissociation 182

Figure 5.17 Matrix-insensitive M^{pro} detection 185

Figure 5.18 Dissociation strategy applied in saliva and EBC 186

Figure 5.19 ESI-MS data of A18–19 peptides 186

Figure 5.20 Arg residue at the C terminus for charge-screening 187

Figure 5.21 Impact of the SGFR fragment on particle dissociation 188

Figure 5.22 UV-vis spectrum of the specificity test 189

Figure 5.23 UV-vis spectrum of the inhibition test 189

Figure 5.24 GC376 inhibitor with AuNP aggregates 190

Figure 5.25 Dissociation strategy using 20 nm AgNPs 190

Figure 5.26 Particle dissociation in 100% human urine, plasma, seawater, and saliva 191

LIST OF TABLES

Table 1.1 Material information of GNR and GNR@PDA nanohybrids. 10

Table 3.1 PA imaging compared to other methods for monitoring heparin. 68

Table 4.1 L, a, b (LAB) color values of the mimicked skin phototypes 147

Table 4.2 Absorption coefficient (μ_a) and reduced scattering coefficient (μ_s') of real and mimicked skin. 147

Table 5.1 A1-A8 peptides to study role of structural components in the dissociation peptide 172

ACKNOWLEDGEMENTS

First, I would like to thank my advisor, Professor Jesse V. Jokerst for giving me the opportunity to pursue a Ph.D. in his lab. Thanks to his trust and endless support in me, I could find my enthusiasm and now dream of my own research career. In the last four years of training under his mentorship, I have grown and incredibly achieved many accomplishments which I cannot imagine without him.

All the lab members of Jokerst lab have been collaborative and supportive. In particular, I would like to thank Dr. Jiajing Zhou, Dr. Zhicheng Jin, Dr. Maurice Retout, Dr. Yong Cheng, Dr. Jingcheng Zhou, Dr. Ming Xu, Dr. Ali Hariri, Dr. Jorge Chavez, Matthew N. Creyer, Lei Fu, Baiyan Qi, Tengyu He, Yu-Ci Chang, Chuxuan Ling, Lekshmi Sasi, Lubna Amer, Saul Chavez, Karen Barrios, and Calos Brambila for all their help and discussions.

I would like to thank all my collaborators, in particular, Prof. Ying Shirley Meng, Prof. Bill R. Miller, Prof. Jinhye Bae, Prof. Tod A. Pascal, Prof. Lingyan Shi, Jiayu Zhao, Kathryn Takemura, Diyi Cheng, Shiv H. Patel, Amanda A. Chen, Zhi Li for all their collaboration and technical help.

Many thanks to my committee members, Prof. Marc A. Meyers, Prof. Jeffrey Rinehart, Prof. Michael J. Sailor, Prof. Donald J. Sirbuly, and Prof. Liangfang Zhang for their comments on my projects and dissertation as well as their advice on my future career.

I would like to thank my family and friends. With their countless love and support, I was able to stay in strong and positive mindset. I thank my parents Mr. Mangyu Yim and Ms. Shinhee Kang for their unconditional love. I thank my brother, Dr. Sejun Yim, and his wife, Kyungjin Lee. I also thank my friends who are like family, Wonsuk Lee and Sung Heo for their true friendship.

Foremost, I would like to thank my love, Dr. Heawon Kim, for your endless love, support, and trust in me. Without meeting you, I could not be the person I am today. I am always grateful for my life since I met you in summer of 2018 in Berkeley. I am not afraid of any difficulties as I am not alone. You are the person who encourages me and helps me become a better person.

Chapter 1, in part, is a reprint of the material as it appears in “Gold nanorod-melanin hybrids for enhanced and prolonged photoacoustic imaging in the near-infrared-II window” by Yim, Wonjun; Zhou, Jiajing; Mantri, Yash; Cryer, Matthew N.; Moore, Colman A.; and Jokerst, Jesse V., ACS Applied Material and Interfaces 2021. The dissertation author was the primary investigator and author of this paper.

Chapter 2, in part, is a reprint of the material as it appears in “Ultrasmall gold nanorod-polydopamine hybrids for enhanced photoacoustic imaging and photothermal therapy in second near-infrared window” by Yim, Wonjun; Borum Raina M.; Zhou, Jiajing; Mantri, Yash; Wu, Zhuohong; Zhou, Jingcheng; Jin, Zhicheng; Creyer, Matthew N.; and Jokerst, Jesse V., Nanotheranostics 2022. The dissertation author was the primary investigator and author of this paper.

Chapter 3, in part, is a reprint of the material as it appears in “Enhanced photoacoustic detection of heparin in whole blood via melanin nanocapsules carrying molecular agents” by Yim, Wonjun; Takemura, Kathryn; Zhou, Jiajing; Zhou, Jingcheng; Jin, Zhicheng; Borum, Raina M.; Xu, Ming; Cheng, Yong; He, Tengyu; Penny, William; Miller, Bill R.; Jokerst, Jesse V., ACS Nano 2022. The dissertation author was the primary investigator and author of this paper.

Chapter 4, in part, is a reprint of the material as it appears in “3D-bioprinted phantom with human skin phototypes for biomedical optics” by Yim, Wonjun; Zhou, Jiajing; Sasi, Lekshmi; Zhao, Jiayu; Yeung, Justin; Cheng, Yong; Jin, Zhicheng; Johnson, Wade; Xu, Ming; Chavez, Jorge Palma; Fu, Lei; Qi, Baiyan; Retout, Maurice; Shah, Nisarg J.; Bae, Jinhye; Jokerst, Jesse V., Advanced Materials 2022. The dissertation author was the primary investigator and author of this paper.

Chapter 5, in part, is currently being prepared for submission for publication of the material. “A goldilocks energy minimum: peptide-based reversible aggregation and biosensing” by Yim, Wonjun; Retout, Maurice; Chen, Amanda A.; Ling, Chuxuan; Amer, Lubna; Jin, Zhicheng; Chang, Yu-ci; Chavez, Saul; Barrios, Karen; Lam, Benjamin; Li, Zhi; Zhou, Jiajing; Shi, Lingyan; Pascal, Tod A.; Jokerst, Jesse V. The dissertation author was the primary researcher and author of this material.

VITA

2017 Bachelor of Science in Materials Science and Engineering, Yonsei University

2018 Master of Engineering in Materials Science and Engineering, University of California Berkeley

2023 Doctor of Philosophy in Materials Science and Engineering, University of California San Diego

PUBLICATIONS

Chang YC, Jin Z, Li Km Zhou J, **Yim W**, Yeung J, Cheng Y, Retout M, Creyer M, Fajtova P, He T, Chen X, O'Donoghue AJ, Jokerst JV. Peptide valence-induced breaks in plasmonic coupling, *Chemical Science* 2023, 14, 2659 - 2668

Cheng Y, Clark AE, **Yim W**, Borum RM, Chang YC, Jin Z, He T, Carlin AF, Jokerst JV. Protease-responsive potential-tunable AIEgens for cell selective imaging of TMPRSS2 and accurate inhibitor screening, *Analytical Chemistry* 2023, 95, 7, 3789–3798

Yim W, Zhou J, Sasi L, Zhao J, Yeung J, Cheng Y, Jin Z, Johnson W, Xu M, Palma-Chavez J, Fu L, Qi B, Retout M, Shah N, Bae J, Jokerst JV. 3D-bioprinted phantom with human skin phototypes for biomedical optics, *Advanced Materials* 2022, 202206385

Jin Z, Li Y, Li K, Zhou J, Yeung J, Ling C, **Yim W**, He T, Cheng Y, Xu M, Creyer MN, Chang Y, Fajtová P, Retout M, Qi B, Li S, O'Donoghue AJ, Jokerst JV. Peptide amphiphile mediated co-assembly for nanoplasmonic sensing, *Angewandte Chemie International Edition* 2022, 202214394

Creyer MN, Jin Z, Retout M, **Yim W**, Zhou J, Jokerst JV. Gold-silver core-shell nanoparticle crosslinking mediated by protease activity for colorimetric enzyme detection, *Langmuir* 2022, 38, 14200−14207

Jin Z, Ling C, Li Y, Zhou J, Li K, **Yim W**, Yeung J, Chang Y, He T, Cheng Y, Fajtová P, Retout M, O’Donoghue AJ, Jokerst JV. Spacer Matters: All-peptide-based ligand for promoting interfacial proteolysis and plasmonic coupling, *Nano Letters* 2022, 22, 8932−8940

Retout M, Jin Z, Tsujimoto J, Mantri Y, Borum R, Creyer MC, **Yim W**, He T, Chang Y, Jokerst JV. Di-arginine additives for dissociation of gold nanoparticle aggregates: A matrix-insensitive approach with applications in protease detection, *ACS Applied Materials & Interfaces* 2022, 14, 52553−52565

Qi B, Hariri A, Nezhad R, Fu L, Li Y, Jin Z, **Yim W**, He T, Cheng Y, Zhou J, Jokerst JV. A miniaturized ultrasound transducer for monitoring full-mouth oral health: a preliminary study, *Dentomaxillofacial Radiology* 2022, 51: 20220220

Xu M, Zhou J, Cheng Y, Jin Z, Clark AE, He T, **Yim W**, Chang YC, Wu Z, Fajtova P, ODonoghue AJ, Carlin AF, Todd MD, Jokerst JV. A self-immolative fluorescent probe for selective detection of SARS-CoV2 Main Protease, *Analytical Chemistry* 2022, 94, 11728-11733

He T, Bradley DG, Xu M, Ko ST, Qi B, Li Y, Cheng Y, Jin Z, Zhou J, Sasi L, Fu, L, Wu Z, Zhou J, **Yim W**, Chang YC, Hanna JV, Luo J, Jokerst JV. Bio-inspired degradable polyethylenimine/calcium phosphate micro-/nano- composites for transient ultrasound and photoluminescence imaging, *Chemistry of Materials* 2022, 34, 7220-7231

Cheng Y, Clark AE, Zhou J, He T, Li Y, Borum RM, Creyer MN, Xu M, Jin Z, Zhou J, **Yim W**, Wu Z, Fajtova P, O'Donoghue AJ, Carlin AF, Jokerst JV. Protease-responsive peptide conjugated mitochondrial-targeting AIEgens for selective imaging and inhibition of SARS-CoV-2-infected cells, *ACS Nano* 2022, 16, 8, 12305-12317

Yim W, Mantri Y, Jokerst JV. Real-time tomography of the human brain. *Nature Biomedical Engineering* 2022*,* 6, 499-500

Fu L, Jin Z, Qi B, **Yim W**, Wu Z, He T, Jokerst JV. Synchronization of RF data in ultrasound open platforms (UOPs) for high-accuracy and high-resolution photoacoustic tomography using the "Scissors" programming method, *IEEE Transactions on Ultrasonics, Ferroelectrics, and Frequency Control* 2022

Retout M, Mantri Y, Jin Z, Zhou J, Noel G, Donovan B, **Yim W**, Jokerst JV. Peptide-induced fractal assembly of silver nanoparticles for visual detection of disease biomarkers, *ACS Nano* 2022, 16, 4, 6165-6175

Shi J, Zhang R, Zhou J, **Yim W**, Jokerst JV, Zhang Y, Mansel BW, Yang N, Zhang Y, Ma, J. Supramolecular assembly of multifunctional collagen nanocomposite film via polyphenol-coordinated clay nanoplatelets, *ACS Applied Bio Materials* 2022, 5, 3, 1319-1329

Wu Z, Zhou J, Nkanga CI, Jin Z, He T, Borum RM, **Yim W**, Zhou J, Cheng Y, Xu M, Steinmetz NF, Jokerst JV. One-step supramolecular multifunctional coating on plant virus nanoparticles for bioimaging and therapeutic applications, *ACS Applied Materials & Interfaces* 2022, 14, 13692-13702

Jin Z, Yeung J, Zhou J, Cheng Y, Li Y, Mantri Y, He T, **Yim W**, Xu M, Wu Z, Fajtova P, Creyer M, Moore C, Fu L, Penny WF, O'Donoghue A, Jokerst JV. Peptidic sulfhydryl for interfacing nanocrystals and subsequent sensing of SARS-CoV-2 protease. *Chemistry of Materials* 2022, 34, 3, 12591268

Yim W, Borum RM, Zhou J, Mantri Y, Wu Z, Zhou J, Jin Z, Creyer M, Jokerst JV. Ultrasmall gold nanorod-polydopamine hybrids for enhanced photoacoustic imaging and photothermal therapy in second near-infrared window, *Nanotheranostics* 2022, 6(1), 79-90

Zhou J, **Yim W**, Zhou J, Jin Z, Xu M, Mantri Y, He T, Cheng Y, Fu L, Wu Z, Hancock T, Penny W, Jokerst JV. A fiber optic photoacoustic sensor for real-time heparin monitoring. *Biosensors and Bioelectronics* 2022, 196, 113692

Yim W, Takemura K, Zhou J, Zhou J, Jin Z, Borum RM, Xu M, Cheng Y, He T, Penny W, Miller III BR, Jokerst JV. Enhanced photoacoustic detection of heparin in whole blood via melanin nanocapsules carrying molecular agents. *ACS Nano* 2022, 16, 683–693

Jin Z, Mantri Y, Retout M, Cheng Y, Zhou J, Jorns A, Fajtova P, **Yim W**, Moore C, Xu M, Creyer M, Borum R, Zhou J, Wu Z, He T, Penny W, O'Donoghue A, Jokerst JV. A charge-switchable zwitterionic peptide for rapid detection of SARS-CoV-2 main protease. *Angewandte Chemie International Edition* 2022, 61 e202112995

Zhou J, Xu M, Jin Z, Borum R, Avakyan N, Cheng Y, **Yim W**, He T, Zhou J, Wu Z, Mantri Y, Jokerst JV. Versatile polymer nanocapsules via redox competition. *Angewandte Chemie International Edition* 2021, 60, 1–7

Creyer MN, Jin Z, Moore C, **Yim W**, Zhou J, Jokerst JV. Modulation of gold nanorod growth via the proteolysis of dithiol peptides for enzymatic biomarker detection. *ACS Applied Material & Interfaces* 2021, 13, 38, 45236–45243

Jin Z, Jorns A, **Yim W**, Wing R, Mantri Y, Zhou J, Zhou J, Wu Z, Moore C, Penny WF, Jokerst JV. Mapping aerosolized saliva on face coverings for biosensing applications. *Analytical Chemistry* 2021, 93, 31, 11025–11032

Zhou J, Creyer MN, Chen A, **Yim W**, Lafleur RPM, He T, Lin Z, Xu M, Abbasi P, Wu J, Pascal TA, Caruso F, Jokerst JV. Stereoselective growth of small molecule patches on nanoparticles. *Journal of the American Chemical Society* 2021, 143, 31, 12138–12144

Xu M, **Yim W**, Zhou J, Zhou J, Jin Z, Moore C, Borum RM, Jorns A, Jokerst JV. The application of organic nanomaterials for bioimaging, drug delivery, and therapy: spanning various domains. *IEEE Nanotechnology Magazine* 2021, 15, 4, 8–28

Yim W, Zhou J, Mantri Y, Creyer MN, Moore C, Jokerst JV. Gold Nanorod-Melanin Hybrids for Enhanced and Prolonged Photoacoustic Imaging in the Near-Infrared-II Window, *ACS Applied Materials & Interfaces*, 2021, 13, 14974–14984

Wu D, Zhou J, Creyer MN, **Yim W**, Chen Z, Messersmith PB, Jokerst JV. Phenolic-enabled Nanotechnology: Versatile Particle Engineering for Biomedicine, *Chemical Society Reviews*, 2021

Yim W, Cheng D, Patel SH, Kou R, Meng YS, Jokerst JV. KN95 and N95 Respirators Retain Filtration Efficiency despite a Loss of Dipole Charge during Decontamination. *ACS Applied Materials & Interfaces,* 2020, 12, 54473-54480

Shah SH, Garg AK, Patel SH, **Yim W**, Jokerst JV, Chao DL. Assessment of respiratory droplet transmission during the ophthalmic slit lamp exam: a particle tracking analysis, *American Journal of Ophthalmology*, 2020, 222, 76-81

Patel SH, **Yim W**, Garg AK, Shah SH, Jokerst JV, Chao DL. Assessing the Physiological Relevance of Cough Simulators for Respiratory Droplet Dispersion, *Journal of Clinical Medicine*, 2020, 9, 3002

FIELD OF STUDY

Major Field: Materials Science & Engineering

Studies in Biosensor, Bioimaging, Nanotechnology, Bio-responsive materials, 3D-bioprinting

ABSTRACT OF THE DISSERTATION

Phenolic-enabled nanoparticle engineering for biomedical applications

by

Wonjun Yim

Doctor of Philosophy in Materials Science & Engineering

University of California San Diego, 2023

Professor Jesse V. Jokerst, Chair

Phenolic materials are naturally occurring molecules present in a wide range of organisms, from fungi to bacterium, and from plants to animals. Their unique structural and chemical features can form covalent or non-covalent interactions with diverse materials including inorganic (*e.g.,* metal ion, metal oxide, silica, gold, silver), organic (*e.g.,* small molecule, polymers), and biomaterials (*e.g.,* proteins, peptides). Since phenolic materials can form multiple physicochemical interactions, highly-crosslinked robust structure, and are easy-to-synthesis, they have been used to create different types of nanostructures including phenolic nanoparticles, phenolic surface coating, and metal-organic frameworks. Phenolic-based

nanoengineering has strong promise in biomedical applications, such as drug delivery, contrast agents for biomedical optics, 3D bioprinting, and cancer therapy. In this dissertation, I will explain how phenolic materials can benefit nanomaterials and their role in bioimaging and biosensing applications.

First chapter reviews the hybrid gold nanorod-polydopamine nanoparticles which enhance photoacoustic performance more than bare gold nanorod both in *in vitro* and *in vivo*. The role of polydopamine shell in protection for gold nanorod is largely described.

Second chapter describes the impact of nanoparticle size in photoacoustic and photothermal therapy. Two different-sized gold nanorods were synthesized and coated with polydopamine. These two different sizes of polydopamine-coated gold nanorod show the same extinction peak (*i.e.,* 1064 nm); however, the small size of gold nanorod exhibits remarkable photoacoustic and photothermal performance compared to large sized particles.

Third chapter studies the polydopamine nanocapsules coated with organic dyes to detect heparin in whole human blood and plasma. The dye-coated polydopamine nanocapsules showed increased photoacoustic signal as a function of heparin concentration due to particle aggregation. Tannic acid-based nanoparticles were used as sacrificial substrates to synthesize nanocapsule structure. In this chapter, how phenolic-based nanocapsule structure can encapsule small molecular dyes and detect heparin in whole human blood will be described

Fourth chapter investigates the impact of skin tone on biomedical optics. Darker skin tones (*i.e.,* phototype) absorb and scatter more incident light before it reaches to target of interest. To understand the impact of skin tone, we mimic human skin using gelatin-based hydrogel and polydopamine nanoparticles (referred as synthetic melanin) in which they have similar chemical and optical properties compared to real melanin. Using 3D-bioprinted skin phantoms, multiple biomedical optics (photoacoustic, fluorescence, and photothermal) were extensively examined.

Fifth chapter describes a peptide-based particle dissociation of gold nanoparticle aggregates for protease detection. Gold nanoparticle aggregation is often hindered by matrix interference in biofluids, and limited utility with clinical samples. In this chapter, peptide-based reversible aggregation will be described to develop a simple and matrix-insensitive plasmonic-based biosensing platform.

CHAPTER 1. Gold nanorod-melanin hybrids for enhanced and prolonged photoacoustic imaging in the near-infrared-II window

1.1. Abstract

Photoacoustic (PA) imaging holds great promise as a noninvasive imaging modality. Gold nanorods (GNRs) with absorption in the second near-infrared (NIR-II) window have emerged as excellent PA probes because of their tunable optical absorption, surface modifiability, and low toxicity. However, pristine GNRs often undergo shape transition upon laser illumination due to thermodynamic instability leading to reduced PA signal after a few seconds of imaging. Here, we report monodisperse GNR-melanin nanohybrids where a tunable polydopamine (PDA) coating was conformally coated on GNRs. GNR@PDAs showed three-fold higher PA signal than pristine GNRs due to the increased optical absorption, cross-sectional area, and thermal confinement. More importantly, the PA signal of GNR@PDAs only decreased by 29% during the 5 min of laser illumination in NIR-II window while significant attenuation (77%) was observed for GNRs. The GNR@PDAs maintained 87% of its original PA signal *in vivo* even after 10 min of laser illumination. This PDA-enabled strategy affords a rational design for robust PA imaging probes and provides more opportunities for other types of photo-mediated biomedicine, such as photothermal and photodynamic regimens.

1.2. Introduction

Photoacoustic (PA) imaging is a light in/sound out approach and holds great promise as noninvasive imaging modality for biomolecular sensing and disease diagnosis.[1-3] It has improved penetration depth and spatiotemporal resolution versus pure optical approaches.[4-6] PA imaging can use endogenous or exogenous contrast media; a myriad of such exogenous contrast agents have been reported such as small-molecule NIR dyes[7] as well as metallic[8] and organic[9] nanoparticles. These have been engineered to image cells, tissues, and biological processes of interest.[10] Plasmonic metallic nanoparticles are particularly popular because of their facile surface modification, tunable localized surface plasmonic resonance (LSPR), high photothermal efficiency, and relatively inert biological activity in the human body.[11-14]However, extensive light-tissue interactions (e.g. scattering and absorbance) can attenuate the input light and impair the PA imaging thus leading to limited penetration depth and decreased imaging sensitivity.[4]

Gold nanorods (GNRs) have recently attracted immense attention to address this challenge for improving the imaging depth and sensitivity.[15-18] Specifically, GNRs with a high aspect ratio can absorb photons in the second near-infrared (NIR-II) window (1000–1700 nm) where biological tissues have lower background absorption.[19-22] The NIR-II window thus offers deeper light penetration and higher maximum permission exposure versus the visible spectral and NIR-I (650–900 nm) range.[23-25] One limitation of the GNRs is their anisotropic structure that is susceptible to deformation after laser illumination. GNRs are easily deformed upon NIR-I and NIR-II laser irradiation because of their thermodynamic instability: It is found that high pulsed laser induces the creation of point and line defects that grow into planar defects (e.g., multiple twins and stacking faults) in the interior of GNRs.[26, 27] Those defects migrate gold atoms at {110} facets to the more stable {100} and {111} facets to minimize their surface energy. [27] Thus, the additional laser energy can cause the rod to deform into a sphere. In addition, melting of GNRs is also observed under laser illumination, converting the shape into a sphere.[27-29] Consequently, the absorbance in the infrared region decays over time (< 1 min) as the absorption peak blue shifts. Thus, the PA signal also attenuates because of the strong correlation between absorption and PA signal.[13] This problem limits the utility of GNRs in PA imaging. Solutions to this problem include coating the GNRs with a stabilizing layer such as silica and metal-organic frameworks.[30, 31] In contrast to these methods, we report organic molecule-mediated formation of GNR-melanin hybrids (GNR@PDAs), which enables a protective polydopamine (PDA) layer on GNRs to improve the optical absorption and thermal confinement.

Melanin is a natural pigment with multiple roles in biology such as photoprotection, metal ion chelation, and free radical scavenging.[32-35] Here, we used auto-oxidation of dopamine into PDA to successfully coat synthetic melanin on the surface of GNRs (Figure 1.1). PDA coating not only serves as a robust polymeric armor for the underlying GNRs but also exhibits a broadband absorption (400 – 1300 nm) suggesting that it may enhance the PA imaging while also protecting the underlying GNR.[36-38] Furthermore, it has been proved that PDA coating can serve as a biocompatible layer, reducing in vivo toxicity of the coated material.[39-41] No obvious toxicity or change in animal behavior was observed in our in vivo experiments; a detailed necroscopy will be performed in subsequent studies. Thus, we investigated PA efficiency of GNR@PDAs in both NIR-I (e.g., 680 nm) and NIR-II (e.g., 1064 nm) lasers versus bare GNRs. Moreover, we compared time-dependent PA signal amplitude and optical extinction of GNR@PDAs with bare GNRs to verify the improved structural and thermal stability of the GNR@PDAs. Lastly, we further removed the GNR core to make rod-shaped PDA capsules to investigate the function of the PDA shell during PA signal generation. This method is a versatile strategy to improve the photothermal efficiency and stability of nanoparticles for biomedical and environmental applications.[33]

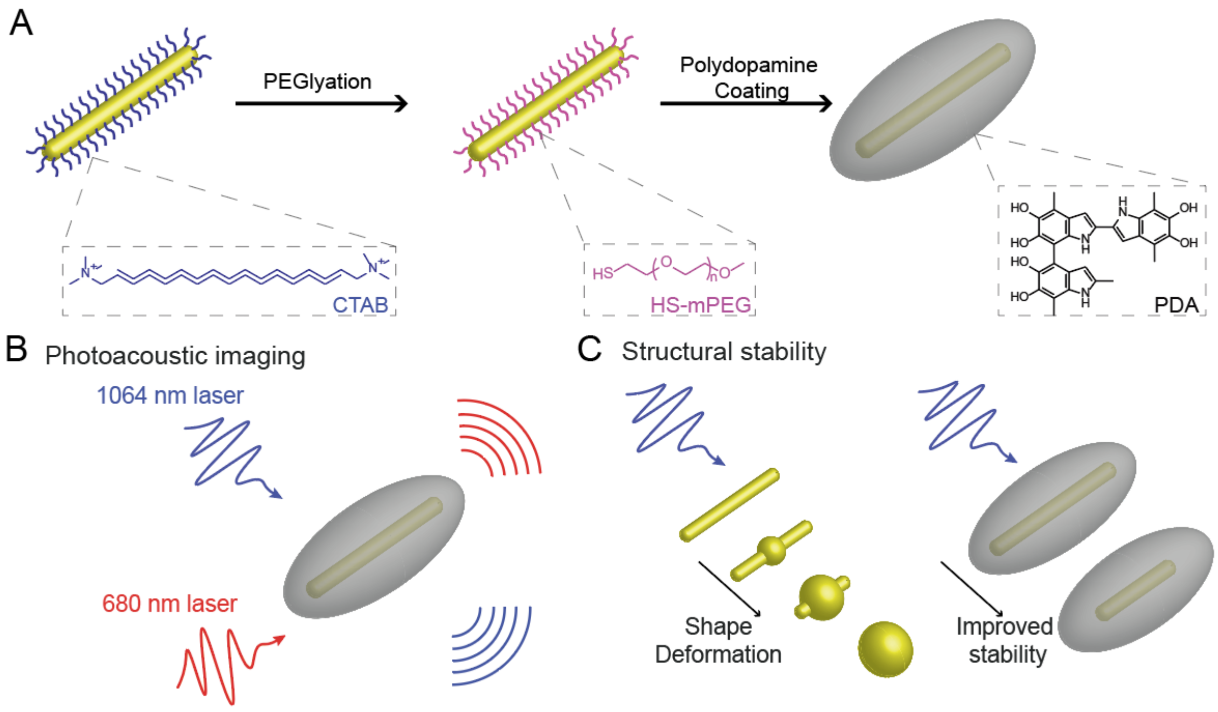

Figure 1.1 Schematic of synthesis and PA imaging of GNR@PDAs
(A) Schematic of the synthesis of GNR@PDA. (B) Comparative photoacoustic signals generated by GNR@PDAs at NIR-I (e.g., 680 nm) and NIR-II (e.g., 1064 nm) irradiations. (C) Morphological deformation of GNR when exposed to the high fluence pulsed laser while GNR@PDAs show the enhanced structural and thermal stability.

1.3. Materials and methods

1.3.1. Synthesis of GNR Particles

We used a seed-mediated growth[42] for the synthesis of GNR particles with a high aspect ratio of 7.7 ± 3.3. Briefly, a seed solution was made by mixing an aqueous solution of 5 mL of CTAB (0.2 M) and 5 mL of $HAuCl_4$ (0.5 mM). Then, 600 µL of $NaBH_4$ (10 mM) was quickly injected to the seed solution under vigorous stirring at 1200 rpm. After 15 s of vigorous $NaBH_4$ reaction, the seed solution was incubated in water bath at 30 °C for 1 h.

A growth solution was made by adding 10 mL of CTAB (0.2 M), 10 mL of $HAuCl_4$ (1.0 mM), and 120 μL of $AgNO_3$ (0.1 M) sequentially. Then, 650 μL of hydroquinone (0.1 M) was added under vigorous stirring at 1200 rpm. The color of the growth solution tuned from yellow to transparent. Finally, 320 μL of the seed solution was injected to the growth solution under vigorous stirring at 1100 rpm. After 15 s of vigorous reaction, the solution was incubated in water bath at 30 ºC for 12 hours before being purified with two centrifugation cycles at 7,500 g for 10 min.

1.3.2. Synthesis of PEGylated GNR Particles

CTAB on the surface of GNRs was replaced by HS-mPEG via ligand exchange. The CTAB-stabilized GNR was dispersed in 2 mL water and added to 4 mL of HS-mPEG (5 mg/mL in water, 1 mM) under vigorous stirring at 1,000 rpm for 6 hours. The resulting PEGylated GNRs were purified by centrifugation at 7,500g for 10 min to remove the excess of HS-mPEG. The PEGylated GNRs were redispersed in the water for future use.

1.3.3. Synthesis of PDA Coated GNR Particles

Typically, 200 μL of concentrated PEGylated GNRs was dispersed in 2 mL bicine buffer (10 mM, pH 8.5) followed by 50, 100, 200, and 300 μL of dopamine solution (4 mg/mL in water) to make different coating thickness. The reaction solution was stirred at 1000 rpm for 12 hours, and the resulting dark-brown product was purified by centrifugation at 7,500 g for 10 min. The GNR@PDAs were redispersed in the water for future use.

1.3.4. Synthesis of Rod-Shaped PDA Capsules

Typically, 100 μL of concentrated GNR@PDAs (0.5 μg/mL) in water was dispersed in 900 μL of DMF solvent and centrifuged at 7,500 g for 10 min to exchange the solvent. Then, GNR@PDAs were redispersed in 900 μL DMF, and 100 μL of $CuCl_2$ (50 mM) was added to remove GNR core. The reaction solution was incubated at 60 ºC for 6 hours with generous stirring at 600 rpm before being purified with centrifugation at 6,000 g for 10 min.

1.3.5. Stability test of PDA coated GNR Particles

In brief, 50 µL of concentrated GNR@PDAs (0.05 µg/mL) were incubated in 100 µL of HCl (10 mM, pH ≈ 2), NaOH (10 mM, pH ≈ 12), NaCl (10 mM), cell culture medium (DMEM) with 20%, 10%, or 5% of mouse serum, respectively for 1 h. Then, 100 µL of the sample was used for the DLS measurement.

1.3.6. In vivo Subcutaneous Injection

All animal experiments were performed in accordance with NIH guidelines and approved by the Institutional Animal Care and Use Committee (IACUC) under protocol S15050 at the University of California, San Diego. Matrigel was used to image nanoparticle in subcutaneous area of a murine model.[43] 150 µL of GNR@PDA in 50% of Matrigel was subcutaneously injected into the mice (n = 3) and imaged 10 min for testing PA signal stability. We used Matrigel only as negative controls. All images were processed by using the Vevo LAB 3.1.0 software.

1.3.7. Instrumentation

TEM samples were examined via a JEOL JEM-1400Plus operating at 80 kV. TEM images were taken by using a Gatan 4K digital camera, and 10 µL of the samples was dropped onto the copper grids for TEM sample preparation. TEM images were processed by using ImageJ software (Bethesda, MD, USA).[44] SEM samples were analyzed via FEI Apreo operating at voltage of 10 kV and the current of 0.10 nA. 10 µL of the samples was dropped on the silicon wafer for the sample preparation. EDX samples were examined by using a ThermoFisher Talos 200X transmission electron microscope operating at 200 kV. STEM images were acquired by using a

Velox software, and the images were processed with Thermo Scientific software. Hydrodynamic diameter and zeta potential of the sample were calculated by using a Malvern Instrument Zetasizer ZS 90. 100 μL of the sample was diluted in 900 μL of distilled water for the measurement. UV–vis–NIR absorption spectra of the sample was measured by using a Perkin Elmer UV-vis-NIR spectrophotometer. Absorbance was read from 400 – 1380 nm with a step size of 2 nm. The ICP-MS analysis was conducted by using a Thermo Scientific ICAP RQ ICP-MS in the Environmental and Complex Analysis Laboratory at UC San Diego. Samples were prepared and digested by using 4% HNO_3 solution and *aqua regia* for the measurements. A Visualsonics Vevo 2100 LAZR imaging system was used to acquire PA imaging from 680 nm to 1064 nm. Samples were imaged by using a 21 MHz-centered LZ 250 transducer. The peak energy is 45 ± 5 mJ at 20 Hz at the source. The specimens were aligned at a depth of 1 cm from the transducer. Laser was optimized and calibrated before the measurement.

1.3.8. Photothermal conversion efficiency of GNR and GNR@PDA

Typically, 1 mL of GNR and GNR@PDA samples (O.D. ≈ 1) were placed in quartz cuvette to measure the photothermal conversion efficiency. We used 1064 nm laser, and the laser power was set up to 1.0 W/cm^2. Temperature was determined by a FLIR C5 camera. The recorded temperature was used to calculate the photothermal conversion efficiency.[38]

1.3.9. Data Analysis

All photoacoustic data was proceeded by ImageJ software.[44] Raw image was converted to 8-bit images. The mean value and standard deviation of the PA intensity was then calculated based on the five regions of interest per tube. Statistical significance was determined by using GraphPad software. The statistical significance was calculated with the two-tailed PA intensity of GNR@PDA's t-test; p-values <0.01 were considered to be significantly different.

1.4. Results and discussion

1.4.1. Synthesis and Characterization

To obtain GNRs with LSPR in the NIR-II spectral range, we used a seed-mediated method[42] to prepare GNRs with dimensions of 95.07 ± 6.92 nm × 12.46 ± 1.36 nm (aspect ratio = 7.7) (Figure 1.2A and Table 1). The GNRs stabilized with cetyltrimethylammonium bromide (CTAB) had positively charged surfaces (45.47 ± 1.12 mV). Adding dopamine directly to CTAB-stabilized GNRs thus caused immediate aggregation because of the strong electrostatic interactions between negative charged dopamine and positive charged GNRs. As a solution, we replaced CTAB with a methoxyl PEG thiol (HS-mPEG). The zeta potential of GNRs decreased to –10.2 ± 0.44 mV after ligand exchange indicating successful conjugation of HS-mPEG. According to Flory-Huggins theory, polymer conformations attached to the interface can be described by Flory radius ($F = n^{3/5}\alpha$).[45] Here, n is the number of monomers per chain, and a is a monomer size (α =3.5Å for PEG).[45, 46] Based on this theory, PEG chains can form either mushroom or brush conformations depending on the grafting density. For example, if the distance (D) between the attachment points of PEG to a surface of GNR is lower than F ($D < F$), then the PEG chains will form a mushroom conformation. They will form a brush conformation if the grafting density is high ($D > F$).[46] At a fixed concentration of CTAB-stabilized GNR (0.2 µg/mL), 1 mg of HS-mPEG was needed to make brush conformation based on the calculation (see Supporting Information). We used 10 mg, 2 mg, 1 mg, 1 µg, and 0.5 µg of HS-mPEG for ligand exchange of the GNRs. The PDA coating on the surface of GNR was unstable when we used 1 µg and 0.5 µg of HS-mPEG while PDA coating became uniform and stable when we used 10 mg, 2 mg, and 1 mg of HS-mPEG (Figure 1.2B–C), indicating that the brush conformation is an ideal condition for the PDA coating. Zeta potential data showed that all PEGylated GNRs had a less positive charged surface compared to the CTAB-stabilized GNRs (Figure 1.2D). Furthermore, PEGylated GNRs with the brush conformation showed improved colloidal stability due to the steric effect and slightly negative charged of PEG (Figure 1.3).

The formation of PDA coating is easily induced by polymerization of dopamine in alkaline conditions. Under basic conditions ($pH > 7.5$), dopamine is first oxidized to the reactive dopamine quinones[47] that undergo successive oxidation, intramolecular cyclization, oligomerization, and self-assembly to form PDA.[42, 48, 49] Together with the universal adhesive properties of PDA, we uniformly coated PDA on the surface of the PEGylated GNRs probably due to metal chelation and hydrogen bonding.[50] Transmission electron microscopy (TEM) and scanning electron microscopy (SEM) clearly showed monodisperse GNR@PDA nanohybrids in aqueous solution (Figure 1.2E – G and Figure 1.4) in bicine buffer (pH 8.5). The PDA thicknesses were easily tunable from 15 nm to 150 nm by adjusting the amount of dopamine feed (4 mg/mL) used for the reaction (Table 1). GNRs with PDA thicknesses of 15 nm, 25 nm, 50 nm, and 70 nm (referred as GNR@PDA15, GNR@PDA25, GNR@PDA50, and GNR@PDA70) were formed by controlling the amount of dopamine used at a fixed GNR concentration (Figure 1.2C, 1.2E–G), but the GNRs aggregated when we added excess dopamine (2.4 mg of dopamine was added to 40 μg of GNRs).

The color of the solution changed from brown to black and became darker as more dopamine was added (Figure 1.2H). GNR@PDA showed broadband optical extinction from UV and visible to NIR spectral range, and the light extinction was proportional to the PDA thickness. Versus GNRs that featured a longitudinal LSPR at 1090 nm, the absorption peaks red-shifted to 1246 nm, 1284 nm, 1286 nm, and 1284 nm for GNR@PDA15, GNR@PDA25, GNR@PDA50, and GNR@PDA70, respectively. Moreover, longitudinal peaks of GNR@PDA in the NIR-II range were no longer distinguished when the PDA thickness became 150 nm (Figure 1.5). Electron-dispersive X-ray spectroscopy (EDX) mapping indicated that GNR@PDA nanohybrids were composed of Au, C, N, and O confirming the core-shell nanostructure of the GNR-melanin hybrids (Figure 1.2I). Zeta potential data revealed that the PEGylated GNRs became more negative charged after PDA coating due to the negative charge of the PDA (Figure 1.2J). Dynamic light scattering (DLS) data showed that GNR@PDA25, GNR@PDA50, and GNR@PDA70 had relatively narrow size distributions (polydispersity index (PDI) < 0.1), and the size of the GNR@PDA nanohybrids increased with thicker PDA coating (Figure 1.2K).

Table 1.1 Material information of GNR and GNR@PDA nanohybrids.
Average diameter, length, volume, PDA thickness, and mean aspect ratio were calculated from 15 measurements.

	Diameter (D, nm)	Length (L, nm)	Volume (V, nm³)	PDA thickness (nm)	Mean aspect ratio
GNR	12.46 ± 1.36	95.07 ± 6.92	11666.1 ± 2468.7	0	7.73 ± 1.10 (rods)
GNR@PDA15	43.34 ± 2.77	108.7 ± 9.25	160916 ± 24781.3	15.37 ± 1.08	
GNR@PDA25	64.58 ± 4.76	131.35 ± 8.96	432813 ± 72065.3	25.06 ± 1.95	
GNR@PDA50	117.41 ± 5.89	169.76 ± 8.27	1839200 ± 187736	52.65 ± 3.82	
GNR@PDA70	155.25 ± 7.95	215.24 ± 9.99	4088595 ± 523600	73.23 ± 3.99	

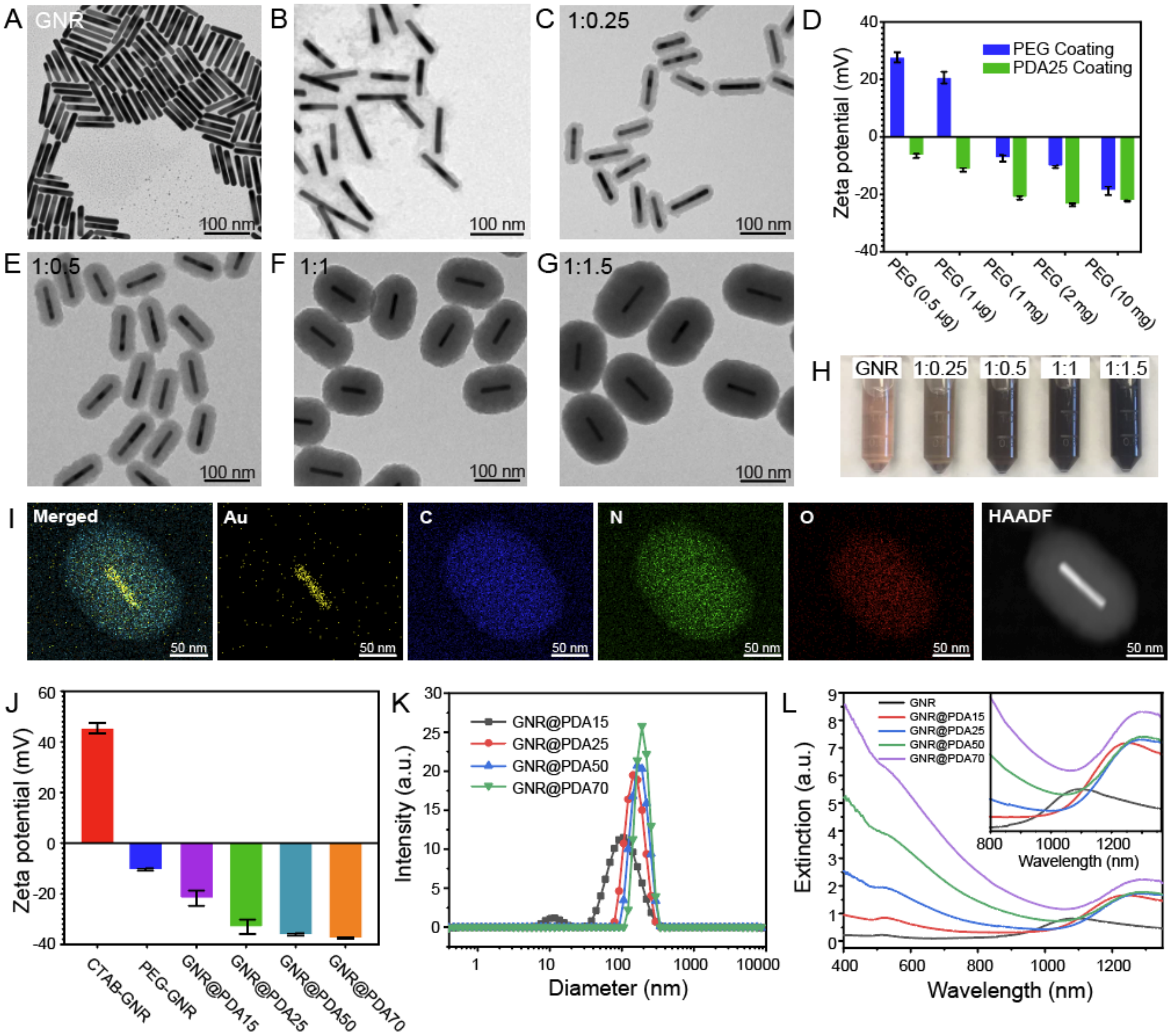

Figure 1.2 Controllable size of GNR@PDAs

(A) TEM images of GNRs. (B-C) TEM images of PDA-coated GNRs where PEG chains had (B) mushroom and (C) brush conformations. (D) Zeta potential of PEGylated GNRs before and after PDA coating (PDA thickness = 25 nm). We used different amounts of HS-mPEG (10 mg, 2 mg, 1 mg, 1 µg, and 0.5 µg) for ligand exchange of the GNRs to make either mushroom or brush conformations of PEG chains. (C, E-F) TEM images with different PDA thicknesses: (C) 15 nm, (E) 25 nm, (F) 50 nm, and (G) 70 nm. The mass concentration of GNR was fixed at 0.2 µg/mL, and 1:0.25, 1:0.5, 1:1, and 1:1.5 indicate the mass ratio of GNR to dopamine concentrations. (H) The color of GNR and GNR@PDA solutions. (I) EDX and HAADF images of GNR@PDA. EDX result shows core-shell nanostructure of GNR@PDA. GNR@PDA includes gold (Au), carbon (C), nitrogen (N), and oxygen (O). (J) Zeta potential of GNR and GNR@PDAs. (K) DLS measurements of GNR@PDA15, GNR@PDA25, GNR@PDA50, and GNR@PDA70. (L) UV–vis–NIR absorption spectra of GNR and GNR@PDAs. Gray, red, blue, green, and purple lines represent GNR, GNR@PDA15, GNR@PDA25, GNR@PDA50, and GNR@PDA70, respectively. Inset image is the magnified absorption spectra from 800 nm to 1350 nm. The error bar represents standard deviation of five measurements.

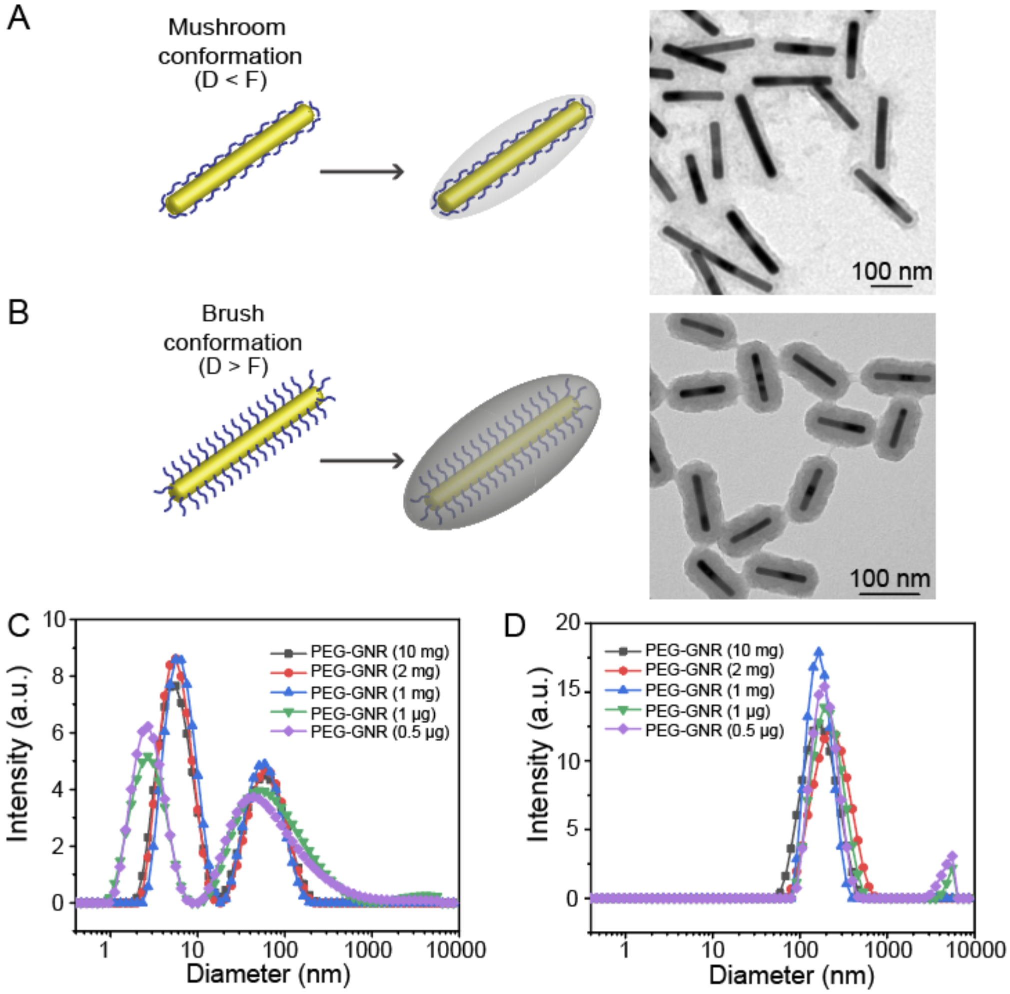

Figure 1.3 Mushroom and brush confirmation.

PEG chains can form either mushroom or brush conformations. (A) PEG chains formed the mushroom conformation and PDA coating was instable when we used a small amount of PEG-SH. (B) PEG chains made the brush conformation when we used large amount of PEG-SH (>1 mg). PDA coating became stable and uniform, showing colloidal stability. (C) DLS data of PEGylated GNRs at different concentration of PEG-SH: 10 mg, 2 mg, 1 mg, 1 μg, and 0.5 μg. (D) DLS data of PDA coated GNRs replaced by different amounts of PEG chain. GNRs were aggregated, and PDA coating was unstable when we used 1 μg, and 0.5 μg (mushroom conformation). The mass concentration of GNR was 200 μg/mL, and we used 1:1 ratio of GNR to dopamine concentration (4 mg/mL).

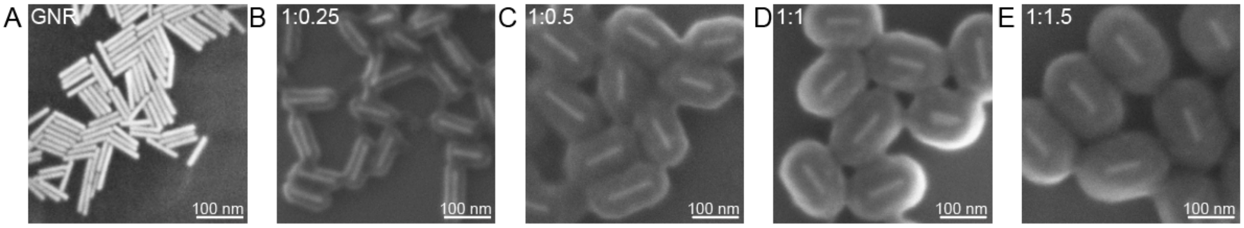

Figure 1.4 SEM images of GNR@PDAs
(A) GNR, (B) GNR@PDA15, (C) GNR@PDA25, (D) GNR@PDA50, and (E) GNR@PDA70.

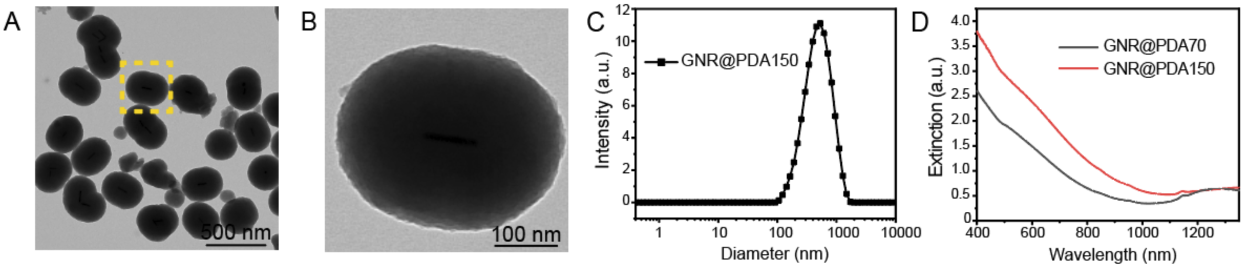

Figure 1.5 GNR@PDA150
(A) GNRs aggregated when we used an excess of dopamine. (B) The yellow dotted square shows TEM image of a single GNR@PDA particle with PDA thickness of 150 nm (referred as GNR@PDA150). (C) DLS data of GNR@PDA150 showed a large size distribution (PDI ~ 0.2). (D) Optical extinction of GNR@PDA70 and GNR@PDA150. Longitudinal peak of GNR@PDA150 was not shown while GNR@PDA70 exhibited longitudinal peak around 1300 nm. This result indicated that longitudinal peak of GNR@PDA was no longer distinguishable when the PDA coating thickness became 150 nm.

1.4.2. Photoacoustic performance of GNR@PDAs

PA signal and excitation energy are influenced by nanoparticle concentration.[51] Thus, we used inductively coupled plasma mass spectrometry (ICP-MS) to measure GNR concentration according to the number of Au ions in each sample (Figure 1.6). UV–vis–NIR absorption spectra data showed that the GNR exhibited two absorption peaks at 512 nm and 1090 nm, which correspond to the transverse and longitudinal LSPR, respectively (Figure 1.2L). The longitudinal peak of the GNR was significantly redshifted when PDA was coated due to the increased refractive index (n) of the surrounding medium ($n_{PDA} \approx 1.7$) compared to the GNRs that were surrounded by the water ($n_{H2O} \approx 1.3$).[52] More importantly, the optical extinction of GNR@PDAs was higher than GNRs due to the absorbance of melanin and the increased size of hybrid nanoparticles. The increase in absorption intensity is important because PA efficiency is a function of the optical and thermoelastic properties of the nanoparticles. The mechanism of PA signal generation has been understood by thermoelastic expansion model according to Equation 2.[1, 13]

$$\rho_o = (\frac{\beta c^2}{C_p})\mu_\alpha F \qquad (2)$$

where ρ_o, β, c^2, C_p, μ_α, and F are thermoelastic expansion, thermoelastic expansion coefficient, speed of the light, specific heat capacity, absorption coefficient, and laser fluence, respectively. According to this mechanism, photons absorbed by nanoparticles are converted to heat with an increase in temperature leading to thermoelastic expansion. This expansion generates transient acoustic waves that can be measured by an ultrasound transducer.[51]

To understand the PA performance of GNR@PDA systems, we first used a NIR-I laser where PDA largely absorbs light (GNRs have small absorption in NIR-I window). Figure 1.7A and

Figure 1.7B show a PA image and its corresponding quantitative PA intensity of GNRs and GNR@PDAs when irradiated at 680 nm. PA signals of GNR@PDA25, GNR@PDA50, and GNR@PDA70 were at least 2-fold higher than that of pristine GNRs under 680 nm laser irradiation. In addition, GNR@PDAs with thicker PDA coating showed higher PA signal amplitude: GNR@PDA50 showed 4-fold higher PA signal than GNR@PDA15 at the same gold mass concentration (0.04 μg/mL).

This increase in PA signal can be understood via three parameters: optical absorption, absorption cross-sectional area, and photothermal conversion efficiency. First, melanin-like PDA coating on GNRs showed at least 2-fold higher optical absorption (Figure 1.2L), and absorption is proportional to PA signal amplitude. Both GNR core and its PDA coating of GNR@PDA absorbed photons. Thus, the GNR@PDAs absorbed 2-fold more photons than pristine GNRs alone. Second, the absorption cross-sectional area of GNR@PDA as measured by electron microscopy was larger than the GNRs. More specifically, the absorption cross-sectional area of GNR@PDA15 was 4-fold larger than that of GNR. The cross-sectional area became larger as the PDA coating became thicker (Figure 1.8).

Finally, thermal confinement from the PDA shell contributes to PA signal.[53] Thermal energy increased in the nanoparticles diffuses to the surrounding medium during the photon absorption. Thus, thermal expansion of the nanoparticles is influenced by their surrounding environment. The heat capacity of water ($C_{p,\ H2O} \approx 4.2$) is 2.5-fold higher than that of PDA ($C_{p,\ PDA} \approx 1.6$) indicating that the GNR surrounded by water is more easily cooling down versus the GNR surrounded by PDA.[54] Therefore, GNR@PDA can have higher thermoelastic expansion than GNR due to its lower heat capacity of surrounding condition (see Equation 2). In addition, the thermal conductivity of water ($k_{H2O} \approx 0.59$) is 4-fold larger than PDA ($k_{PDA} \approx 0.13$), meaning that heat accumulation easily occurs in GNR@PDA via reduced thermal conductance.[54]

We then evaluated the PA signal generation of GNR@PDA in the NIR-II window where GNRs have a large optical absorption. Figure 1.7C and Figure 1.7D show PA images and the corresponding quantitative PA intensity when irradiated at 1064 nm. GNR@PDAs showed similar results as in 680 nm: GNR@PDA25, GNR@PDA50, and GNR@PDA70 had higher PA signal than pristine GNRs, and the PA signal amplitude increased as the PDA coating became thicker. Interestingly, GNR@PDA15 showed weaker PA signal than GNR. GNR@PDA15 had 2-fold lower absorption coefficient at 1064 nm versus GNRs because of the redshifted absorption peak (Figure 1.2L). This result indicates that the optical absorption of the nanoparticle largely affects PA signal generation. In addition to the optical absorption, the laser fluence (F) also plays an important role in generating PA signal (see Equation 2). The laser fluence at 680 nm was 3 mJ higher than at 1064 nm, and the GNR and GNR@PDA nanohybrids showed higher PA signal at 680 nm than at 1064 nm (Figure 1.7B and Figure 1.7D). Lastly, the optical extinction of GNR linearly increased with elevated concentration according to the Beer-Lambert law[55] (Figure 1.9), thus leading to a linear increase in PA signal of GNR and GNR@PDA50 at 1064 nm irradiation (Figure 1.7E–F).

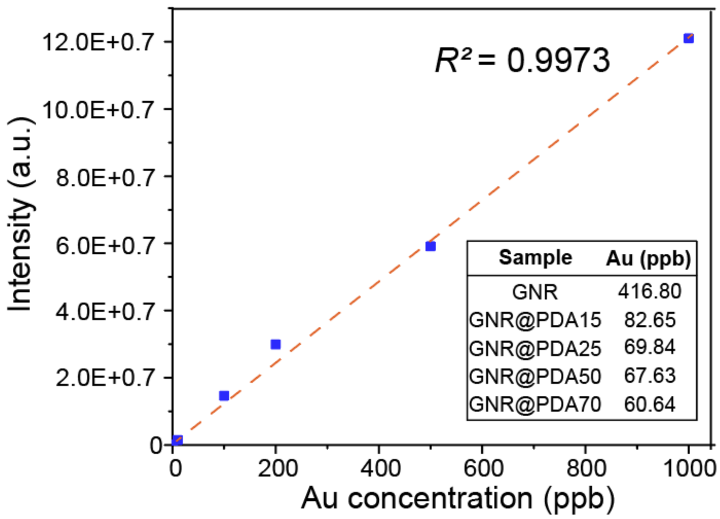

Sample	Au (ppb)
GNR	416.80
GNR@PDA15	82.65
GNR@PDA25	69.84
GNR@PDA50	67.63
GNR@PDA70	60.64

Figure 1.6 ICP-MS data
The number of GNRs in GNR, GNR@PDA15, GNR@PDA25, GNR@PDA50, and GNR@PDA70 was calculated by using ICP-MS method. Inset table indicates the concentration of Au ions in each sample solution.

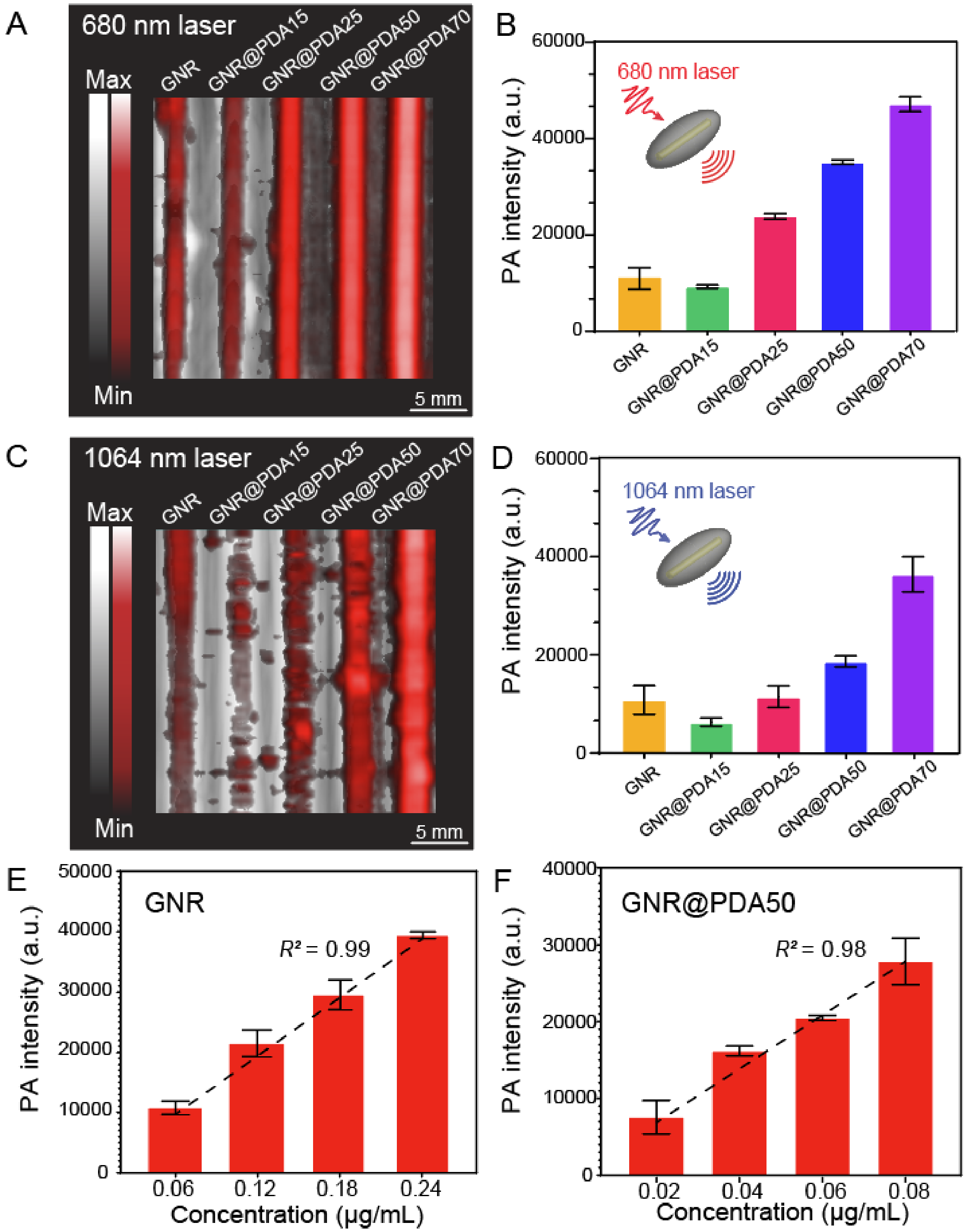

Figure 1.7 PA peformance of GNR@PDA.
(A, B) PA image and its corresponding PA intensity when illuminated by a 680 nm laser. (C, D) PA image and its corresponding PA intensity when illuminated by a 1064 nm laser. GNR@PDAs showed a higher PA signal amplitude than pristine GNRs. (E) PA intensity of GNR and (F) PA intensity of GNR@PDA50 with the elevated concentration when illuminated by a 1064 nm laser. Figure 1.9 shows the PA intensity of GNR@PDA50 irradiated at 680 nm laser. The error bars represent the standard deviation of five regions of interest.

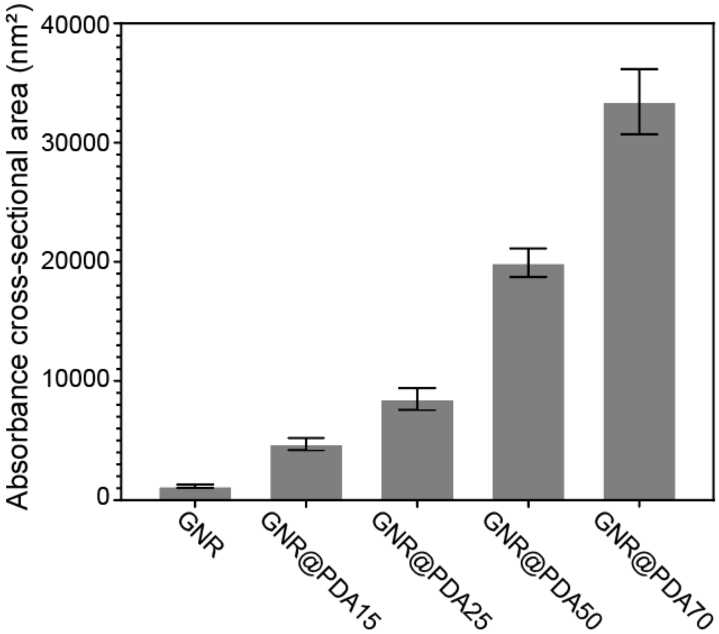

Figure 1.8 Absorption cross-sectional area of GNR@PDAs
Absorption cross-sectional area was exponentially increasing as PDA coating became thicker. Absorption cross-sectional area (nm^2) of GNR@PDA nanoparticles was calculated by the formula of diameter (D) × length (L) based on the TEM images. Error bar represents the standard deviation of fifteen GNR@PDA nanoparticles.

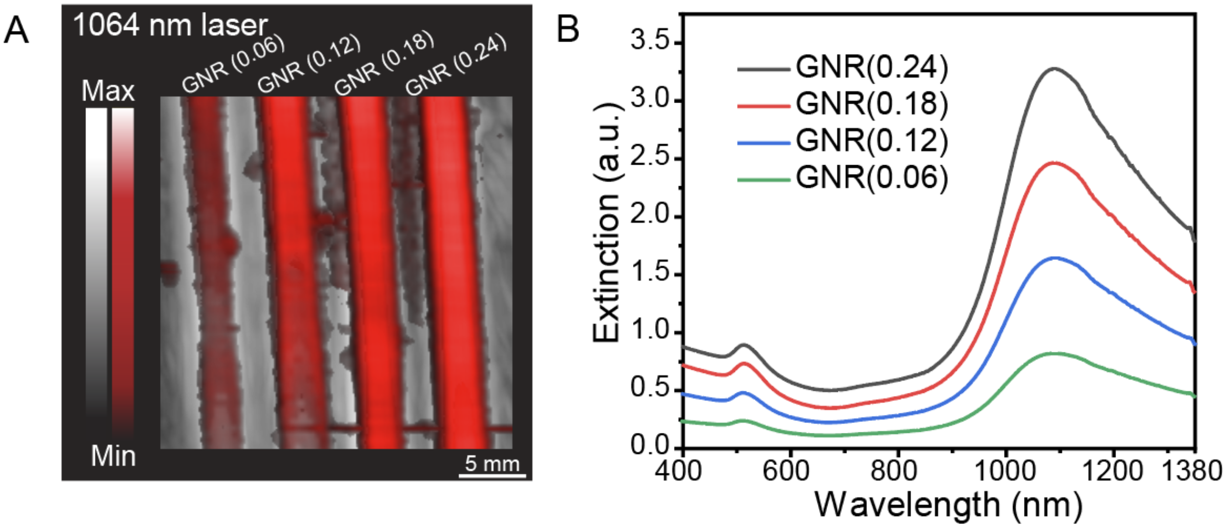

Figure 1.9 PA signal of GNR
(A) PA image when illuminated with a 1064 nm laser, and (B) optical extinction of GNR at various concentrations (240, 180, 120, and 60 μg/mL). The optical absorption is proportional to the concentration leading to higher PA signal.

1.4.3. Thermal and structural stability of GNR@PDAs

Under the laser illumination, free electrons undergo a collective dipolar oscillation generating high local heat energy that leads to the migration of atoms at {110} facets[26, 56] (Figure 1.10). The atomic rearrangement transforms the anisotropic structure of GNRs into a spherical shape that can minimize surface energy (Figure 1.10). The shape transition of GNRs can be also explained by the absorbance decrease according to Equation 4.[56]

$$[(A_{\lambda,0} - A_{\lambda,1})/\sigma b)] = \rho \sigma^{(n)} I^{(n)} \quad (4)$$

where $A_{\lambda,0}$ is the sample absorbance at a given wavelength (λ) before the laser illumination, $A_{\lambda,1}$ is the sample absorbance at a given wavelength (λ) after the laser illumination, σ is the absorption cross-section of the nanoparticles, b is the path length, ρ is the density of the nanoparticles, and n is the number of photons absorbed. I is laser fluence. Equation 4 can be rearranged to (see Supporting Information)

$$\ln [(A_{\lambda,0} - A_{\lambda,1})/ A_{\lambda,0}] = \mathrm{n}\ln(\mathrm{I}) + \mathrm{constant} \quad (5)$$

where $(A_{\lambda,0} - A_{\lambda,1})/ A_{\lambda,0}$ represent the percentage of absorbance changes during the laser illumination. Hence, the shape transition of GNRs was confirmed by a decrease in optical extinction during the laser illumination (Figure 1.11A). The longitudinal peak of GNRs exhibited an 84% decrease in intensity and was blue-shifted after 5 min of the illumination, which corresponds to the TEM observations where most GNRs became spherical (Figure 1.11B). In contrast, GNRs covered by a PDA shell retained their rod-like shape and optical extinction. Specifically, GNRs with a PDA thickness of 50 nm (referred as GNR@PDA50) maintained their rod shapes, and the longitudinal peak of GNR@PDA50 showed an 11% decrease in intensity after 5 min of the illumination (Figure 1.11C–D). In addition, the longitudinal peaks of GNR@PDAs weakened less with increasing PDA coating thickness. Longitudinal peaks of GNR@PDA15, GNR@PDA25, and GNR@PDA70 decreased 47%, 33%, and 9%, respectively and maintained their rod-like shape (Figure 1.12–1.13). PDA coating did not melt even after 15 min of laser illumination (Figure 1.14).

The PDA coating prohibits photon-induced shape transition process and improves the thermal stability of GNRs. GNRs with a thicker PDA coating showed less of a drop in optical absorption at 680 nm and 1064 nm (Figure 1.11E); GNR@PDA15, GNR@PDA25, GNR@PDA50, and GNR@PDA70 showed 48%, 42%, 15%, and 10% drop in absorbance at the wavelength of 1064 nm after 5 min of laser illumination. We also monitored the PA intensity of GNR and GNR@PDAs during the laser illumination. The PA signal amplitude of GNR decreased 73% after 5 min while GNR@PDA15, GNR@PDA25, GNR@PDA50, and GNR@PDA70 decreased 44%, 35%, 40%, and 25%, respectively (Figure 1.11F).

We hypothesize that PDA coating can stabilize the GNRs from the shape transition for two main reasons. First, the stiffness and chemical properties of the surrounding medium affects the shape transition.[26, 57] Gold atoms at the surface of GNR@PDAs are tightly pinned because of the aromatic PDA shell that is highly cross-linked and π-stacked dense structure.[58, 59] Thus, PDA coating makes a physical barrier for atomic rearrangement in the GNRs, requiring more energy, and retards the surface atom diffusivity. In addition, Ostwald ripening also influences shape transition. PDA coating increases activation energy for dissolution and re-deposition processes in the Ostwald ripening, thus preventing shape transition of GNRs.[60] Poly(styrenesulfonate)-coated GNRs showed a similar result that shape transition of GNR@PSS was prevented due to the retard of the Ostwald ripening.[60] Secondly, shape transition of GNR is due to the amount of fluence incident on the GNRs (Equation 5). The PDA coating absorbs photons and reduces the fluence on the GNRs. Thus, GNRs covered by PDA shell are damaged less than pristine GNRs.

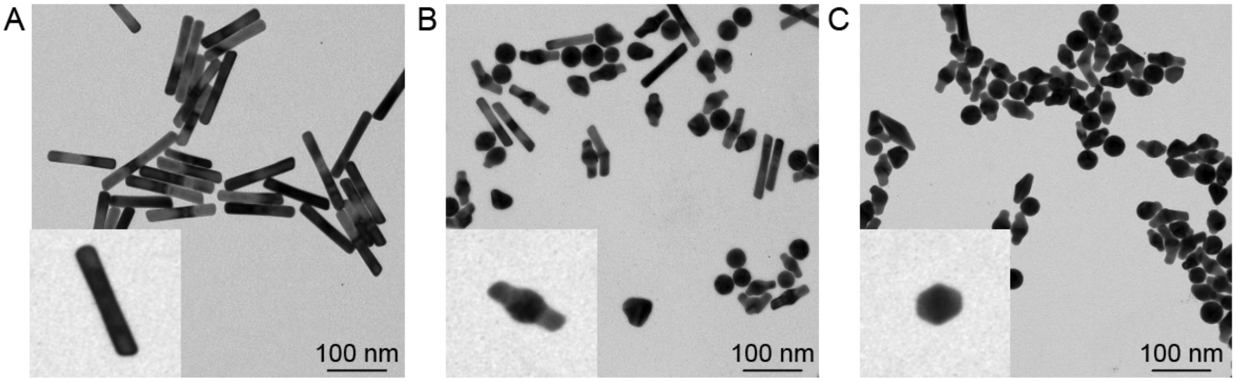

Figure 1.10 Shape transition of GNR under the laser illumination
(A) pristine GNRs, (B) shape transition of GNRs after 1 min of laser illumination, and (C) shape transition of GNRs after 5 min of laser illumination. Atomic rearrangement occurs at {110} facets of GNRs to minimize their surface energy, converting into spherical shape.

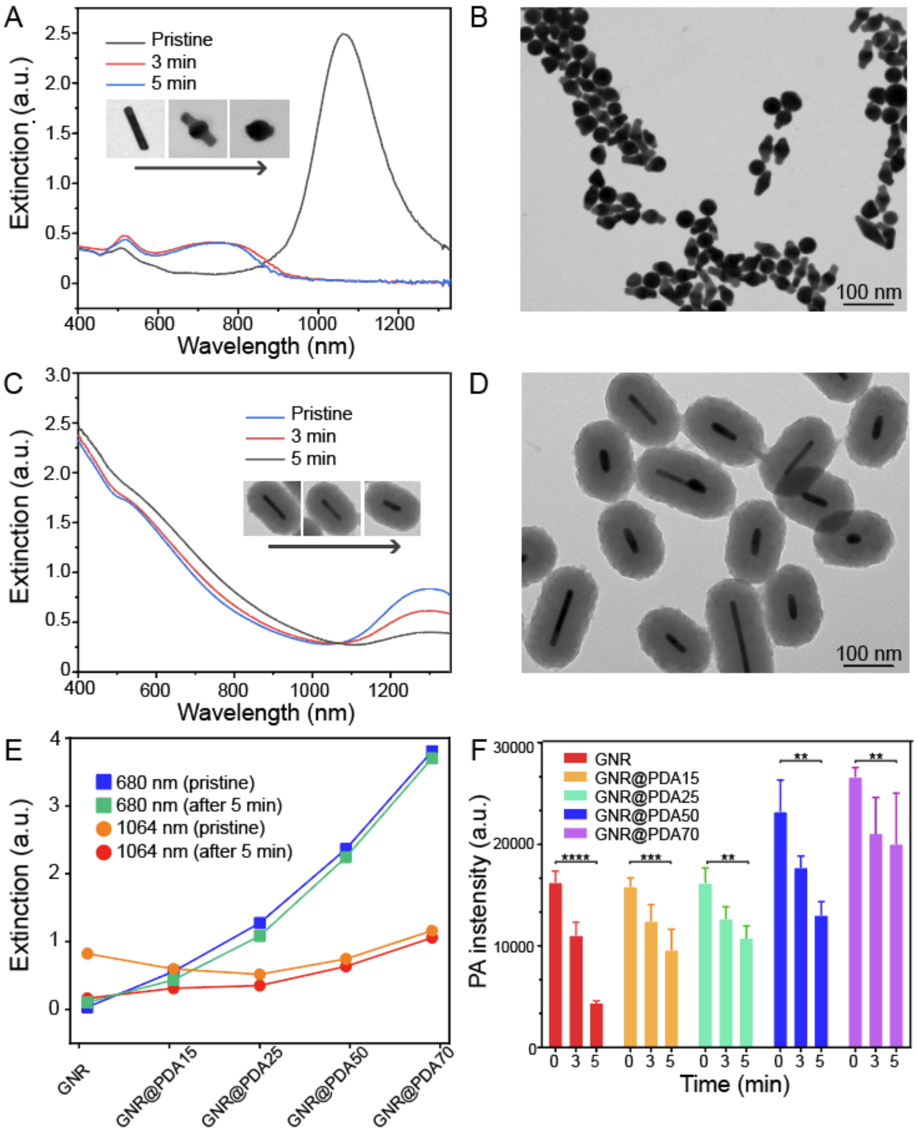

Figure 1.11 GNR@PDA stability test
Changes of optical extinction of GNRs before (blue line) and after 3 min (red line) and 5 min (gray line) of the laser illumination. Inset images show the shape transition of single GNR nanoparticle. (B) Morphology of GNRs was deformed after 5 min of the laser illumination. (C) Changes of optical extinction of GNR@PDA50 before (blue line) and after 3 min (red line) and 5 min (gray line) of the laser illumination. Inset images indicate PDA coating protects GNR from the shape transition retaining their rod-like structure. (D) Morphology of GNR@PDA50 after 5 min of the laser illumination. (E) Changes of optical extinction at 680 nm and 1064 nm of GNR and GNR@PDAs before and after the laser illumination. (F) Time-dependent PA intensity of GNR and GNR@PDAs. We used 1064 nm laser for PA measurements. The error bars represent the standard deviations of five regions of interest. The statistical significance was calculated with the PA intensity of GNR@PDA's t test; **, ***, and **** indicates $p < 0.01$, 0.001, and 0.0001 versus the pristine condition, respectively.

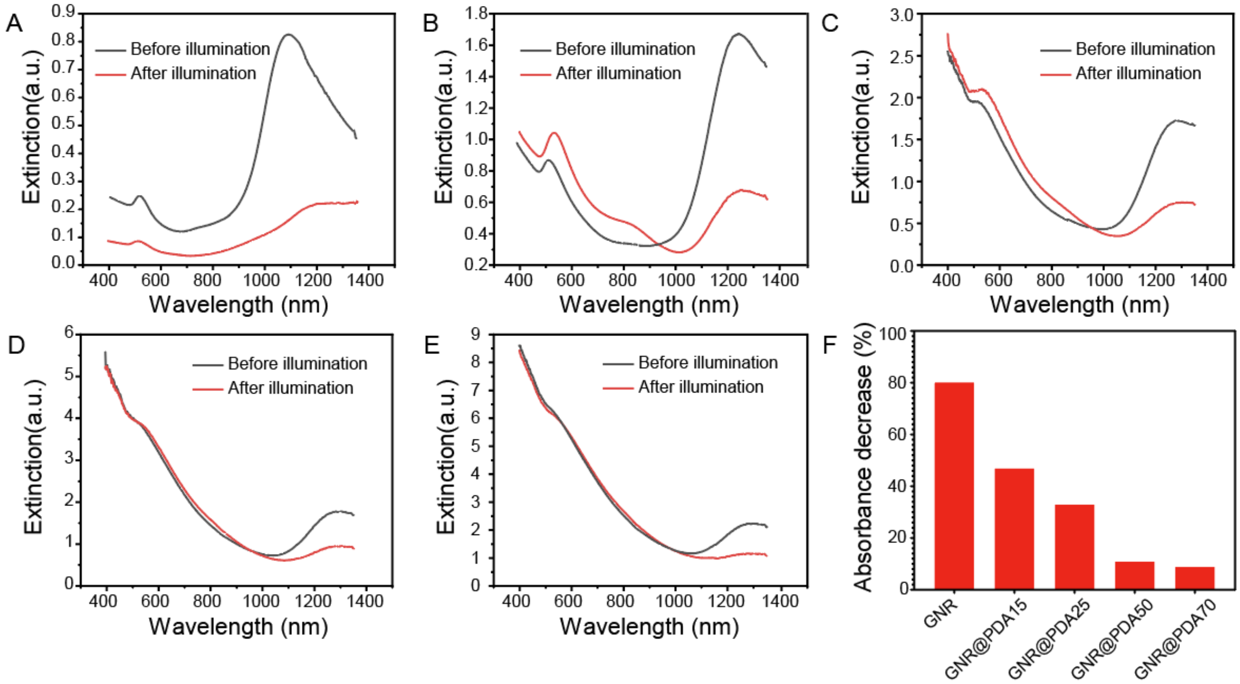

Figure 1.12 Changes of UV-vis-NIR spectra

Changes of UV-vis-NIR spectra of GNR and GNR@PDAs before and after 5 min of the laser illumination. GNR, (B) GNR@PDA15, (C) GNR@PDA25, (D) GNR@PDA50, (E) GNR@PDA70, and (F) longitudinal absorption peaks of GNR, GNR@PDA15, GNR@PDA25, GNR@PDA50, and GNR@PDA70 decreased by 80%, 47%, 33%, 11%, and 9%, respectively.

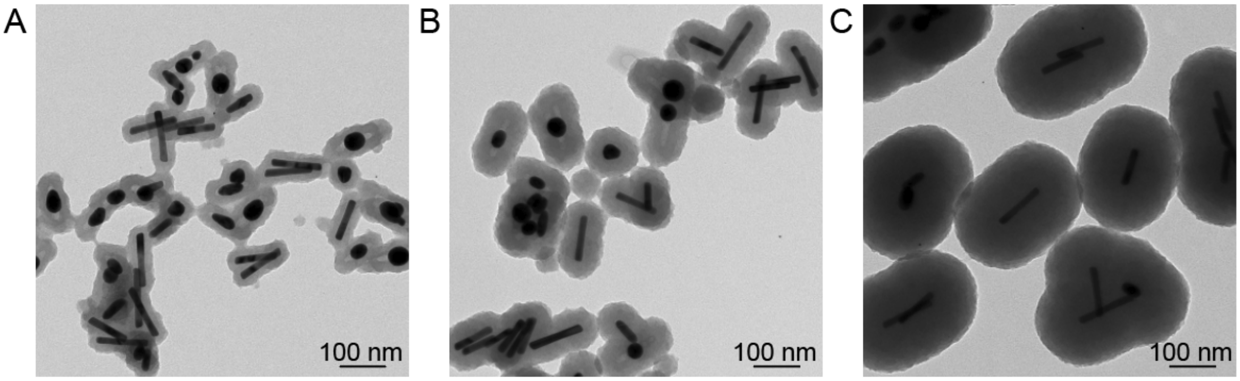

Figure 1.13 Shape transition of GNR@PDAs

(A) GNR@PDA15, (B) GNR@PDA25, and (C) GNR@PDA70 after 5 min of the laser illumination

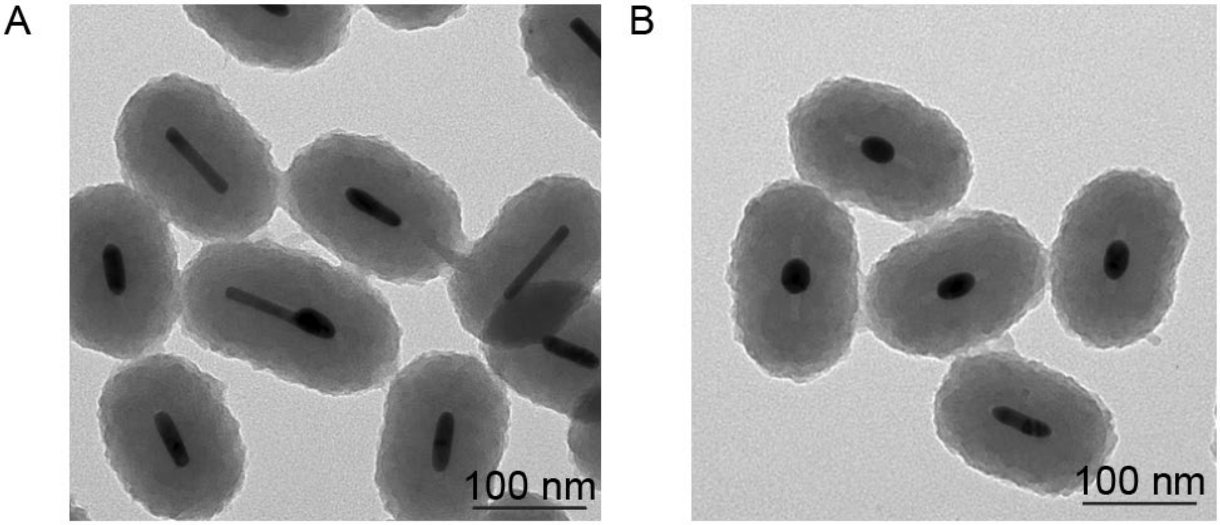

Figure 1.14 Shape transition of PDA@GNR50
after 5 min (A) and15 min (B) of the laser exposure. PDA coating maintained its original structure while most of the coated GNRs melt, showing that PDA is highly robust.

1.4.4. Photoacoustic performance of rod-shaped PDA Capsules

Next, we studied the PA performance of PDA shells alone to better understand their contribution to the hybrid system. The GNR core was removed with a Cu^{2+}-mediated method where Cu ions formed AuCu alloys in dimethylformamide (DMF) solvent leading to a decrease of Au stability.[61] After centrifugation to remove surfactants, we enabled to synthesize rod-shape PDA hollow capsules with 15 nm, 25 nm, 50 nm, and 70 nm shell thicknesses (referred as $PDA_{capsule}15$, $PDA_{capsule}25$, $PDA_{capsule}50$, and $PDA_{capsule}70$). TEM data clearly showed that PDA capsules had a rod-like cavity inside indicating that the GNR core was removed by the Cu ions (Figure 1.15A–D).

UV–vis–NIR absorption spectra data revealed that rod-shaped PDA capsules had a broadband optical absorption but no longitudinal absorption peak in the NIR II window (Figure 1.15I). The absorption intensity of the PDA capsule again increased with a thicker shell thickness. $PDA_{capsule}70$ showed a five-fold higher intensity than $PDA_{capsule}25$. We then studied PA performance of PDA capsules from 680 nm to 1064 nm illuminations (Figure 1.15J). PDA capsules exhibited 3-fold higher PA signal at 680 nm than at 1064 nm due to the 4.4-fold higher optical absorption and stronger laser fluence at 680 nm. In addition, a thicker PDA capsule had a higher PA intensity than a thinner PDA capsule. For instance, $PDA_{capsule}70$ had 2-fold higher PA intensity than $PDA_{capsule}25$ (Figure 1.15J), and $PDA_{capsule}50$ showed 40% of PA intensity of its original structure (e.g., GNR@PDA50). This suggests that PDA alone can produce photoacoustic signal but that there is a synergetic effect in PA signal generation when the capsule is combined with GNR. Moreover, this PDA coating strategy can be applied to diverse nanoparticle via the adhesive property of PDA for improving PA imaging (Figure 1.17). By virtue of this binding ability, PDA can load a variety of materials (e.g., 6.4% for Gd (III) by Lemaster JE. et al.[49], 37.4% for doxorubicin by Li W. et al. [62]) because of the catechol groups in PDA.[36] Thus, PDA coating can deliver photosensitizer for photodynamic therapy.[22] Additionally, the GNR@PDA probe showed 2% higher photothermal conversion efficiency than GNR, indicating that PDA coating can serve as an excellent photothermal transducer for photothermal therapy (Figure 1.18).

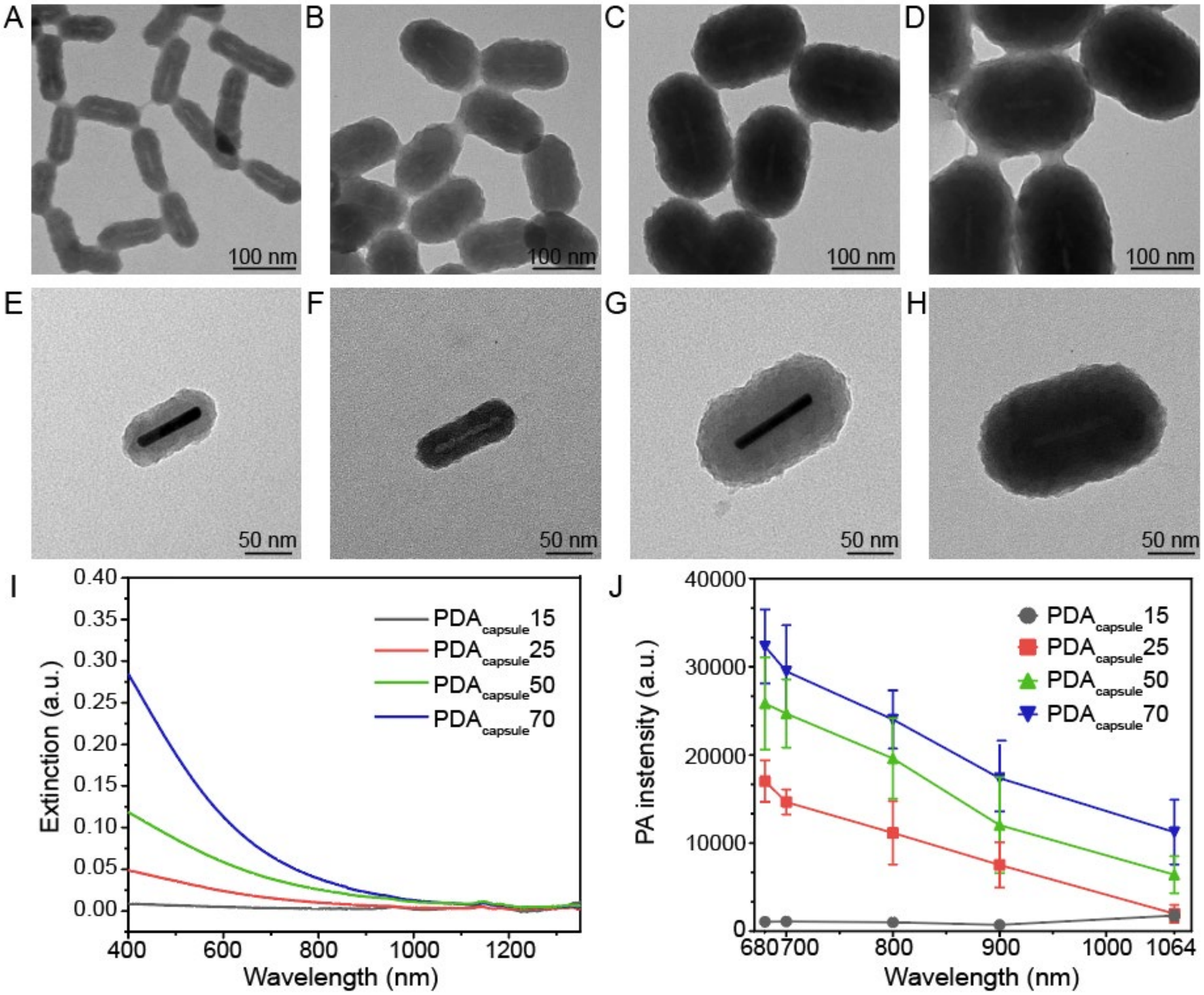

Figure 1.15 PA performance of rod-shape PDA capsules.
TEM images of (A) PDA$_{capsule}$15 (B) PDA$_{capsule}$25 (C) PDA$_{capsule}$50, and (D) PDA$_{capsule}$70. TEM images of single nanoparticle with high magnification: (E) GNR@PDA15, (F) PDA$_{capsule}$15, (G) GNR@PDA50, and (H) PDA$_{capsule}$50. Single nanoparticles with PDA thickness of 25 nm and 70 nm are shown in Figure 1.16. (I) UV–vis–NIR absorption spectra of PDA capsules. PDA capsules showed similar extinction spectrum (e.g. broadband absorption) like PDA nanoparticles.[49] (J) PA intensity of PDA capsules at 680, 700, 800, 900, and 1064 nm. The error bars represent standard deviation of five regions of interest.

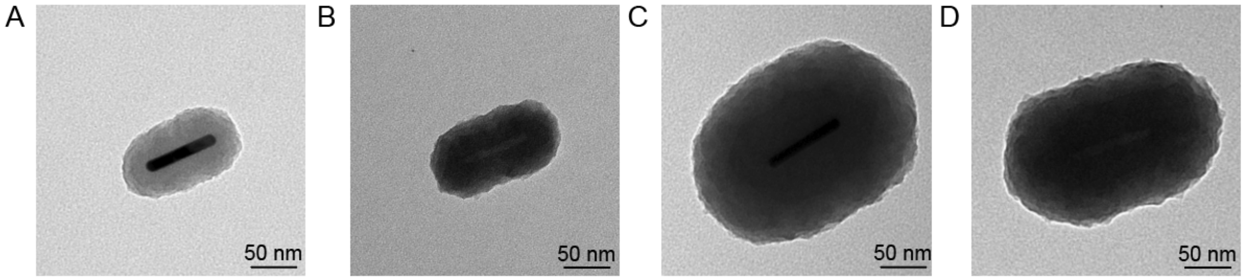

Figure 1.16 TEM images of single PDA capsule particle
(A) GNR@PDA15, (B) $\text{PDA}_{\text{capsule}}15$, (C) GNR@PDA70, and (D) $\text{PDA}_{\text{capsule}}70$.

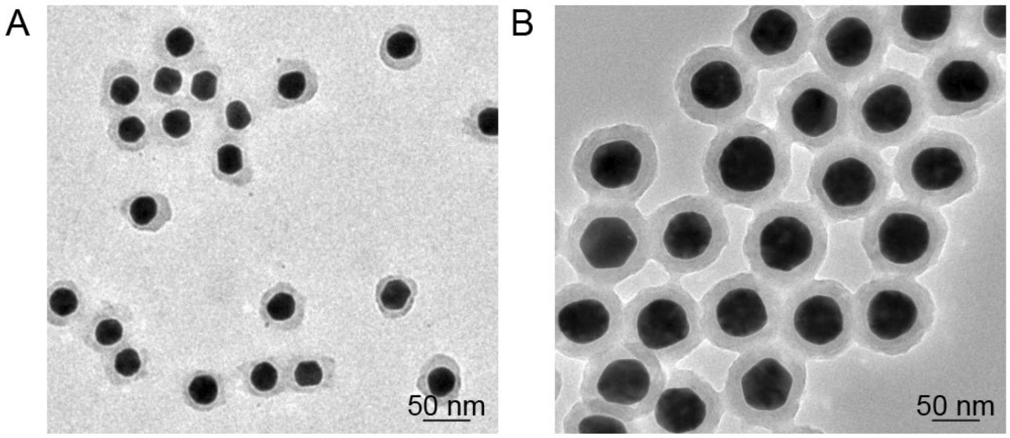

Figure 1.17 PDA coated gold nanospheres (GNSs)
30 nm and (B) 60 nm GNSs covered by PDA shell. These images indicate that PDA coating strategy can be applied to various types of nanoparticles for improving PA performance.

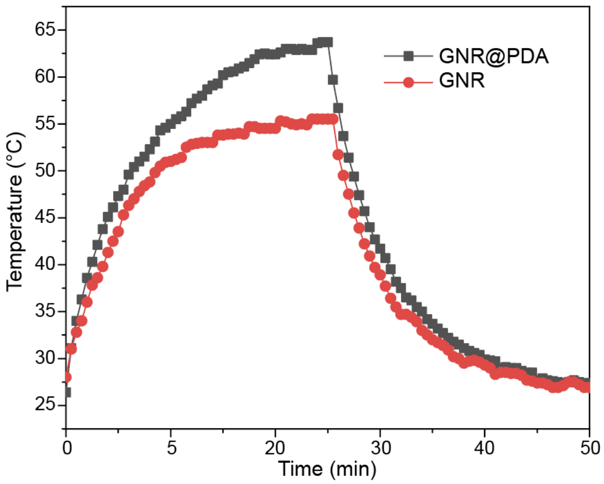

Figure 1.18 Photothermal conversion efficiency of GNR and GNR@PDA.
Photothermal conversion efficiency of GNR@PDA (40 %) was 2 % higher than that of GNR (38 %), indicating that PDA coating can be used for photothermal therapy. 1064 nm laser with 1 W/cm^2 was used for the measurement.

1.4.5. In vivo stability of GNR@PDA

Finally, we conducted *in vivo* experiments of GNR@PDA to investigate PA signal stability in biological samples. We first implanted GNR and GNR@PDA in 50% Matrigel (150 µL). The same mass of gold was used for both GNR and GNR@PDA50 (0.2 µg/mL). The material was subcutaneously injected into the mice (n=3) and imaged 10 min after the injection. We can clearly see the anatomical images from the B-mode (ultrasound) and confirm the PA signal was from our GNR@PDA probes (Figure 1.19A–B). Surprisingly, GNR@PDA50 maintained 87% of its original PA signal even after 10 min of laser illumination while there was no PA signal of the GNR likely due to the shape deformation and background scattering (Figure 1.19C). Furthermore, PA intensity of GNR@PDA was ten-fold higher than the bare GNR (p <0.0001) indicating that PDA coating can improve PA performance of GNR in the NIR-II window (Figure 1.19D). These results are consistent with our *in vitro* experiments (Figure 1.7D and Figure 1.11F).

The colloidal stability of GNR@PDA50 was further studied in different medium (e.g., 10 mM HCl, 10 mM NaOH, 10 mM NaCl, and DMEM with 20%, 10%, or 5% of mouse serum). DLS data showed that GNR@PDA50 had a high colloidal stability in NaCl, 20% mouse serum, pH 2 and pH 12 (PDI < 0.1). Negligible aggregation or disassembly of PDA coating was found in those conditions (Figure 1.19E). These results indicate PDA coating is highly robust and stable in biological or extreme conditions might due to abundant catechol and amino groups in PDA as well as its covalently crosslinked structure.[36] Therefore, our PDA coating strategy not only leads to outstanding PA performance over the original GNR probe but also gives these nanoparticles excellent colloidal stability in diverse biological conditions.

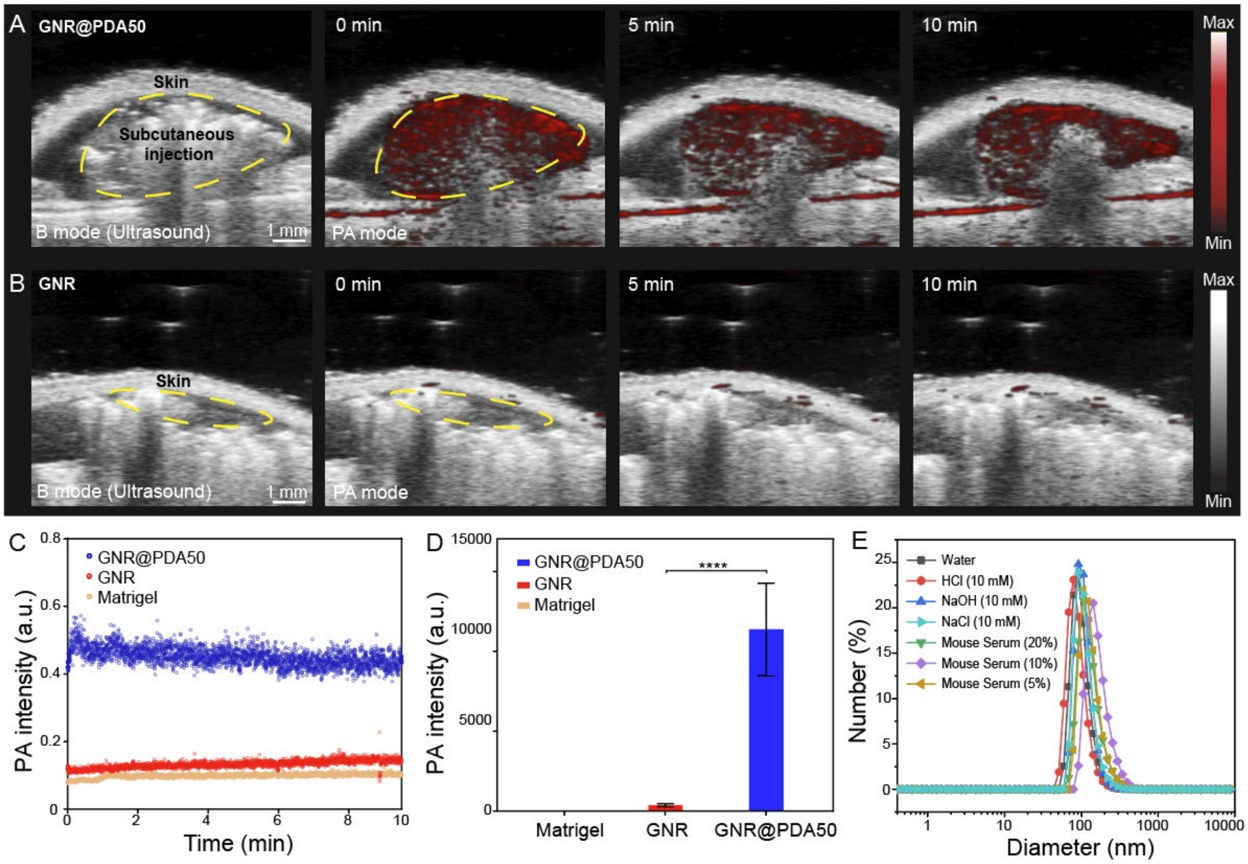

Figure 1.19 PA imaging of GNR@PDA *in vivo*

B-mode ultrasound (gray scale) and photoacoustic (red scale) images of subcutaneously injected (A) GNR@PDA50 and (B) GNR, showing that GNR@PDA50 had higher PA intensity and signal stability than GNR. The same amount of GNR or GNR@PDA50 was injected into the mice (*n*=3) based on a gold mass concentration of 0.2 µg/mL. PA signals of GNR and GNR@PDA50 were continuously measured in one spot for 10 min. The yellow circle is the subcutaneously injected area. (C) Time-dependent *in vivo* PA intensity of different materials. Blue, red, and orange circle indicates GNR@PDA50, GNR, and Matrigel, respectively. (D) Quantification of the PA signal comparing GNR and PDA@GNR50 at 0 min. The statistical significance was calculated with PA intensity of the GNR and GNR@PDA via a *t* test; ****, $p < 0.0001$. Error bars represent three regions of interest. (E) GNR@PDA50 was incubated in different media for 1 h. DLS data showed that GNR@PDA was highly stable in different biological conditions.

1.5. Conclusion

Stable PA signal is essential to achieve high-quality and reliable imaging in biomedical applications. In this study, we synthesized GNR-melanin hybrids (i.e., GNR@PDA) with a tunable PDA protective coating to overcome the poor thermal stability of GNR. By virtue of the robust PDA structure, GNR@PDAs showed enhanced structural and thermal stability than pristine GNRs. Specifically, GNR@PDAs showed an improved structural integrity of the built-in GNR core and a two-fold higher signal even after 5 min of the laser illumination. PDA coating can provide a synergetic effect in improving optical absorption, thermal confinement, and absorption cross-section area leading to a 3-fold stronger PA signal than GNR. Surprisingly, GNR@PDA still generated 87% of its original PA signal *in vivo* even after 10 min of laser illumination unlike bare GNRs that decreased by 75%. Furthermore, our nanoprobe showed a high colloidal stability in biological conditions. These findings highlight the potential use of PDA coating in developing photo-mediated contrast agents in a broad spectral range including NIR-II window and expand on understanding the PA mechanism occurring in the nanoparticles Moreover, this PDA coating strategy not only gives opportunities for other types of photo-meditated biomedicines but also holds high potential as nanocarriers in living subjects.

1.6. Acknowledgement

The authors acknowledge the National Science Foundation under award 1845683 and 1937674. We also acknowledge National Institutes of Health under awards DP2 HL 137187, R21 DE029917, and R21 AI157957. The authors also acknowledge infrastructure support under awards S10 OD021821 and S10 OD023555. M.C. acknowledges fellowship funding under NIH award T32 CA153915. This material is based upon work supported by the NSF Graduate Research

Fellowship Program under Grant No. DGE-1650112. Transmission electron micrographs were taken in the Cellular and Molecular Medicine electron microscopy core facility, which is supported in part by National Institutes of Health award number S10 OD023527.

Chapter 1, in part, is a reprint of the material as it appears in “Gold nanorod-melanin hybrids for enhanced and prolonged photoacoustic imaging in the near-infrared-II window” by Yim, Wonjun; Zhou, Jiajing; Mantri, Yash; Cryer, Matthew N.; Moore, Colman A.; and Jokerst, Jesse V., ACS Applied Material and Interfaces 2021. The dissertation author was the primary investigator and author of this paper.

CHAPTER 2. Ultrasmall gold nanorod-polydopamine hybrids for enhanced photoacoustic imaging and photothermal therapy in second near-infrared window

2.1. Abstract

Gold nanorods (GNRs) have attracted great interest for photo-mediated biomedicines due to their tunable and high optical absorption, high photothermal conversion efficiency and facile surface modifiability. GNRs that have efficient absorption in second near-infrared (NIR-II) window hold further promise in bio-applications due to low background signal from tissue and deep tissue penetration. However, bare GNRs readily undergo shape deformation (termed as 'melting effect') during the laser illumination losing their unique localized surface plasmon resonance (LSPR) properties, which subsequently leads to PA signal attenuation and decreased photothermal efficiency. Polydopamine (PDA) is a robust synthetic melanin that has broad absorption and high photothermal conversion. Herein, we coated GNRs with PDA to prepare photothermally robust GNR@PDA hybrids for enhanced photo-mediated theranostic agents. Ultrasmall GNRs (SGNRs) and conventional large GNRs (LGNRs) that possess similar LSPR characteristics as well as GNR@PDA hybrids were compared side-by-side in terms of the size-dependent photoacoustic (PA) imaging, photothermal therapy (PTT), and structural stability. *In vitro* experiments further demonstrated that SGNR@PDA showed 95% ablation of SKOV3 ovarian cancer cells, which is significantly higher than that of LGNRs (66%) and SGNRs (74%). Collectively, our PDA coating strategy represents a rational design for enhanced PA imaging and efficient PTT via a nanoparticle, i.e., nanotheranostics.

2.2. Introduction

Nanotechnology has significantly advanced the development of bioimaging and light-activated phototherapy such as photoacoustic (PA) imaging and photothermal therapy (PTT).[10, 63] In PA imaging, a pulsed laser illuminates biological tissues or a contrast agent, and the absorbed light energy is converted into heat energy thereby leading to transient expansion of the absorber and generating acoustic waves detected via ultrasonic transducers.[13] PA imaging is noninvasive and offers high spatial resolution, deep penetration, and fast imaging speed. It has attracted immense attention of researchers for biomedical imaging.[64-66] Both endogenous (e.g., hemoglobin or melanin) and exogenous (e.g., plasmonic nanoparticles) contrast agents can be used for PA imaging to monitor specific biological processes or to improve imaging depth and quality in tissue.[67]

PTT is a spatiotemporally controllable cancer treatment that has shown great promise in the cancer therapy.[68] Like PA imaging, PTT is based on the conversion of light into heat, but it uses heat for thermal ablation against cancer cells. Compared to other conventional methods including radio- or chemo-therapy, PTT is attractive because of high inherent specificity, low cost, and limited invasiveness.[69] For example, PTT causes limited damage to the surrounding healthy tissues because thermal effect occurs only in the presence of PTT agents.[70] Currently, the research topics on photothermal theranostics has expanded rapidly, which greatly benefits from the advances made in novel nanomaterials design, including inorganic, organic, and hybrid nanoparticles.[24, 38, 71, 72]

Particularly, gold nanorods (GNRs) are widely investigated for both PA imaging and PTT due to their high absorption efficiency, photothermal conversion efficiency, and low toxicity. Moreover, the localized surface plasmonic resonance (LSPR) of GNRs is easily tunable by controlling their aspect ratio. GNRs with high aspect ratio show optical absorption in second near-infrared (NIR-II) window (1000 – 1350 nm) which offers deep penetration of light, low background noises from the tissue, and maximum permission exposure (MPE) compared to NIR-I window (650 – 950 nm).[73-75] However, pristine GNRs have a significant limitation: laser-induced shape deformation from thermodynamic instability. Under laser irradiation, the thermodynamic tendency to lower the surface energy makes the rod-like GNRs form nanospheres with greater stability (reduced surface area to volume ratio).[26] Specifically, it is found that a high-pulsed laser induces both point and line defects that grow into planar defects in the interior of GNRs.[27] These defects consequentially convert GNR {110} facets into the energetically stable {100} and {111} facets to minimize surface energy.[26] As a result, GNRs lose their NIR absorption peak due to the structural deformation thus attenuating PA signal and photothermal efficiency. Therefore, improving thermal stability of GNR could improve the potential use of GNR in photo-mediated applications.

Size reduction is one strategy that can improve photothermal stability. Recently, Emelianov and Gambhir *et al.* reported a seedless method to synthesize ultrasmall GNRs (SGNRs) [76]. These SGNRs are 50% smaller than conventional large GNRs (LGNRs), but they maintained a comparable aspect ratio and demonstrated 3-fold PA enhancement due to their higher surface-to-volume ratio. More interestingly, these SGNRs were more photothermally stable than LGNRs after laser irradiation.[76] Nevertheless, further GNR miniaturization for thermal stability optimization is difficult; proper synthesis relies on a wide set of factors that can influence particle growth like choice in concentration, surfactant, reducing agent, and pH. Alternatively, core–shell nanostructures can provide further improvement in photothermal stability and performance of SGNRs. Many groups have investigated a variety of materials such silica, metal oxide, and polymers as coatings for GNRs.[77-80] However, the inherent properties of many of these coatings limit their use in biomedical applications. For example, polysarconsine-coated GNRs show high colloidal stability, but they have poor surface modification.[81] CuO or MnO_2-coated GNRs have facile surface tunability but suffer from cytotoxicity.[82, 83] In contrast to these methods, we used polydopamine (PDA) to protect pristine GNR probe from the shape deformation. PDA coatings are robust, biocompatible, and surface functionalization.[49, 84] We thus hypothesized that PDA is a pragmatic choice as a GNR shape-preserving coating for theranostic applications.

PDA is a synthetic melanin that is a highly crosslinked structure with broadband absorption. Its abundant catechol moieties accommodate a wide class of noncovalent interactions (e.g., hydrophobic, electrostatic, hydrogen bonding, and π–π stackings) with diverse materials (e.g., inorganic, organic, and protein).[33, 36] We previously validated PDA coatings improve PA performance and thermal stability of pristine LGNR.[85] However, a critical size limit of nanoparticles is ~ 100 nm for in vivo applications.[86] For example, FDA-approved anticancer nanomedicines (e.g., doxorubicin and paclitaxel) which are in size range of 100 ~ 200 nm showed limited accumulation and penetration in tumors,[87, 88] while nanomedicines with the size below 100 nm demonstrated superior penetration and retention in tumor tissues.[89-91] Furthermore, photothermal performance of GNR@PDA still remains unclear. Herein, we investigated PDA-coated SGNR to improve photoacoustic and photothermal performance of the core SGNR nanoparticles. First, we synthesized LGNR and SGNR that have comparable longitudinal absorption peak in NIR-II window (Figure 2.1a). We then coated PDA on both LGNR and SGNR to investigate both PA efficiency and photothermal conversion efficiency (Figure 2.1b-c). Finally, human ovarian adenocarcinoma (SKOV3) cancer cells were used to evaluate photothermal therapeutic efficiencies between LGNR (66%), SGNR (74%), and SGNR@PDA (95%). Together, these size-dependent and PDA coating effects provide comprehensive insight in designing stable GNR nanoprobes for photo-mediated nanomedicine applications.

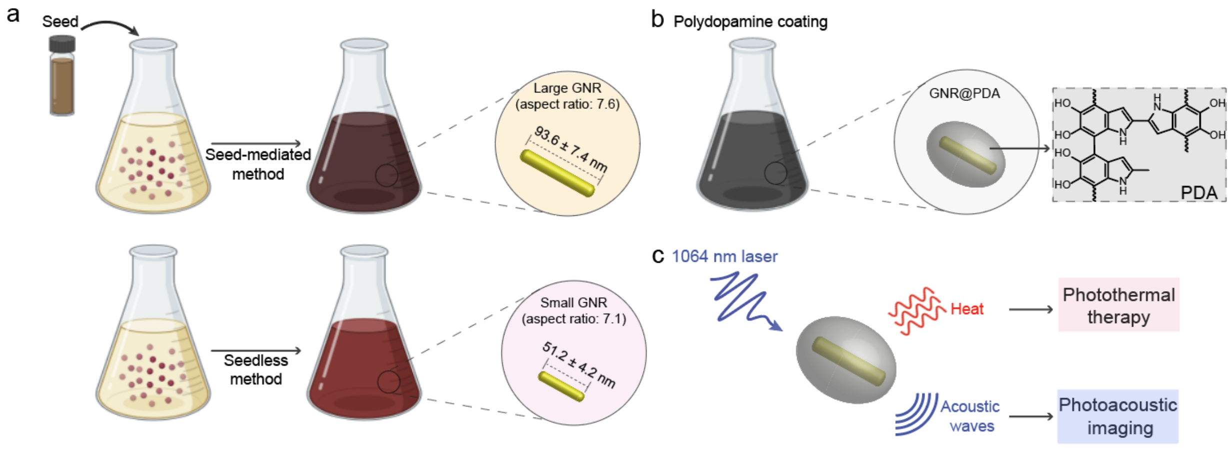

Figure 2.1 Schematic of synthesis SGNR@PDA
(a) Schematic of the synthesis of LGNRs (seed-mediated method, 93.6 ± 7.4 nm in length) and SGNRs (seedless method, 51.2 ± 4.2 nm in length) which have similar aspect ratio of ~7. (b) The CTAB-stabilized GNRs were replaced with HS-mPEG$_{2k}$ to make GNR@PDA hybrids with the PDA thickness of 25 nm. (c) PA imaging and PTT of GNR@PDAs were studied using a laser irradiation with the wavelength of 1064 nm.

2.3. Materials and methods

2.3.1. Synthesis of large GNR

We used a seed-mediated growth to synthesize regular size of GNR nanoparticles with a high aspect ratio of 7.1.[92] A seed solution was prepared by mixing an aqueous solution of 5 mL of CTAB (0.2 M) and 5 mL of HAuCl$_4$ (0.5 mM). Then, 600 µL of NaBH$_4$ (10 mM) was quickly injected to the aqueous solution under vigorous stirring at 1200 rpm. After 15 s of vigorous reaction of NaBH$_4$, the stir bar was removed, and the seed solution was incubated in a water bath at 30 °C for 1 h.

A growth solution was made by adding sequentially aqueous solution of 5 mL of CTAB (0.2 M), 5 mL of HAuCl$_4$, and 60 µL of AgNO$_3$ (0.1 M). Then, 325 µL of hydroquinone (0.1 M) was injected under vigorous stirring at 1200 rpm. The color of the growth solution changed from yellow to transparent; 165 µL of the seed solution was then injected to the growth solution under vigorous stirring at 1200 rpm for 15 s. The solution was incubated in water bath at 30 °C for 12 h before being purified with centrifugation at 7,500 *g* for 10 min. After centrifugation, CTAB-stabilized LGNRs were redispersed in 2 mL of deionized water.

2.3.2. Synthesis of ultrasmall GNR

We used a seedless method to synthesize ultrasmall of GNR nanoparticles with a high aspect ratio of 7.7 [76]. Briefly, 5 mL of CTAB (0.2 M), 4 mL of $HAuCl_4$ (0.5 mM), 30 µL of $AgNO_3$ (0.1 M), 20 µL of HCl (1.0 M), and 530 µL of hydroquinone (0.1 M) were sequentially added. The color of solution was bright yellow and stirred at 1000 rpm for 15 min. Finally, 20 µL of fresh $NaBH_4$ (10 mM) solution (prepared within 10 min of use and stored on ice) was quickly injected under vigorous stirring at 1100 rpm. After 15 s of $NaBH_4$ reaction, the solution was incubated in water bath at 30 °C for 12 h before being purified with centrifugation at 20,000 *g* for 15 min. After centrifugation, CTAB-stabilized SGNR was redispersed in 2 mL of deionized water.

2.3.3. Surface modification of large and ultrasmall GNRs

CTAB on the surface of LGNR and SGNR was replaced with HS-mPEG (M_w, 2k Da) via ligand exchange. Both CTAB-stabilized LGNR and SGNR were dispersed in 2 mL of deionized water and added to 4 mL of HS-mPEG (5 mg/mL, 1mM) under generous stirring at 900 rpm for 12 h. The PEGylated LGNR was purified by centrifugation at 7,500 *g* for 10 min while the PEGylated SGNR was purified by centrifugation at 20,000 *g* for 15 min to remove excess of HS-mPEG in supernatant. The PEGylated LGNR and SGNR were redispersed in 2 mL of water for future use.

2.3.4. Synthesis of PDA coated GNRs

The 200 µL of LGNR solution was dispersed in 2 mL of bicine buffer (10 mM, pH 8.5). Then, 200 µL of dopamine solution (4 mg/mL) was added under vigorous stirring at 1300 rpm for 12 h. Similarly, 200 µL of SGNR solution was dispersed in 2 mL of bicine buffer (10 mM, pH 8.5) followed by 200 uL of dopamine solution (4 mg/mL) under vigorous stirring at 1300 rpm for 12 h. The color of solution was dark-brown, and the resulting product was purified by centrifugation at 7,500 *g* for 10 min. Both LGNR@PDAs and SGNR@PDAs were redispersed in water for future use.

2.3.5. Cell culture and preparation

Human ovarian adenocarcinoma (SKOV3) cells were cultured in complete McCoy's 5A medium (1.5 mM L-glutamine, and 2.2 g/L sodium bicarbonate and supplemented with 10% fetal bovine serum and 1% penicillin/streptomycin). Cell cultures were incubated under 5% CO_2 at 37 °C. Cultures were given at least three passages before they were used for experiments. Cells were passaged from 75 to 80% confluency using 0.25 % Trypsin-EDTA. Photobleaching was used to confirm healthy and dead cells.

2.3.6. Cytotoxicity assay

SKOV3 cells were seeded overnight in a 96-well plate at a concentration of 20,000 cells/well. After seeding, LGNR, SGNR, and SGNR@PDA were incubated with the SKOV3 cells at equal concentration (10 µM) for 24 h. Each well was then washed three times with cold phosphate-buffer saline (PBS) to remove the free nanoparticles. A resazurin assay was used to analyze cytotoxicity of LGNR, SGNR, and SGNR@PDA following a general protocol: After cells were incubated with resazurin for 4 hours, cell viability was calculated by measuring the subtracted background absorbance of each cell at 600 nm from resazurin absorbance at 570 nm. The absorbance of experimental wells was compared to that of the controlled well including healthy and dead cells. All experiments were performed in triplicate, and the results were averaged.

2.3.7. In vitro PTT in NIR-II Window

SKOV3 cells were seeded in a 96-well plate at 20,000 cells/well overnight. Each sample well was spaced out by an empty well to rule out the interference of heat transfer from the other wells during the laser irradiation. 100 µL of LGNR, SGNR, and SGNR@PDA at the same concentration in 1.0 µL in McCoy's 5A medium was incubated with SKOV3 cells for 24 h. Each sample well was then exposed to a 1064 nm laser for 10 min. After NIR-II laser irradiation, samples were incubated for another 12 h, and the photothermal cytotoxicity was calculated by using a resazurin assay as described above. All experiments were done in triplicate, and the results were averaged.

2.3.8. Cell staining with Calcein AM and Propidium Iodide Dyes

Calcein AM and Propidium Iodide (PI) were used to stain the living and dead cells before and after NIR-II laser irradiation following a general protocol. SKOV3 cells were seeded in a 24-well plate (50,000 cells/well) overnight and then incubated with LGNR, SGNR, and SGNR@PDA with the same concentration of 1.0 µM for 24 h. After NIR-II laser irradiation, each sample well was incubated for 12 h, and cells without laser irradiation was used as a control. 900 µL of mixture solution of calcein AM (2 µM) and PI (6 µM) was added to stain the SKOV3 cells. The fluorescence images of each sample well were taken by using an EVOS FL fluorescence microscope after washing with PBS.

2.3.9. Instrumentations

The diluted GNR and GNR@PDA samples were dropped onto copper grids for transmission electron microscopy (TEM) measurements. TEM images were examined with a JEOL JEM 1400 Plus operating at 80 kV. The TEM images were taken via a Gatan 4k digital camera. Electron-dispersive X-ray spectroscopy (EDX) samples were examined using a Thermo Fisher Talos 200X operating at 200 kV. Scanning TEM (STEM) images were examined, and EDX maps were acquired by using a Thermo Scientific software. The hydrodynamic diameter and the zeta potential of each sample were measured by using a Malvern Instrument Zetasizer ZS 90; 100 µL of each sample was diluted in 900 µL of distilled water. Ultraviolet–visible–NIR (UV–vis–NIR) absorption spectra of each sample were measured using a PerkinElmer UV–vis–NIR spectrophotometer. Absorbance was read from 400 nm to 1350 nm with a step size of 3 nm. The inductively coupled plasma mass spectrometry (ICP-MS) analysis was performed using a Thermo Scientific iCAP RQ ICP–MS in the Environmental and Complex Analysis Laboratory at UC San Diego. Samples were digested using *aqua regia* and prepared in 10 mL of 4% HNO_3. Regression analysis (R-squared) was calculated by using Microsoft Excel.

2.3.10. Photoacoustic imaging of LGNR, SGNR, and SGNR@PDA

A VisualSonics Vevo 2100 LAZR imaging system was used for PA imaging at 1064 nm. Samples were imaged using a 21 MHz-centered LZ 250 transducer. The NIR-II laser was calibrated and optimized before the sample measurement. The specimens were positioned at a depth of 1 cm from the transducer. Temperature-dependent PA imaging was performed in the water bath at different temperatures (e.g., 4, 10, 20, 37, and 45 °C). Real-time temperature of water bath was measured using a Hg thermometer. Ice and hot plate were used to cool or heat the water bath. All PA data were processed using Image J software [93]. The average value and standard deviation of the PA intensity were calibrated based on the five regions of interest per tube. The R-squared and slope of PA intensity was calculated using GraphPad Prism software.

2.3.11. Photothermal conversion efficiency of LGNR, SGNR, SGNR@PDA

Typically, 1 mL of LGNR, SGNR, and SGNR@PDA samples at the same concentration was placed in a quartz cuvette to measure photothermal conversion efficiency. We used a 1064 nm laser with the power density of 1.0 W/cm^2. Real-time temperature was monitored every 30 s by using a FLIR C5 camera. Each sample was irradiated with 1064 nm for 30 min. The laser turned off after 30 min of irradiation, and the cooling rate was carefully recorded to calculate photothermal conversion efficiency following equation (see Supporting Information).

2.4. Results and discussion

2.4.1. Synthesis and characterization of SGNR@PDA

GNRs have long been synthesized via seed-mediated growth methods [94, 95]. We used a conventional seed-mediated method to make LGNRs with 93.6 ± 7.4 nm (length) ×12.4 ± 1.4 nm (width) dimensions and an aspect ratio of 7.6 (Figure 2.2a) [94]. To miniaturize GNRs while maintaining high aspect ratio, the size and number of gold seeds became a limiting factor [76]. We therefore used a seedless method to make SGNRs with 51.1 ± 4.2 nm (length) × 7.2 ± 1.2 nm (width) dimensions and an aspect ratio of 7.1 (Figure 2.2b). Both LGNRs and SGNRs were stabilized with CTAB and had a positive surface charge (45.5 ± 2.1 mV for LGNRs, and 37.0 ± 0.6 mV for SGNRs). The formation of PDA coating is easily induced by auto-oxidation of dopamine under basic conditions ($pH > 7.5$). Under weak alkaline conditions, dopamine undergoes successive oxidation, intramolecular cyclization, oligomerization, and then self-assembly into polymerized PDA [96]. Taking advantages of strong adhesive properties of PDA, we uniformly coated PDA on the surface of both LGNRs and SGNRs in bicine buffer (pH 8.5). TEM images show monodispersed LGNR@PDA and SGNR@PDA nanohybrids with same 25 nm PDA coating thickness (Figure 2.2c-d). The coating thickness was readily tunable from 5 nm to 50 nm by adjusting the amount of dopamine feed (4 mg/mL) in the reactions (Figure 2.3). EDX mapping and high-angle annular dark-field imaging (HAADF) confirmed the core–shell nanostructures of SGNR-polydopamine hybrids composed of Au, C, N, and O (Figure 2.2e and Figure 2.4). Furthermore, EDX line scanning indicated that SGNR nanoparticles were covered by carbon—the main component of PDA (Figure 2.2f). Adding dopamine directly to CTAB-stabilized LGNRs and SGNRs led to particle aggregation due to strong electrostatic interactions between positively charged GNRs and negatively charged dopamine. Therefore, we replaced CTAB with a methoxy PEG thiol of M_w 2k Da (HS-mPEG) to accommodate stable PDA coating (Figure 2.5). Using strong Au-thiol bonding formation [97], we successfully exchanged the surfaces of both LGNRs and SGNRs with HS-mPEG, where the zeta potential of LGNRs and SGNRs decreased to 8.3 ± 2.6 mV and 4.6 ± 0.6 mV, respectively (Figure 2.2g). PEGylated LGNRs and SGNRs carry more negative charges after PDA coating due to the phenolic hydroxyl groups on PDA. Histogram of SGNR@PDA and LGNR@PDA sizes as measured by TEM shows that the size of LGNR@PDA nanohybrids is two-fold larger than that of SGNR@PDA nanohybrids (Figure 2.2h).

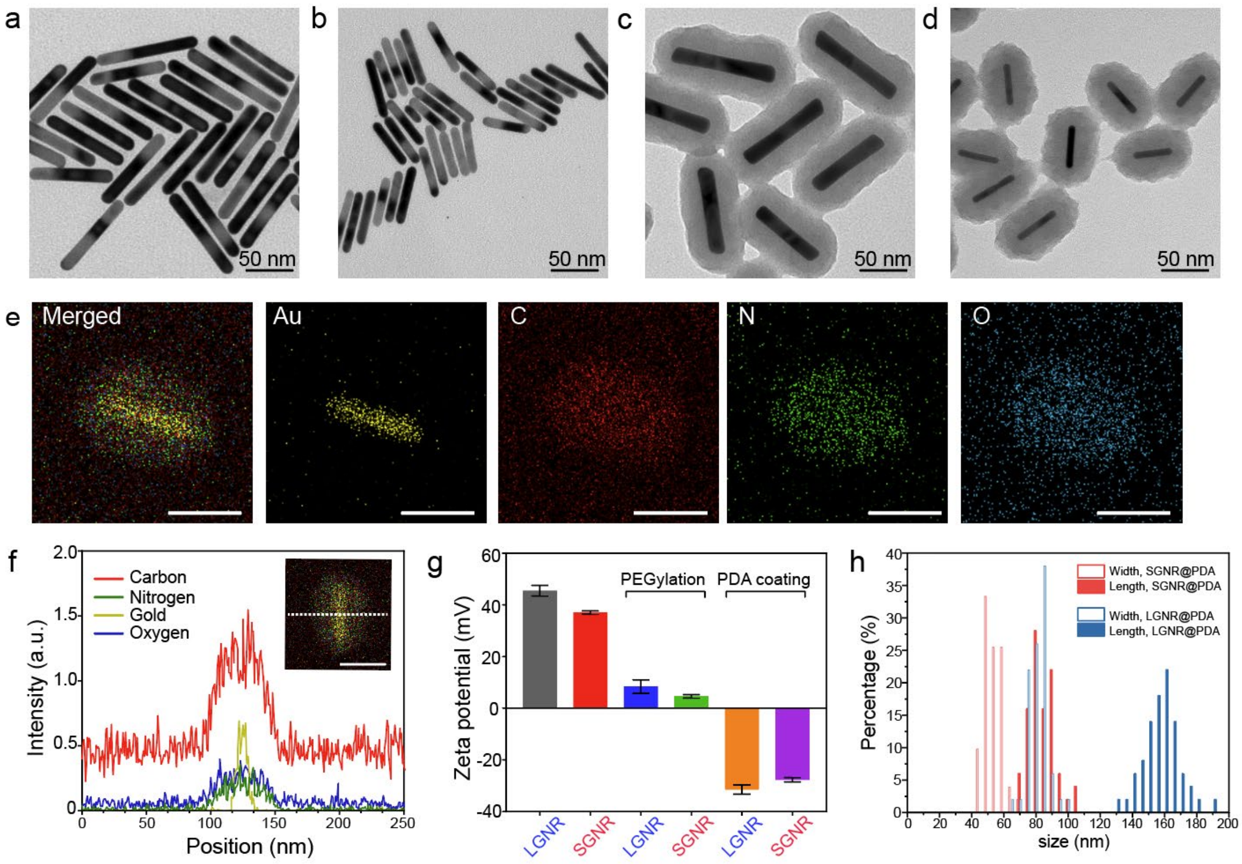

Figure 2.2 PDA-coated large and ultrasmall GNRs

TEM images of (a) LGNRs, (b) SGNRs, (c) LGNR@PDA, and (d) SGNR@PDA. Same PDA thickness about 25 nm was coated on both LGNRs and SGNRs. (e) EDX mapping of SGNR@PDAs shows the core–shell nanostructure of SGNR-polydopamine nanohybrids. The scale bar represents 50 nm. (f) EDX line scanning of SGNR@PDAs. The inset image indicates the location of SGNR@PDAs that were used to analyze the signal intensity of Au, C, N, and O. (g) Zeta potential of LGNR and SGNR before and after PEGylation and PDA coating. Zeta potential of CTAB-stabilized GNRs decreased after ligand exchange, and the surface charge of PEGylated GNRs further decreased when coated with negatively charged PDA. The error bar represents standard deviation of five measurements. (h) Histogram of SGNR@PDA and LGNR@PDA indicates that the length of LGNR@PDA is 2-fold larger than that of SGNR@PDA. Fifty nanoparticles were used to calibrate the width and length of the GNR@PDA nanohybrids.

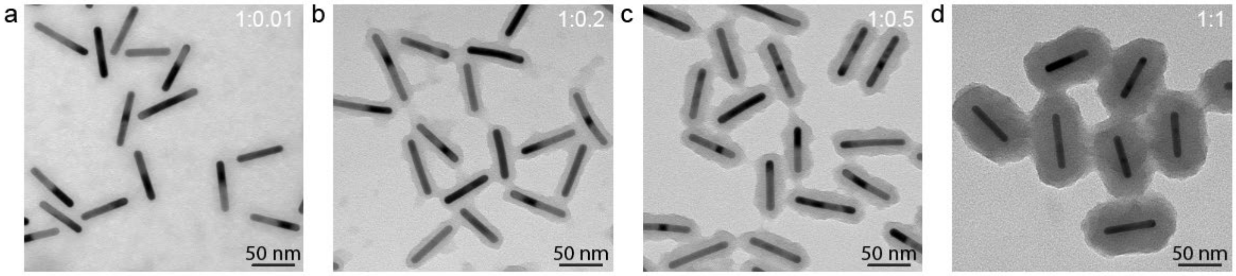

Figure 2.3 TEM images with different PDA shell thicknesses
(a) 0, (b) 5, (c) 10, and (d) 25 nm. PDA thickness is controllable by adding different amount of dopamine at a fixed GNR concentration (0.2 µg/mL). 1:0.01, 1:0.2, 1:0.5, and 1:1 indicate the mass ratio of SGNRs to the dopamine concentrations.

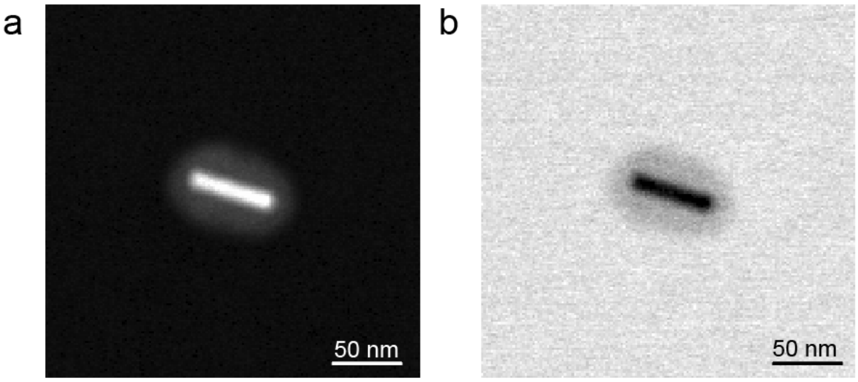

Figure 2.4 HAADF and bright field image of SGNR@PDA
HAADF and bright field image of SGNR@PDA which had PDA thickness of 25 nm, confirming the core-shell nanostructure of SGNR-polydopamine nanohybrids.

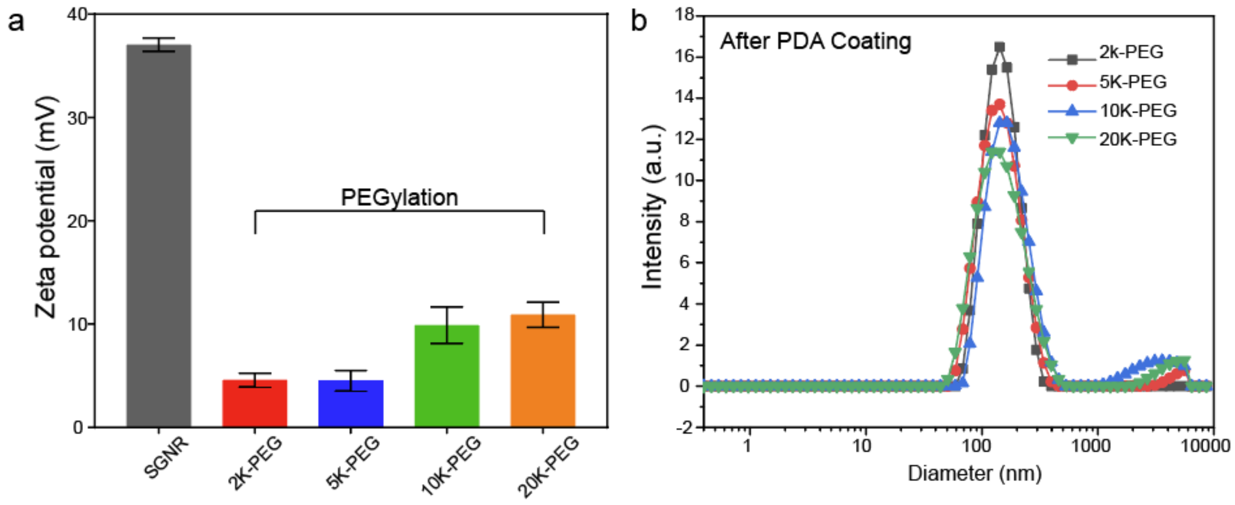

Figure 2.5 Size and charge of PEGylated SGNRs
SGNRs with the size of 51.1 ± 4.2 nm (length) × 7.2 ± 1.2 nm (width) were PEGylated with different molecular weights (e.g., 2k, 5k, 10k and 20k) of methoxy PEG thiol, thus decreasing zeta potential to 4.6 ± 0.6 mV, to 4.5 ± 0.98 mV, to 9.9 ± 1.8 mV, to 10.9 ± 1.2 mV. (b) Interestingly, PEGylated SGNRs with HS-mPEG$_{2k}$ was highly uniform (PDI < 0.1), while slight particle aggregations occurred when SGNRs were PEGylated with 5k, 10k and 20k molecular weight of HS-mPEG. This result suggests that molecular weight of PEG can affect ligand exchange of SGNRs as well as optical PEG configuration for PDA coating.

2.4.2. Photoacoustic performance of SGNR@PDAs

When LSPR nanoparticles are in solution, light is mainly absorbed by the nanoparticles rather than the solvent. The plasmonic SGNR nanoparticles convert absorbed light energy into heat generating acoustic energy into the surrounding medium. Both heat and stress leak out from the nanoparticles during nanosecond-pulsed laser irradiation due to high thermal conductivity of gold and nanometric volume of the particles [98]. Therefore, PA signal is determined by optical absorption of nanoparticles as well as heat transfer rate from gold to water [99]. UV–vis–NIR absorption spectra showed that LGNR had two absorption peaks at 504 nm and 1076 nm that correspond to the transverse and longitudinal LSPR, respectively. Likewise, SGNR exhibited two absorption peaks at 512 nm and 1064 nm, validating that GNR aspect ratio determines its LSPR absorption peaks (Figure 2.6a and Figure 2.7) [100]. The longitudinal peaks of both GNRs were significantly redshifted when PDA was coated due to the increased refractive index (n) from the surrounding medium ($n_{PDA} \approx 1.7$, and $n_{water} \approx 1.3$) [52].

We illuminated optical density (OD)-matched GNR solutions at 1064 nm to measure PA performance of LGNR and SGNR. Consistent with a previous study [76], SGNR (OD ≈ 1 at 1064 nm) showed 3-fold higher PA intensity than LGNR (OD ≈ 1 at 1064 nm) because of its higher surface-to-volume ratio that can improve heat transfer (Figure 2.6b) [100]. We then used inductively coupled plasma mass spectrometry (ICP-MS) to match each GNR and GNR@PDA concentrations based on the number of Au ions in each sample (Figure 2.8). As a result, optical extinctions of both LGNR@PDA and SGNR@PDA were higher than pristine LGNR and SGNR due to the absorbance of PDA coating and the increased size of GNR-melanin hybrid nanoparticles. The increase in absorption intensity is important because PA signal is directly a function of the optical and thermoelastic properties of nanoparticles according to the thermoelastic expansion model (equation 1) [13].

$$\rho_o = \left(\frac{\beta c^2}{\mathrm{C}_P}\right) \mu_\alpha F \qquad \text{---- (1)}$$

where, ρ_o, β, c, C_P, μ_α, and F are pressure gradient, thermoelastic expansion coefficient, speed of sound in the medium, specific heat capacity, absorption coefficient, and laser fluence, respectively.

PDA coating further improved PA performance of both LGNR and SGNR (Figure 2.6b). LGNR@PDA and SGNR@PDA showed three-fold higher PA signals than their corresponding pristine LGNR and SGNR. Moreover, SGNR@PDA showed 3-fold higher PA intensity than LGNR@PDA due to the inherent PA enhancement from the core SGNRs. This significant improvement in PA performance of GNR@PDAs can be explained by three parameters: optical absorption, cross-sectional area, and thermal confinement. First, the melanin-like PDA coating improved optical absorption of GNR as observed in Figure 2.6a. Consequently, GNR@PDAs can absorb more photons than pristine GNR and therefore generate more acoustic energy. Second, the cross-sectional area of GNR@PDA, as measured by electron microscopy, became larger because the PDA coating itself can absorb light. Lastly, thermal confinement obtained from the PDA shell leads to higher PA signal. The heat capacity of water ($C_{water} \approx 4.2$) is 2.5 times higher than that of PDA ($C_{PDA} \approx 1.6$) which means that the GNR surrounded by water requires higher energy to heat versus GNR surrounded by a PDA shell [54]. Furthermore, the thermal conductivity of water ($K_{water} \approx 0.59$) is 4 times larger than that of PDA ($K_{PDA} \approx 0.13$) indicating that heat can readily accumulate in GNR@PDAs due to the reduced thermal conductance [54]. Collectively, the PDA coating gave both LGNR and SGNR higher thermoelastic expansions than GNR alone to significantly increase PA signals.

PA signal generation is also dependent upon other factors including particle concentration and thermal expansion of surrounding solvent. As optical extinction of nanoparticles is linearly proportional to particle concentration, a linear increase in PA signal was observed with elevated concentrations (Figure 2.6c). Importantly, SGNR@PDA at the concentration of 0.2 μM still showed high PA signal which was 15-fold higher than that of SGNR (Figure 2.6c). The thermal expansion coefficient is an inherent material-based property, and PA signal is generated by a sum of the thermal expansion of the nanoparticle and its surrounding solvent. During nanosecond-pulsed laser irradiation, heat is not only confined within the nanoparticles but also diffused into the solvent, leading to a shell-like layer of the solvent around the nanoparticles with the increased temperature [13]. To study the thermal expansion of GNR@PDAs, we measured their PA signals in different temperatures: 4, 10, 20, 37, and 45 °C. Since water was the most dense at 3.98 °C, thermal expansion of water became very low [99]. That is, PA signal at 3.98 °C is mainly due to the thermal expansion of nanoparticles. LGNR, SGNR, LGNR@PDA, and SGNR@PDA nanoparticles showed the lowest PA signals at 4 °C indicating that the thermal expansion of the solvent around the nanoparticles is involved in PA signal generation (Figure 2.6d). Importantly, the PA signal from SGNR@PDA at 10 °C significantly increased (~3 times higher than that at 4 °C) while PA signal of SGNR alone remained low. This result indicates that thermal confinement of PDA shell contributed to thermal expansion of SGNR@PDA (Figure 2.6d).

The PA signals of LGNR, SGNR, LGNR@PDA, and SGNR@PDA linearly increased with increased temperature of the solvent. More importantly, the Grüneisen parameter of LGNR, SGNR, LGNR@GNR, or SGNR@PDA was measured based on the slope of temperature versus PA intensity because the Grüneisen parameter is a function of the thermal expansion coefficient and specific heat capacity, which are temperature-dependent [13, 99]. The Grüneisen parameter (dimensionless) of SGNR@PDA (0.066) was 2.4-fold higher than that of SGNR (0.027). Likewise, Grüneisen parameters of LGNR@PDA (0.038) was 1.7-fold higher than that of LGNR (0.022). These results confirm that the PDA coating can improve the thermal conversion efficiency of core GNR nanoparticles.

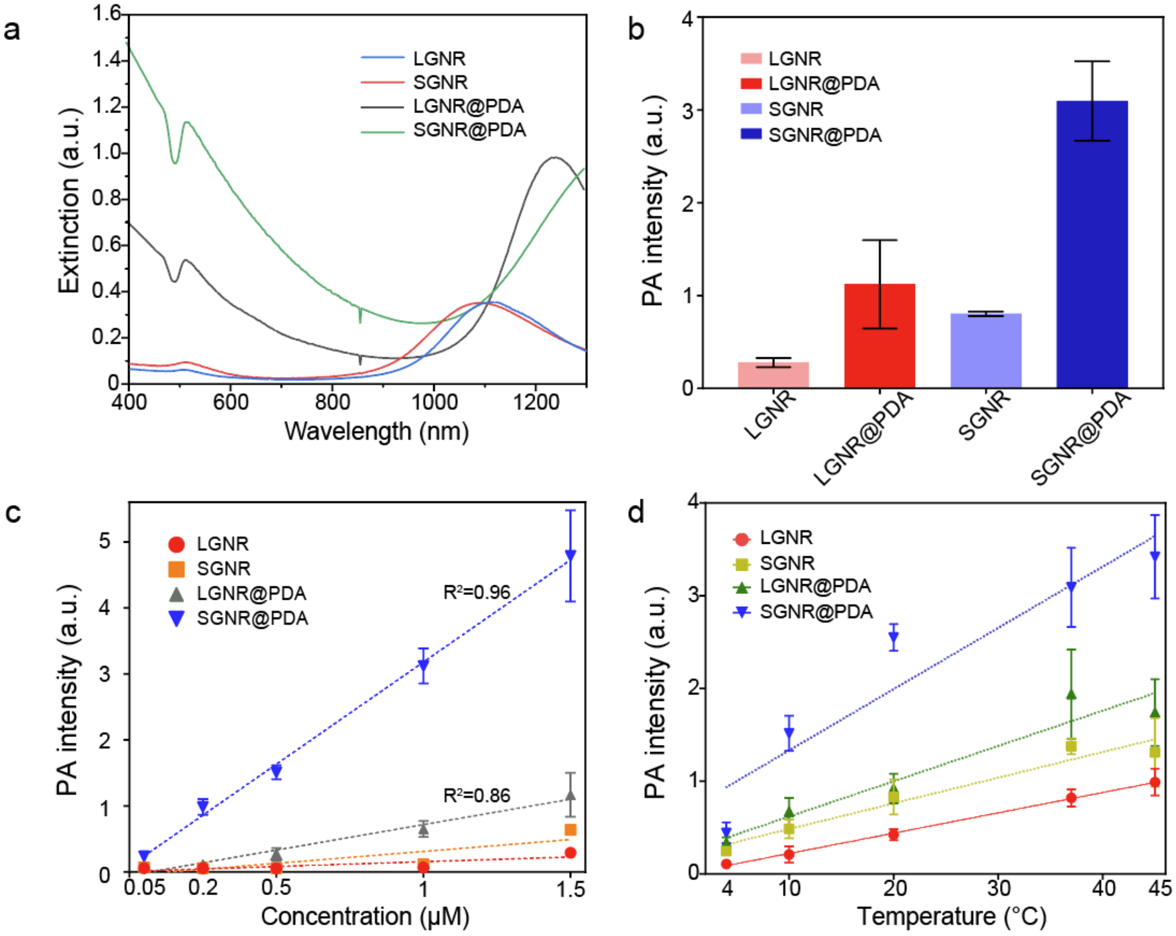

Figure 2.6 PA imaging of GNR@PDAs

(a) UV–vis–NIR absorption spectra of LGNR, SGNR, LGNR@PDA, and SGNR@PDA. Longitudinal absorption peaks of LGNR and SGNR redshifted after PDA coating due to the increased refractive index. Molar concentrations of pristine GNR and GNR@PDA are the same. (b) PA intensity of LGNR, LGNR@PDA, SGNR, and SGNR@PDA under NIR-II (1064 nm) laser irradiation. PDA coating improved PA performance of core GNR particles. (c) PA intensity of LGNR, SGNR, LGNR@PDA, and SGNR@PDA with the elevated sample concentration under NIR-II (1064 nm) laser irradiation. SGNR@PDA showed 4-fold higher PA signal generation than pristine SGNR. (d) PA intensity of LGNR, SGNR, LGNR@PDA, and SGNR@PDA measured in different temperature (e.g., 4, 10, 20, 37, and 45 °C). Slopes of temperature versus PA intensity of LGNR, SGNR, LGNR@PDA, and SGNR@PDA are 0.022, 0.027, 0.038, and 0.066, respectively. The error bars represent the standard deviation of five regions of interest.

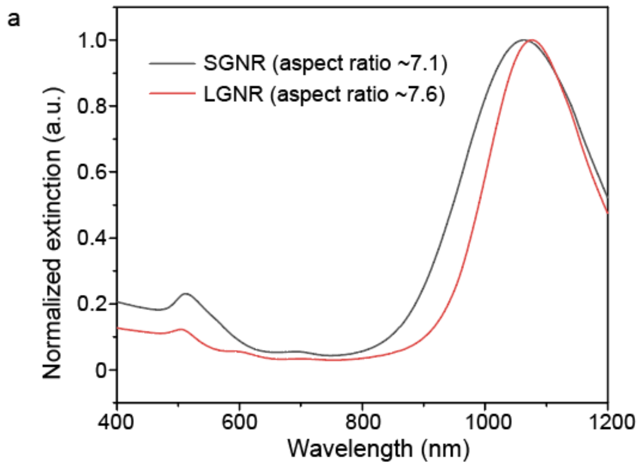

Figure 2.7 UV-vis-NIR spectra of LGNR and SGNR
UV–vis–NIR spectra data of LGNR and SGNR. LGNR and SGNR have longitudinal absorption peaks at 1064 nm and 1076 nm, respectively, due to their high aspect ratio.

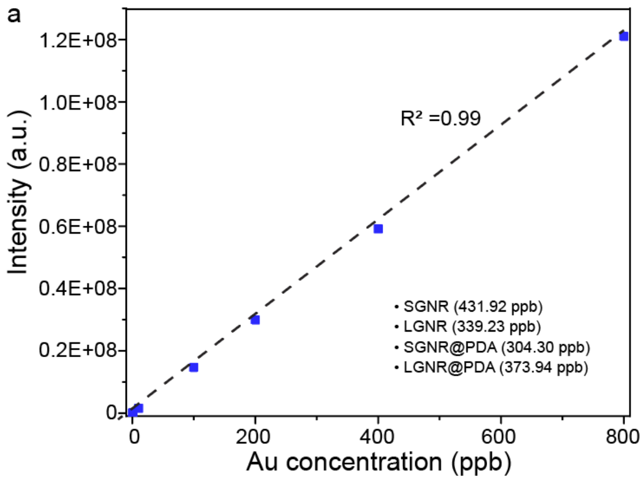

Figure 2.8 ICP-MS data
ICP-MS was used to calculate the Au concentration in each sample. Then, GNR and GNR@PDA concentrations were matched according to the number of Au ions.

2.4.3. Photothermal performance of SGNR@PDAs

Next, we examined the photothermal performance of LGNR, SGNR, and SGNR@PDA in NIR-II using a laser of 1064 nm for excitation. The skin-tolerance threshold set by the America Standards Institute is MPE of 1.0 W/cm^2 for 1064 nm laser (ANSI Z136.1-2007); we therefore chose a 1064 nm laser power of 1.0 W/cm^2 to evaluate the photothermal properties of GNR-melanin nanohybrids. Figure 2.9a shows that the temperature of LGNR, SGNR, SGNR@PDA at the same concentration of 10 µg/mL increased to 46.5 °C, 49.8 °C and 57.3 °C, respectively within 10 min; temperature change of water was negligible. Photothermal conversion efficiency is the capacity of nanoparticle to convert laser energy into heat. The laser turned off after 30 min of irradiation, and the cooling rate was recorded every 30 seconds to measure heat transferring from the nanoparticles to surroundings. Compared to other agents such as GNR@Ag (28.8%), Au@Metal-Organic Framework (30.2%) [101, 102], the SGNR@PDA showed high photothermal conversion efficiency (40%) at 1064 nm. This value was also higher than SGNR (30%) and LGNR (27%) (Figure 2.9b). Furthermore, the photothermal conversion efficiency of PDA nanoparticle was 18% at 1064 nm indicating that GNR-melanin nanohybrids can offer outstanding photothermal performance (Figure 2.10). Superior photothermal efficiency of SGNR@PDA results from a higher optical absorption, large surface area of PDA, and improved thermal conversion efficiency (Grüneisen parameter) due to the thermal confinement of the PDA shell. Likewise, photothermal conversion efficiency of LGNR@PDA was 4% higher than LGNR (Figure 2.11). The thermal images also showed SGNR@PDA rapidly increased temperature to 50 °C within one minute compared to SGNR and LGNR, which required three to four minutes to achieve a similar temperature (Figure 2.9c).

SGNR@PDAs showed excellent conversion stability in four successive cycles confirming its good photostability in the NIR-II window (Figure 2.9d). In addition, SGNR@PDAs did not show any disassembly of PDA coating or morphology changes after four successive cycles of laser irradiation (Figure 2.12). The PDA coating can improve photothermal stability of GNR during laser irradiation because gold atoms on the surface of GNR@PDAs are tightly immobilized because of the highly crosslinked PDA shell and π-stacking structure [85]. Therefore, the PDA shell serves as physical barrier while the atomic rearrangement in the GNR requires more energy. On the other hand, pristine GNRs alone cannot afford extensive heating [85]. We further studied the photothermal property of SGNR@PDA in different particle concentrations and power densities. The temperature changes (ΔT) showed that the temperature increase was linearly proportional to the particle concentration. For example, ΔT of SGNR@PDA was 19.1 °C, 22.2 °C, 24.4 °C, and 25.5 °C for concentrations of 4, 6, 8, and 10 µg/mL after 7 min of NIR-II laser irradiation at the same power density of 1.0 W/cm^2 (Figure 2.9e).

The ΔT of SGNR@PDA also corresponded to the laser power density. For example, the temperature of SGNR@PDA increased to 20.8 °C, 25.4 °C, 27.5 °C, and 36.7 °C at the laser power densities of 0.9 W/cm^2, 1.1 W/cm^2, 1.3 W/cm^2, 1.5 W/cm^2 at the fixed concentration of 10 µg/mL (Figure 2.9f). Collectively, these findings corroborated distinctive thermophilic characteristics and high photothermal conversion efficiency of SGNR@PDA highlighting its potential use in therapeutic agent for cancer treatment.

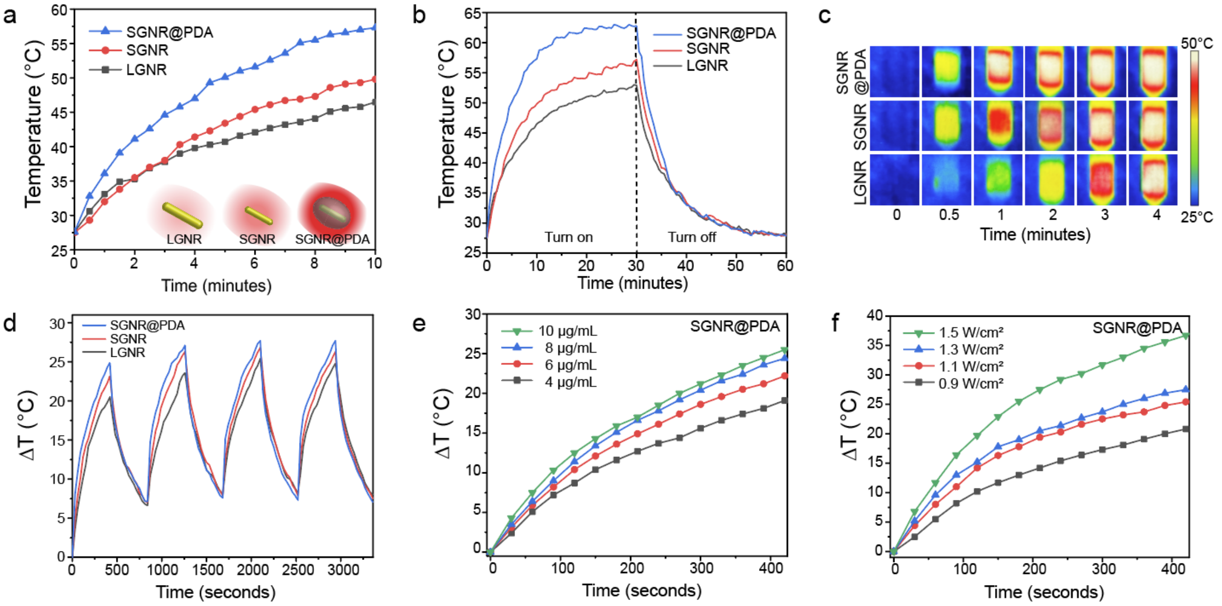

Figure 2.9 Photothermal performance of SGNR, LGNR, and SGNR@PDA

Schematic illustration of the photothermal performance of LGNR, SGNR, and SGNR@PDA triggered by NIR-II (1064 nm) laser. (b) Temperature curves of LGNR, SGNR, and SGNR@PDA for 1 h under NIR-II (1064 nm) laser irradiation, showing that the temperature of SGNR@PDA largely increased compared to SGNR and LGNR. (c) Thermal images of LGNR, SGNR, and SGNR@PDA irradiated at 1064 nm. (d) Temperature changes of LGNR, SGNR, and SGNR@PDA under repeated "on and off" laser irradiation for four times cycle. (e) Temperature changes of SGNR@PDA with the elevated concentrations (e.g., 4, 6, 8, and 10 µg/mL) for 7 min irradiation. (f) Temperature changes of SGNR@PDA at different power densities (0.9, 1.1, 1.3, and 1.5 W/cm^2) for 7 min irradiation. Temperature curves of SGNR and LGNR are shown in Figure 2.13.

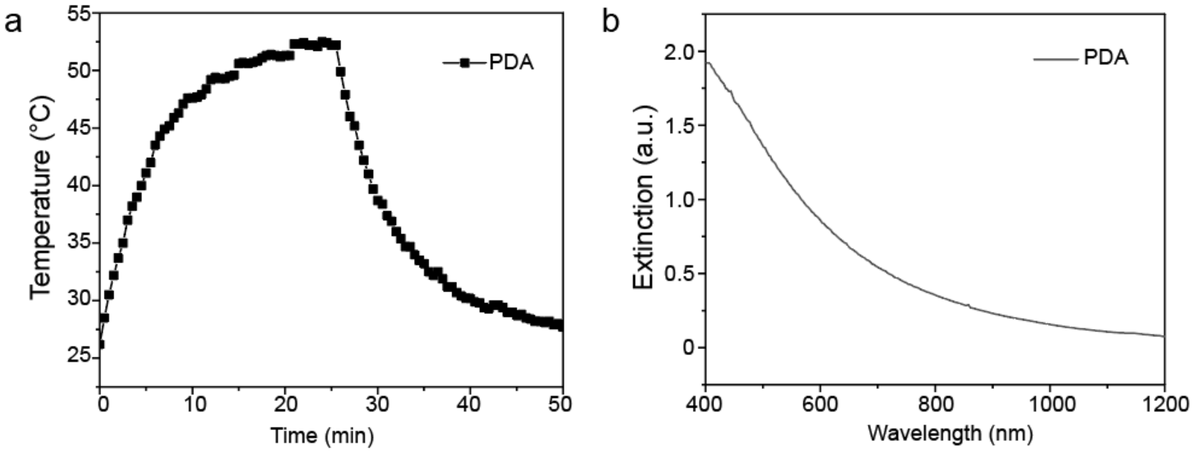

Figure 2.10 Temperature curve and UV-vis-NIR of PDA

Temperature curve (a) and UV–vis–NIR spectra (b) of PDA nanoparticles with the size of 100 nm. Photothermal conversion efficiency of PDA nanoparticle was 18% which is significantly lower than GNR-melanin nanohybrids because PDA nanoparticles had low absorption efficiency in NIR-II window as observed in UV–vis–NIR spectra. The NIR-II laser turned off after 25 min of irradiation, and the cooling rate was recorded every 30 s to measure photothermal conversion efficiency.

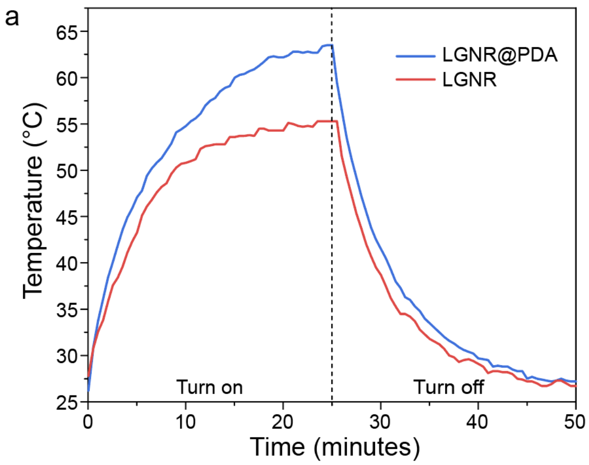

Figure 2.11 Temperature curves of LGNR and LGNR@PDA

Temperature curves of LGNR and LGNR@PDA for 50 min under NIR-II (1064 nm) laser irradiation. The temperature of LGNR@PDA at 25 min of irradiation was 7 °C higher than LGNR indicating that PDA coating enhances photothermal performance of LGNR.

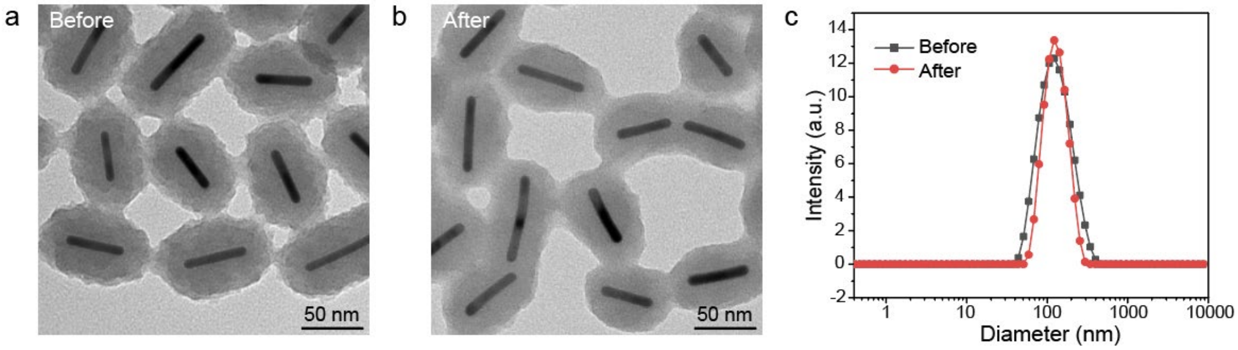

Figure 2.12 Robust SGNR@PDA before and after four cycles of 1064 nm laser irradiation
TEM images before (a) and after (b) four cycles of irradiation. (c) Negligible aggregation or disassembly of PDA coating was observed in DLS measurements.

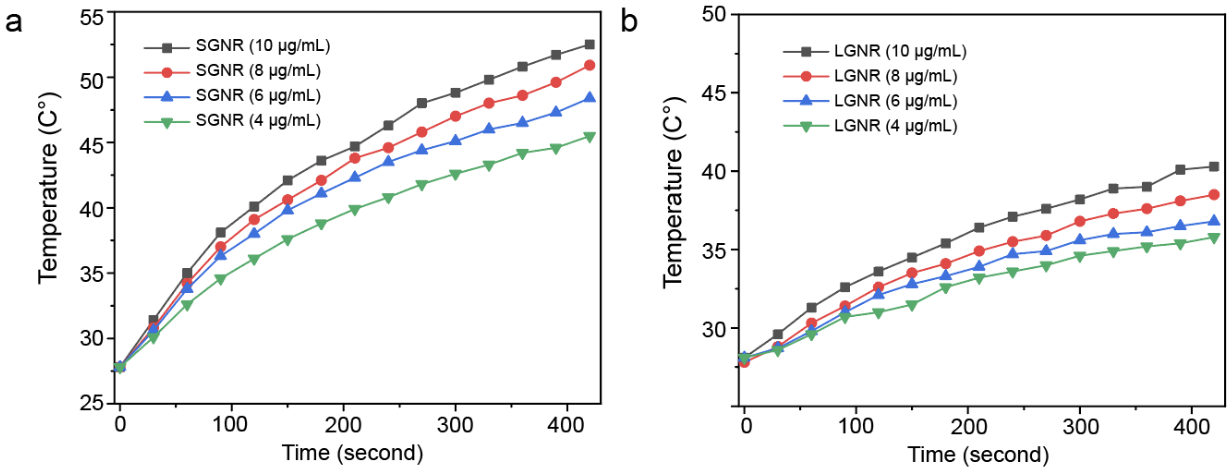

Figure 2.13 Temperature curves of SGNR and LGNR
Temperature curves of SGNR and LGNR with the elevated concentrations (e.g., 4, 6, 8, and 10 µg/mL) for 7 min at 1064 nm laser irradiation. These results indicate that increases in temperature are concentration-dependent due to improved optical absorption.

2.4.4. Photothermal treatment of SGNR@PDA *in vitro*

We investigated the PTT efficacy of the SGNR@PDA at the NIR-II window *in vitro*. SKOV3 cancer cells were incubated with LGNR, SGNR, or SGNR@PDA with different concentrations from 0.2 μM to 1.2 μM for 24 h. After co-incubation for 24 h, the cell viabilities of SKOV3 were greater than 90% indicating that both PEGylated GNRs and GNR@PDAs had negligible cytotoxicity (Figure 2.14a). We then studied photothermal ablation toward SKOV3 cells when they were incubated with LGNR, SGNR, or SGNR@PDA at the same concentration (1.0 μM). Importantly, SGNR@PDA showed effective cell ablation (95%) after 10 min of laser irradiation at 1064 nm while cell ablations from LGNR and SGNR were 66% and 74%, respectively (Figure 2.14b). SKOV3 cells without nanoparticles retained high cell viability before (100%) and after (99%) laser irradiation validating that LGNR, SGNR, and SGNR@PDA are the main factors to elicit photothermal ablation of SKOV3 cells (Figure 2.14b).

The photothermal treatment from LGNR, SGNR, and SGNR@PDA was further studied and visualized via live-dead cell fluorescent stanning. Calcein-AM (green fluorescence for live cells) and PI (red fluorescence of dead cells) were used in these experiments. Strong green fluorescence was observed when SKOV3 cells were incubated with LGNR, SGNR, or SGNR@PDA before NIR-II laser irradiation (Figure 2.14c). After 10 min of NIR-II laser irradiation, SKOV3 cells treated with LGNR, SGNR, or SGNR@PDA showed red fluorescence. SKOV3 cells incubated with SGNR@PDA showed strong red fluorescence, which corresponds to quantitative data: The cell ablation of SGNR@PDA was 95% (Figure 2.14b-c). The SKOV3 cells alone were irradiated with NIR-II laser for 10 min to validate the lack of involvement of the laser toward the photothermal ablation; strong green fluorescence was observed before and after laser irradiation (Figure 2.14c). These results indicated that the NIR-II laser alone could not cause cell death, and photothermal performance of SGNR significantly improved when PDA was coating due to higher temperature induced from the PDA shell. Finally, the colloidal stability of SGNR@PDA was investigated in different media (e.g., 10 mM, HCl, 10 mM NaOH, 10 mM NaCl, DMEM with 10% fetal bovine serum, and DMEM with the human serum of 10%). DLS data showed that SGNR@PDA maintained its GNR-melanin assemblies and showed negligible aggregation under those conditions (PDI ~ 0.1) (Figure 2.15). These results indicate that PDA coating is highly intact and stable under biological conditions. Therefore, our PDA coating strategy can improve photothermal performance over the SGNR probe with excellent colloidal stability.

Although proof-of-concept, this work invites more studies to improve the viability of melanin-GNRs for anticancer therapy *in vivo*. One limitation of this work is lack of tumor targeting *in vivo*. In a mouse model, the photothermal performance of LGNR, SGNR, and SGNR@PDA species could be less efficient due to tissue thickness, light scattering, and absorbance from the tissue. More importantly, we do show higher photothermal performance of SGNR@PDA than SGNR due to improved optical absorption, and higher thermal conversion efficiency due to the thermal confinement of PDA shell. Future work will include photothermal treatment of SGNR@PDA in mouse model for clinical application of NIR-II PTT.

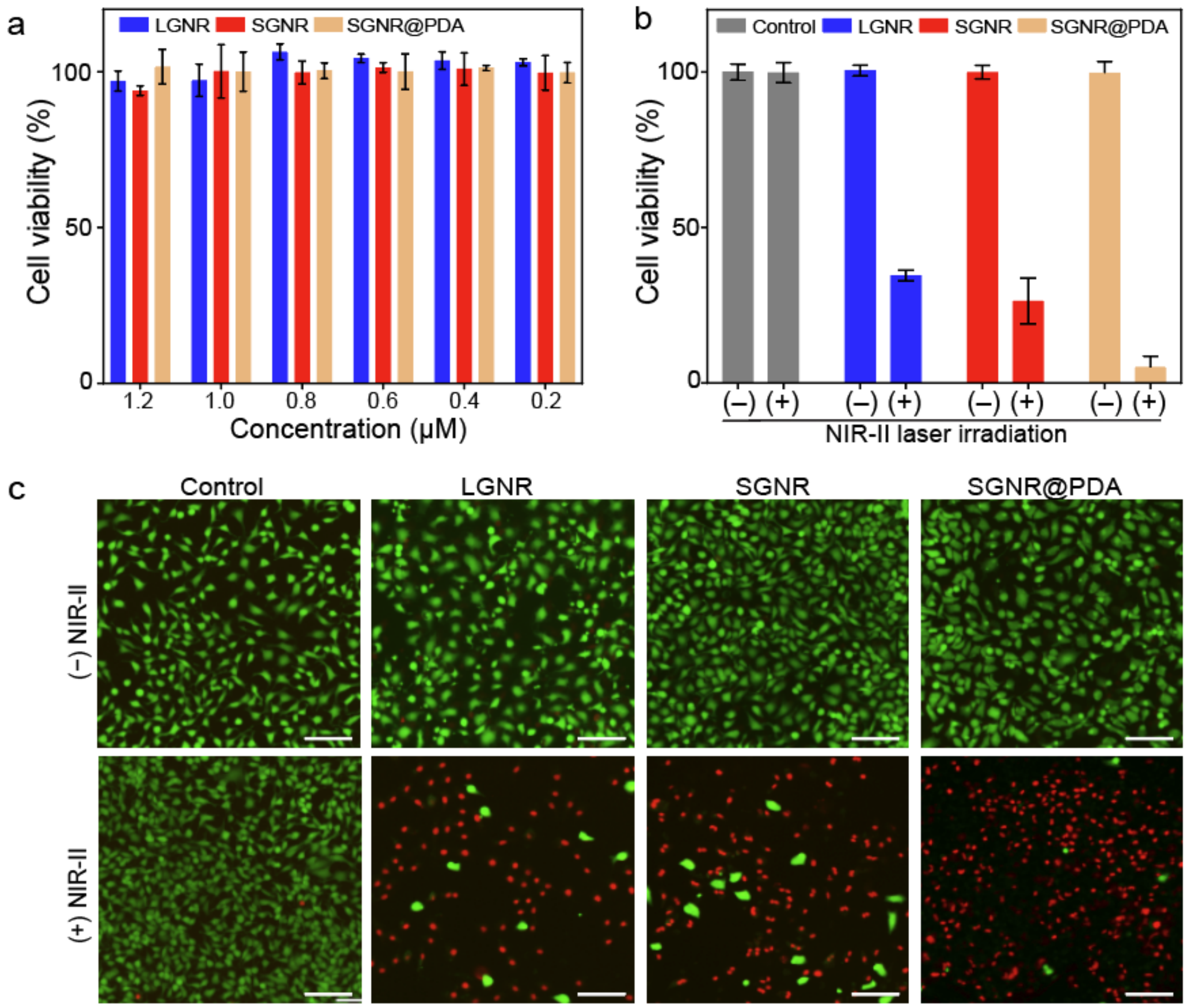

Figure 2.14 Photothermal performance of SGNR@PDA on SKOV3 cancer cell.
(a) Cell viability of SKOV3 cells after co-incubated for 24 h with LGNR, SGNR, and SGNR@PDA at different concentrations. (b) Cell viability of SKOV3 cells before and after photothermal treatment (1.0 W/cm^2 for 1064 nm, 10 min) at the same concentration of LGNR, SGNR, and SGNR@PDA (1.0 μM), indicating that SGNR@PDAs showed high photothermal-induced cell ablation compared to LGNR and SGNR. SKOV3 cells without injecting nanoparticles (referred as Control) were exposed to the laser, showing that there was no involvement of cell medium to kill the SKOV3 cells. The error bar represents the standard deviation of three measurements. (c) Fluorescence images of Control, LGNR, SGNR, and SGNR@PDA stained with Calcein AM and PI before and after laser irradiation at 1064 nm (1.0 W/cm^2 for 1064 nm, 10 min). Photobleaching was used to confirm healthy and dead SKOV3 cells (Figure 2.16). The scale bar indicates 100 μm.

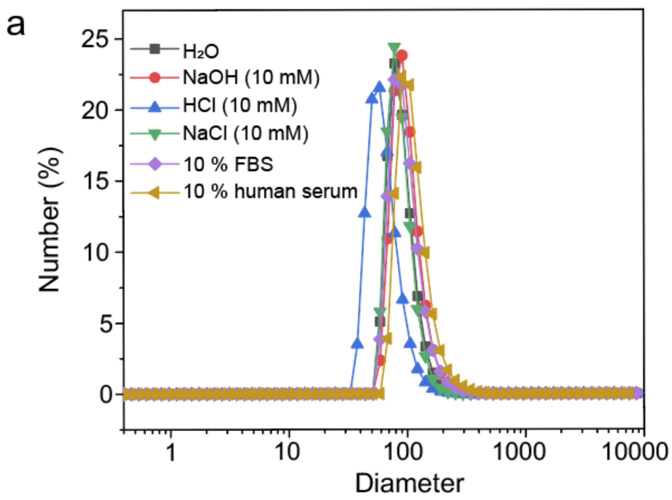

Figure 2.15 Colloidal stability of SGNR@PDA in different conditions
The colloidal stability of SGNR@PDA in different media (10 mM of HCl (~ pH 2), 10 mM of NaOH (~ pH 12), 10 mM of NaCl, DMEM of 10 % fetal bovine serum (FBS), and the human serum of 10 %). DLS data showed SGNR@PDA had high colloidal stability under different biological and extreme conditions. No disassembly of PDA coating or negligible aggregation was found, indicating that PDA coating is robust and stable.

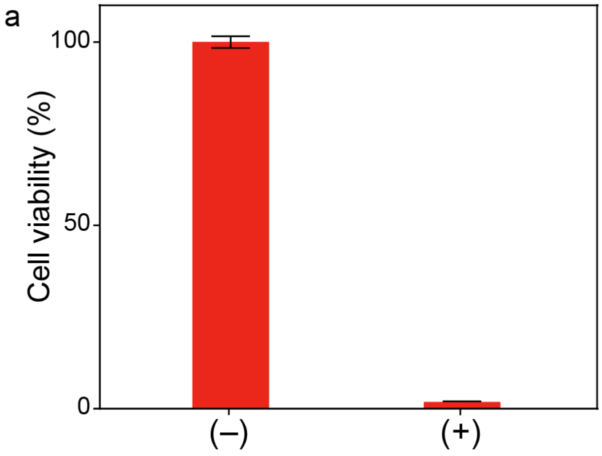

Figure 2.16 Photobleaching of SKOV3 cancer cells
Photobleaching is known to kill SKOV3 cancer cells. We conducted photobleaching for positive and negative controls, confirming healthy (without photobleaching) and dead SKOV3 (with photobleaching) cancer cells.

2.5. Conclusion

Plasmonic nanomaterials, especially GNRs, hold great promise in photo-mediated applications due to their tunable and high absorption efficiency. However, anisotropic nanostructures under the laser irradiation become unstable, losing their unique optical properties. In this study, we synthesized both large GNR and ultrasmall GNR to investigate ‘size-effect’ and further synthesized GNR-melanin hybrids (i.e., GNR@PDA) to study ‘PDA coating effect’ altogether. SGNRs showed higher PA performance over large GNR due to high surface-to-volume ratio. Furthermore, SGNR@PDA showed three-fold higher PA signal than core SGNR nanoparticles and 10% higher photothermal efficiency over SGNR due to improved optical absorption and 2.4-fold higher thermal conversion efficiency. These SGNR@PDA nanohybrids also elicited effective photothermal ablation of SKOV3 cancer cells (95%) which was significantly higher than LGNR (66%) and SGNR (74%). These findings indicate high potential use of the PDA coating strategy in developing photo-mediated biomedicines in NIR-II window and expand our understanding photothermal conversion mechanism occurring in hybrid nanostructures.

2.6. Acknowledgement

The authors acknowledge the National Science Foundation under award 1937674 and 1845683. We also thank National Institute of Health under awards DP2 HL137187. The authors also acknowledge infrastructure support under awards S10 OD021821 and S10 OD023555. MNC and RMB acknowledge fellowship support under T32 CA153915. Transmission electron micrographs were taken in the Cellular and Molecular Medicine Electron Microscopy Core Facility, which is supported by National Institutes of Health award number S10 OD 023527. This work was performed in part at the San Diego Nanotechnology Infrastructure (SDNI) of University of California San Diego, a member of the National Nanotechnology Coordinated Infrastructure (NNCI), which is supported by the National Science Foundation (Grant ECCS-1542148).

Chapter 2, in part, is a reprint of the material as it appears in “Ultrasmall gold nanorod-polydopamine hybrids for enhanced photoacoustic imaging and photothermal therapy in second near-infrared window” by Yim, Wonjun; Borum Raina M.; Zhou, Jiajing; Mantri, Yash; Wu, Zhuohong; Zhou, Jingcheng; Jin, Zhicheng; Creyer, Matthew N.; and Jokerst, Jesse V., Nanotheranostics 2022. The dissertation author was the primary investigator and author of this paper.

CHAPTER 3. Enhanced photoacoustic detection of heparin in whole blood via melanin nanocapsules carrying molecular agents.

3.1. Abstract

Photoacoustic (PA) imaging has proved versatile for many biomedical applications from drug delivery tracking to disease diagnostics and post-operative surveillance. It recently emerged as a tool for accurate and real-time heparin monitoring to avoid bleeding complications associated with anticoagulant therapy. However, molecular-dye-based application is limited by high concentration requirements, photostability, and strong background hemoglobin signal. We developed polydopamine nanocapsules (PNC) *via* supramolecular template and loaded them with molecular dyes for enhanced PA-mediated heparin detection. Depending on surface charge, the dye-loaded PNCs undergo disassembly or aggregation upon heparin recognition: both experiments and simulation have revealed that the increased PA signal mainly results from dye-loaded PNC–heparin aggregation. Importantly, Nile blue (NB)-loaded PNCs generated 10-fold higher PA signal than free NB dye, and such PNC enabled the direct detection of heparin in a clinically-relevant therapeutic window (0–4 U/mL) in whole human blood ($R^2 = 0.91$). Furthermore, the PA signal of PNC@NB obtained from 17 patients linearly correlated with ACT values ($R^2 = 0.73$) and cumulative heparin ($R^2 = 0.83$). This PNC-based strategy for functional nanocapsules offers a versatile engineering platform for robust biomedical contrast agents and nanocarriers.

3.2. Introduction

Heparin-based anticoagulant drugs—including unfractionated heparin, low molecular weight heparin, and synthetic heparin—are key elements of surgical and cardiovascular medicine to prevent blood clots, but bleeding risks associated with anticoagulants require close monitoring to prevent heparin overdose.[103-107] Infants are particularly susceptible to heparin overdoses due to their small weight and miscalculation of dosage level.[108-110] Thousands of children have suffered from hemorrhages or emboli and infant deaths have been attributed to heparin errors.[109, 111] The conventional toolkit for monitoring heparin activity uses activated coagulation-time assays, *e.g.,* activated partial thromboplastin time (aPTT), anti-Xa analysis, and activated clotting time (ACT).[112] aPTT has been widely used to monitor heparin; however, it suffers from long turnaround times, and can be impacted by variations (*e.g.*, sample volume, diurnal changes, fibrinogen).[113] While anti-Xa test is not impacted by collection tubes or fibrinogen, it is costly and requires extensive sample processing (~1h).[114] Lastly, all these tools are limited by low frequency of sampling which means they are limited to periodic determination.[115, 116] Thus, a variety of methods have been proposed to provide real-time information of heparin anticoagulation therapy.

Photoacoustic (PA) imaging has advantages *versus* other alternatives for monitoring heparin (Table 3.1). For example, fluorescence-based methods are sensitive but can be difficult to use in biological conditions, *e.g.,* serum, whole blood.[117-121] Fluorescence is also difficult to use in biological tissues due to light scattering while PA signal can propagate through the tissue and monitor specific biological events.[122] Colorimetric methods are simple but are limited to color changes in whole human blood.[123-125] Heparin detection in whole human blood is valuable because it can avoid drawing blood and does not require blood fractionation to collect plasma. It can expedite the sensing process, thus closely monitoring heparin in real time. Electrochemical methods allow for heparin sensing in whole blood, but they still require elaborate pre-treatments: blood samples were diluted 100-fold with PBS and 5 mM of potassium ferrocyanide.[126-128] All these methods have yet to be broadly studied for clinical care (Table 3.1). In contrast, PA imaging is real-time, non-invasive and can directly monitor heparin without any pre-treatments even in whole human blood. Therefore, PA imaging is proposed here to improve the standard of care in monitoring heparin.[10, 76, 129, 130] PA imaging uses a light in–sound out approach, where the light excites target materials to generate acoustic waves detected by ultrasonic transducers.[13] A previous study demonstrated that PA imaging can monitor heparin in whole human blood *via* MB dye. Increased PA signal of MB dye was a function of heparin concentration due to strong MB–heparin association that improves heat transfer.[129] However, the use of free molecular dyes to monitor heparin suffers from several drawbacks such as high concentration requirements (*e.g.,* 1 mM of free MB dye), photostability, and broadly interfering background signal from hemoglobin.[129, 131-133] Incorporating these molecular dyes into a rigid nanostructure is an effective method to overcome the above limitations by modulating the PA-related processes (*e.g.,* optical absorbance, fluorescence quenching, photo-protection, heat confinement, and heat transfer).[134-138] For example, indocyanine green (ICG)-loaded mesoporous silicon nanoparticle (MSN) showed higher PA performance than free ICG dye due to low thermal conductivity of MSN.[136] However, synthesizing porous nanostructures often requires strong acidic solvents (*e.g.,* hydrofluoric acid) for template removal and tedious shell fabrication (*e.g.,* layer-by-layer).[136, 139, 140]

In this work, we report polydopamine nanocapsules (PNCs) loaded with small molecular dyes to monitor heparin *via* PA imaging (Figure 3.1a). *Versus* other templates (*e.g.,* polymer, silica, and metal nanoparticles), we used a simple supramolecular template which is size-tunable (*e.g.,* 50–650 nm) and highly stable in various aqueous conditions (*e.g.,* acidic and alkaline environments) but can readily disassemble in organic solvents (*e.g.,* dimethylformamide (DMF)).[80, 140] Using supramolecular networks, we successfully developed a synthetic hollow melanin that has superior loading capacity over compact polydopamine (PDA) nanoparticles. Furthermore, various molecular dyes can be easily loaded into the nanocapsule due to the desirably adhesive nature of PDA originated from catechol groups.[33, 141] We empirically demonstrated multiple noncovalent interactions (*e.g.,* electrostatic, π–π stacking, hydrophobic interactions) that are involved in dye–PNC assemblies and validated them with molecular dynamic (MD) simulations. These dye-loaded PNCs showed exceptional PA enhancement compared to the free molecular dyes due to the lower thermal conductivity of PDA, fluorescence quenching, local concentration of free dyes, and photo-protection. Specifically, MB-loaded PNC generated 10-fold PA enhancement over free MB dye at the same dye concentration. Our results also revealed two phenomena: (1) surface charge-dependent disassembly (*i.e.,* release) of dyes from PNC and (2) aggregation of dye-loaded PNC during heparin interactions (Figure 3.1b). Intriguingly, heparin-mediated aggregation of dye-loaded PNC led to a decreased optical absorbance with a concurrent increase in PA signal. The increased PA signal is likely due to the reduced degrees of freedom of particles that induced poor heat transfer and increased the thermal gradient between aggregates and solvent.[142] This PDA-enabled strategy highlights the approach of designing functionalized nanocapsules for enhanced PA imaging with increased insight into the PA mechanism occurred in nanoparticles.

Table 3.1 PA imaging compared to other methods for monitoring heparin.
Clinical validation means that the methods validate with human samples.

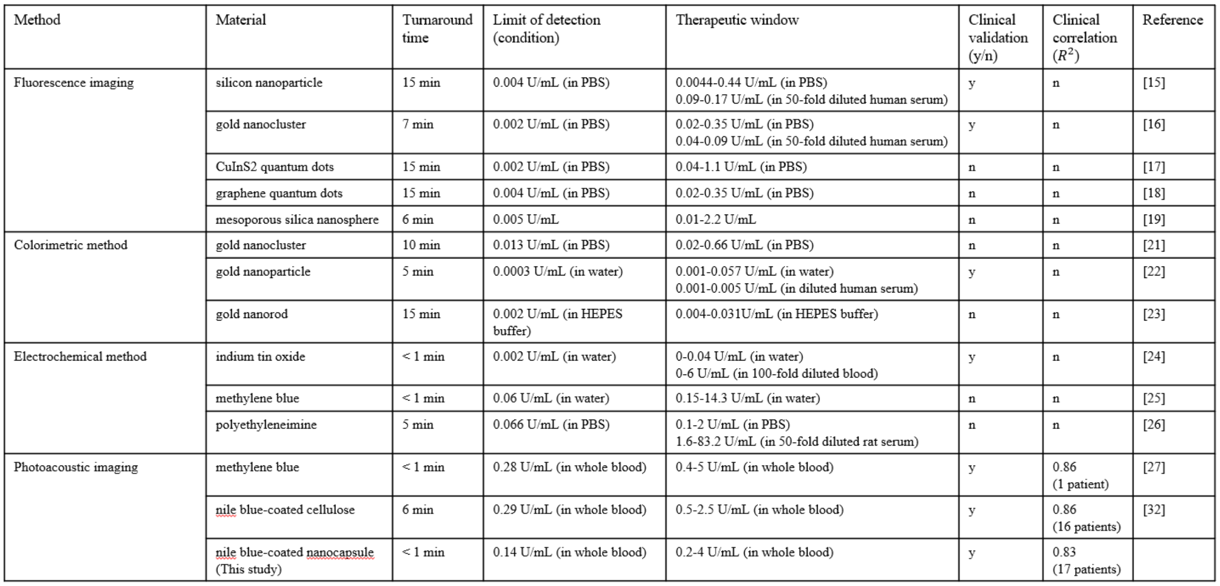

Method	Material	Turnaround time	Limit of detection (condition)	Therapeutic window	Clinical validation (y/n)	Clinical correlation (R^2)	Reference
Fluorescence imaging	silicon nanoparticle	15 min	0.004 U/mL (in PBS)	0.0044-0.44 U/mL (in PBS) 0.09-0.17 U/mL (in 50-fold diluted human serum)	y	n	[15]
	gold nanocluster	7 min	0.002 U/mL (in PBS)	0.02-0.35 U/mL (in PBS) 0.04-0.09 U/mL (in 50-fold diluted human serum)	y	n	[16]
	CuInS2 quantum dots	15 min	0.002 U/mL (in PBS)	0.04-1.1 U/mL (in PBS)	n	n	[17]
	graphene quantum dots	15 min	0.004 U/mL (in PBS)	0.02-0.35 U/mL (in PBS)	n	n	[18]
	mesoporous silica nanosphere	6 min	0.005 U/mL	0.01-2.2 U/mL	n	n	[19]
Colorimetric method	gold nanocluster	10 min	0.013 U/mL (in PBS)	0.02-0.66 U/mL (in PBS)	n	n	[21]
	gold nanoparticle	5 min	0.0003 U/mL (in water)	0.001-0.057 U/mL (in water) 0.001-0.005 U/mL (in diluted human serum)	y	n	[22]
	gold nanorod	15 min	0.002 U/mL (in HEPES buffer)	0.004-0.031U/mL (in HEPES buffer)	n	n	[23]
Electrochemical method	indium tin oxide	< 1 min	0.002 U/mL (in water)	0-0.04 U/mL (in water) 0-6 U/mL (in 100-fold diluted blood)	y	n	[24]
	methylene blue	< 1 min	0.06 U/mL (in water)	0.15-14.3 U/mL (in water)	n	n	[25]
	polyethyleneimine	5 min	0.066 U/mL (in PBS)	0.1-2 U/mL (in PBS) 1.6-83.2 U/mL (in 50-fold diluted rat serum)	n	n	[26]
Photoacoustic imaging	methylene blue	< 1 min	0.28 U/mL (in whole blood)	0.4-5 U/mL (in whole blood)	y	0.86 (1 patient)	[27]
	nile blue-coated cellulose	6 min	0.29 U/mL (in whole blood)	0.5-2.5 U/mL (in whole blood)	y	0.86 (16 patients)	[32]
	nile blue-coated nanocapsule (This study)	< 1 min	0.14 U/mL (in whole blood)	0.2-4 U/mL (in whole blood)	y	0.83 (17 patients)	

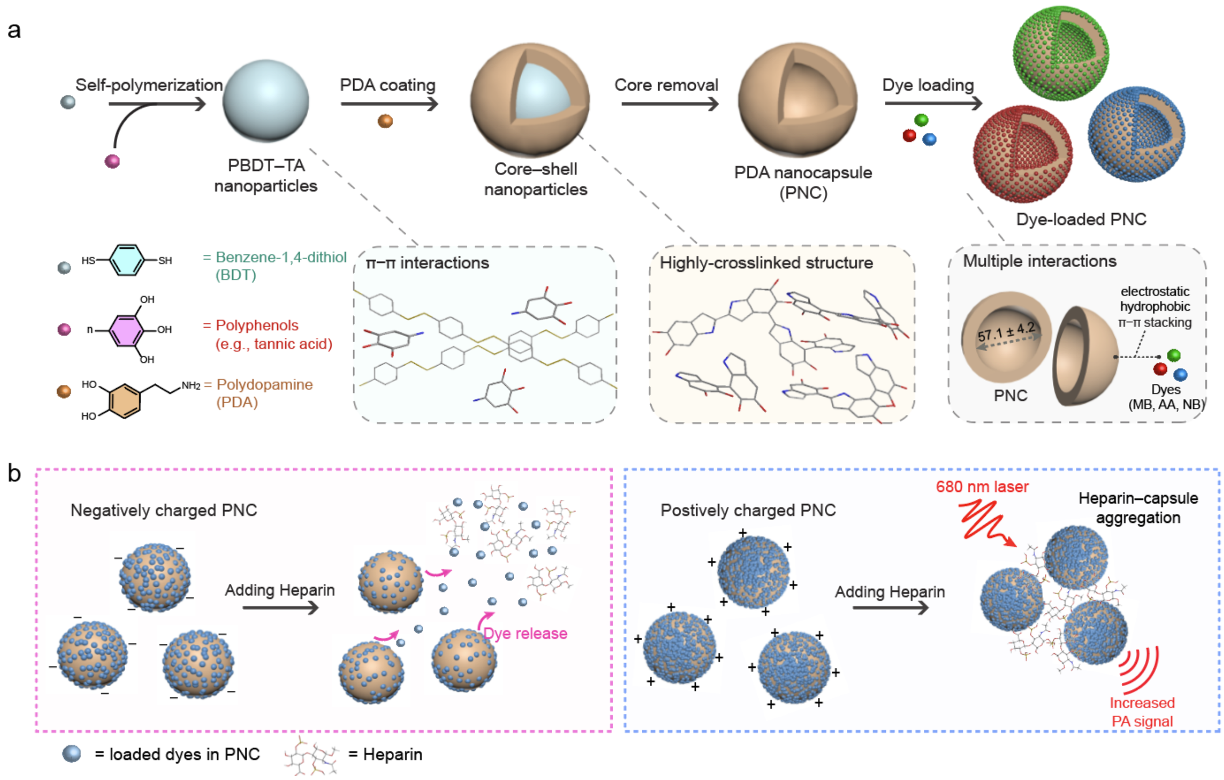

Figure 3.1 Synthetic pathway and charge-dependent behaviors of functionalized PNC

a Schematic of simple synthesis of dye-loaded PNCs. PNC was synthesized using a supramolecular template (PBDT–TA). By virtue of glue-like nature of PDA, PNC was loaded with small molecular dyes (*e.g.,* NB, AA, and MB) *via* multiple interactions. b During heparin interactions, negatively charged PNCs released the loaded dyes in PNCs, while positively charged PNCs showed particle aggregation that increased PA signal.

3.3. Materials and methods

3.3.1. Synthesis of PBDT–TA nanoparticles

For synthesis of PBDT–TA nanoparticles with the diameter of 80 nm, 375 μL of TA solution (16 mg mL^{-1} in water) was added to 12 mL of bicine buffer (pH 8.5, 10 mM) under vigorous stirring at 1200 rpm.[80] Then, 1.44 mL of BDT solution (4 mg mL^{-1} in DMF) was added and stirred for 12 h. The size of PBDT–TA nanoparticles was tunable by adding more BDT solution at the fixed TA concentration. The resulting PBDT–TA nanoparticles were purified by centrifugation (9,000 *g* for 10 min) twice to remove the excess complexes. The pellet was resuspended in water for future use.

3.3.2. Synthesis of PBDT–TA@PDA nanoparticles

The concentrated PBDT–TA nanoparticles was first dispersed in 8 mL of bicine buffer (10 mM, pH 8.5), followed by the addition of 1 mL of dopamine solution (4 mg mL^{-1} in water) under vigorous stirring at 1200 rpm for 12 h. The color of solution changes from white to dark brown as polydopamine was coated on the PBDT–TA nanoparticles. The resulting product was purified by centrifugation (9,000 *g* for 10 min) twice. The thickness of PDA coating is tunable from 25 to 100 nm by adjusting the amount of dopamine solution from 1.0 to 6.0 mg mL^{-1} while fixing the concentration of PBDT–TA nanoparticles. The pellet was resuspended in water for future use.

3.3.3. Synthesis of PEGylated PNCs

To obtain PNC, the core PBDT–TA nanoparticles were dissolved by DMF. Briefly, 100 μL of the PBDT–TA@PDA nanoparticles was incubated in 1.5 mL of DMF solvent at 60 °C and then shaken at 700 rpm for 12 h to completely disassembly PBDT–TA complex. For the washing process, the resulting product was spun down by centrifugation (9,000 *g* for 10 min) and the supernatant was removed. The pellet was resuspended in water for future use.

For PEGylation, the obtained 1 mL of PNC was first dispersed in 1 mL bicine buffer (pH 8.5, 10 mM) under generous stirring. Then, 100 μL of the SH-mPEG (5mg mL^{-1} in water) was added and gently stirred for 12 h. The resulting product was purified by centrifugation, and the pellet was resuspended in water for future use.

3.3.4. Synthesis of dye-loaded PNCs

The PEGylated PNCs were first dispersed in 2 mL bicine buffer (pH 8.5, 10 mM) for 30 min while 15 mM of dyes (*e.g.,* MB, AA, NR, or NB) were freshly prepared. We chose MB, AA, NR, and NB dyes which are approved by US Food & Drug Administration (FDA) and can interact with heparin, changing their absorbance and fluorescence. 10–25 μL of the prepared dyes was added to the solution under generous stirring at 7000 rpm for 12 h. For washing process, the resulting product was purified by four-times centrifugations (5,000 *g* for 10 min), and the supernatants were used to calculate the loading efficiency. The pellet was resuspended in water for future use.

3.3.5. Stability test of dye-loaded PNCs

In brief, 200 μL of dye-loaded PNCs were incubated in 1 mL of 10 mM SDS, 10 mM Triton X-100, 10 mM NaCl, 10 mM urea, 10 mM HCl (pH ≈ 2), 10 mM NaOH (pH ≈ 12), DMSO, and DMF. The solution was mixed using a vortex mixer for 5 s and then incubated for 1h. Then, the samples were spun down by centrifugation (12,000 *g* for 10 min), and the supernatant was used to calculate the amount of the disassembled dyes in different conditions.

3.3.6. Computational methodology

The molecular structure of heparin was constructed *via* GLYCAM carbohydrate builder software.[143] Specifically, the four monosaccharide units that were used in this study were YZB, WYS, YuA, and QYS. This pattern was repeated six times to construct the heparin polysaccharide. Dopamine-based tetramers and trimers were used for constructing PDA molecular structure.[144] Each monosaccharide, PDA tetramer, PDA trimer and dye was parametrized using Gaussian HF/6-31G* through the WebMO interface.[145, 146] All systems employ explicit solvent, which models each water molecule. TIP3P solvent parameters were used exclusively. The generated systems were minimized in seven restrained steps to eliminate bad contacts, heated in one step to 300 K, and equilibrated in seven steps, with each step reducing the imposed restraints on the systems. These preparatory operations and the unrestrained simulations were all completed using AMBER 16 with the ff14SB and GAFF force fields, while also utilizing additional parameters provided by GLYCAM.[147-149] All unrestrained simulations were run for 130 ns, with a time step of 2 fs, and at constant temperature and pressure of 300 K and 1 atm, respectively. Visualization and distance analyses were completed using visual molecular dynamic (VMD) and the *cpptraj* module of Amber, respectively.[150, 151] Distance analysis was performed to calculate the number of interactions between PNC@NB and heparin. An "interaction" was defined as a measured distance between centers of mass of two moieties that was less than 6.0 Å.

3.3.7. Decomposition analysis of Gibbs free energy

Free energy analysis was performed on each simulation using the MMPBSA.py module of AMBER. This yielded the contributions of Van der Waals, electrostatic, polar and nonpolar solvation to the energetics of a heparin/PDA interaction. In this context, a destabilizing force is one that inhibits the interaction, and is shown as a positive value. A stabilizing force is shown as a negative value and supports the interaction.

3.3.8. Human blood sample preparation, aPTT assay, hemolysis, and specificity test with different biological samples

All work with human subjects was done in accordance with IRB guidelines and approval. All subjects gave informed consent. Whole human blood was collected in citrate tubes from a healthy donor according to the institutional guidelines and stored at 2 °C. For PA imaging, 50 μL samples were treated with 50 μL heparin (0–4 U/mL) and imaged within 1 h. To determine the correlation between PA intensity and blood clotting time, poor human plasma that included heparin with the concentration of 0, 0.2, 0.4, 0.6, 0.8, and 1 U/mL was used for aPTT analysis. Blood clotting times were measured in triplicate with an ST4 semi-automated mechanical coagulation instrument (Diagnostica Stago, NJ). Briefly, 50 μL of aPTT reagent was added to 50 μL of citrated plasma and incubated at 37 °C with stirring magnetic ball for 5 min. Then, 50 μL of 25 mM $CaCl_2$ was injected to initiate blood clotting. The time required for blood clot was calculated in seconds. For hemolysis analysis, whole human blood cells were incubated with different concentrations of samples (*e.g.,* PNC@MB, PNC@AA, PNC@NB, and PNC) for 4 h. The DPBS and deionized water were used as negative and positive controls, respectively. Then the samples were centrifuged at 4,000 rpm, and the supernatant were collected for the absorbance measurement. For specificity test, PNC@NB was incubated with different biological conditions (*e.g.,* water, heparin, BSA, Hgb, human pooled plasma (55%), thrombin, DMEM, PSS, relevant ions (*e.g.,* Cl^-, Ca^{2+}), and heparin analogue (*e.g.,* chondroitin sulfate) at the same mass concentration (2 μg/mL)). After 1h, samples were imaged three times independently.

3.3.9. Clinical sample collection

All work with human subjects was done in accordance with institutional review board (IRB) guidelines and approval of UCSD (#180923) and San Diego Veterans Administration hospital (#H170005). All subjects gave informed consent. Clinical samples were collected from 17 patients undergoing invasive clinical cardiac procedures that need anticoagulation with high dose iv. heparin. 2–5 mL of each clinical sample was collected in parallel with the specimens obtained for the activated clotting time (ACT) from the baseline prior to heparin infusion to the end of heparin infusion for the maintenance of the anticoagulation. The samples were collected at different points of heparin infusion until reaching steady-state anticoagulation (> ACT of 470 s). Then, plasma of each sample was separated and stored at –80 °C. The amount of heparin infused in parallel with ACT value was recorded for comparison to the photoacoustic technique. All samples were thawed at 37 °C and studied within 12 h of thawing. 50 μL of PNC@NB reacted with 100 μL of each clinical specimen. After 15 min of reaction, the samples were placed into polyethylene tubes (~2 cm long) and imaged with a customized holder.

3.3.10. Surface area calculation

Surface area of PDA nanoparticle and PNC was calculated using the diameter of PDA nanoparticle (60 nm), outer and inner diameter of PNC (80 nm and 40 nm) based on the mathematical formula (πr^2). Fifty nanoparticles were used to calibrate the diameters of PNC and PDA nanoparticle.

3.3.11. Limit of detection calibration

The limit of detection (LoD) was calculated using the limit of blank (LoB).[152] The LoB is the highest signal generated from a sample that contains no analyte. It can be calculated by using the mean and standard deviation (SD) of a blank sample.

$\text{LoB} = \text{mean}_{\text{blank}} + 1.645(\text{SD}_{\text{blank}})$

LoD is the lowest analyte concentration that can be reliably distinguished from the LoB. LoD is calculated by using the LoB and the standard deviation of the sample. The LoD indicates an analyte concentration in which 95% of measured samples are readily distinguished from the LoB while remaining 5% can contain no analyte.

$\text{LoD} = \text{LoB} + 1.645(\text{SD}_{\text{low concentration sample}})$

In our experiment, the LoB and LoD were calculated from Figure 4b and Figure S29 using 0 U/mL, 0.1 U/mL (in water), and 0.2 U/mL (in whole human blood).

3.3.12. Loading capacity calculation

Loading capacity of dye-loaded PNCs was calculated using supernatants. The dye-loaded PNCs were centrifuged four times, and the supernatants were saved for absorbance measurement to calculate the amounts of dyes loaded in PNCs. The amounts of free dyes in the supernatants were determined by measuring the absorbance of the supernatant. Then, the amounts of dye loaded in PNCs were calculated by using the absorbance of total free dye used for the reaction and the supernatants obtained from each wash.

3.3.13. Data analysis

PA images were analyzed using ImageJ software (Bethesda, USA).[44] Images were changed to 8-bit images and analyzed with region of interest (ROI) by using integrated density function in ImageJ software. Average value, standard deviation, and linear regression were calculated using prism and origin software.

3.3.14. General characterizations

Scanning electron microscopy (SEM) images were acquired using a FEI Apreo operating at a voltage of 10 kV and a current of 0.10 nA. Transmission electron microscopy (TEM) images were obtained using a JEOL JEM-1400 Plus operating at 80 kV. TEM images were taken using a Gatan 4k digital camera, and TEM images were processed using ImageJ software (Bethesda, USA).[44] Electron-dispersive X-ray spectroscopy (EDX) were examined using a Thermo Fisher Talos 200X operating at 200 kV.Hydrodynamic size and zeta potential were calculated using dynamic light scattering (DLS) with a Malvern Instrument Zetasizer ZS 90. Absorbance and fluorescence spectra were measuring using a BioTek Synergy H1 plate reader. Samples were measured at the 150 μL scale in 96-well plates. Absorbance was collected from 400 to 900 nm with a step size of 2 nm. Fluorescence emission scans were collected with an excitation wavelength of 600 nm with a step size of 2 nm. Nanoparticle tracking analysis (NTA) measurement was performed using a ViewSizer 3000 (Horiba Scientific, CA, USA).[153] The temperature was controlled at 27 °C during the measurement. Automated noise analysis is used to determine the optimal wavelength for representing each nanoparticle. 8-bit composite video is generated for analysis, and 15 videos were recorded at a framerate of 30 fps for 10 s (300 frames for seconds). A quartz cuvette cell with a minimum volume of 0.8 mL was used for measurement. For the measurement, 50 μL of each sample was diluted in 2 mL of Millipore water. NTA measurement also can image nanoparticles with three lasers with different wavelengths (*e.g.,* red: 630 nm, green: 520 nm, and blue: 445 nm). Red laser is used to scatter large nanoparticles (300–500 nm), while blue laser is used to scatter small nanoparticles (20–200 nm). In this study, both PNC and PBDT@PDA nanoparticles were imaged using blue laser. ImageJ was used to change the color of PBDT–TA@PDA nanoparticle from blue to pink for particle comparison. PA imaging was acquired using a Vevo 2100 LAZR (Visual Sonics, USA) with a 21 MHz transducer (LZ-250). 20 μL samples were loaded into polyethylene tubes and fixed within a 3D printed holder. The samples were aligned at a depth of 1 cm from the transducer. The laser was optimized and calibrated before the measurement. An installed motor with the step size of 0.054 mm was used to acquire 3D images. PA spectra were measured from 680 to 970 nm with the step size of 2 nm.

3.4. Results and Discussion

3.4.1. Synthesis of dye-loaded PNC

6 mg of natural polyphenol (*e.g.,* tannic acid, TA) and 3 mg of aromatic dithiol (*e.g.,* benzene-1,4-dithiol, BDT) precursors are used to make polymerized BDT nanoparticles (referred as PBDT–TA) that serve as simple sacrificial templates.[80] First, we synthesized monodispersed PBDT–TA nanoparticles, where the size was easily tunable from 70 to 120 nm by increasing the concentration of BDT from 0.5 to 1.25 mg mL^{-1} at the fixed concentration of TA at 0.5 mg mL^{-1} (Figure 3.2). PDA was then coated on the PBDT–TA forming a highly uniform core–shell nanoparticle (PBDT–TA@PDA) as clearly observed by transmission electron microscopy (TEM) (Figure 3.3a and Figure 3.4–3.5). The removal of the PBDT–TA templates with DMF led to monodisperse PNCs that were 30-nm thick (Figure 3.3b and Figure 3.6). The rugged surface morphology of the PNC is shown in scanning electron microscopy (SEM) images (Figure 3.3c). Energy-dispersive X-ray spectroscopy (EDX) revealed that PNC was composed of C, N, and O. The low signal of S in EDX indicated that PBDT–TA templates were successfully removed. The voids were observed in the high-angle annular dark-field-scanning transmission electron microscopy (HAADF-STEM) images (Figure 3.3d).

We then loaded diverse dyes into the nanocapsules. The preliminary results showed that adding positively charged dyes directly into the negatively charged PNC causes particle aggregation due to strong electrostatic attraction (data not shown). To prevent particle aggregation and improve colloidal stability, we used HS-mPEG to interact with catechol functional groups in

PDA *via* a Michael reaction (Figure 3.7). Notably, the PEGylated PNCs showed great loading capacity with high colloidal stability than sodium dodecyl sulfated (SDS)-modified PNCs (Figure 3.8). Four representative molecular dyes (MB, Nile Blue (NB), Azure A (AA), and Neutral Red (NR)) were chosen for heparin sensing and successfully loaded in PEGylated PNC (referred as PNC@XX, XX = MB, AA, NB, and NR). *Versus* PNC that features a broadband absorbance, dye-loaded PNC showed distinct absorption spectra relative to the cargo's absorption: PNC@MB, PNC@AA, PNC@NR, and PNC@NB showed maximum absorption wavelengths at 666 nm, 614 nm, 482 nm, and 620 nm, respectively (Figure 3.3e). Likewise, dye-loaded PNC emitted dye-specific fluorescence behaviors while PNC alone showed no inherent fluorescence (Figure 3.9).

The color of the solution changed from brown (PNC) to dark green (PNC@MB), red (PNC@NR), or blue (PNC@NB and PNC@AA) after dye encapsulation (Figure 3.3f). The negatively charged surface of PNC (–27.7 ± 0.1 mV) increased to –21.8 ± 0.2 mV (PNC@AA), –16.7 ± 1.0 mV (PNC@NR), –16.0 ± 0.6 mV (PNC@MB), and –5.3 ± 0.6 mV (PNC@NB) because of the loaded positively charged dyes (Figure 3.3g). Dynamic light scattering (DLS) data showed that PNC, PNC@MB, PNC@AA, PNC@NR, and PNC@NB had narrow size distributions (polydispersity index (PDI) < 0.1). The hydrodynamic diameter of the PNC increased (~55 nm) due to the loaded dyes (Figure 3.3h). Monodispersed PBDT–TA@PDA and PNC were observed using nanoparticle tracking analysis (NTA) that further verified the size distribution of nanoparticles from DLS data (Figure 3.3i and Figure 3.10).

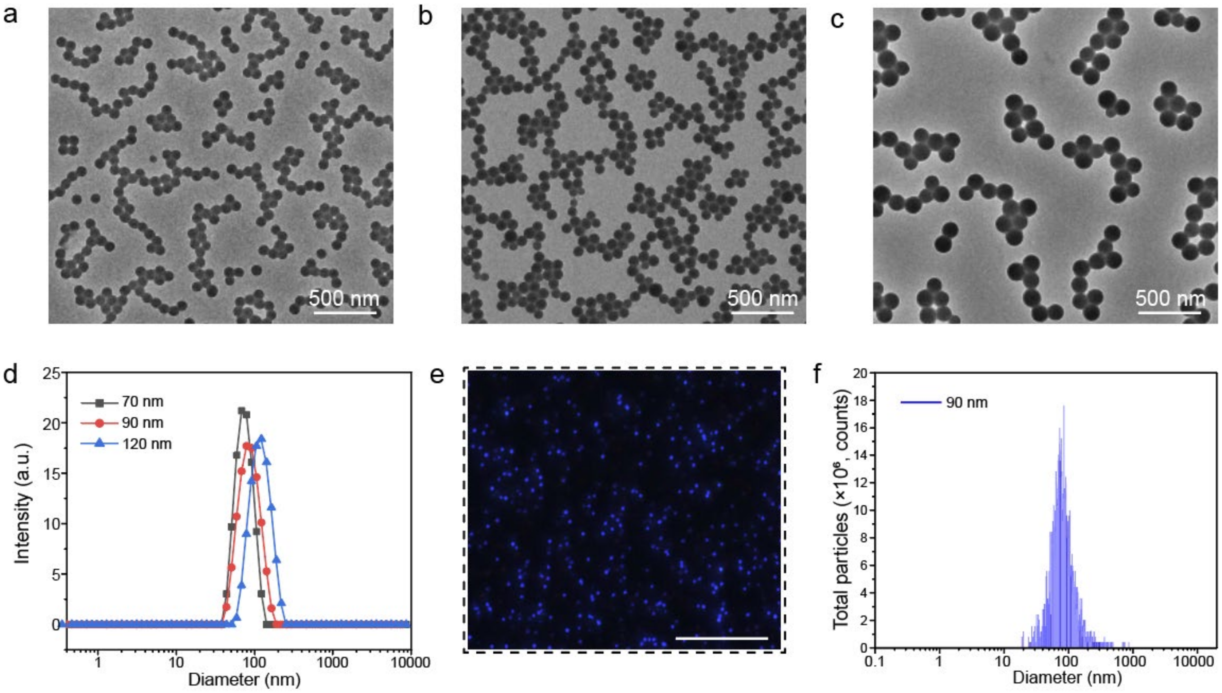

Figure 3.2 PBDT–TA core nanoparticles
TEM image of PBDT–TA nanoparticles with diameters of (a) 70 nm, (b) 90 nm, and (c) 120 nm. The size is readily tunable by adjusting the amount of BDT used for the reaction. The ratio of BDT and TA was 0.3:1 (70 nm), 0:5 (90 nm), and 1:1 (120 nm). d DLS data shows that PBDT–TA nanoparticles were highly uniform and monodispersed (PDI < 0.1). e NTA images of PBDT–TA nanoparticles. The scale bar represents 10 µm. f Size distribution of PBDT–TA nanoparticles with the average diameter of 90 nm measured by NTA technique.

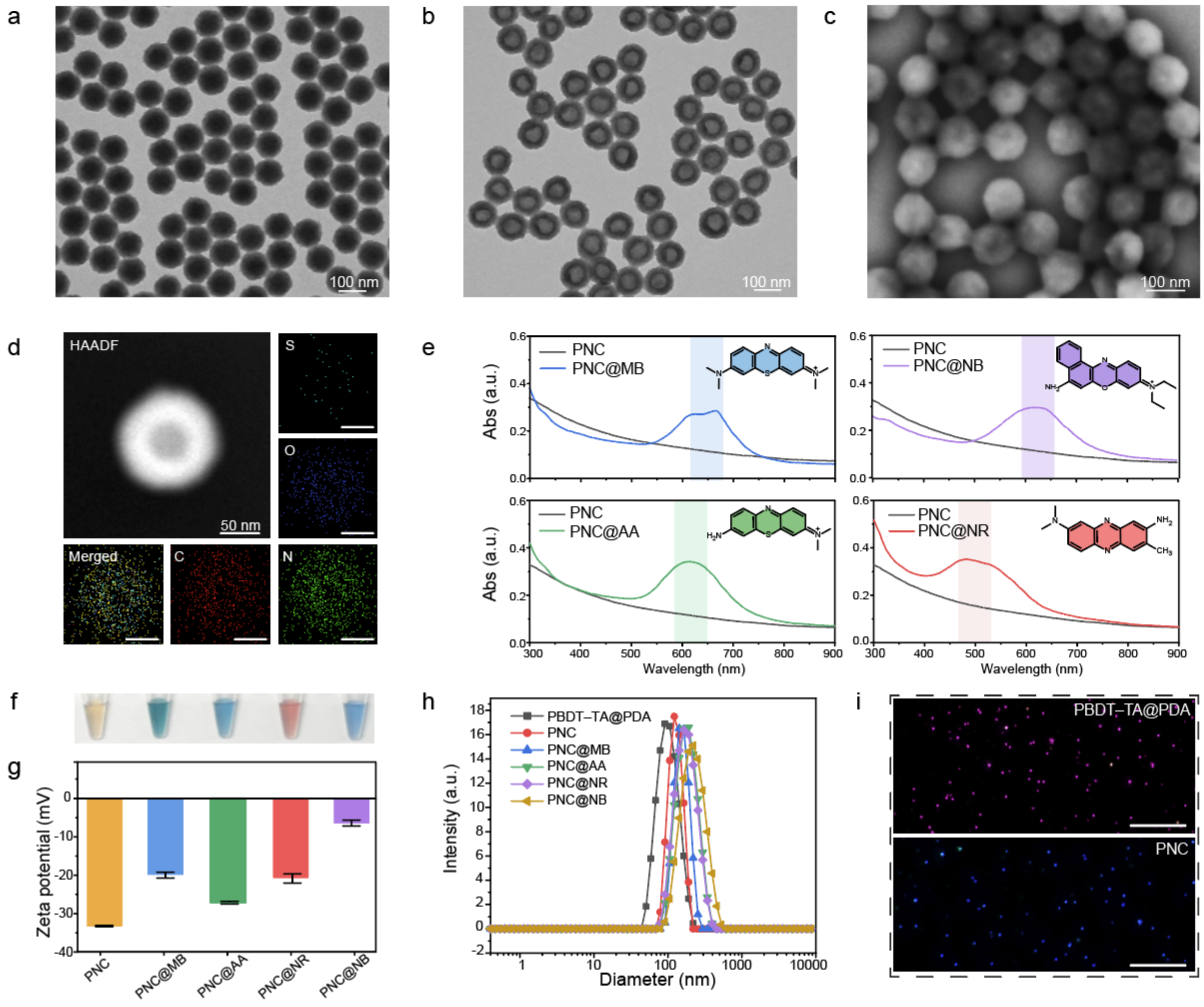

Figure 3.3 Dye-loaded PNC

TEM image of (a) PBDT–TA@PDA and (b) PNC. c SEM image of PNC. d EDX and HAADF-STEM images of PNC. The scale bars represent 50 nm. e UV–vis–NIR absorption spectra of PNC@MB, PNC@AA, PNC@NR, and PNC@NB with respect to PNC alone. Black and colored curves represent PNC alone and dye-loaded PNCs. f Photograph of PNC (brown), PNC@MB (dark green), PNC@AA (blue), PNC@NR (red), and PNC@NB (blue) in aqueous solution. g Zeta potential of PNC, PNC@MB, PNC@AA, PNC@NR, and PNC@NB. The error bars represent the standard deviation of three separate measurements. h DLS data of PBDT–TA@PDA, PNC, PNC@MB, PNC@AA, PNC@NR, and PNC@NB. i NTA images of PBDT–TA@PDA and PNC. Pink and blue dots represent monodispersed PBDT–TA@PDA and PNC. The scale bars represent 10 µm.

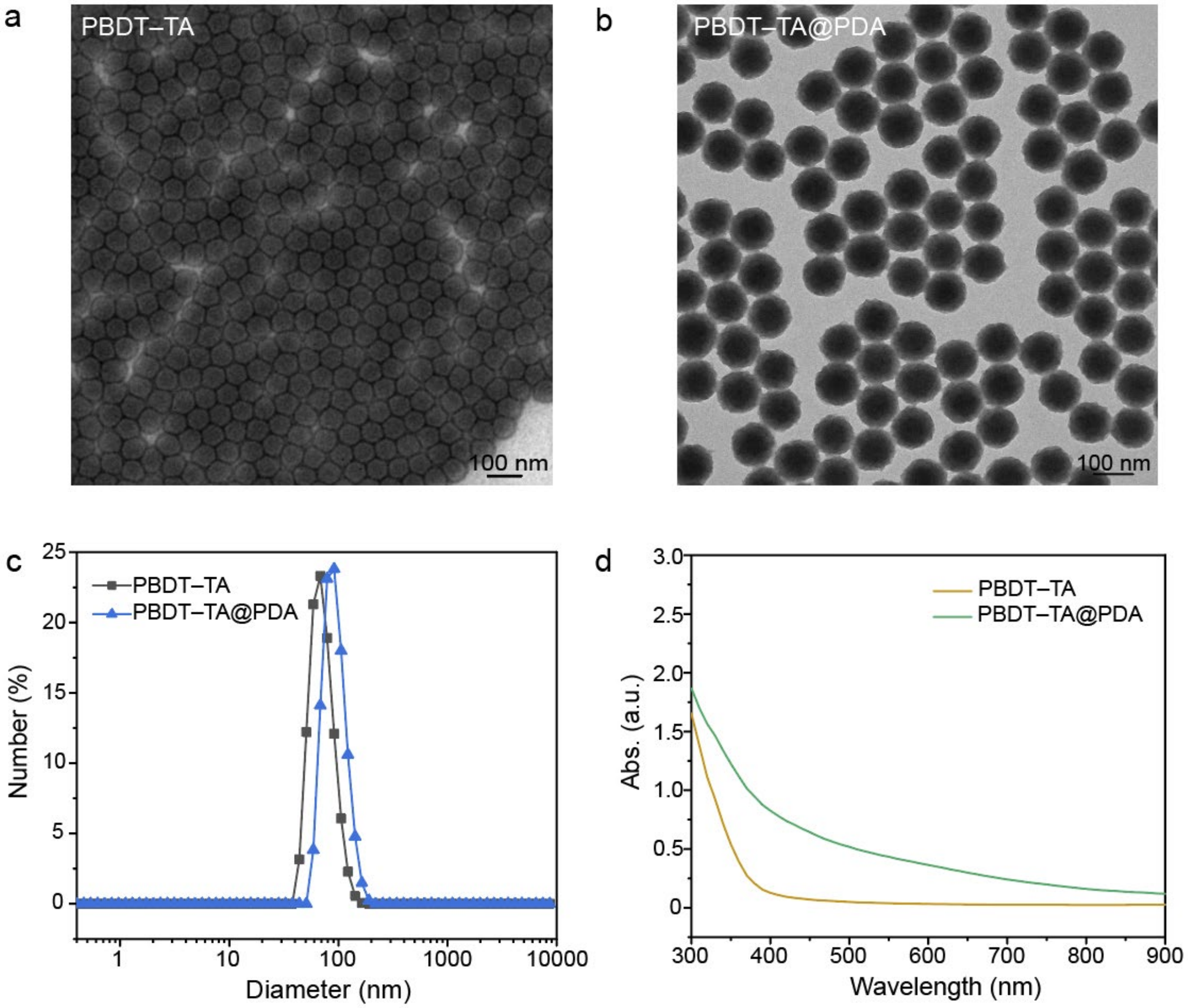

Figure 3.4 Characterization of core–shell nanoparticles

TEM image of (a) PBDT–TA core and (b) PBDT–TA@PDA core–shell nanoparticles. c DLS data shows that the size of PBDT–TA nanoparticles increased after PDA coating. d UV–vis–NIR spectra of PBDT–TA and PBDT–TA@PDA nanoparticles.

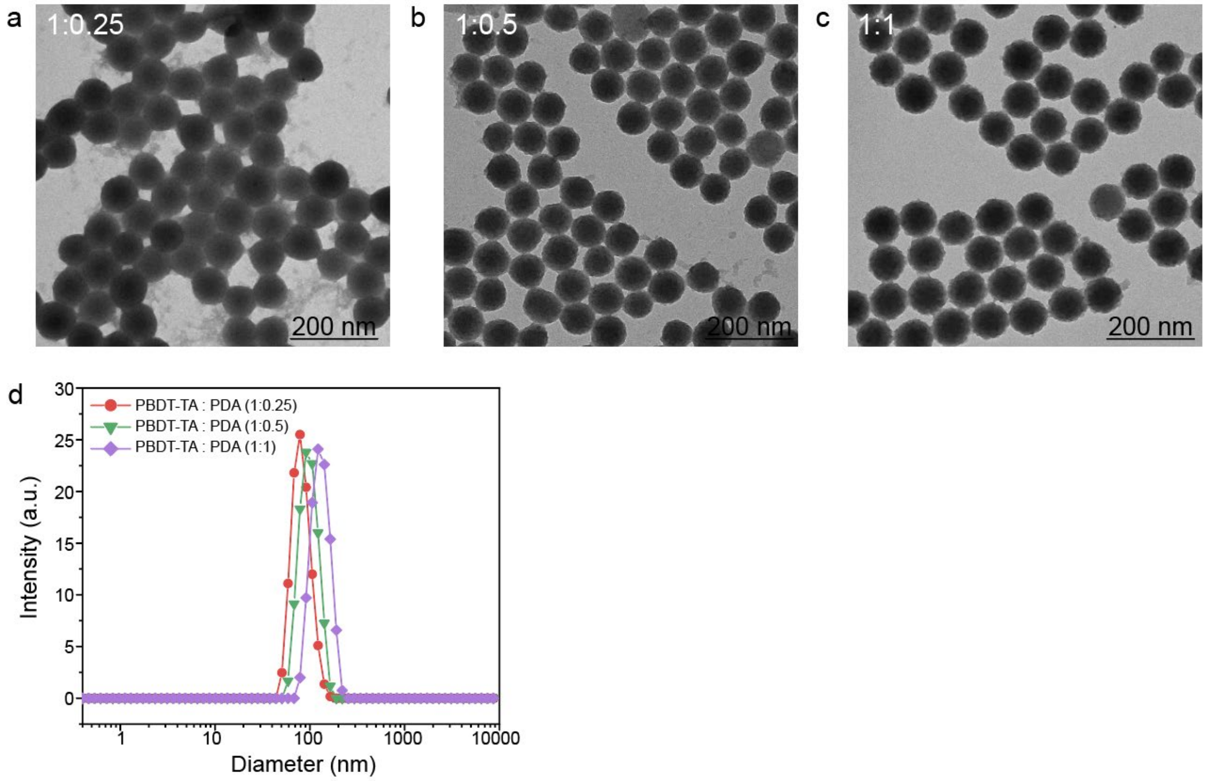

Figure 3.5 PBDT–TA@PDAs with different PDA thicknesses

PDA thickness is tunable by adding different amounts of dopamine at the fixed concentration of PBDT–TA nanoparticle. 1:0, 1:0.25, 1:0.5, and 1:1 indicate the ratio of fixed concentration of PBDT–TA to dopamine concentrations. TEM image with different PDA shell thicknesses: (a) 5 nm, (b) 10 nm, and (c) 30 nm. d DLS data shows that the particle size increased as adding more dopamine. The diameter of the core–shell particle was 75.2 nm ± 6.2 nm, 83.5 nm ± 7.7 nm, and 101.2 ± 3.7 nm, respectively. The average and standard deviation were calculated from 30 core–shell nanoparticles.

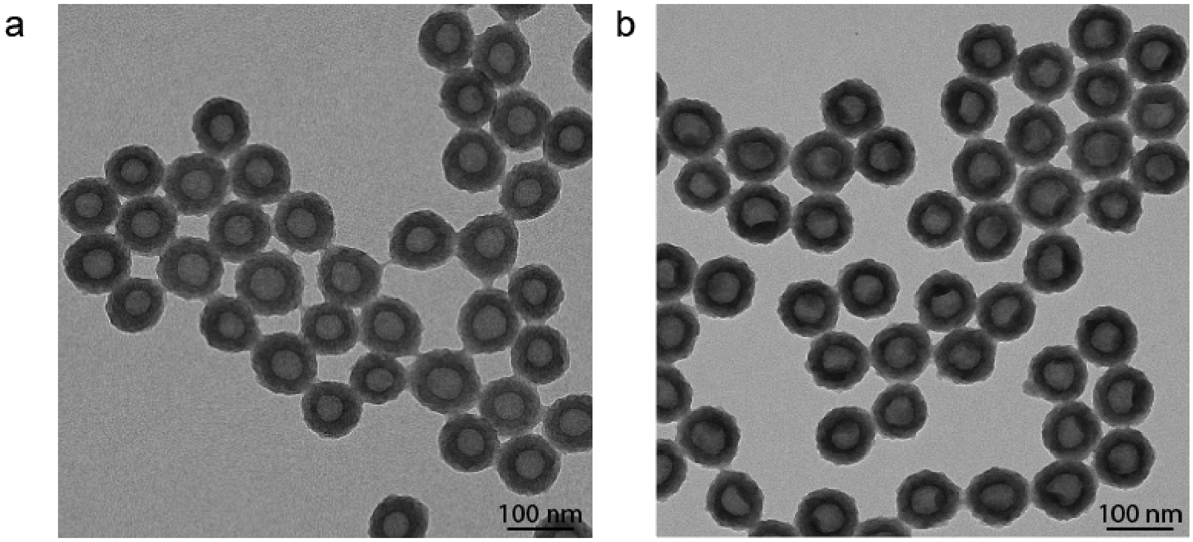

Figure 3.6 Monodisperse PNC
TEM image of robust PNC after (a) 1 h, and (b) 12 h of PBDT–TA@PDA incubation in DMF. PBDT–TA templates are easily disassembled in organic solvent due to the breakage of π–π stacking.[80]

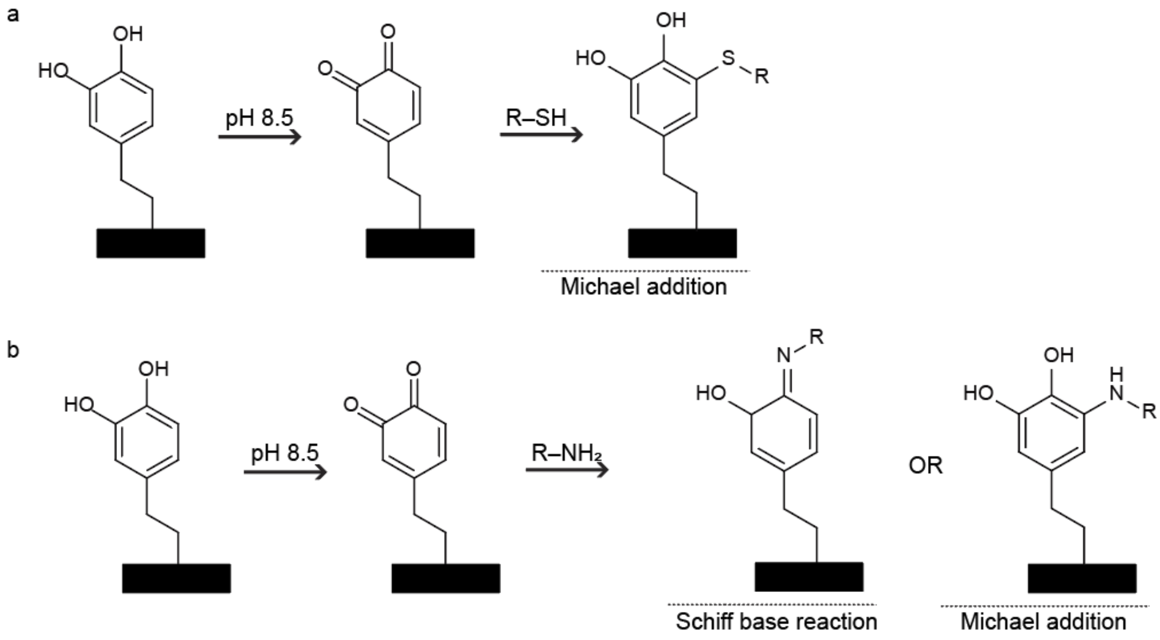

Figure 3.7 Michael addition and Schiff base reactions of PDA
Schematic illustration of Michael addition and Schiff base reactions of (a) thiol or (b) amine ligands with reactive dopamine quinone.[154] It is known that thiol ligand can interact with catechol groups in PDA based on covalent bonding-mediated Michael addition.

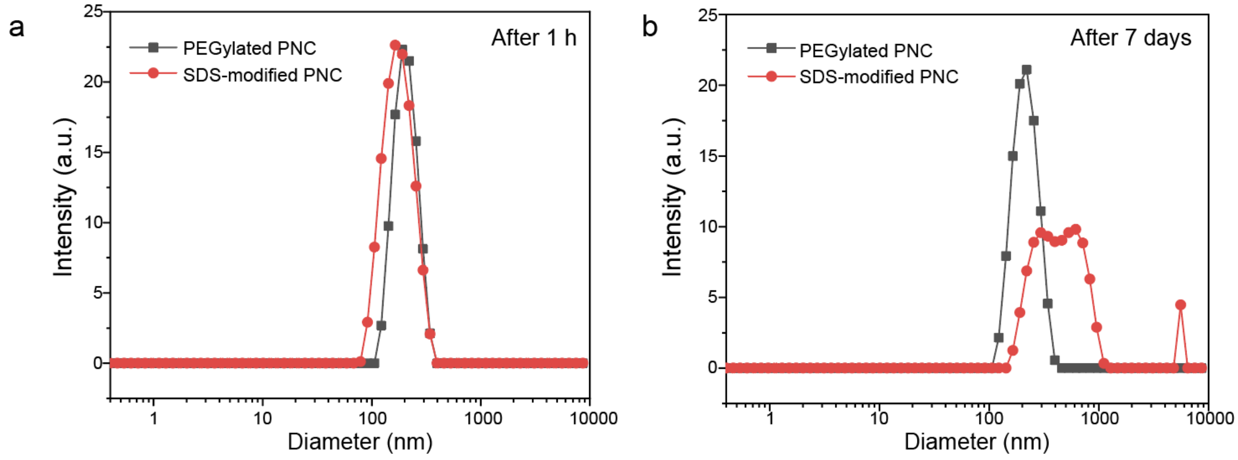

Figure 3.8 Colloidal stability of PEGylated PNC
PEGylated PNC successfully loaded free MB dye and maintained colloidal stability as observed by DLS data of after (a) 1 h and (b) 7 days of loading free MB dyes. However, SDS-modified PNC showed particle aggregation after 7 days of loading free MB dyes.

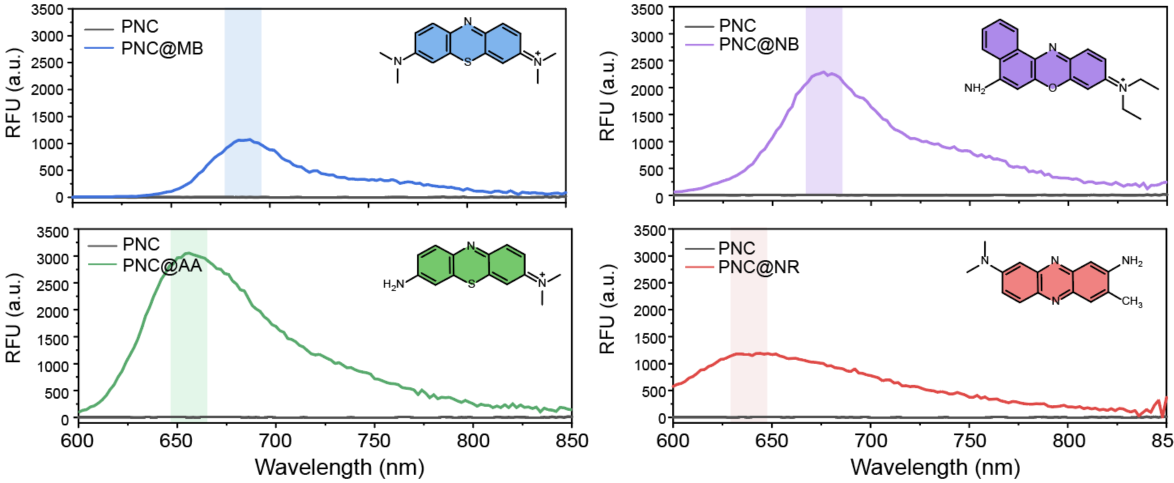

Figure 3.9 Fluorescence of dye-loaded PNC
After loading free molecular dyes (*e.g.,* MB, AA, NR, and NB) in PNCs, dye-loaded PNCs emitted fluorescence, while PNC alone had no fluorescence. Excitation wavelength of 600 nm was used for the measurement.

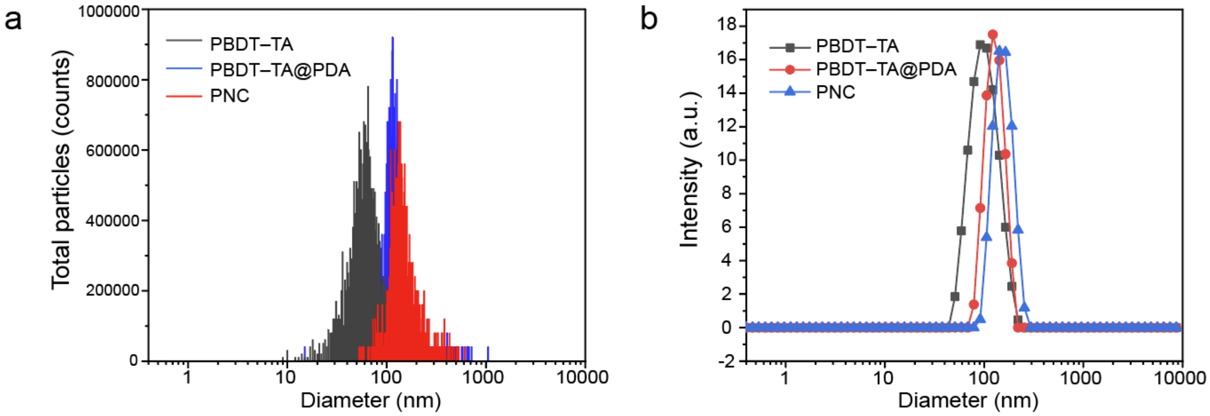

Figure 3.10 Nanoparticle tracking analysis of PNC
NTA technique was used to calibrate particle concentration and size distribution of PBDT–TA, PBDT–TA@PDA, and PNC. Size distribution of PBDT–TA, PBDT–TA@PDA, and PNC measured by NTA technique (a) was matched with DLS data (b). The average sizes of PBDT–TA, PBDT–TA@PDA, and PNC were 72 nm, 133 nm, and 161 nm, respectively.

3.4.2. Multiple interactions in the dye-PNC assemblies

PDA is composed of abundant amine and catechol groups, and thus it can accommodate multiple noncovalent interactions (*e.g.,* hydrogen bonding, electrostatic, π–π stacking, hydrophobic interactions) that enable it to efficiently load a variety of small molecular dyes.[155, 156] More free dye was loaded in the PNC where the surface of PNC was less PEGylated as confirmed by DLS and absorbance (Figure 3.11a and Figure 3.12). This is because PEG neutralizes the surface charge and the steric bulk of PEG reduces dye-PDA interactions (Figure 3.13).[157] However, the PEGylated PNC enabled a three-fold increase in dye loading efficacy in a basic solvent (pH 8.5) over water due to PDA deprotonation (Figure 3.14). Furthermore, the PEGylated PNCs showed higher loading efficiency of MB (81%), AA (80%), and NB (73%) dyes compared to PDA nanoparticles: MB (72%), AA (71%), and NB (60%) (Figure 3.11b). Correspondingly, the dye-loaded PNC featured 1.3-fold higher absorption peak than the dye-loaded solid PDA nanoparticles, indicating that hollow PDA nanostructure can load more dyes due to the 1.73-fold increased surface area (Figure 3.15).[139]

MB, AA, and NB dyes are positively charged and heterocyclic aromatic molecules that contain *p*-orbital electrons. These dyes can potentially interact with PDA through a variety or combination of noncovalent interactions such as hydrophobic, π–π, and electrostatic interactions.[158] To corroborate which interactions govern the stability of different dye–PDA assemblies, PNC@MB, PNC@AA, and PNC@NB were all incubated in 10 mM of NaCl, HCl, NaOH, urea, Triton X-100, DMSO, DMF, and SDS (Figure 3.11c-d). First, DMSO and DMF are organic solvents that can break π–π interactions:[36] PNC released the loaded MB, AA, and NB dyes under the organic solvents as a result of π–π interactions being interrupted. Second, SDS or TritonX-100 are surfactants that can destroy ionic or non-ionic interactions.[159] Likewise, PNC released the loaded dyes under the ionic or non-ionic surfactants due to the disassembly of weak ionic or hydrophobic interactions. Lastly, PNCs also released the loaded dyes in acidic condition (pH ≈ 2), but there was no release of the loaded dye in 10 mM of NaOH (pH ≈ 12), NaCl, and urea that can destroy hydrogen bonding. Thus, we conclude that electrostatic, hydrophobic, and π–π interactions were involved in the formation of PNC@MB, PNC@AA, and PNC@NB.

Molecular dynamics (MD) simulations were also conducted in to further validate the forces contributing to the interaction of PDA, dyes (*e.g.,* MB and NB), and heparin (Figure 3.11e). Decomposition analysis through the Molecular Mechanics Poisson-Boltzmann Surface Area (MMPBSA) approach yielded the magnitude and sign of the forces associated with the interaction of the dye, heparin, and PDA. Electrostatic and Van der Waals (VDW) energetic contributions dramatically stabilized the interaction of heparin, dyes, and PDA (Figure 3.11e). The electrostatic portion is associated with the interaction of the positively charged dye and the negatively charged sulfate groups on heparin. The VDW fraction is clearly mostly associated with the PDA. Nonpolar solvation is correlated with the change in surface area and entropic contributions when aggregates of PDA form. While the energetic contribution of nonpolar solvation is comparatively very small, it is a slightly stabilizing force, as is shown in the small negative value. Finally, polar solvation, which describes the process of solvating a moiety, was found as destabilizing force with respect to the interaction of PDA, heparin, and the dyes. Collectively, it is clear that the energetics of the dye—which is dominated by electrostatic interactions with heparin but also has contributions from VDW interactions with PDA—is necessary to facilitate the interaction between PDA and heparin.

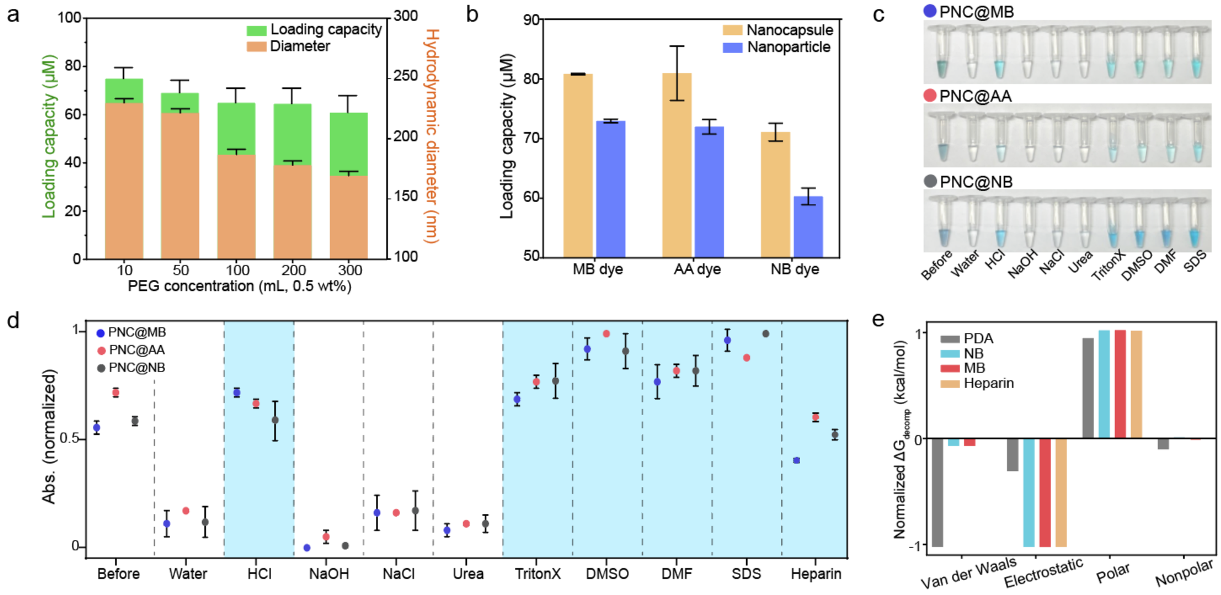

Figure 3.11 Dye–PNC assemblies

a Loading capacity and hydrodynamic diameter of PNC@MB, where the surface of PNC was modified with different concentration of HS-mPEG. b Loading capacity comparison between PDA nanocapsule and PDA nanoparticle. c Photograph of the released dyes in different media (from left to right: before centrifugation, water, HCl, NaOH, NaCl, Urea, TritonX-100, DMSO, DMF, and SDS). d Quantification of data in panel c: Release of the loaded dye in PNC in different media. Blue area indicates where the loaded dyes were released. e Decomposition analysis of the normalized Gibbs free energy of PDA, NB, MB, and heparin using MD simulation. Van der Waals, electrostatic, polar/nonpolar solvation were investigated for the analysis. The error bars represent the standard deviation of three separate measurements.

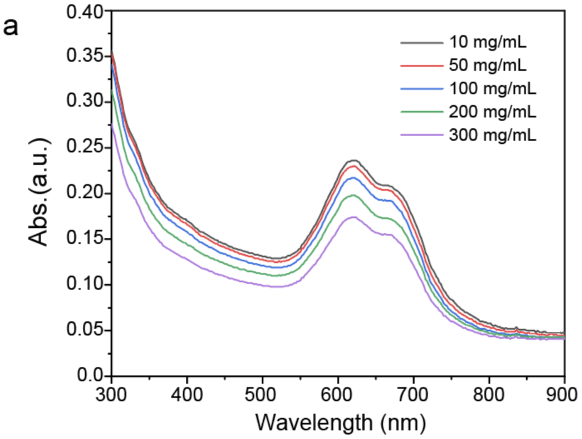

Figure 3.12 PNC modified with different concentrations of HS-mPEG

PNC modified with different concentration of HS-mPEG (*e.g.,* 10, 50, 100, 200, and 300 mL of 0.5 wt% HS-mPEG as a starting concentration for PEGylation) to load free MB dye. After PEGylation, samples were centrifuged twice to remove excess of HS-mPEG. a UV–vis–NIR spectra of PNC@MB that modified with different concentration of HS-mPEG. Less PEGylated PNC (*e.g.,* 10 mL) had higher absorption peak than more PEGylated PNC (*e.g.,* 300 mL) after loading free MB dye. b There was self-quenching of fluorescence on PNC@MB when free MB dyes were over-loaded in PNC.

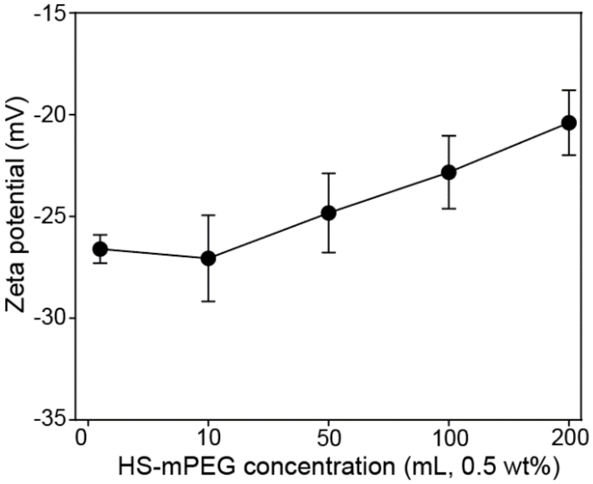

Figure 3.13 Surface charge of PEGylated PNC

Zeta potential of PNC modified with different amounts of SH-mPEG (*e.g.,* 0, 10, 50, 100, and 200 as a starting concentration for PEGylation). The surface charge of PNC increased as more SH-mPEG conjugated on the PNC surface. This is because the neutral PEG chain on the exterior layer of PNC can shield the terminal hydroxyl group in PDA, thus reducing the net negative charge of PNC for capturing positively charged dyes. The error bars represent the standard deviation of three separate measurements.

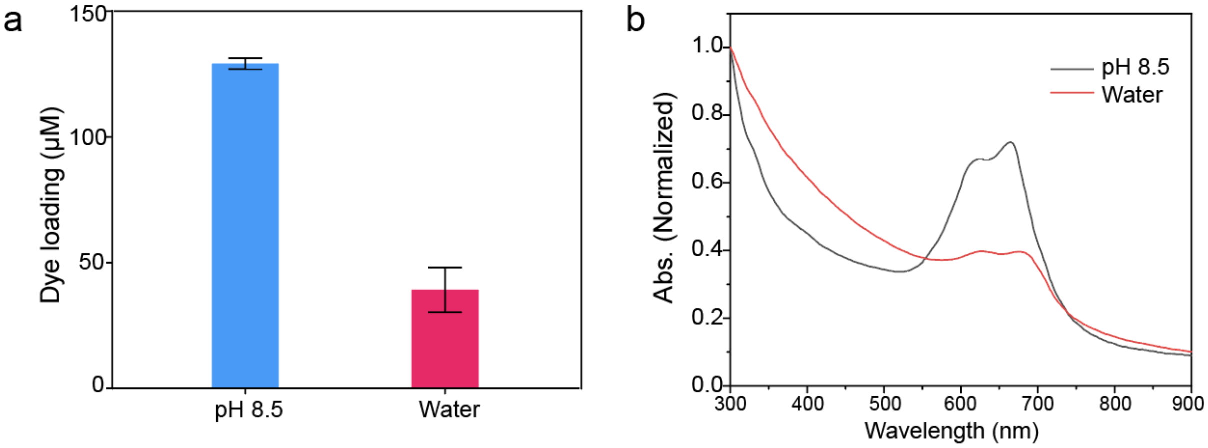

Figure 3.14 Loading free dyes in PNC in a basic condition

a Amounts of MB dyes loaded in PEGylated PNCs under basic condition and water. The error bars represent the standard deviation of three separate measurements. b UV–vis–NIR spectra of PNC that loaded MB dyes under pH 8.5 and water. PNC@MB that loaded free MB dyes under the basic condition showed two-fold higher absorption peak at 666 nm than PNC@MB that loaded free MB dyes under the water.

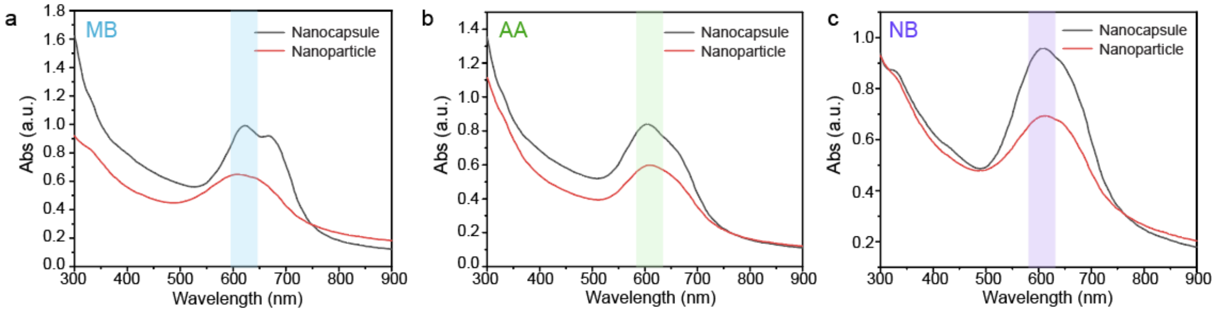

Figure 3.15 Absorbance of dye-loaded PNC and PDA nanoparticles

UV–vis–NIR spectra of (a) MB, (b) AA, and (c) NB-loaded PNCs compared to dye-loaded PDA nanoparticles. Dye-loaded PNCs showed at least 1.3-fold higher absorption peak than dye-loaded PDA nanoparticles. These results indicate that hollow PDA structure can load more free dye than PDA nanoparticles due to the increased surface area.

3.4.3. Release of the loaded dye in negatively charged PNC

We previously showed that free dyes can interact with heparin for increased PA signal.[129] To identify the dyes' roles in this study, PNC@MB, PNC@AA, and PNC@NB were centrifuged four-times to completely remove free dyes in the solution (Figure 3.16). Then, PNCs loaded with 50 µM of MB, AA, or NB dye were incubated with heparin from 0 to 5 U/mL, which led to optical and PA changes. During this interaction, the color of the solution rapidly changed within 1 min (Figure 3.17a). Consequently, the absorbance peak of each nanocapsule (MB, AA, and NB) decreased and blue-shifted; the fluorescence largely attenuated (Figure 3.17b and Figure 3.18).

We suspect that the loaded dye could be competitively extracted from the PNC due to strong local electrostatic attractions between the dye and heparin.[142] To verify this, PNC@MBs were spun down to collect the supernatant after they were incubated with heparin. The absorbance obtained from the supernatant was consistent with the absorbance of free MB dye–heparin interactions, indicating release of the loaded MB dyes (Figure 3.17c and Figure 3.19). Moreover, there was a slight decrease in hydrodynamic diameter of PNC@MB, PNC@AA, and PNC@NB upon incubation with heparin while maintaining its hollow structure without shrinking or disassembly of the PDA shell during the interactions (Figure 3.17d-e). It is noteworthy that PNC alone did not undergo any change in absorbance, fluorescence, hydrodynamic diameter, and PA intensity after interacting with heparin (Figure 3.20). However, the release of the loaded dyes from the PNC led to a decrease in PA intensity (Figure 3.17f). We hypothesized that incorporating the free dyes into PNC greatly enhances PA performance of the free dyes due to four reasons: (1) PDA's the four-fold lower thermal conductivity of PDA ($k_{\mathrm{PDA}} \approx 0.13$) than water ($k_{\mathrm{water}} \approx 0.59$), (2) fluorescence quenching of free dyes, (3) local concentration of loaded dyes as opposed to free state, and (4) the ability to protect the dyes from thermal degradation; the disassembly of dye–PNC assemblies would therefore expose free dyes resulting in decreased PA signal.[136, 137]

To verify this mechanism, we compared PA signal of dye-loaded PNCs and free dyes with different concentrations from 10 to 1000 μM. Notably, background-corrected PNC@MB, PNC@AA, and PNC@NB showed 10-fold higher PA signal compared to the free MB, AA, and NB dyes at same concentration (50 μM) (Figure 3.17g). We also confirmed that dye-loaded PNCs showed 90% fluorescence quenching of free dyes and generated higher PA signal than free dye–heparin interactions (Figure 3.17h and Figure 3.21). These results indicate that the release of the loaded dye from PNC decreases PA signal due to decreased local concentration of the loaded dyes in PNC and relatively lower PA signal generated from the released dye–heparin interactions.

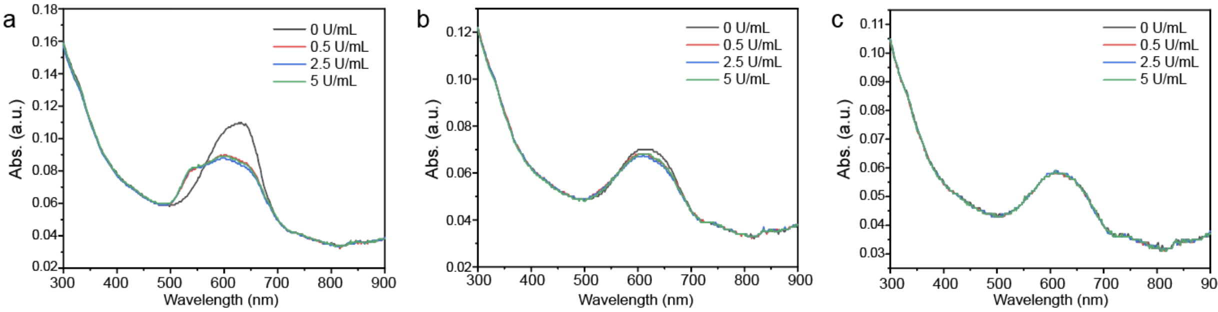

Figure 3.16 Ruling out the interference of free dye in heparin-dye interactions
After incorporating free MB dyes into PNC, we conducted four rounds of centrifugations to remove free MB dyes in supernatant. UV–vis–NIR spectra of interaction between heparin and the collected supernatant from (a) first (b) second, and (c) third-times centrifugations. These results indicate that there was negligible involvement of free MB dyes upon heparin interaction after three times of centrifugation. Dye-loaded PNCs were purified by four rounds of centrifugations to remove free molecular dyes in the supernatant.

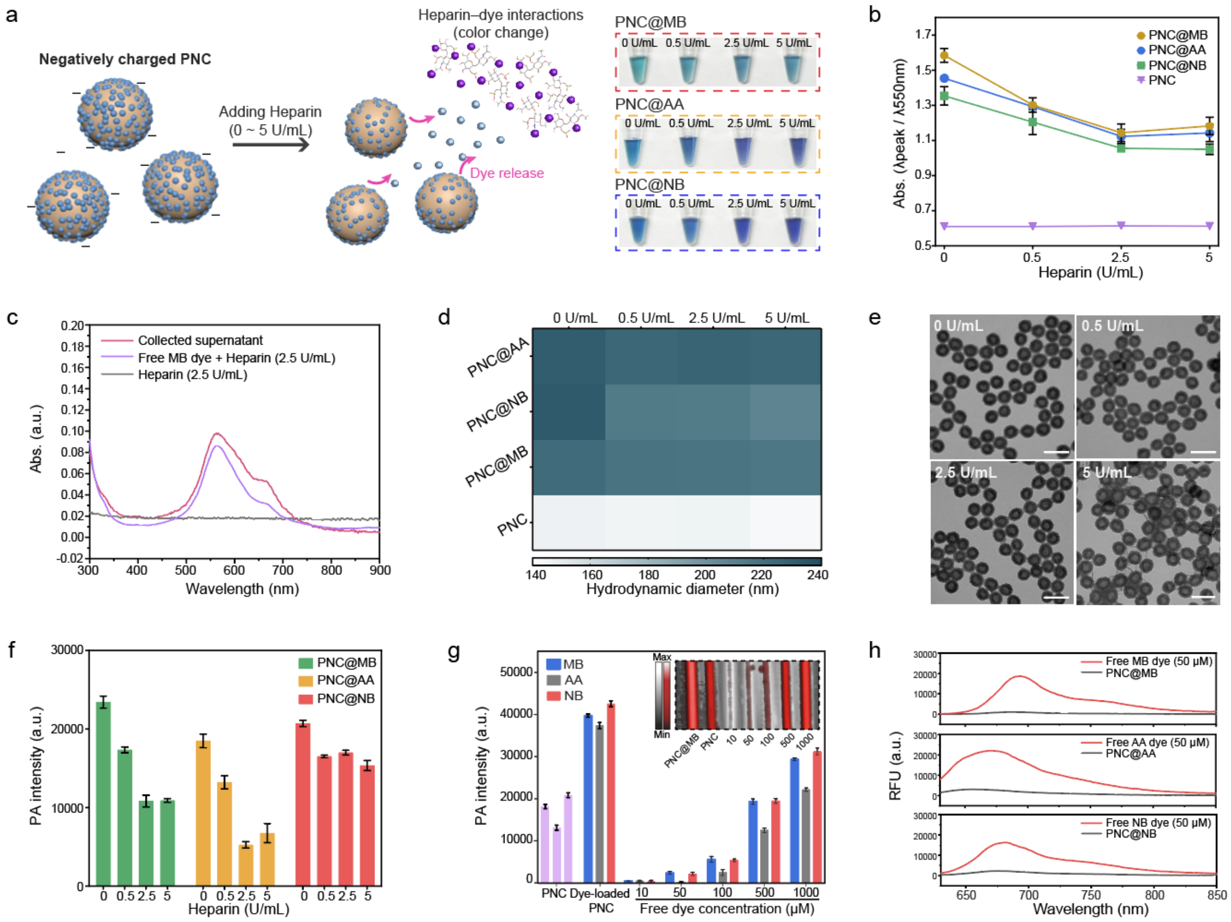

Figure 3.17 Disassembly of the loaded dyes in negatively charged PNC

a Schematic of releasing loaded dyes in negatively charged PNC during heparin interaction. Photograph shows color change of PNC@MB, PNC@AA, and PNC@NB after heparin interaction. b Absorbance change of dye-loaded PNC after heparin interaction. The error bars represent the standard deviation of three separate measurements. c PNC@MBs were centrifuged down to collect the supernatant after heparin interaction. UV–vis–NIR spectra shows that the absorbance obtained from the collected supernatant was matched with free MB dye–heparin interaction. d Hydrodynamic diameter of PNC@MB, PNC@AA, PNC@NB, and PNC after heparin interaction. e TEM images of PNC@MB after heparin interaction. The scale bars represent 200 nm. f Decrease in PA signal after releasing the loaded dyes in PNC during heparin interaction. The error bars represent the standard deviation of five regions of interest. g PA signal comparison between free dyes and dye-loaded PNC that loaded 50 µM dye. Purple bars represent PA signal of PNC alone. The inset image represents PA image of PNC@MB compared to free MB dye. The error bars represent the standard deviation of five regions of interest. h Fluorescence of free MB, AA, and NB dyes compared to MB@PNC, AA@PNC, and NB@PNC that loaded 50 µM dye. The experiments in f and g were repeated independently three times with similar results.

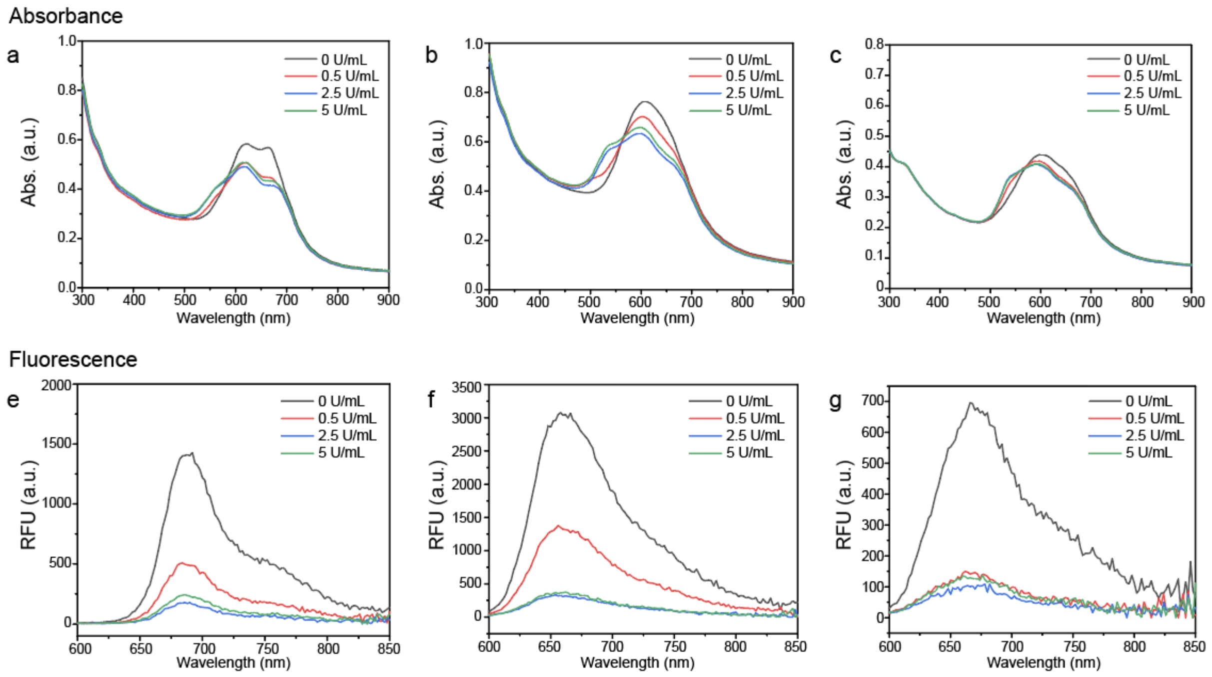

Figure 3.18 Optical changes of dye-loaded PNC

Absorbance and fluorescence changes of PNC@MB (a, e), PNC@AA (b, f), and PNC@NB (c, g) were observed after heparin interactions from 0 to 5 U/mL. After heparin interactions, the absorption peaks of PNC@MB, PNC@AA, and PNC@NB decreased and blue-shifted. Likewise, the fluorescence of PNC@MB, PNC@AA, and PNC@NB largely attenuated.

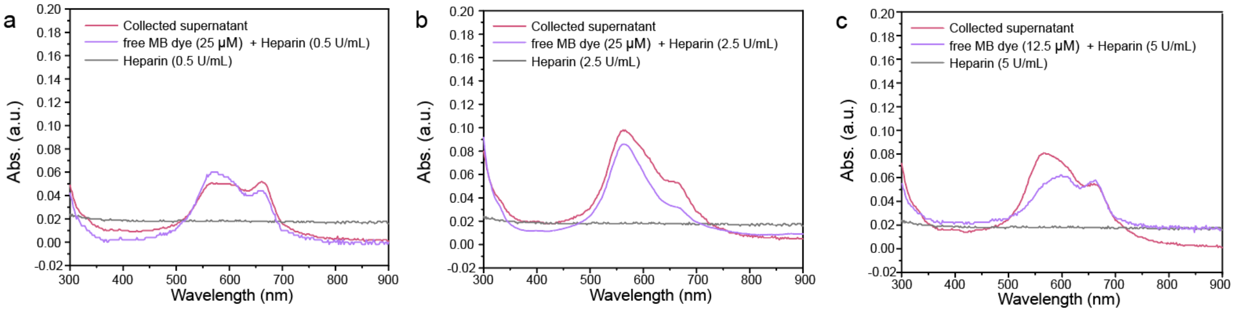

Figure 3.19 Release of the loaded MB dye in PNC

After heparin interaction, PNC@MB were centrifuged down, and the supernatant was collected to measure the absorbance. UV–vis–NIR spectra shows that the absorbance obtained from the collected supernatant at heparin concentration of (a) 0.5 U/mL, (b) 2.5 U/mL, and (c) 5 U/mL was matched with the absorbance of free MB dye–heparin interaction at the same heparin concentration. These results validate that the loaded dyes in PNCs disassembled during heparin interaction.

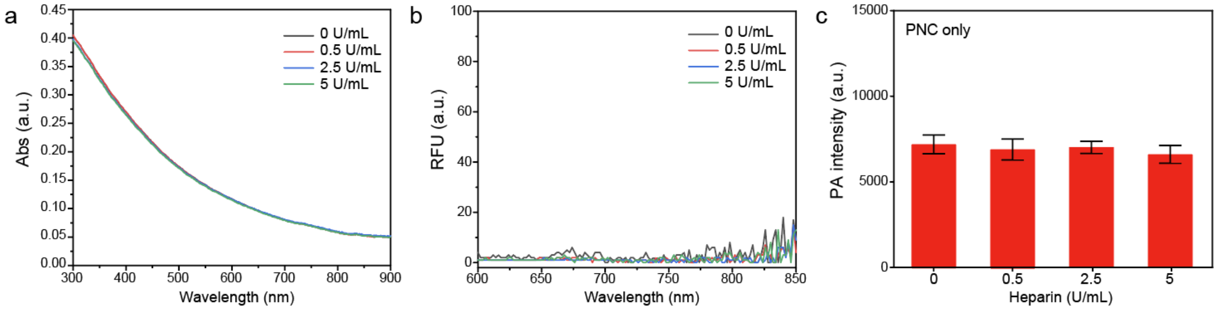

Figure 3.20 No interaction between PNC alone and heparin
a Absorbance and (b) fluorescence of PNC when interacting with heparin concentration from 0.5 to 5 U/mL. UV–vis–NIR spectra shows that there was no change of absorbance and fluorescence of PNC. c Importantly, there was no change of PA intensity of PNC after heparin interactions. These results indicate that the loaded dye in PNC is a function of heparin interaction. The error bars represent the standard deviation of five regions of interest.

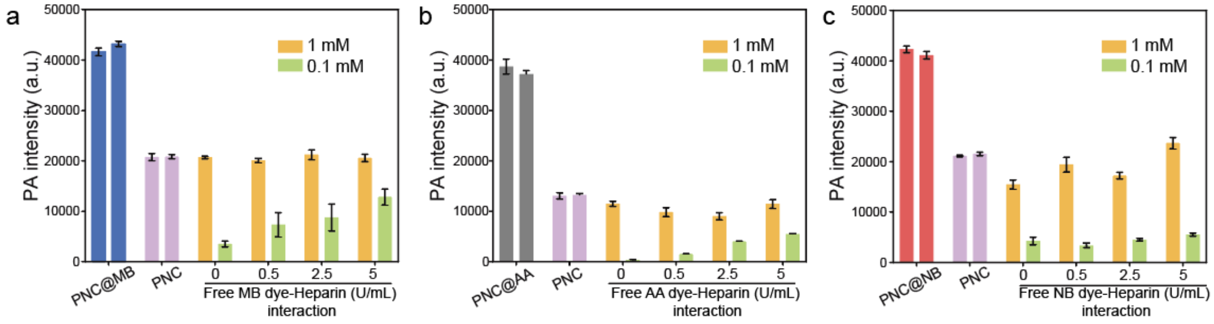

Figure 3.21 PA intensity comparison
PA intensities of (a) PNC@MB, (b) PNC@AA, and (c) PNC@NB were compared to free dye–heparin interactions. 1 mM and 0.1 mM of each free dyes interacted with heparin concentration from 0.5 to 5 U/mL, and measured PA signal for the comparison. These results indicate that dye-loaded PNCs generated higher PA signal than free dye–heparin interaction. Blue, gray, and red bars represent PA signal of PNC@MB, PNC@AA, and PNC@NB, respectively. Purple bar represents PA signal of PNC alone. The error bars represent the standard deviation of five regions of interest.

3.4.4. PA enhancement of positively charged PNC

The surface charge of dye-loaded PNCs is dependent on the amount of the loaded dye while the colloidal stability relies on the net surface charge after conjugating with heparin. Encouraged by our results, another routine for sensing heparin was developed (Figure 3.22a). After loading a higher amount of NB dye (~80 μM) into PNC, PNC@NB showed positively charged surface (+8.5 mV). However, PNC@MB and PNC@AA still showed negatively charged surface at the same loading concentration (Figure 3.23). Intriguingly, there was an increase in PA intensity when positively charged PNC@NB interacted with heparin either in water ($R^2 \approx 0.82$) or whole human blood ($R^2 \approx 0.91$), while negatively charged PNC@NB (–7.0 mV) inversely showed decrease in PA signal (Figure 3.22b and Figure 3.23–3.24). The limit of detection of PNC@NB was 0.063 U/mL in water and 0.14 U/mL in whole human blood. 8×10^6 particles/mL is required to induce PNC@NB–heparin aggregation (Figure 3.25). Furthermore, positively charged PNC@NBs loaded with 80 μM dye showed higher PA signal over free NB dye of 5 mM when they interacted with heparin in whole human blood (Figure 3.26).

PNC@NB showed particle aggregation as a function of heparin concentration that increased PA signal, as confirmed by size, surface charge, photograph, and decreased absorbance in water (Figure 3.22c and Figure 3.27–3.28). This finding is significant because the mechanism of PA signal generation has been understood by the conventional thermoelastic expansion model where the optical absorption of the nanoparticle is proportional to PA signal generation.[122] We believe that the PNC@NB–heparin aggregation may enhance thermal conductivity and could improve heat transfer, or the fluorescence that quenched during the aggregation can contribute to heat generation (Figure 3.28).[137] This aggregation-induced PA enhancement showed stable PA signal for 15 min, and the induced PA signal was reversible when protamine (known heparin antagonist)[160] was added to the interaction (Figure 3.29–3.30).

Importantly, we tested PNC@NB with clinical specimens collected from 17 patients undergoing cardiac procedure that required a high dose of heparin infusion. This work shows that our approach is not just measuring heparin concentration, but also clotting time:[161] The PA signal of PNC@NB was linearly increased as a function of cumulative heparin ($R^2 = 0.83$) and ACT values ($R^2 = 0.73$) (Figure 3.22d). In addition, ACT values were linearly correlated with cumulative heparin ($R^2 = 0.91$) (Figure 3.31). Collectively, this prototype of heparin sensing system can linearly generate PA signal in whole human blood as well as clinical specimens, demonstrating great promise for medical applications. Furthermore, PNC@NB showed high colloidal stability in different media (*e.g.,* DMEM, plasma, 2.5 or 5% of human serum) (Figure 3.32).

To further investigate the specificity of aggregation-induced PA signal, PNC@NBs were incubated with other complex sample matrices such as bovine serum albumin (BSA), hemoglobin (Hgb), human pooled plasma, thrombin, Dulbecco's modified Eagle Medium (DMEM), poly(sodium-4-strynesulfornate) (PSS), relevant ions (*e.g.,* Cl^-, Ca^{2+}), heparin analogue (*e.g.,* chondroitin sulfate (Chs)),[117] and heparin at the same mass concentration (2 μg/mL), respectively. Although it is generally accepted that electrostatic-mediated particle interaction has poor specificity, there was significant increase in PA signal when PNC@NB interacted with heparin due to induced PNC@NB–heparin aggregation (Figure 3.22e). Our previous study showed that free NB dye can interact with heparin causing aggregation that increased PA signal.[131] Likewise, the increased PA signal of PNC@NB was due to the induced PNC@NB-heparin aggregation which is corresponding to the increased size of PNC@NB (PDI > 0.5 in heparin) (Figure 3.22f).

Notably, PNC@NB in other biomolecular conditions (*e.g.,* BSA, plasma, and thrombin) showed small polydispersity (PDI ≤ 0.2) and hydrodynamic diameter compared to PNC@NB in heparin (Figure 3.22f).The induced PNC@NB aggregation during heparin sensing was also clearly observed by TEM images (Figure 3.22g). PA signal of PNC@NB is proportional to particle concentration, and PNC@NB showed no hemolysis (Figure 3.25 and 3.33). The PA response from PNC@NB had a linear correlation with aPTT values at a heparin concentration of 0.2 to 1 U/mL (Figure 3.34). Taking advantage of adhesive nature of PDA, small molecule dyes could be coated on inert materials (Figure 3.35), suggesting the potential use of this dye-PNC scaffold for functionalizing catheters to monitor heparin.

Lastly, MD simulations were used to further investigate the interactions of heparin with the PNC@NB. The aggregation of PDA began quickly (~2 ns) along with the formation of the PDA@NB (Figure 3.22h). Negatively charged heparin interacted strongly with the positively charged NB dyes, which resulted in the formation of the PNC@NB-heparin complex (Figure 3.36) to subsequently crosslink the PNC and induce aggregation. However, there was no observed aggregation between heparin and PDA alone (Figure 3.37). To quantitatively evaluate PNC@NB–heparin interactions, all possible distances were measured between all possible combinations of all PDA molecules with each heparin monosaccharide in the simulation. This distance data was then analyzed to elucidate the number of "individual interactions", *i.e.*, interactions between PDA and a monosaccharide unit that was not present within the past 10 frames of the simulation to avoid double counting the same interaction. Over 130 ns of unrestrained simulation, the simulation with NB dye present had 645 individual interactions between heparin and PDA. This stands in stark comparison to the simulation with no dye present and had only 90 individual interactions between heparin and PDA (Figure 3.22i). This explains the experimentally observed dye-loaded PNC–

heparin aggregation; there was no interaction between PNC alone and heparin (Figure 3.22c and Figure 3.20).

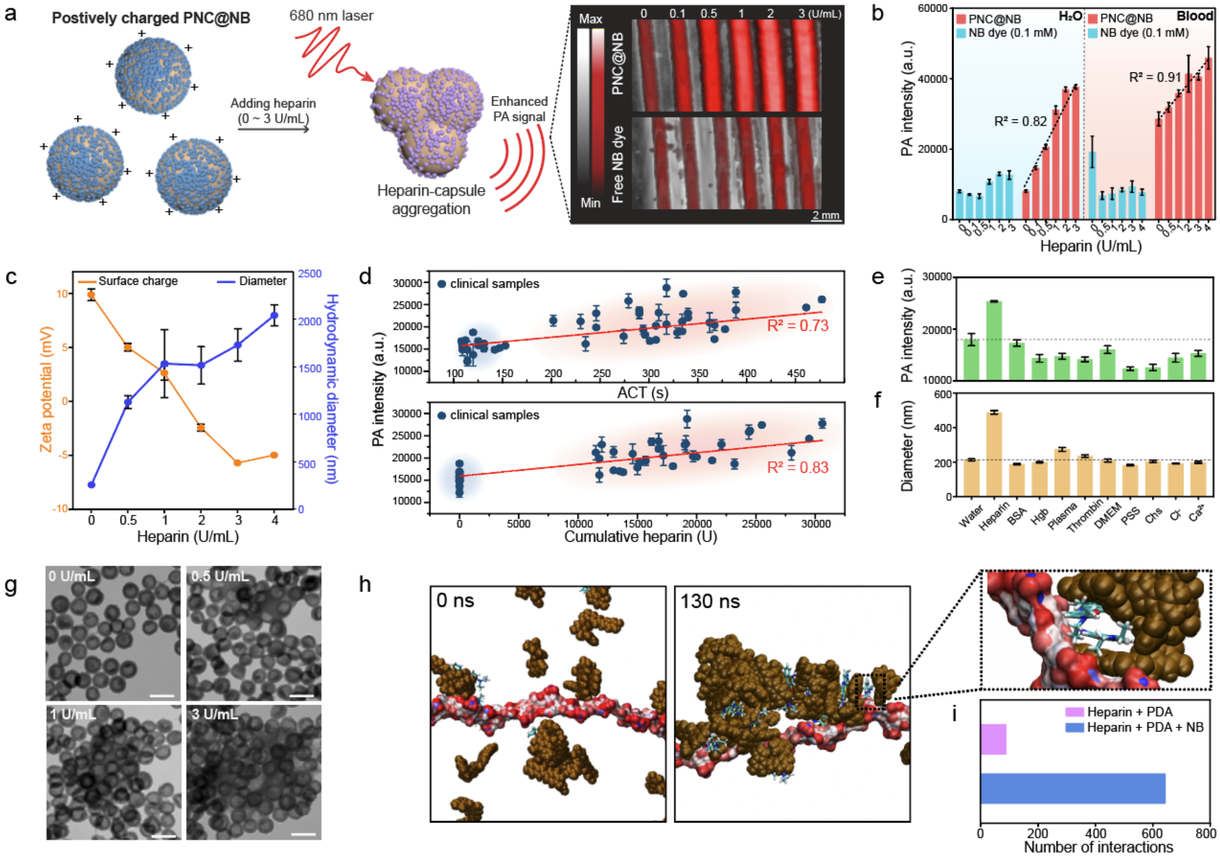

Figure 3.22 Aggregation-induced PA enhancement of positively charged PNC
a Schematic of induced PNC@NB–heparin aggregation. Photograph indicates outstanding PA performance of PNC@NB over free NB dye (100 μM) for monitoring heparin. b PA signal comparison between PNC@NB and free NB dye at the same dye concentration either in water ($R^2 = 0.82$) or whole human blood ($R^2 = 0.91$). The error bars represent the standard deviation of five regions of interest. c DLS data and the surface charge of PNC@NB after heparin interaction in water. The error bars represent the standard deviation of three separate measurements. d PA signal of PNC@NB tested with clinical samples. PA signal was linearly increased as a function of cumulative heparin ($R^2 = 0.83$) and ACT values ($R^2 = 0.73$). Clinical samples were collected from 17 patients undergoing cardiac procedures. Blue and red regions indicate before (blue) and after (red) heparin infusion. The error bars represent the standard deviation of five regions of interest. e PA intensity and (f) corresponding size when PNC@NB interacted with other complex sample matrices. The error bars represent the standard deviation of three separate measurements. g TEM images of aggregated PNC@NB during heparin interaction. The scale bars represent 200 nm. h Evolution profiles of the size of the complex, comprised of PDA (brown), heparin (red/white), and free NB dye, showing the aggregation in explicit water. Magnified interface section shows that NB dye bridged interaction between PDA and heparin. i Number of interactions between heparin and PDA for both PDA+heparin+NB and PDA+heparin systems. The experiments in b, d and e were repeated independently three times with similar results.

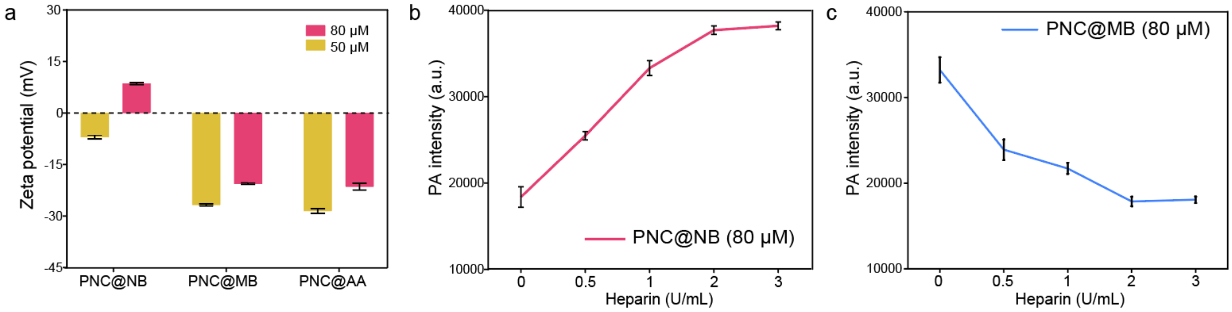

Figure 3.23 Surface charge-dependent PA signal

a Zeta potential of PNC@MB, PNC@AA, and PNC@NB that loaded 50 or 80 µM dyes in PNC. PNC@NB which loaded 80 µM showed positively charged surface (+8.5 mV), while PNC@MB (–20.6 mV) and PNC@AA (–21.5 mV) showed negatively charged surface. The error bars represent the standard deviation of three separate measurements. PA signal of (b) PNC@NB and (c) PNC@MB that loaded 80 µM dye after heparin interaction from 0 to 3 U/mL. PA intensity of positively charged PNC@NB increased after heparin interactions, while PA signal of negatively charged PNC@MB decreased. The error bars represent the standard deviation of five regions of interest.

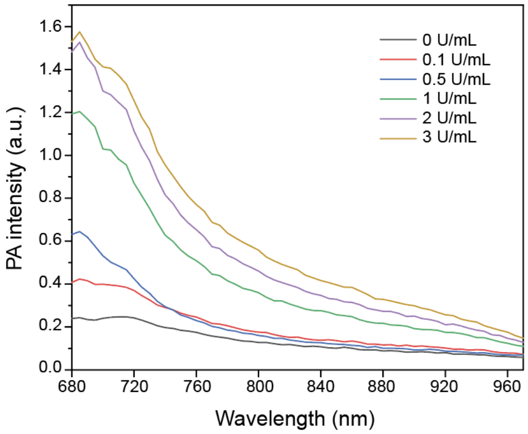

Figure 3.24 PA spectra of PNC@NB

PNC@NB showed increased PA signal of PNC@NB from 650 nm to 970 nm wavelength after heparin interactions with heparin concentration from 0 to 3 U/mL.

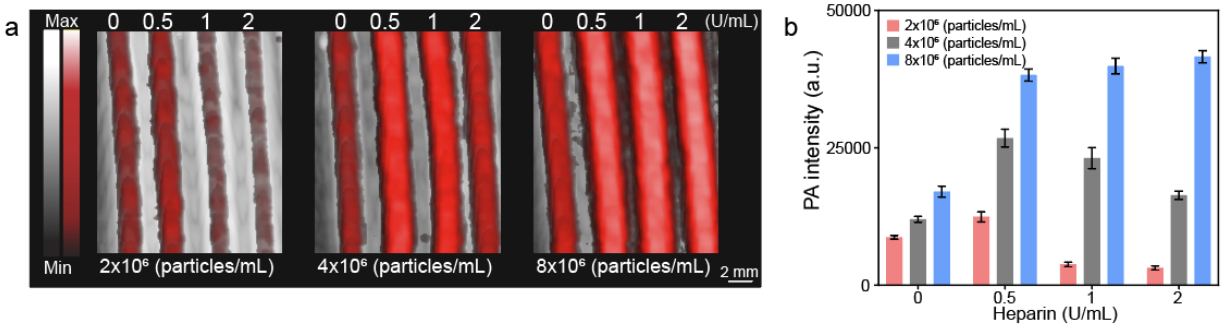

Figure 3.25 Concentration-dependent PA signal

a PA image and (b) PA intensity of PNC@NB with different particle concentrations (*e.g.*, 2, 4, and 8×10^6 particles/mL) that interacted with heparin concentration from 0.5 to 2 U/mL. These results indicate that particle concentration (~8×10^6 particles/mL) was required to increase PA signal for heparin sensing. Particle concentration of each sample was measured using NTA technology. The error bars represent the standard deviation of five regions of interest.

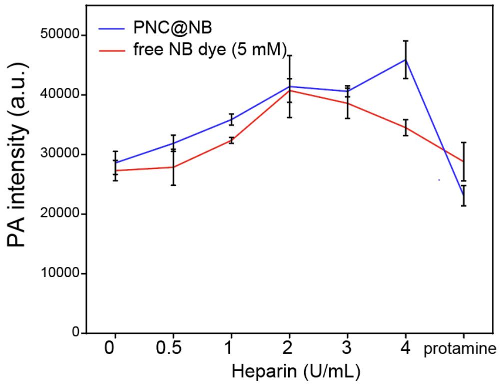

Figure 3.26 PA intensity comparison in whole human blood

PA intensity of PNC@NB that loaded 80 µM of NB dye showed higher PA signal and had a broader therapeutic window than free NB dye with the concentration of 5 mM in whole human blood. The error bars represent the standard deviation of five regions of interest.

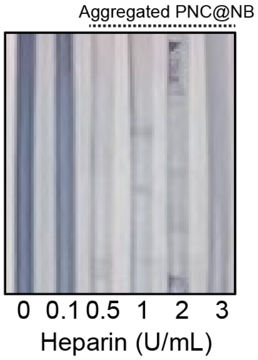

Figure 3.27 Photograph of PNC@NB-heparin interaction
Photograph shows particle aggregation of PNC@NB after interacting with heparin concentration.

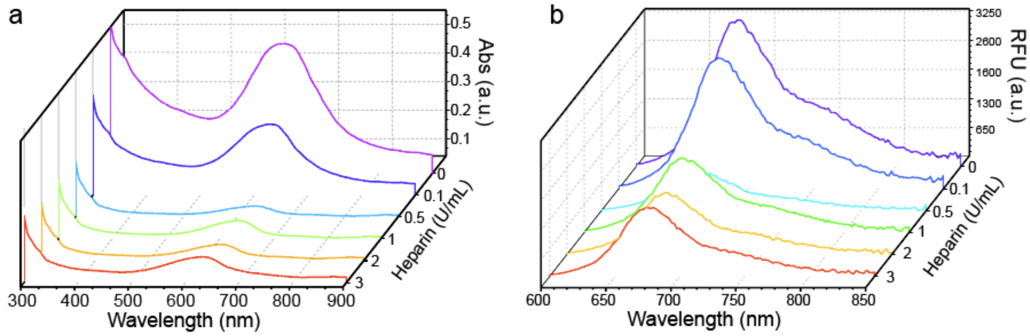

Figure 3.28 Decreased absorbance and fluorescence of PNC@NB
Decrease in absorbance (a) and fluorescence (b) was observed after heparin interactions. The quenched fluorescence as a result of particle aggregation could lead to more PA signal.[137]

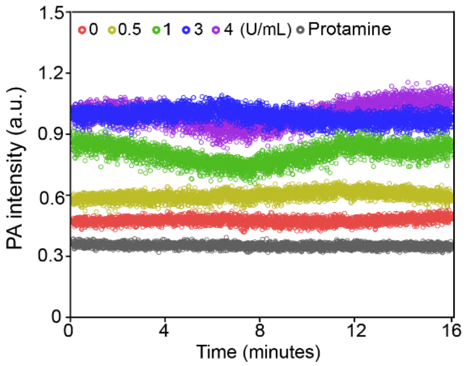

Figure 3.29 PA signal stability of PNC@NB
PA signal generated from PNC@NB–heparin aggregation was stable for 15 min in whole human blood.

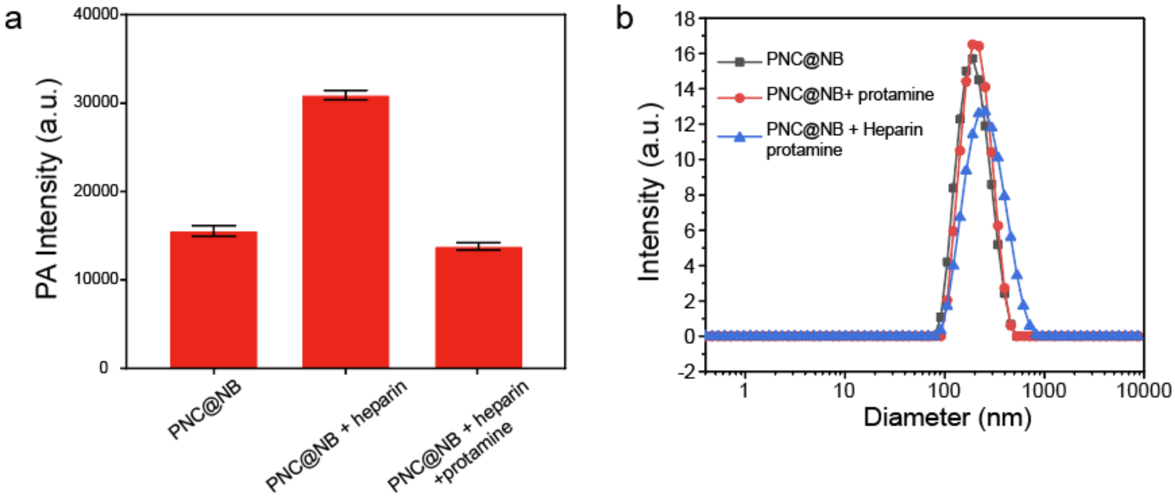

Figure 3.30 PA response of PNC@NB with/without protamine

a In the presence of protamine, the increased PA signal of PNC@NB–heparin interaction turned off. Protamine is a positively charged heparin antagonist which can prevent interaction between heparin and PNC@NB. 1 U/mL of heparin and 80 µg of protamine were used for the reversal test.[129] The error bars represent the standard deviation of five regions of interest. b DLS data shows that there was no particle aggregation or disassembly of PNC@NB occurred in the presence of protamine.

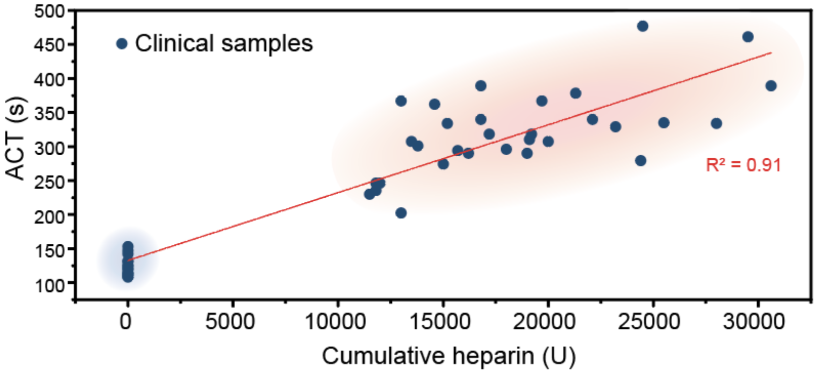

Figure 3.31 Linear correlation between ACT and cumulative heparin

ACT values were linearly correlated with cumulative heparin ($R^2 = 0.91$). Clinical specimens were collected from 17 patients. Blue and red area indicate before (blue) and after (red) heparin infusion.

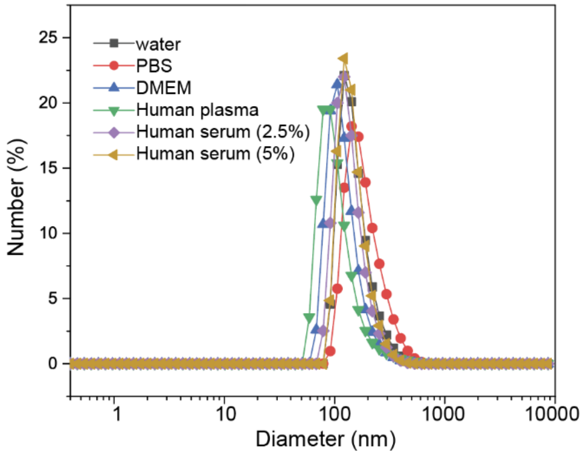

Figure 3.32 Colloidal stability of PNC@NB

PNC@NB was incubated in different media (PBS, DMEM, human pooled plasma, 2.5% and 5% human serum) for 1 h, and showed negligible aggregation.

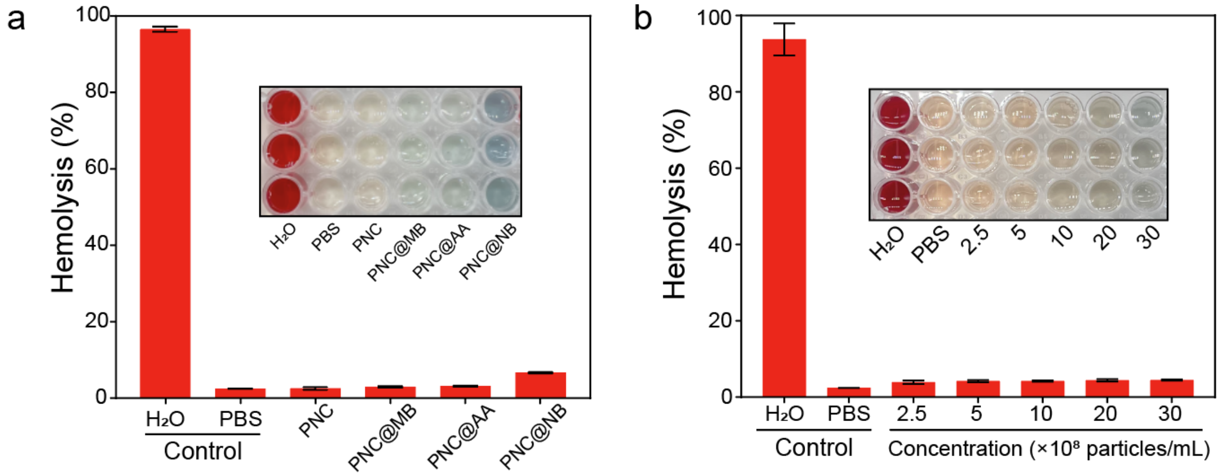

Figure 3.33 Hemolysis analysis of PNC, PNC@MB, PNC@AA, and PNC@NB

a Hemolysis of PNC, PNC@MB, PNC@AA, and PNC@NB after incubation with red blood cells with the concentration of 30 ×10^8 particles/mL used for heparin sensing. b Hemolysis of PNC@NB after incubation with red blood cells with the various concentrations (*e.g.,* 2.5 to 30 ×10^8 particles/mL). PBS and deionized water were measured for negative and positive control. Inset image represent photograph of the solution supernatant after centrifugation at 4,000 *g* for 10 min. The error bars represent the standard deviation of three separate measurements.

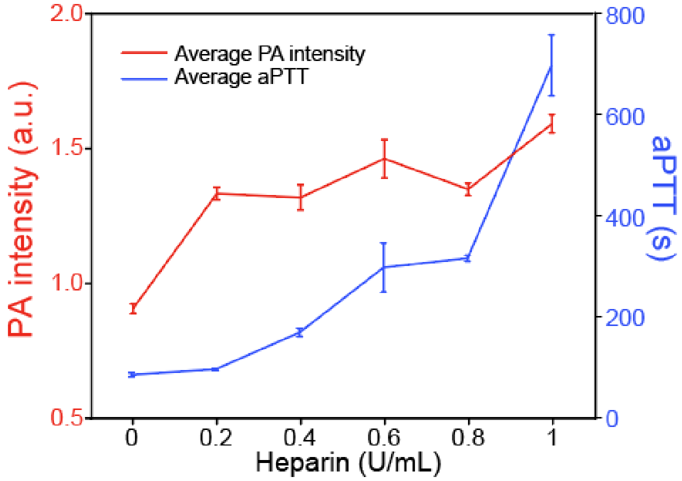

Figure 3.34 Correlation of aPTT and PA response of PNC@NB.
PA intensity of PNC@NB interacting with heparin concentration from 0.2 to 1 U/mL in human whole blood; the corresponding aPTT values were plotted against the heparin concentration. The error bars represent the standard deviation of three separate measurements.

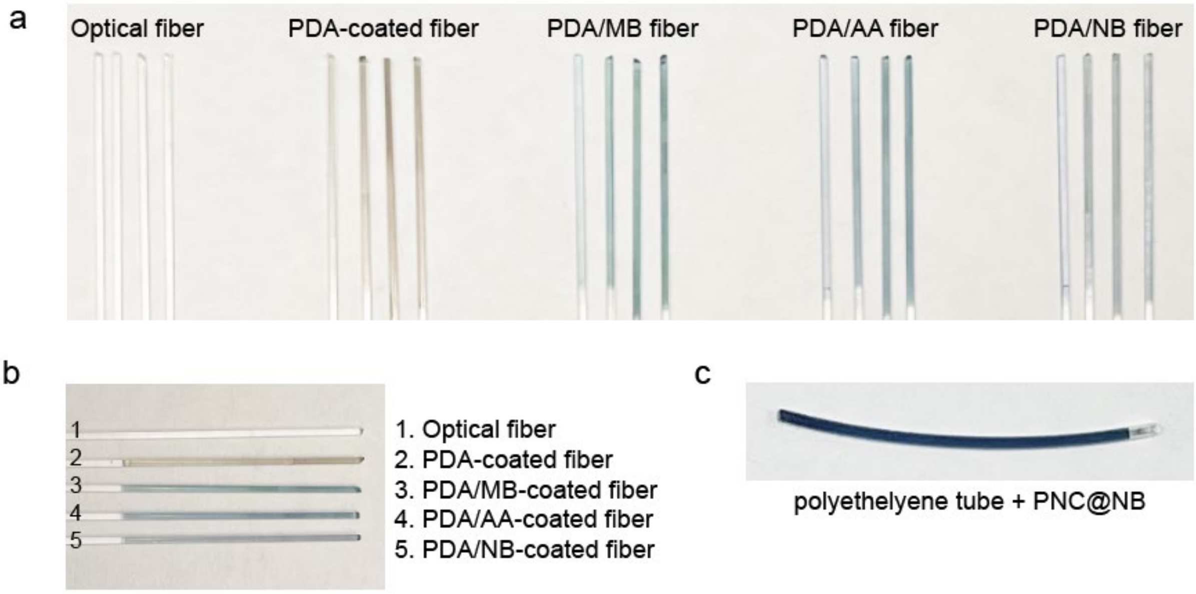

Figure 3.35 Proposed functional optic fiber for heparin detection
a Taking advantage of adhesive nature of PDA, optical fibers were successfully coated with small molecular dyes (*e.g.,* MB, AA, and NB) with different dye concentration from low (left) to high (right). b Dye-coated optical fibers, enabled by PDA coating, and (c) PNC@NB-loaded polyethylene tube for future work for heparin detection *via* PA imaging.

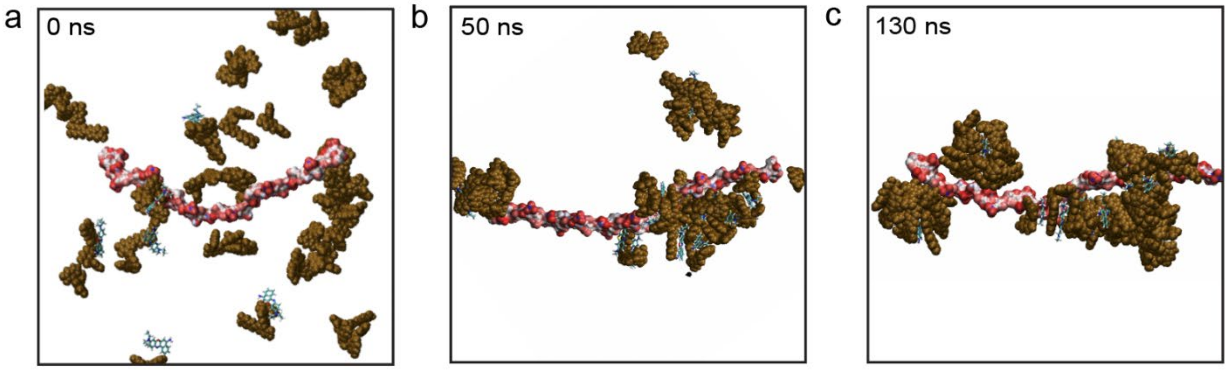

Figure 3.36 PDA–heparin interactions with NB dye
MD simulation of interaction between PDA (brown) and heparin (red) in the presence of NB dyes at (a) 0 ns, (b) 50 ns, and (c) 130 ns. These results indicate that NB dyes bridged interaction between the PDA (brown) and heparin (red).

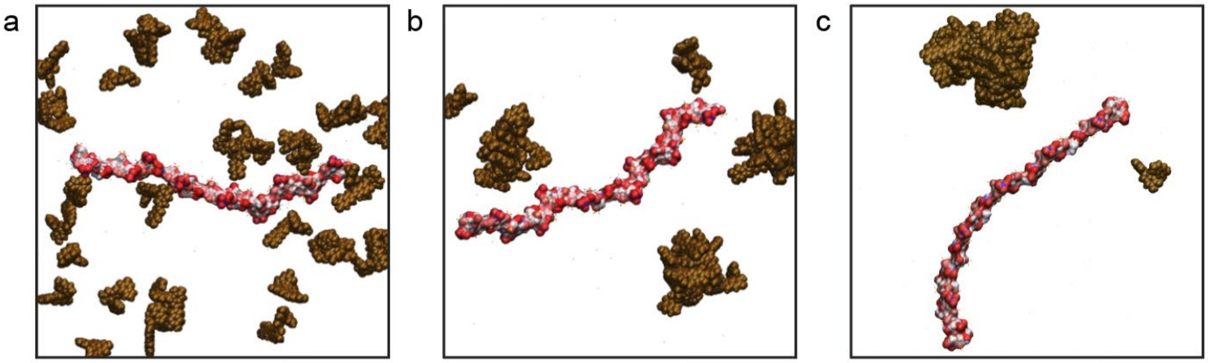

Figure 3.37 PDA–heparin interactions without NB dye
MD simulation of interaction between PDA (brown) and heparin (red) at (a) 0 ns, (b) 50 ns, and (c) 130 ns. There was no observed particle aggregation when PDA alone interacted with heparin.

3.5. Conclusions

We developed small molecular dye–PNC nanosystems as a viable heparin-sensitive platform for PA imaging due to the adhesive nature, fluorescence quenching, and low thermal conductivity of PDA. These dye–PDA assemblies allow quantitative heparin monitoring *via* enhanced PA signal generation. We validate mechanisms that were present in the significant PA enhancement of dye-loaded PNC compared to the free dyes. Comprehensive insights of charge-dependent aggregation of dyes–PNC *versus* disassembly of dyes–PNC were highlighted to better understand the on/off PA amplification. Encouraged by this results, future work includes the development of advanced heparin sensing platform (*e.g.,* functionalizing catheter) for *in Vivo* PA imaging and the use of other molecular agents to increase sensitivity for the heparin detection.[72, 162, 163] This PDA-enabled strategy for designing functionalized nanocapsules will provide better pathway for tailoring diverse molecular contrast agents and expand approach of eliciting PA signal for biomedical applications.

3.6. Acknowledgements

We thank Dr. Ali Harri, Dr. Jorge Palma-Chavez, and SW Kwak for helpful discussions. This work was performed in part at the Nano3 platform at University of California San Diego Materials Research Science and Engineering Center (UCSD MRSEC), supported by NSF (Grant DMR-2011924), San Diego Nanotechnology Infrastructure (SDNI) of University of California San Diego, supported by NSF (ECCS-1542148), and by Cellular and Molecular Medicine Electron Microscopy Core facility (NIH S10 OD 023527). R.M.B. acknowledges fellowship support under T32 CA153915. We thank funding from NIH under DP2 HL137187, S10 OD 023555, S10 OD 021821, and NSF 1845683.

Chapter 3, in part, is a reprint of the material as it appears in “Enhanced photoacoustic detection of heparin in whole blood via melanin nanocapsules carrying molecular agents” by Yim, Wonjun; Takemura, Kathryn; Zhou, Jiajing; Zhou, Jingcheng; Jin, Zhicheng; Borum, Raina M.; Xu, Ming; Cheng, Yong; He, Tengyu; Penny, William; Miller, Bill R.; Jokerst, Jesse V., ACS Nano 2022. The dissertation author was the primary investigator and author of this paper.

CHAPTER 4. 3D bioprinted phantom with human skin phototypes for biomedical optics

4.1. Abstract

We report 3D-bioprinted skin-mimicking phantoms with skin colors ranging across the Fitzpatrick scale. These tools can help understand the impact of skin phototypes on biomedical optics. Synthetic melanin nanoparticles of different sizes (70–500 nm) and clusters were fabricated to mimic the optical behavior of melanosome. The absorption coefficient and reduced scattering coefficient of the phantoms are comparable to real human skin. We further validated the melanin content and distribution in the phantoms *versus* real human skins *via* photoacoustic (PA) imaging. The PA signal of the phantom could be improved by (i) increasing melanin size (>1,000-fold), (ii) increasing clustering (2–10.5-fold), and (iii) increasing concentration (1.3–8-fold). We then used multiple biomedical optics tools (*e.g.,* PA, fluorescence imaging and photothermal therapy) to understand the impact of skin tone on these modalities. These well-defined 3D-bioprinted phantoms may have value in translating biomedical optics and reducing racial bias.

4.2. Introduction

Human skin offers important physical and immunological protection. It protects against injury, shields radiation, and offers antioxidant defense.[164, 165] Skin consists of a lamellar structure with diverse cell types (*e.g.,* immune cells, melanocytes, and basal cells) that periodically detach from the basement membrane, move to the surface, and die for self-renewal.[166] Melanocytes are a critical cell type that generate melanin to absorb ultraviolet (UV) light (290–400 nm), which is a major risk for skin diseases (*e.g.,* melanoma) due to DNA damage.[167-170] Here, melanin-containing organelles called melanosomes are transferred to the surrounding keratinocytes. This increase in melanosome concentration leads to darker skin phototypes, and darker phototypes can be a function of racial background or previous sun exposure, i.e., tanning.[171] Indeed, skin pigmentation depends on variations in the size, number, clustering phase, and the proportions between melanin species (*e.g.,* eumelanin and pheomelanin).[172] Skin pigmentation has been quantified using melanosome volume fraction (M_f) parameter: 1.3–6.3% for lightly pigmented adults, 11–16% for moderately pigmented adults, and 18–43% for darkly pigmented adults.[173]

Variations in skin phototype can complicate biomedical optics. Melanin absorption increases linearly from 800 to 600 nm and exponentially from 600 to 300 nm.[174, 175] Darker skin phototypes can absorb and scatter more photons: As a result, incident light is attenuated before it reaches the target of interest, and signal transmission can be impeded back to the sensor. Therefore, variations in skin phototypes have negatively affected many forms of medical optic technology including pulse oximetry,[176] optical coherence tomography,[177] wearable electronics,[178, 179] photoacoustic imaging,[180] fluorescence imaging,[181] and photothermal therapy.[182] In one recent study, 48,000 pairs of pulse oximetry measurements in 8675 White patients and 1362 Black patients were compared with arterial oxygen saturation.[176] The results found that pulse oximetry had trouble in diagnosing hypoxemia in 11% Black patients and 3% White patients due to strong light absorption by melanin at 660 nm. Furthermore, wearable electronics (*e.g.,* smartwatches) have reported inaccuracies in heart rate readings occurring more often in users with dark skin than light skin.[178, 179] Clearly, the impact of differences in skin phototypes underscore the ongoing need to understand and correct racial bias in optical technologies. While larger cohort studies are ideal to define and rectify such bias, tissue-mimicking phantoms that recreate the optical properties of human skin as a function of skin phototypes could offer dramatic time- and cost savings.[183, 184] These phantoms would be attractive to regulatory agencies, device development firms, and patients.

Here, we engineered 3D-bioprinted phantoms with skin phototypes containing synthetic melanin with controllable particle sizes and clustering to mimic the epidermis of different skin phototypes ranging from Fitzpatrick (Fitz) scale 1 to 6.[183, 185] The photoacoustic (PA) signal of human skin changes as a function of melanin absorption:[186] The light absorbed by melanin is converted to spatially-confined heat that generates acoustic waves.[187] This implies that PA can indirectly measure melanosome content and distribution in human skin. Fitz. 5 human cadaver skin showed 3.5-fold higher PA signal than Fitz. 2 human cadaver skin due to higher melanosome content (Figure 4.1a and Figure 4.2).

To mimic variable melanosomes in human skin, we studied optical properties and PA signal of synthetic melanin (i.e., polydopamine) over (i) different sizes (ii) mixtures of different sized particles, and (iii) clustering phases which are biologically relevant to real melanosomes.[188] Gelatin methacrylate (GelMA)—biomacromolecule gelatin obtained from denatured collagen—was used as a bio-ink (*i.e.,* matrix).[189] 3D bioprinting was then used to fabricate a customized GelMA-based phantom with a thin melanin-containing layer (*i.e.,* mimicking the epidermal layer in human skin) (Figure 4.1b). Finally, we quantitatively examined the impact of skin phototypes on PA imaging, fluorescence imaging, and photothermal imaging at different wavelengths (*e.g.,* 680, 800, and 1064 nm) (Figure 4.1c). Our skin-tone phantom built up by 3D bioprinting is expected to serve as a benchmark calibration tool of light-mediated diagnostics toward clinical use and further underpin development of biomedical optics.

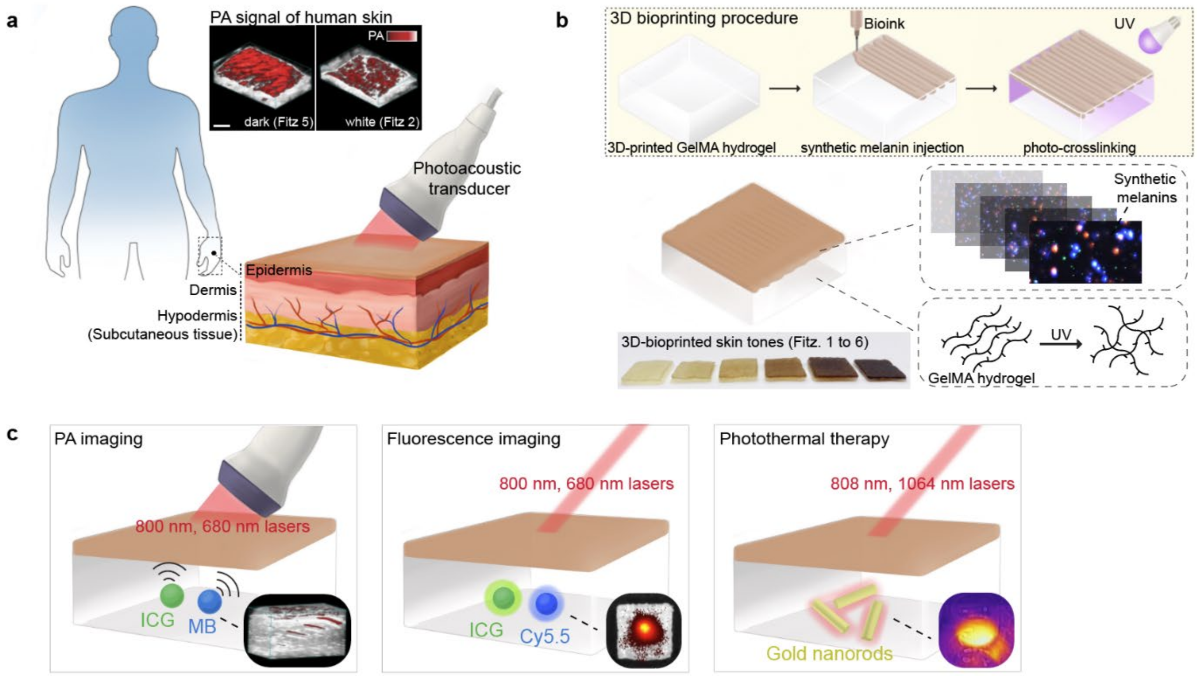

Figure 4.1 Mimicking human skin phototype for biomedical optics
a, PA transducer imaged melanosomes in human skins of Fitz. 5 and Fitz. 2. The scale bar represents 4 mm. b, The 3D bioprinting procedure to mimic human skin phototypes using synthetic melanin and GelMA hydrogel. Red and blue dots in the insert image are real PDA nanoparticles measured by M-NTA. c, Evaluation of skin phototypes impact on multiple biomedical optics (e.g., PA imaging, fluorescence imaging, and photothermal therapy). MB, ICG, Cy5.5, and gold nanorods were used to investigate the impact in different wavelengths (680–1064 nm). Insert images describe PA signal, fluorescence, and temperature of the probes under the skin-tone phantoms during the examination.

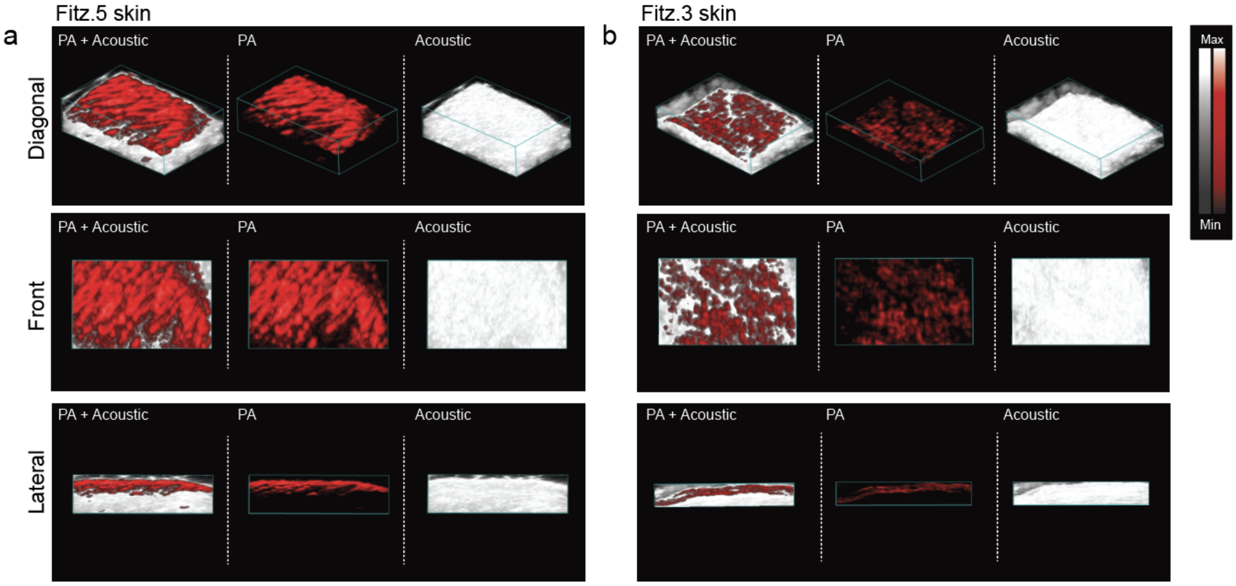

Figure 4.2 PA image of human skin specimens
PA imaging and ultrasound (US) images of human skin with different skin phototypes: Fitz. 5 (a) and Fitz. 2 (b). Fitz. 5 skin showed 3.5-fold higher PA signal compared to the Fitz. 2 skin due to higher melanosome content in the epidermis. The PA signal of melanosomes was randomly distributed showing that melanosomes were arbitrarily located in the human skin. The PA image presents different perspectives (*e.g.,* diagonal, front, and lateral view).

4.3. Materials and method

4.3.1. Synthesis of GelMA hydrogel

Briefly, gelatin from a porcine skin was fully dissolved in PBS (10% w/v) at 55 C°,[189] and then methacrylic anhydride (MA) was added dropwise (0.5 ml/min) until the target volume reached . For the methacrylation reaction, the mixture was vigorously stirred at 1000 rpm for 2 h. The solution was then centrifuged at 1000 g for 2 min to remove excess MA. Supernatants were diluted five times with additional PBS to stop the reaction followed by dialysis against distilled water (12-14 kDa cut-off, refreshed water five times) for 5 days at 40 C°. Unreacted MA and salts were further removed during the dialysis. The GelMA hydrogel was placed at –80 C° overnight and lyophilized for 5 days, thus forming a porous white foam. The product was stored at –80 C° for future use (Figure 4.3).

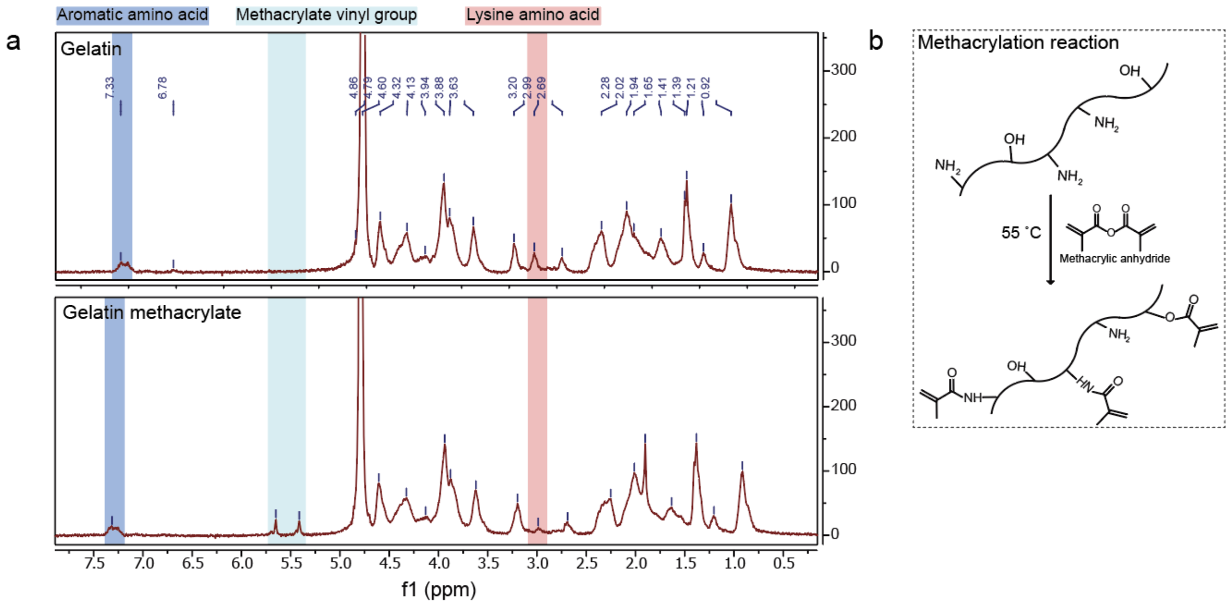

Figure 4.3 NMR spectra of gelatin and gelatin methacrylate
a, The ^{1}H NMR (300 MHz, D_2O) spectra of gelatin includes the phenylalanine signal (6.9-7.5 ppm) and lysine amino acid (2.8-2.95 ppm). After methacrylation reaction, the methacrylate vinyl signal (6.3-5.8 ppm) appeared suggesting the formation of gelatin methacrylate. b, Schematic of methacrylation reaction and molecular components of gelatin methacrylate.

4.3.2. Synthesis of synthetic melanin

Briefly, 5 ml of distilled water and 2 ml of ethanol were mixed under vigorous stirring at room temperature followed by addition of 500 µL of fresh dopamine solution (40 mg/mL in distilled water).[33] Then, 100 µL of ammonium hydroxide solution was added to trigger the polymerization. The color immediately changed from yellow to dark brown within 20 minutes. The solution was stirred at 900 rpm overnight. The size of the polydopamine could be readily controlled by adjusting the amount of dopamine. For example, 500, 600, 700, and 800 µL of dopamine solution forms polydopamine with sizes of 70, 120, 300, and 500, respectively. The samples were purified with centrifugation at 14,000 *g* (for PDA_{70}), 7,000 *g* (for PDA_{120}), 2,000 *g* (for PDA_{300}), and 1,000 *g* (for PDA_{500}) for 10 min. The pellet was redispersed in water for future use.

4.3.3. Bio-ink preparation and bio-printing procedure

Briefly, freeze-dried GelMA macromers were dissolved in PBS (10% w/v) at 50 C° for 20 minfollowed by adding alginic acid (4% w/v) and photo-initiator (0.5% w/v).[190] During bio-ink preparation, the sample was covered by aluminum foil (to prevent photo-crosslink from the light) and gently mixed for 1 h. Synthetic melanin was added in GelMA macromer before adding the photo-initiator. Different skin phototypes were readily tunable by adjusting different amounts of synthetic melanin in GelMA macromer. For example, 4, 8, 12, 16, 20, and 30 μL of PDA mixtures (0.01 mg/ml) that contain 20% of PDA clusters, 30% of PDA_{120}, and 50% of PDA_{300} were mixed with 1 mL of GelMA macromer to prepare bio-inks for different skin phototypes from Fitz. 1 (4 μL) to Fitz. 6 (30 μL). The 10 – 100 μL of PDA mixtures were deposited on the interface between the epidermis and the dermis to mimic basal layers (the innermost layer of the epidermis) where most of melanin resides. The prepared bio-inks were then stored at 4 C° and warmed at 37 C° for 30 min before bioprinting. The 3D-bioprinting procedure was performed using an BioX 3D bioprinter (CELLINK+). The bioprinting procedure was done at room temperature with 20-70 kPa pressure and 1.5–2.5 mm/s printing speed. After bioprinting, 365 nm of UV light with an intensity of 25 mW/cm^2 was used to trigger photo-crosslinking for 1 min. Specifically, good bioprinting quality could be achieved by careful selections of the needle (e.g., gauge (20G)), printing speed (2 mm/s), pressure (25 kPa), temperature (room temperature) as well as the rheology of the bio-ink. The printed skin phantoms were then stored in a petri dish sealed with parafilm for future use.

4.3.4. Human skin preparation

All work with human subjects was done in accordance with institutional review board (IRB) guidelines. Two donated human skin tissues (15 cm × 15 cm, white and dark) were from UCSD and UCI Health Centers. Human skin samples were stored in –80 C°. Prior to the experiments, the skin was thawed at the room temperature and razor blades were used to cut the skin specimens with the size of 2 cm × 2 cm. The specimens were immersed in the formalin fixation buffer overnight for fixation.

4.3.5. Multi-laser nanoparticle tracking analysis

Multi-laser nanoparticle tracking analysis (M-NTA) measurement was performed using a ViewSizer 3000 (Horiba Scientific, CA, USA).[153] The temperature was controlled at 25 °C, and automated noise analysis was used to calibrate the optimal wavelength for representing each nanoparticle. An 8-bit composite video was generated, and 10 videos were recorded at a framerate of 30 fps for 10 s (300 frames for seconds) for the analysis. A quartz cuvette with a minimum sample volume of 0.8 mL was used for measurement. 50 µL of each sample was diluted in 5 mL of Millipore water. M-NTA measurements was used to image the nanoparticles based on the light scattering. Three lasers with different wavelengths (*e.g.,* red: 630 nm, green: 520 nm, and blue: 445 nm) were used to scatter the nanoparticles: Red and green lasers are used to scatter large nanoparticles (300–500 nm). A blue laser is used to scatter small nanoparticles (20–200 nm). Here, polydopamine nanoparticles with the size of 70, 120, 300, and 500 nm were tested at the same operating conditions (intensity of blue laser: 70 mW, green laser: 15 mW, red laser: 8 mW).

4.3.6. Reversibility of (Ca^{2+}–EDTA) test

Briefly, particle aggregation can be induced by reducing electrostatic interaction between nanoparticles based on DLVO theory (described on page 32). 100 µL of 10 mM Ca^{2+} solution was added to 3 ml of concentrated PDA_{120} to induce particle aggregation. Next, 100 µL of EDTA (1M , pH: 8.5) was added to redisperse the aggregated PDA_{120} using strong affiliation between Ca^{2+} and EDTA. Each time of injection, 50 µL of sample was taken out and stored for DLS and PA measurement. After 4 cycles of Ca^{2+}-EDTA interaction, the aggregated PDA_{120} could no longer be redispersed (data not shown).

4.3.7. PDMS synthesis

Briefly, an elastomer base and the curing agent were mixed at the ratio 10:1. The mixed materials were poured into the Petri dish with the scaffold followed by desiccation for 1 h. After incubation in an 60°C oven for 2 h, the transparent PDMS was removed from the Petri dish.

4.3.8. Synthesis of gold nanorods (GNRs)

We used a seed-mediated growth method to synthesize GNRs with a high aspect ratio of 7.3.[191] Briefly, a seed solution was prepared by mixing aqueous solutions of 5 mL of CTAB (0.2 M) and 5 mL of $HAuCl_4$ (0.5 mM). Then, 600 µL of $NaBH_4$ (10 mM) was quickly injected under vigorous stirring at 1200 rpm. After 10 s of reaction of $NaBH_4$, the star bar was removed, and the seed solution was incubated in water bath for 1 h at 30 ºC. A growth solution was prepared by sequentially adding aqueous solution of 5 mL of CTAB (0.2 M), 5 mL of $HAuCl_4$ (1.0 mM), and 60 µL of $AgNO_3$ (0.1 M) for 1 min. Then, 325 µL of hydroquinone (0.1 M) was injected and the color of growth solution changed from yellow to transparent. Lastly, 160 µL seed solution was injected and vigorously stirred at 1200 rpm for 15 s. The solution was incubated in water bath overnight at 30 ºC before being purified with centrifugation at 7,500 *g* for 10 min. After purification, CTAB-stabilized GNRs were re-dispersed in MQ water.

Likewise, we used a seed-mediated growth method to synthesize GNRs with an aspect ratio of 3.3. Briefly, a seed solution was made by mixing aqueous solutions of 5 mL of CTAB (0.2 M) and 5 mL of $HAuCl_4$ (0.5 mM, 0.2 mg/ml). Then, 600 µL of $NaBH_4$ (10 mM) was quickly injected under vigorous stirring at 1200 rpm for 10 s. The stir bar was removed, and the seed solution was incubated for 1h at 30 ºC. A growth solution was prepared by adding 6 mL of CTAB, 6 mL of $HAuCl_4$ (1.0 mM, 0.4 mg/ml), and 240 µL of $AgNO_3$ (0.1 M) for 1 min. Then, 100 µL of LAA (80 mM) was injected, and the color was changed to transparent. Lastly, 14.4 µL seed solution of quickly injected and generously stirred (800 rpm) for 10 s. The solution was incubated in water bath overnight at 30 ºC before being purified with centrifugation at 8,000 *g* for 10 min. After purification, CTAB-stabilized GNRs were stored with MQ water.

4.3.9. PA measurement

PA imaging was acquired using a Vevo 2100 LAZR (Visual Sonics, USA) with a 21 MHz transducer (LZ-250). Laser intensity was optimized and calibrated before the measurement. 20 µL of each sample was loaded into polyethylene tubes and fixed within a 3D-printed holder. The samples were aligned at a depth of 1 cm from the transducer. An installed motor with a step size of 0.054 mm was used to acquire 3D images. PA spectra were measured from 680 to 970 nm with a step size of 2 nm. To scan mimicked phantoms and human skin, the specimens were placed on the glass slide, and the laser was focused onto the epidermis of each sample using a B-mode (ultrasound). PA signals of phantoms and human skin were collected under the same conditions (*e.g.,* gain (0 dB)); 100 mM methylene blue was imaged as a reference for normalization. The 3D images were acquired using the installed motor, and the scanned surface area was 15 mm × 15 mm.

4.3.10. Data analysis

PA images were analyzed using an ImageJ software (Bethesda, USA).[44] Images were analyzed with region of interest (ROI) by using integrated density function in ImageJ software. MATLAB software was used to analyze PA signal of human skins and mimicked phantoms. PNG files were converted to RGB files and analyzed with 'surf' function. Average values, and standard deviations were calibrated using prism and origin software.

4.3.11. General characterization

Scanning electron microscopy (SEM) images were obtained using a FEI Apreo operating at a voltage of 10 kV and a current of 0.10 nA. 50 μL of samples stored in distilled water was dropped on the silicon wafer and dried overnight for the measurement. To image PDA in the skin phantom (Fig 4c), 3D-bioprinted skin phantom was sectioned using a cutter, and the sectioned sample was placed on the carbon tape. Transmission electron microscopy (TEM) images were acquired using a JEOL JEM-1400 Plus operating at 80 kV. TEM images were taken using an installed Gatan 4k digital camera in the machine. Electron-dispersive X-ray spectroscopy (EDX) were mapped using a Thermo Fisher Talos 200X operating at 200 kV. Next, 2 μL of each sample was dropped on the carbon grids and dried overnight for the measurement. The hydrodynamic size and zeta potential were measured using dynamic light scattering (DLS) with a Malvern Instrument Zetasizer ZS 90. Absorbance spectra were measuring using a BioTek Synergy H1 plate reader; 150 μL of each sample was measured in 96-well plates. Absorbance was collected from 400 to 800 nm with a step size of 2 nm. Fourier transform infrared (FTIR) measurements was performed USING A Bruker Tensor II FTIR spectrophotometer. Optical microscope (VHX-7000) was performed to image cross-sectional image of the printed and real human skins. Laser power intensity was measured using a Juno adaptor. Starlab 3.20 software was also used to monitor laser power at different wavelengths (*e.g.,* 680, 800, and 1064 nm). Nuclear magnetic resonance (NMR) spectrometer was used to calculate the degree of methacryloyl functionalization following the described method.[192] Briefly, 10 mg of gelatin and methacrylated gelatin were dissolved in 1 mL of deuterium oxide (D_2O). For calibration, all the NMR data were referenced to the solvent residual in D_2O (4.79 ppm).[193] NMR spectra was taken using Bruker Advance III HD spectrometer with 300 MHz. represents the concentration of gelatin. The degree of methacrylation was quantified using the percentage of ε-amino groups in gelatin before and after methacrylation.[192] Total transmittance and diffuse reflectance of the printed samples were measured from 400–800 nm using an integrating sphere spectrophotometer (Lambda 1050, PerkinElmer, Waltham, MA). Absorption coefficient (μ_a) and reduced scattering coefficient (μ_s') were calculated from transmittance and reflectance using the inverse an adding-doubling (IAD) algorithm.[194] The sample thickness was measured using digital calipers with 0.02 mm resolution. Fluorescence imaging used an IVIS instrument (Perkin Elmer IVIS Spectrum system). The Cy 5.5 and MB dyes were dissolved in agarose at the same dye concentration and then solidified at room temperature. After sample preparation, fluorescence images were obtained using an installed 2D optical camera in IVIS; the fluorescence efficiency was measured using a Living Image software. Samples were covered by mimicked skin phototypes phantoms, and the data was collected at the same exposure time and laser power. A photothermal study was performed using 808 and 1064 nm lasers with a power density of 1.0 W/cm^2. Real-time temperature was monitored every 30 seconds by using a FLIR C5 thermal camera. Two different GNRs with the same O.D. were irradiated by lasers under the mimicked skin phototypes: GNRs with absorption peak at 800 nm and 1064 nm in water were irradiated by an 808 and 1064 laser, respectively.

4.4. Results and discussion

4.4.1. Design of synthetic melanin

Melanin biogenesis occurs through an oxidation process of tyrosine to dopaquinone by tyrosinase.[195] Melanosomes in human skin vary in terms of size (100 nm up to 500 nm), shape (*e.g.,* spherical or elliptical), and number of clusters (Figure 4.4a).[172, 188] Although the overall structure of melanin remains unclear, the basic structural unit of melanin is a mixed polymer predominantly containing indoles.[195] Melanin from human skin or hair is challenging to obtain because it requires harsh extraction conditions (*e.g.,* strong acids or bases) and multiple purification steps.[196] Thus, polydopamine (PDA) was employed here because of its similarity to real melanin in optical absorption, chemical composition, and structure.[33, 197] Dopamine can be oxidized into dopamine quinone under basic conditions and further self-polymerize into indole-rich PDA:[198] This structure is widely considered to be a synthetic melanin[197] (Figure 4.4b). To mimic the variable sizes of melanosomes, we synthesized spherical PDA nanoparticles with different diameters of 70, 120, 300, and 500 nm (referred to as PDA_{70}, PDA_{120}, PDA_{300}, and PDA_{500}, respectively) as confirmed by transmission electron microscopy (TEM), scanning electron microscopy (SEM), and multi-laser nanoparticle tracking analysis (M-NTA) (Figure 4.4c and Figure 4.5). The size was adjusted by varying the amount of dopamine feed (2–4 mg/ml) used for the reaction. The particle size confirmed by M-NTA was consistent with dynamic light scattering (DLS) data, showing that different sized PDA nanoparticles were uniform and monodispersed (PDI $\approx$ 0.1) (Figure 4.4d). The formation of PDA nanoparticles occurred under basic condition (pH 12), which induced self-oxidization and polymerization (Figure 4.4e). Fourier transform infrared spectra (FTIR) data confirmed peaks at 1,303, 1,510, and 1,602 cm^{-1} attributed to the C–N stretching of the indole ring, the C=N of the indole imine, and the C=C of the benzene ring, respectively (Figure 2f).[199]

The extinction of the PDA increased from 900 to 400 nm similar to real melanin.[200] PDA_{500} absorbs more light (>1,000-fold) than PDA_{120} at the same particle number (*N*) due to larger absorption cross-sectional area (>18-fold) as measured by electron microscopy. (Figure 2g and Figure 4.6). Therefore, the PA signal of PDA_{500} at the same *N* was significantly higher (>1,000-fold) than that of PDA_{120} because PA signal is a function of optical absorption (Figure 4.4h and

Figure 4.7). Interestingly, PDA_{500} still showed significantly higher (>1,000-fold) PA signal than PDA_{70} at the same extinction (680 nm) because PDA_{120} scatters more light than PDA_{500} due to 12.8-fold higher N (Figure 4.8). This result also indicates that PA signal depends on the particle-size effect and the specific heat capacity (C_p) in which C_p increases with decreasing in particle size due to higher thermal vibration energy of surface atoms.[201] In summary, PDA_{500} generated much higher PA signal than PDA_{120} likely due to its large absorption area, improved heat accumulation, and heat capacity.

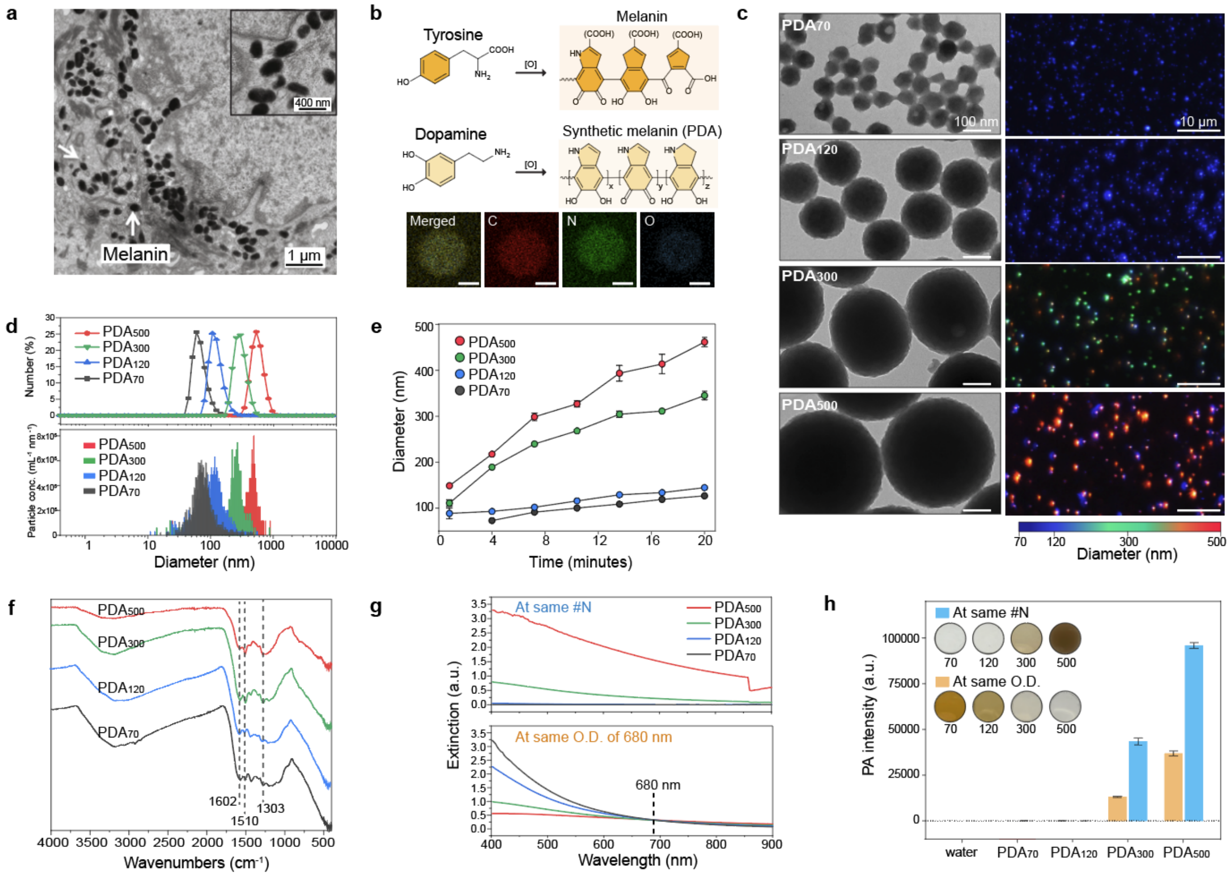

Figure 4.4 Material characterization of synthetic melanin

a, TEM image of melanin in human skin. b, Chemical structure of melanin and synthetic melanin (PDA). EDX mapping showed that PDA consists of C, N, and O, i.e., components of melanin in human skin. The scale bars represent 50 nm. c, TEM (left column) and M-NTA (right column) images of PDAs with different sizes from 70 to 500 nm. Blue (70–150 nm), green (300 nm), and red (>400 nm) dots represent actual PDAs scattered in the water during M-NTA measurements. d, Hydrodynamic diameter confirmed by DLS (top) and NTA (bottom). e, Oxidization process of dopamine, showing time-dependent PDA growth. f, FTIR data of PDA nanoparticles. The peaks in PDAs at 1303, 1510, and 1602 cm^{-1} indicate that PDAs consist of the indole structure. Ultraviolet-visible (UV-vis) spectra (g) and PA signal (h) of PDA at same N and extinction of 680 nm. PA signal of PDA$_{500}$ was significantly (>1,000-fold) higher than PDA$_{70}$ at both the same N and extinction of 680 nm. Insert images show the color of PDA$_{70}$, PDA$_{120}$, PDA$_{300}$, and PDA$_{500}$ dispersed in the water. The error bars represent the standard deviation of six regions of interest. The experiment in (h) was repeated independently three times with similar results. Panel a reproduced with permission from Elsevier.[188]

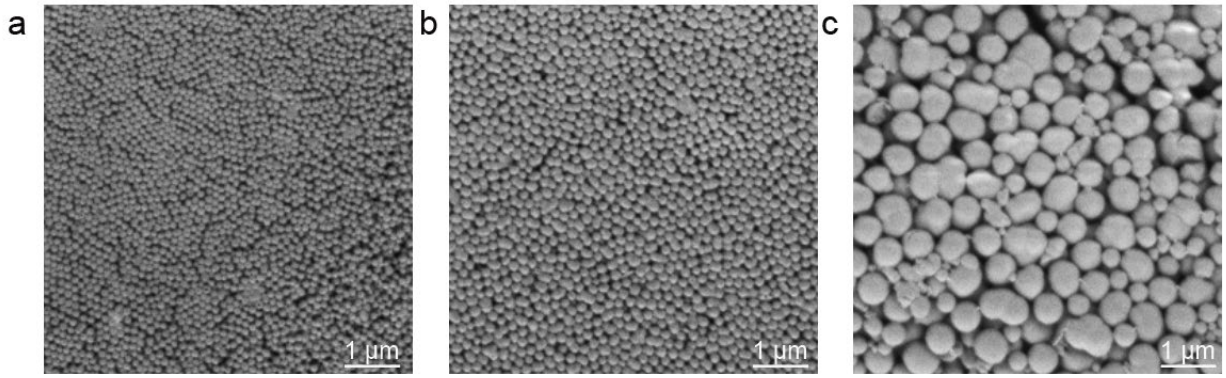

Figure 4.5 SEM image of PDA nanoparticles
SEM images of PDA nanoparticles with different sizes: (a) 70, (b) 120, and (c) 500 nm. PDA_{70}, PDA_{120}, and PDA_{500} show PDI (polydispersity) of 0.07, 0.04, and 0.09, respectively.

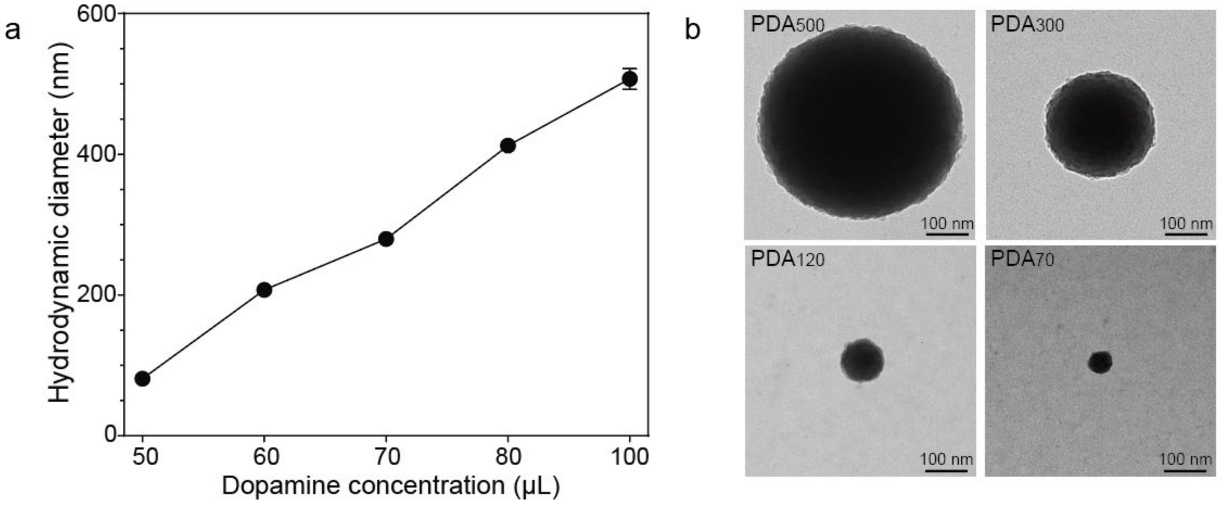

Figure 4.6 Size-controllable PDA nanoparticles
a, The size of PDA nanoparticle was readily tunable (from 70 nm to 500 nm) by tuning the dopamine feed used in the reaction. b, TEM images of PDA nanoparticles with sizes of 500, 300, 120, and 70 nm.

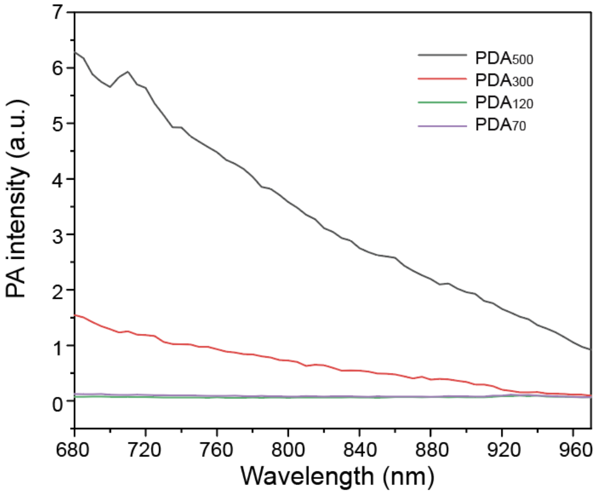

Figure 4.7 PA spectrum of PDA at the same O.D.

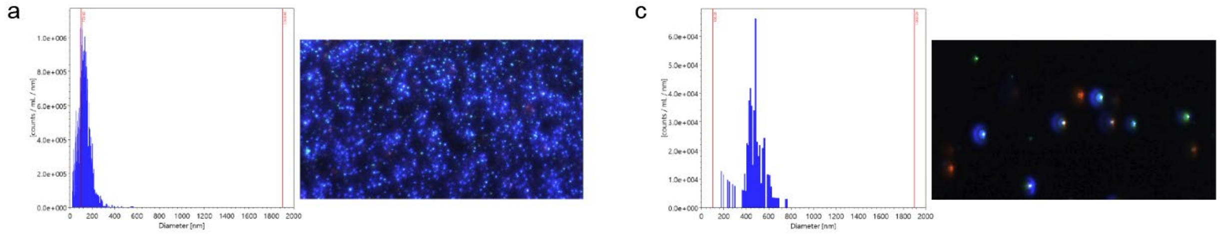

b

Results	
Total frames / Processed frames	2100 / 2100
Binning	Logarithmic binning, max 20 um
Integration range	100 [nm] to 1900 [nm]
Counts within range* / Total tracks*	1364 / 1913
Concentration within range	7.7E+07 [particles/mL]
Diluent sample name	-
Diluent concentration within range	-
Concentration with diluent subtracted	7.7E+07 [particles/mL]
Average size within range of integration	155 [nm]
Standard deviation of size / CV	47 [nm] / 0.3
Modal size	111 [nm]
D10 / D50 / D90*	60.76 [nm] / 125.41 [nm] / 196.84 [nm]
Average viscosity during measurement	0.95 [cP]

d

Results	
Total frames / Processed frames	2100 / 2100
Binning	Logarithmic binning, max 20 um
Integration range	100 [nm] to 1900 [nm]
Counts within range* / Total tracks*	106 / 106
Concentration within range	6.1E+06 [particles/mL]
Diluent sample name	-
Diluent concentration within range	-
Concentration with diluent subtracted	6.1E+06 [particles/mL]
Average size within range of integration	476 [nm]
Standard deviation of size / CV	95 [nm] / 0.2
Modal size	483 [nm]
D10 / D50 / D90*	386.10 [nm] / 477.75 [nm] / 596.90 [nm]
Average viscosity during measurement	0.95 [cP]

Figure 4.8 M-NTA data of PDA_{120} and PDA_{500} at the same O.D.

The size distribution (a) and particle concentration (b) of PDA_{120} measured by M-NTA. Likewise, the size distribution (c) and particle concentration (d) of PDA_{300} measured by M-NTA. PDA_{120} has 12.8-fold higher number of particle than PDA_{300} at the same O.D. of 680 nm, thus indicating that PDA_{120} might scatter more lights due to the increased scattering coefficient from higher particle concentration.

4.4.2. Cluster-dependent PA performance

Melanosomes are individually distributed or form clusters in the human skin.[188] To investigate the function of clusters of melanosomes, various metal ions (Na^+, Mg^{2+}, Fe^{2+}, Ca^{2+}) and other stimuli (NaOH, HCl, sugar, cysteine (Cys)) were applied to make PDA clusters. Metal ions induce PDA clustering because the catechol group in PDA can chelate metal ions, thus forming metal–phenolic networks (Figure 4.9).[198, 202] The PA signal increased as PDA nanoparticles were clustered (as assessed by DLS). The highest PA signal was observed in Ca^{2+} which caused significant PDA_{120} aggregation because of its strong binding affinity among the tested metal ions (Figure 4.10a and Figure 4.11).[203] Different Ca^{2+} concentrations (2–200 mM) were used to study the relationship between cluster size and PA signal. The results showed that PDA clusters induced by 200 mM of Ca^{2+} led to a 1.84-fold higher PA signal than PDA clusters induced by 20 mM of Ca^{2+}. There was no increase in PA signal at low Ca^{2+} concentrations (*e.g.,* 2–5 mM) because this concentration could not induce PDA clusters (Figure 4.10b). The formation of PDA clusters significantly decreased the extinction in the range of 400–550 nm while the extinction was increased from 552 to 900 nm likely due to the increased scattering by larger aggregates (Figure 4.10c and Figure 4.12).

We could disassemble PDA clusters *via* the strong chelating agent ethylenediaminetetraacetic acid (EDTA). After adding EDTA, PDA clusters were entirely disassembled due to the breakdown of metal coordination bonds (Figure 4.13). Collectively, the metal chelation was a dominant driving force for PDA clusters.[198] The PA signal of PDA clusters can be activated and deactivated by repeatedly adding EDTA and Ca^{2+} ions over four cycles (Figure 4.10d and Figure 4.14). We explained this increase in PA signal of PDA clusters through two reasons. First, the increased particle size by clustering could have a larger absorption cross-sectional area than small individuals.[188] The ~1 μm PDA clusters have 579-fold larger cross-sectional area than PDA_{120}. Second, PA signal is a function of thermoelastic expansion that occurs when the surrounding medium is locally heated. The aggregated nanoparticles could cause overlapping thermal fields that improve the rate of heat transfer and amplify PA signal.[204]

Human skin involves different-sized melanosomes, and thus we also studied the PA signal of PDA mixtures that contained both PDA_{300} and PDA_{120} at different ratios. The PDA mixture containing 66% of PDA_{300} and 33% of PDA_{120} had 1.8-fold higher PA signal than the PDA mixture containing 33% of PDA_{300} and 66% of PDA_{120} (Figure 4.10e). In addition, the PA signal of the PDA mixtures further increase by Ca^{2+}-induced PDA clustering. Notably, PDA clusters formed by PDA_{120} exhibited significantly higher (10.5-fold) PA signal than PDA_{120} while the PDA clusters formed by PDA_{300} only increased 1.13-fold, thus indicating that this aggregation-derived PA signal is affected by particle size. To understand the relationship between particle size and aggregation, we used M-NTA to monitor aggregation of PDA mixtures (Figure 4.10f and Figure 4.15). The results showed that PDA_{120} were more prone to aggregate than PDA_{300} because small nanoparticles have a higher surface area-to-volume ratio, which implies a higher surface energy than the large particles (Figure 4.16).[205] This explains why PDA_{120} dramatically increased their size (from 120 nm to >1 μm), thus significantly increasing PA signal. In summary, our PA experiments revealed that the PA signal of PDA can be improved by increasing (i) size (>1,000-fold: PDA_{300} *versu*s PDA_{120}), (ii) clustering (2–10.5-fold:10 mM *versu*s 200 mM Ca^{2+}), and (iii) concentration (1.3–8-fold: 1 μg/ml *versus* 8 μg/ml of PDA mixtures).

To use these materials in a phantom, we used a GelMA-based scaffold which can provide three dimensional supports with characteristics of the native extracellular matrix (Figure 4.17). The average thicknesses of dermis and epidermis in human skin are 2.5 mm and 0.2 mm, respectively,[206] and thus GelMA hydrogel with a thickness of 2.5 mm was first printed to provide the baseline of the epidermis. A PDA-included hydrogel with a thickness of 0.2 mm was then built on the top to mimic human skin phototypes. The dimension (20 mm × 20 mm × 2.7 mm) of the printed sample was precisely adjustable using 3D-bioprinting. Finally, UV light (365 nm) was used to initiate radical polymerization and form covalently crosslinked hydrogels (Figure 4.10g).

To study the function of PDA clusters when bio-printed, we next prepared three different bio-inks containing clustered PDAs by using 0, 20, and 200 mM Ca^{2+}. Each bio-ink had the same total number of PDA_{120} and PDA_{300}. 3D-bioprinted PDA with 200 mM of Ca^{2+} showed 3-fold higher PA signal than PDA with 20 mM of Ca^{2+}. There was significantly (>10-fold) higher PA signal than PDA with 0 mM of Ca^{2+} similar to the solution phase data in Figure 3e. We also found that the number of PA peaks exponentially increased corresponding to the number of induced PDA clusters: The printed samples with 0-, 20-, and 200-mM of Ca^{2+} showed 2, 11, and 85 of PA peak clusters, respectively (Figure 4.10h). In contrast, all three printed samples had the same international commission in illumination (CIE) coordinates of Fitz. 6 (i.e., skin phototype), thus indicating that skin phototype is more correlated with the number of PDA *nanoparticles* than the PDA clusters (Figure 4.10i and Figure 4.18).

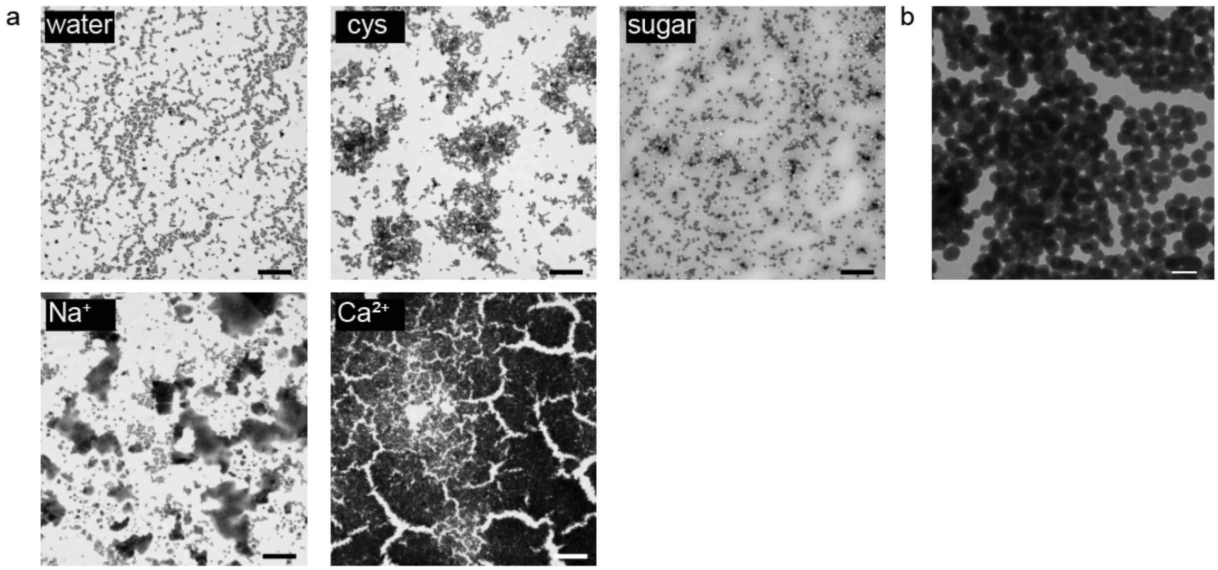

Figure 4.9 TEM images of PDA clusters
a, TEM image of individual PDA$_{120}$ in water, cys, sugar, Na^{+}, and Ca^{2+}. Metal ions such as Ca^{2+} caused large aggregates due to metal-phenolic coordination. The scale bars represent 2 µm. b, High magnified TEM image of the metal ion-induced PDA clusters, showing that PDA$_{120}$ maintained its spherical shape and showed no particle agglomeration. The scale bar represents 200 nm.

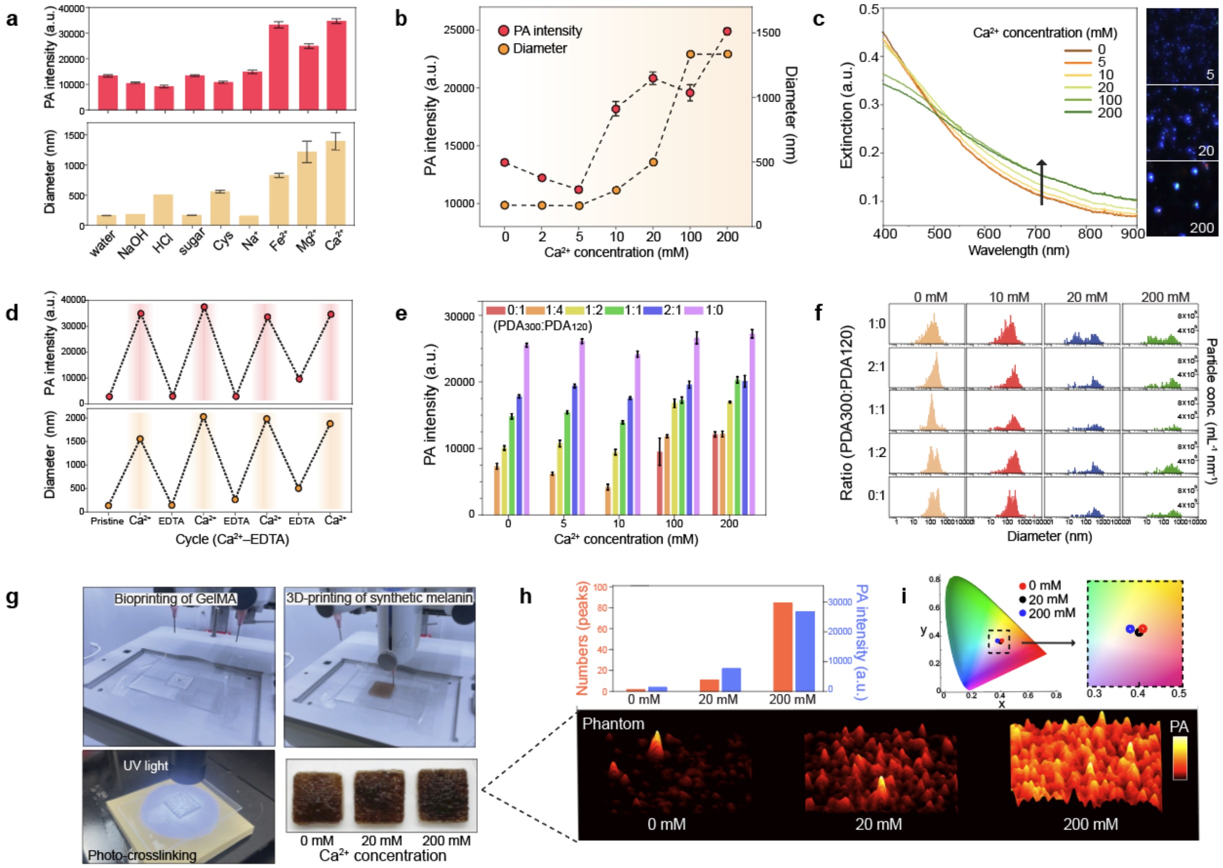

Figure 4.10 Clusters of synthetic melanin

a, PA signal of PDA clusters. Different metal ions and other sample matrices were used to induce PDA clusters. The error bars represent the standard deviation of six regions-of-interest. b, PA signal of PDA clusters induced by different Ca^{2+} concentrations (from 0 to 200 mM). The error bars represent the standard deviation of six regions of interest. c, UV-vis spectra of PDA clusters at different Ca^{2+} concentration. M-NTA image shows higher light scattering (i.e., brighter) of PDA clusters (200 mM) than individual PDAs (0 mM). The intensity of the blue dots is proportional to light scattering. d, Reversible PA signal upon assembly–disassembly of PDA clusters. PA signal turned "on and off" under repeatedly adding EDTA and Ca^{2+} ions. e, PA signal of PDA mixtures at the same total number of particles. 0:1, 1:4, 1:2, 1:1, 2:1, and 1:0 indicate the particle number ratio of PDA_{300} to PDA_{120}. f, Particle distributions of PDA mixtures at different Ca^{2+} concentrations. g, 3D bioprinting process of skin-tone phantom. The photograph shows the same skin phototype (Fitz. 6) of three-printed phantoms. h, PA signal of 3D-bioprinted phantoms containing PDA mixtures with 0, 20, and 200 mM of Ca^{2+} ions. PA signal increased as more PDA clusters led to PA punctuate images. i, CIE coordinates of 3D-printed phantoms containing different amounts of PDA clusters. The experiments in a, b, d, and h were repeated independently three times with similar results.

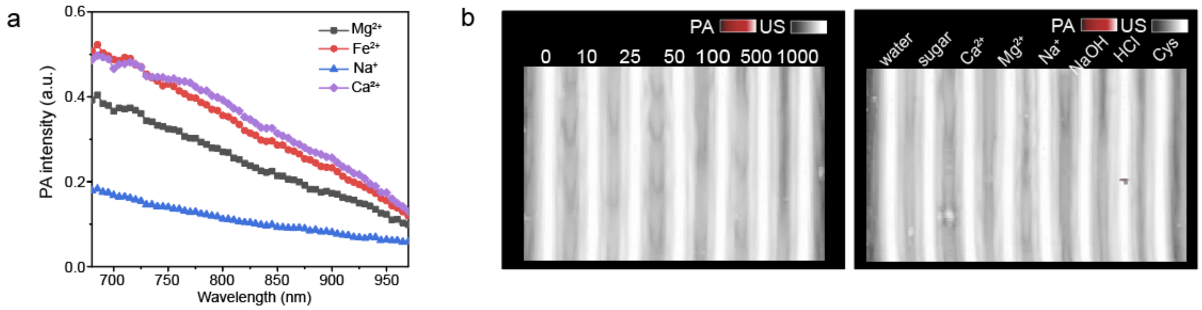

Figure 4.11 PA signal of PDA clusters

a, PA spectrum of metal-ion induced PDA clusters. Various metal ions such as Fe^{2+}, Mg^{2+}, Na^{2+}, and Ca^{2+} at same molar concentration (100 mM) were used to induce PDA clusters. The results showed that higher nuclear charges (M^{2+}> M^{1+}) and higher affinity of metal chelation caused the largest aggregation and generated the highest PA signal. b., PA image of different concentration of Ca^{2+} (0, 10, 25, 50, 100, 500, and 1000 mM) and other stimuli (sugar, Mg^{2+}, Na^{+}, NaOH, HCl, cys), showing that there was no background PA signal.

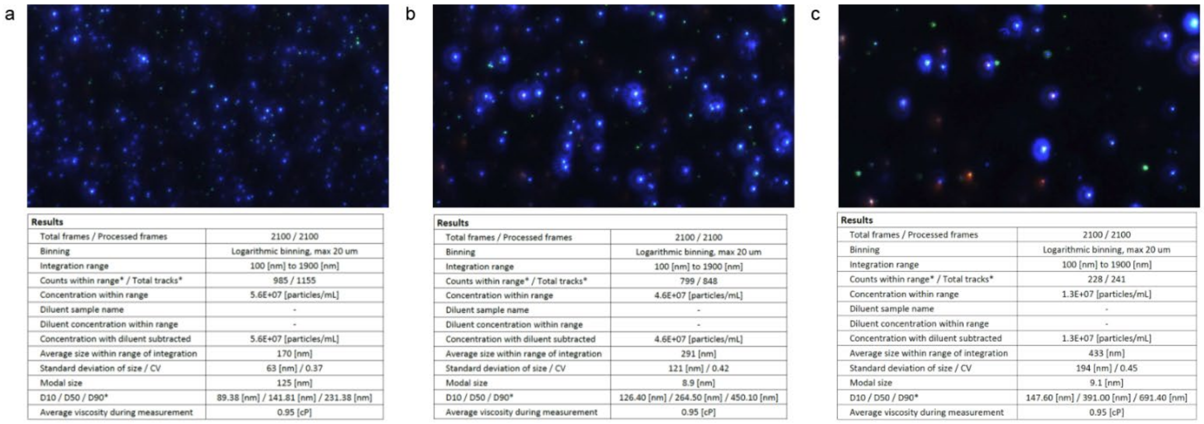

Results	
Total frames / Processed frames	2100 / 2100
Binning	Logarithmic binning, max 20 um
Integration range	100 [nm] to 1900 [nm]
Counts within range* / Total tracks*	985 / 1155
Concentration within range	5.6E+07 [particles/mL]
Diluent sample name	-
Diluent concentration within range	-
Concentration with diluent subtracted	5.6E+07 [particles/mL]
Average size within range of integration	170 [nm]
Standard deviation of size / CV	63 [nm] / 0.37
Modal size	125 [nm]
D10 / D50 / D90*	89.38 [nm] / 141.81 [nm] / 231.38 [nm]
Average viscosity during measurement	0.95 [cP]

Results	
Total frames / Processed frames	2100 / 2100
Binning	Logarithmic binning, max 20 um
Integration range	100 [nm] to 1900 [nm]
Counts within range* / Total tracks*	799 / 848
Concentration within range	4.6E+07 [particles/mL]
Diluent sample name	-
Diluent concentration within range	-
Concentration with diluent subtracted	4.6E+07 [particles/mL]
Average size within range of integration	291 [nm]
Standard deviation of size / CV	121 [nm] / 0.42
Modal size	8.9 [nm]
D10 / D50 / D90*	126.40 [nm] / 264.50 [nm] / 450.10 [nm]
Average viscosity during measurement	0.95 [cP]

Results	
Total frames / Processed frames	2100 / 2100
Binning	Logarithmic binning, max 20 um
Integration range	100 [nm] to 1900 [nm]
Counts within range* / Total tracks*	228 / 241
Concentration within range	1.3E+07 [particles/mL]
Diluent sample name	-
Diluent concentration within range	-
Concentration with diluent subtracted	1.3E+07 [particles/mL]
Average size within range of integration	433 [nm]
Standard deviation of size / CV	194 [nm] / 0.45
Modal size	9.1 [nm]
D10 / D50 / D90*	147.60 [nm] / 391.00 [nm] / 691.40 [nm]
Average viscosity during measurement	0.95 [cP]

Figure 4.12 M-NTA data of PDA_{120} in 0, 20, and 200 mM Ca^{2+}

The average size and particle concentration of PDA_{120} in 0 mM (a), 20 mM (b), and 200 mM (c) of Ca^{2+}. The results showed that PDA_{120} increased the size due to particle aggregation. M-NTA uses light scattering to collect particle information. PDA clusters (blue dots in 200 mM) showed higher light scattering (i.e., brighter) than individual PDAs (blue dots in 0 mM).

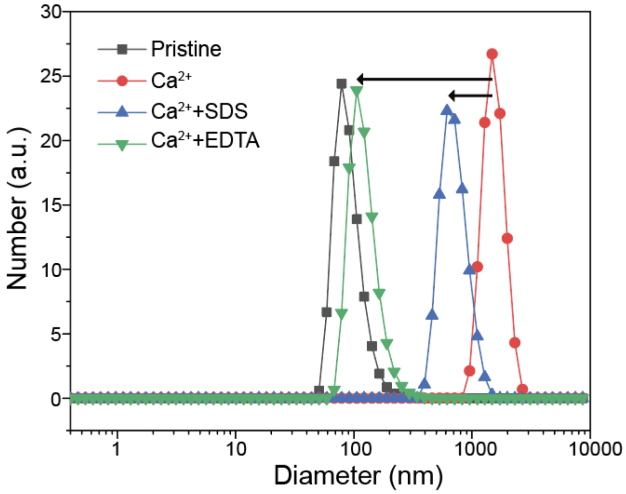

Figure 4.13 Disassembly of PDA clusters

Ca^{2+} readily induced PDA aggregation due to metal-phenolic coordination. To dissemble PDA clusters, both SDS and EDTA at the same molar concentration (100 mM) were added to the PDA clusters. Interestingly, EDTA (green line) showed better reversibility than SDS (blue line) which means metal chelation is a dominant interaction inducing the PDA clusters.

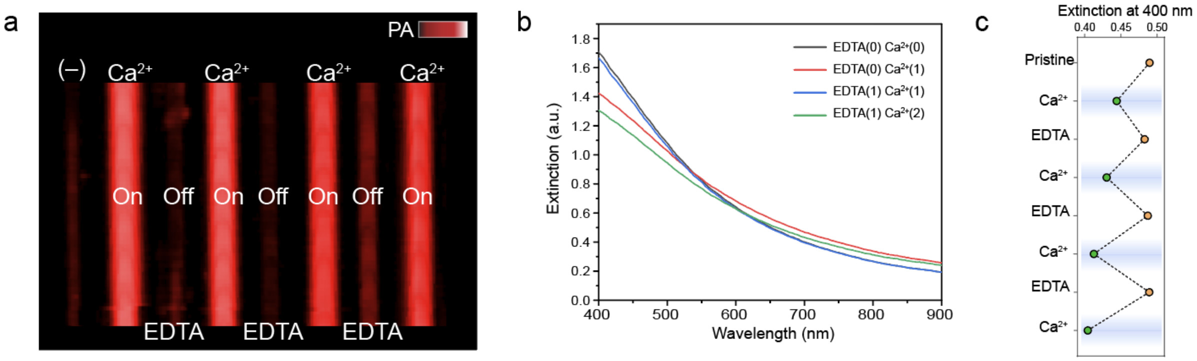

Figure 4.14 Assembly-disassembly of PDA clusters

a, PA image showed that PA signal of PDA clusters turned "on and off" under repeatedly adding EDTA and Ca^{2+} ions. b, UV-vis spectra of PDA clusters when EDTA or Ca^{2+} ions were added to the clusters. Number in parenthesis means that the number of EDTA or Ca^{2+}applied to the PDA clusters. For example, EDTA(0) Ca^{2+}(0) represent pristine condition. c, Normalized extinction value at 400 nm under repeatedly adding EDTA and Ca^{2+}.

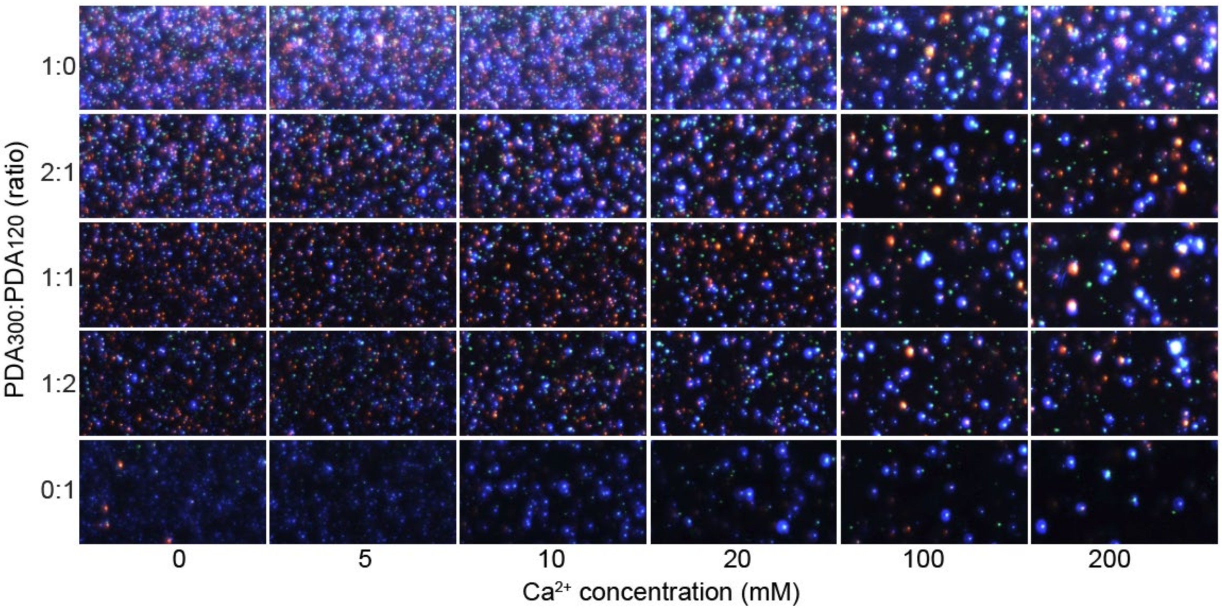

Figure 4.15 M-NTA image of PDA mixtures
M-NTA was used to image PDA mixtures that contained two different sizes (e.g., PDA_{120} and PDA_{300}) during the particle aggregation. Small PDA_{120} readily scatters with blue laser, while large PDA_{300} scatters with red laser. Blue and red colored dots represent scattered PDA nanoparticles. Most PDA nanoparticles aggregated at 100 mM and 200 mM Ca^{2+}, thus showing a lower number of nanoparticles.

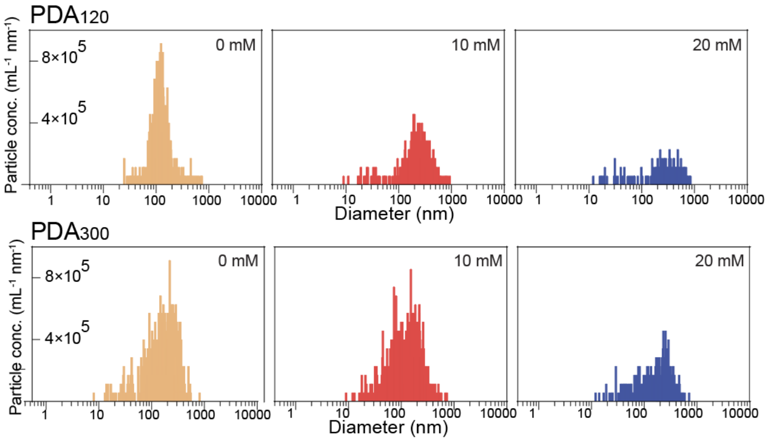

Figure 4.16 Particle distribution of PDA_{120} and PDA_{300}
PDA_{120} and PDA_{300} with the same total number of particles were clustered by 10 and 20 mM of Ca^{2+}. 50% of PDA_{120} was aggregated with 10 mM of Ca^{2+} ions while PDA_{300} required 20 mM of Ca^{2+} ions to induce similar aggregation. These results confirmed that small nanoparticles readily clustered than large particles because of higher surface energy (see DLVO theory on page 32).

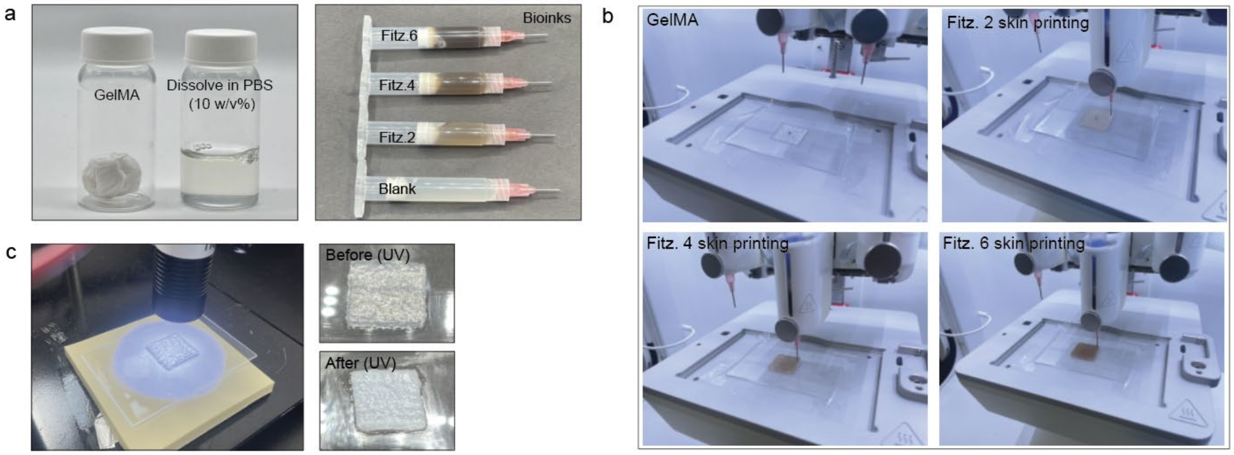

Figure 4.17 Bio-ink preparation and 3D-bioprinting process

a, Freeze-dried GelMA hydrogel was dissolved in PBS at 50°C to prepare a 10 w/v% GelMA bio-ink. Bio-inks with different color tones (*e.g.,* Fitz. 2, Fitz. 4, Fitz. 6) were prepared by adjusting amounts of PDA mixture. b, The GelMA bio-ink only was first printed to mimic dermis layer which provided the baseline of epidermis. Then, a single layer of epidermis was printed to mimic human skin phototype. c UV light with the wavelength of 365 nm was used for photo-crosslinking. Inset images are 3D-printed GelMA hydrogel before and after UV irradiation. The thickness of the phantom is precisely controllable (0.1–50 mm) using a 3D bio-printing software.

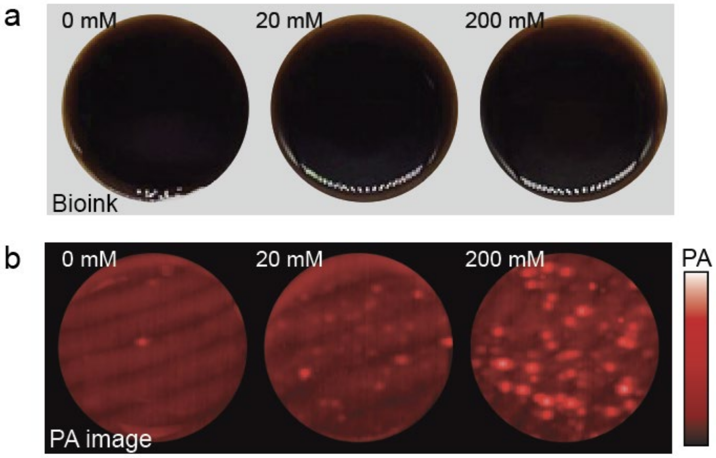

Figure 4.18 Bio-inks including PDA clusters

Bio-inks containing Ca^{2+} (*e.g.,* 0, 20, and 200 mM) were prepared to control the amounts of PDA clusters, and each bio-ink contained the same number of PDA_{120} nanoparticles. a, Photograph of bio-inks, showing that there was no color difference. However, PA image (b) showed that PDA clusters generated strong PA peaks with 3-fold higher signal than pristine samples.

4.4.3. PA characterization of real and mimicked human skin

Melanosomes have been intensively characterized and studied in dermatology.[172, 188, 207] A recent study measured variable melanosome contents in the different human skin phototypes. It showed that Fitz. 5 human skin contained more and larger melanin than Fitz. 2 human skin; melanin clusters were more often found in Fitz. 2 skin.[188] To mimic the variable contents of melanosomes, we used PDA mixtures composed of PDA clusters, PDA_{120}, and PDA_{300} (Figure 4.19). Both real and mimicked human skins had the same thickness of epidermis (about 0.2 mm) and contained melanin with the same color scale (Figure 4.20a and Figure 4.21). Different ratios of individual and clustered PDAs were mixed to understand the relationship between PDA contents *versus* variable skin phototypes. The results showed that skin phototypes are predominantly dependent on the particle concentration (M_f) rather than particle size or PDA clusters (Figure 4.20b and Figure 4.22). As PDA concentration increases (from 1- to 8-fold), PA signal linearly increased from 1.3- to 8-fold, and the color of skin phototype changed from Fitz. 1 to Fitz. 6. In addition, PDA_{120}, PDA_{300}, and PDA clusters were arbitrarily distributed and maintained their spherical shapes in the epidermis of printed skin phantom as confirmed by SEM (Figure 4.20c).

PA signal of our mimicked skins was matched to that of real human skins: Fitz. 5 skin had 3.5-fold higher PA signal than Fitz. 2 skin in both real and mimicked samples (Figure 4.20d). Furthermore, the PA images of real and mimicked skins visualized melanin distribution, indicating that both real and synthetic melanin were randomly distributed; strong PA signal peaks were found where melanosomes were crowded and/or clustered (Figure 4.20e-f and Figure 4.23). Real and mimicked skins showed a comparable PA spectrum from 680 nm to 970 nm (Figure 4.20g). The mimicked skin had stable PA signal for 5 min implying stable PDA mixtures under the 680-nm laser illumination (Figure 4.20h). Ultrasound (US) images revealed 4 mm thickness of human skin composed of the epidermis, dermis, and hypodermis. A strong PA signal was exclusively observed in the basal layer of epidermis where most melanosomes were located (Figure 4.20i). Likewise, mimicked skins had comparable skin thickness and strong PA signal generated from the epidermis. Finally, we inverted the Fitz. 2 and Fitz. 5 human skin samples to investigate tissue scattering in the underlying fat tissue layers of the dermis. No PA signal was observed in the epidermis of either human skin sample due to large light scattering in the dermis. The fat tissue layers in the dermis have low absorption at 680 nm to generate PA signal (Figure 4.20j and Figure 4.24).

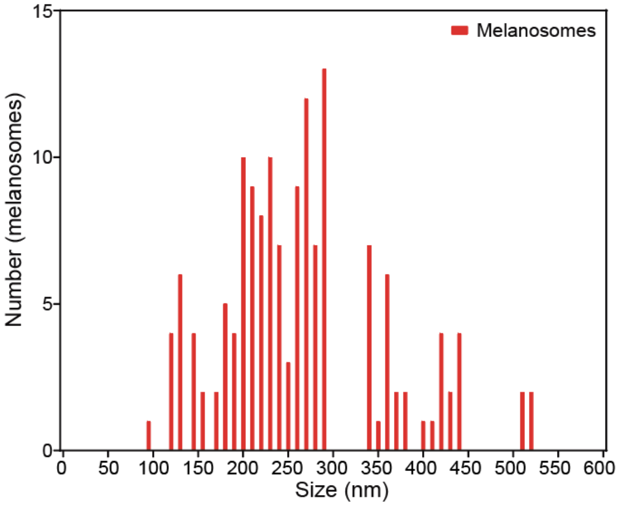

Figure 4.19 Histogram of variable sized melanosomes in human skin
The size of 113 individual melanosomes in epidermis was measured using TEM images in the previous study.[188] The histogram shows that the size range of melanosomes was from 100 to 300 nm, and more than 50% of melanosomes was larger than 200 nm. We also observed some clusters of melanosomes in the TEM image.[188] Clustered melanosomes were more often observed in lightly pigment skin(54.93%) than highly pigmented skin(6.64%).[188]

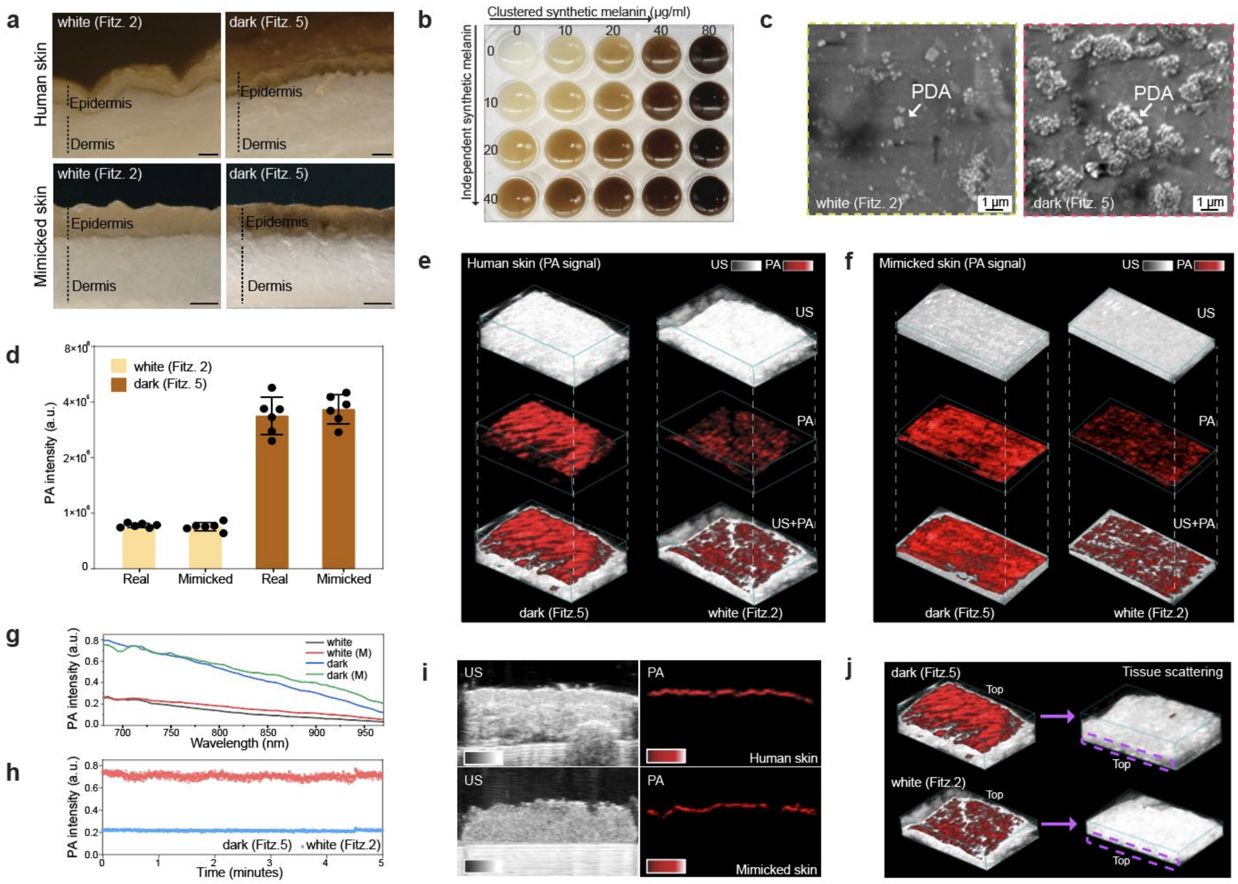

Figure 4.20 PA comparison between real and mimicked skin

a, Optical images (cross-section) of real and mimicked skins. The scale bars represent 0.5 mm. b, Skin phototype variations. Skin colors were readily tunable (From Fitz. 1 to Fitz. 6) by adjusting PDA contents. c, SEM image of PDA mixtures in the printed skin (epidermal layer). d, PA signal comparison between real and mimicked skins. PA signal of mimicked skin was comparable to that of real human skin at the same skin phototype. The error bars represent the standard deviation of six regions of interest. PA and US image of real (e) and mimicked (f) human skins, showing randomly distributed melanosomes in epidermis. g, Spectral PA signal from 680 nm to 970 nm of real and mimicked (M) skins. h, PA signal stability of mimicked skins. i, PA signal of epidermis in real and mimicked skins. j, Tissue scattering in real human skins. Purple dotted area indicates the region of epidermis after turning the samples upside-down. The experiments in g, i, and j were repeated independently three times with similar results.

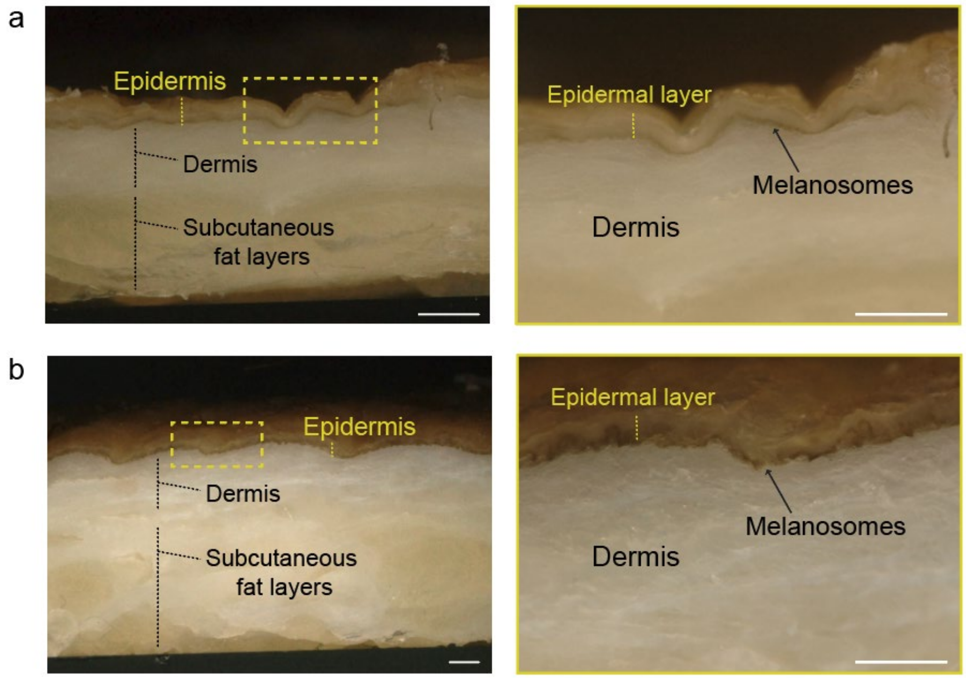

Figure 4.21 Cross-sectional image of human skin specimens
Optical microscope was used to image cross-sectional area of Fitz. 2 (a) and Fitz. 5 (b) human skin, showing epidermis, dermis, and hypodermis (subcutaneous fat layers). The scale bars represent 5 mm. Yellow dotted area zoomed in to show high magnification of epidermal layer.

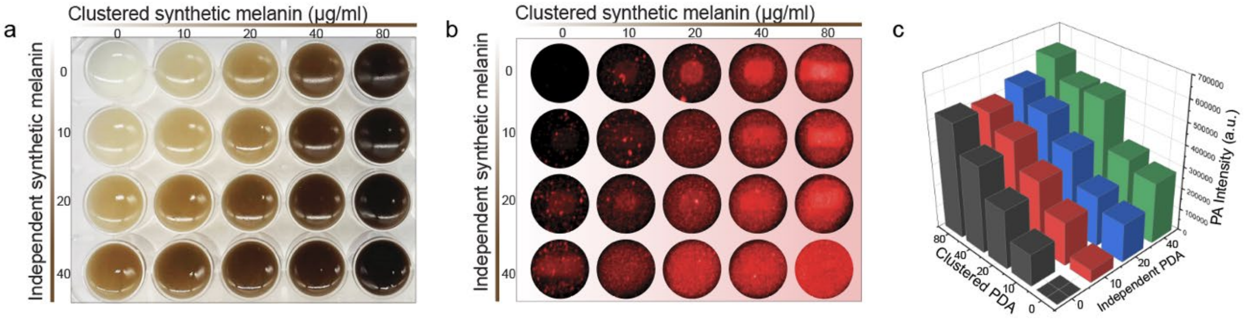

Figure 4.22 Mimicking skin phototypes using PDA mixtures
, Photograph of mimicked skin phototypes. Various skin phototypes (from Fitz. 1 to Fitz. 6) were readily controllable by adjusting PDA contents added during bio-ink preparation. The image showed that skin phototype mostly depends on concentration rather than size or clusters. b, PA image and quantified PA signal (c) of mimicked skin phototypes, showing that PA signal improved as increasing particle number, size, and clusters. Independent synthetic melanin represents PDA_{300}, and clustered synthetic melanin indicates PDA clusters formed by PDA_{120} using Ca^{2+} ions. Different amounts of independent PDA (from 0 μg to 40 μg) and clustered PDA (from 0 μg to 80 μg) were mixed to show color variations.

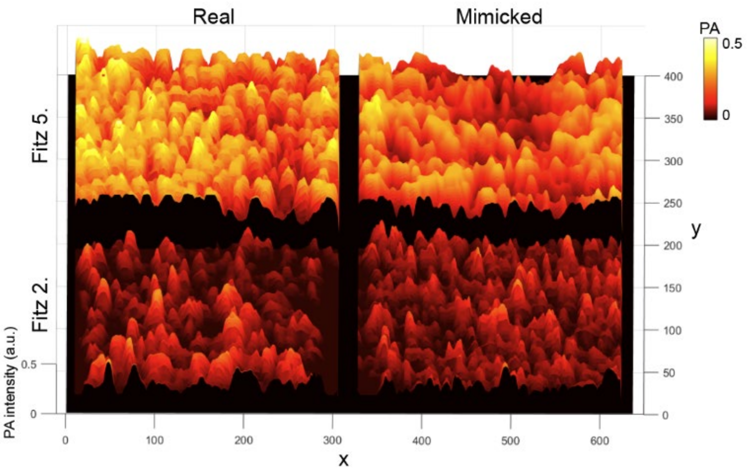

Figure 4.23 Randomly distributed PA signal of melanosomes in epidermis
PA images of the real and the mimicked skins, showing that the melanosomes were randomly distributed, and PA signal peaks were found where the melanosomes were crowded and/or clustered.

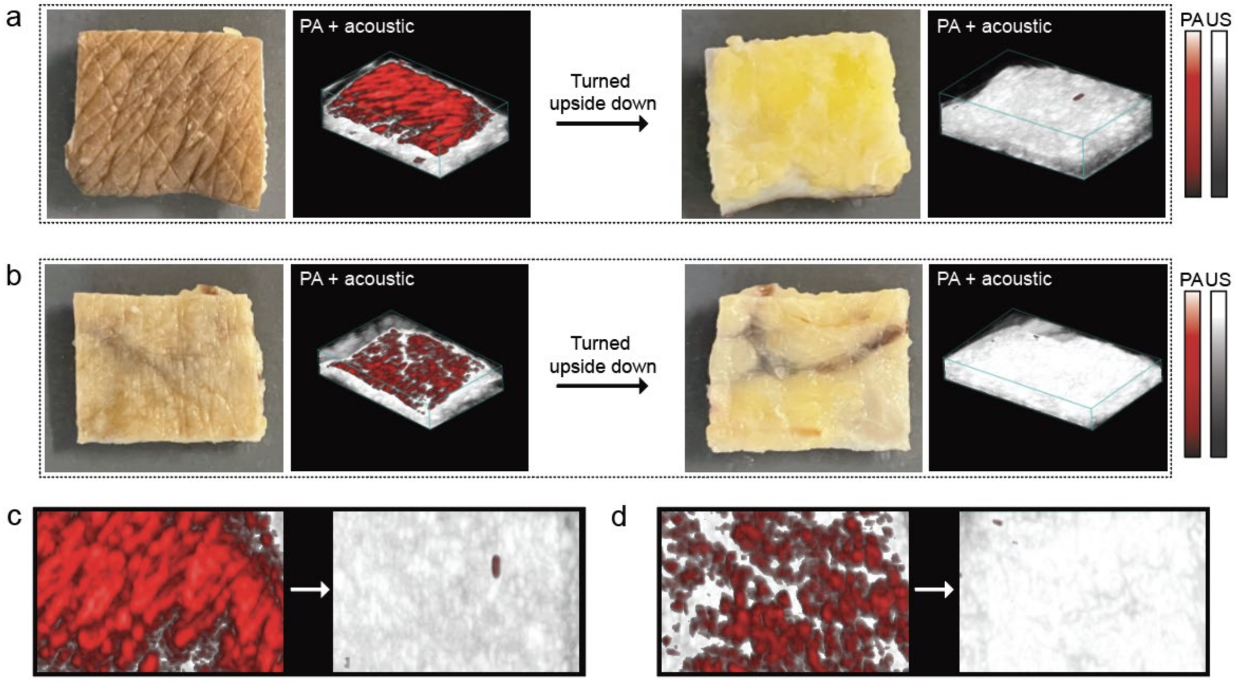

Figure 4.24 Light scattering in the dermis
Photograph and PA image (diagonal view) of Fitz. 2 (a) and Fitz. 5 (b) human skin before and after the specimens turned upside down. PA signal of the epidermis was largely attenuated due to the tissue scattering occurred in the dermis. The PA images (front view) of the epidermis of Fitz. 2 (c) and Fitz. 5 (d) human skin before and after the specimens turned upside down.

4.4.4. Impact of skin phototype on biomedical optic modalities

3D-bioprinted phantoms with skin phototypes from Fitz. 1 to 6 were successfully developed by adjusting the PDA contents used for bio-inks: Fitz. 1, Fitz. 3, and Fitz. 5 contained a M_f of 3%, 12%, and 20%, respectively (Figure 4.25). The phantom without skin prototype was also fabricated as a negative control (referred to as Fitz. 0). Both the CIE color space and a colorimeter were used to quantify our phantoms with different skin phototypes (Figure 4.26 and Table 4.1). Titanium oxide (TiO_2) was also used to mimic tissue scattering in the dermis.[208] We then measured the energy attenuation from 680, 800, and 1064 nm laser beams caused by the mimicked skin phototypes (Figure 4.27a). The results showed that darker skin attenuated more laser energy (mJ) than lighter skin: Fitz. 1, 3, and 5 skin phantoms decreased 1, 3, and 6 mJ energy at 680 nm which is relevant to the absorption peak of deoxyhemoglobin (660 nm).[183] Moreover, the 680-nm laser attenuated 1.3- and 1.98-fold more energy than 800 nm and 1064 nm lasers, respectively, because of higher light absorption and scattering of synthetic melanin. To further evaluate this, the absorption coefficient (μ_a) and the reduced scattering coefficient (μ_s') of skin-tone phantoms (Fitz. 1, 3, and 5) were characterized using the inverse adding double (IAD) manual based on reflectance and transmittance measurements of samples in an integrating sphere spectrophotometer (Figure 4.27b). Both the μ_a and μ_s' of mimicked skin phototypes exponentially increased from 400–600 nm and linearly in the 600–900 nm region: The μ_a of Fitz. 5 at 680 nm was 1.37-fold higher than that at 800 nm. More importantly, μ_a ($1.03\ \mathrm{mm}^{-1}$) and μ_s' ($4.33\ \mathrm{mm}^{-1}$) values of our mimicked skins were comparable to that of real human skins (μ_a ($0.72 \pm 0.29\ \mathrm{mm}^{-1}$) and μ_s' ($4.89 \pm 1.15\ \mathrm{mm}^{-1}$) at 692 nm) (see Table 4.2).[175, 209] The μ_a and μ_s' of 3D-bioprinted phantoms were tunable by controlling the particle ratio between PDA_{300} and PDA_{120} in the epidermis. For example, the μ_a of the Fitz. 1 skin phantom with 100% of PDA_{300} showed a 1.1-fold higher than that of Fitz. 1 skin phantom with 100% PDA_{120}.

We next used these mimicked skin-tone phantoms to study the impact of skin phototypes on biomedical optics technology including PA imaging, fluorescence imaging, and photothermal therapy. For PA imaging, methylene blue (MB) and indocyanine green (ICG) dyes were chosen as contrast agents to demonstrate the utility of the phantom at 680 nm and 800 nm, respectively. Here, MB and ICG dyes (100 µM to 25 mM) were linearly aligned in the tubes and imaged under the Fitz. 1, 3, and 5 skin phantoms (Figure 4.27c and Figure 4.28). The PA signal and spectra of the ICG dye was less compromised by skin phototypes *versus* MB dye (Figure 4.29–4.30). Specifically, MB dye showed 14%, 55%, and 65% PA signal attenuation with Fitz. 1, 3, and 5 skin. ICG showed a 10%, 37%, and 55% decrease in PA signal at the same dye concentration (Figure 4.27d). Samples in the yellow dotted area in Figure 5c were intentionally uncovered to show that there was no decrease in laser power or/and photobleaching of the dye during the measurement. We further studied the imaging depth of MB and ICG dye with the phantoms. The 5-mm-thick GelMA phantom including TiO_2 (0.5 mg/ml) was 3D-printed, and each sample was injected at heights 1 mm apart (Figure 4.27e and Figure 4.31). The Fitz. 5 skin phantom has PA signal of MB dye that was attenuated by 44%, 97%, and 100% at depths of 1, 2, and 3 mm, respectively. The PA signal of the ICG dye was decreased by 43%, 63%, and 85% of PA signals at the same depths (Figure 4.27f). These results indicated that ICG dye had higher imaging depth due to its longer absorption wavelength (800 nm). In this region, melanin has lower light absorption and scattering. We further designed a blood vessel scaffold to measure the PA signal of real human blood under different skin phototypes to investigate the impact of imaging deoxyhemoglobin (Figure 4.32). PA images showed that 33%, 52%, and 70% of PA signals decreased under the Fitz. 1, 3, and 5 skin phantoms. There was a yellow dotted area that remained uncovered. This showed no decrease in laser power or sample degradation (Figure 4.27g).

Fluorescence could also be affected by melanin. Thus, cyanine5.5 (Cy5.5) and ICG dyes at the same dye concentration (100 µM) were used to evaluate the impact of skin phototypes on their corresponding excitation (i.e., 680 and 800 nm, respectively). Not surprisingly, Cy5.5 signal decreased by 32% and 69% under the Fitz. 3 and 5 phantoms, respectively; the ICG dye only decreased by 6% and 53%, thus confirming the wavelength-dependent fluorescence attenuation (Figure 4.27h). Photothermal therapy also often uses near-infrared (NIR) light. Here, gold nanorods (GNRs) with two different aspect ratios (*e.g.,* 3.3 and 7.3) were synthesized and had a longitudinal absorption peak at 800 nm and 1062 nm, respectively (Figure 4.33). Two different NIR lasers (i.e., 808 and 1064 nm) were used to irradiate GNRs at an O.D. (= 1) underneath different skin phantoms. A thermal camera was used to record the temperature (Figure 2.7i). The results revealed that the temperature increase facilitated by the GNRs decreased as a function of phototype: Fitz. 1 (8%), Fitz. 3 (14%), and Fitz. 5 (17%) *versus* Fitz. 0 when irradiated by the 808 nm laser. GNRs irradiated by 1064 nm exhibited relatively minor decreases in temperature: Fitz. 1 (4%), Fitz. 3 (7%), and Fitz. 5 (8%). The 1064 nm (NIR-II) laser was significantly less influenced by skin phototypes.

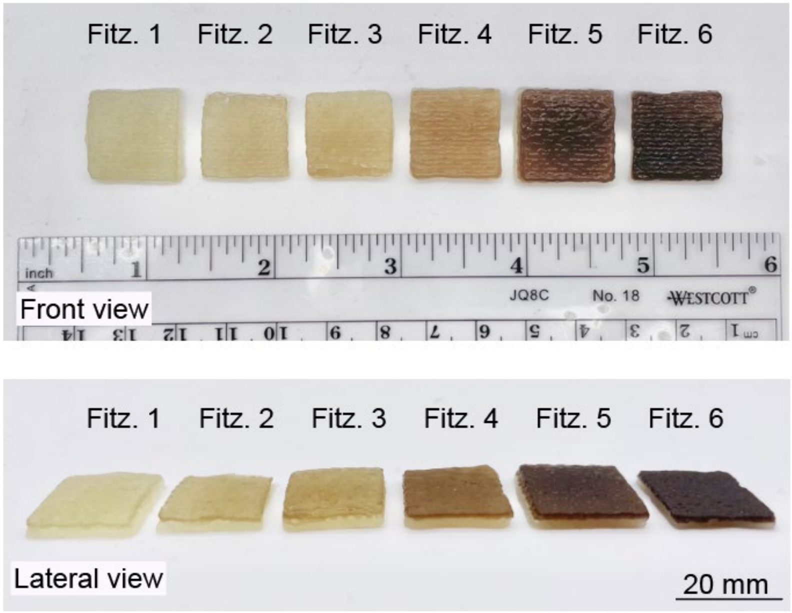

Figure 4.25 Photograph of mimicked skin phototypes
Taking advantage of 3D bioprinting, mimicked skin phototypes ranging from Fitz. 1 to Fitz 6 were developed. L (luminance), and b (yellow/blue component) values were measured and shown in Supplementary Table S1.

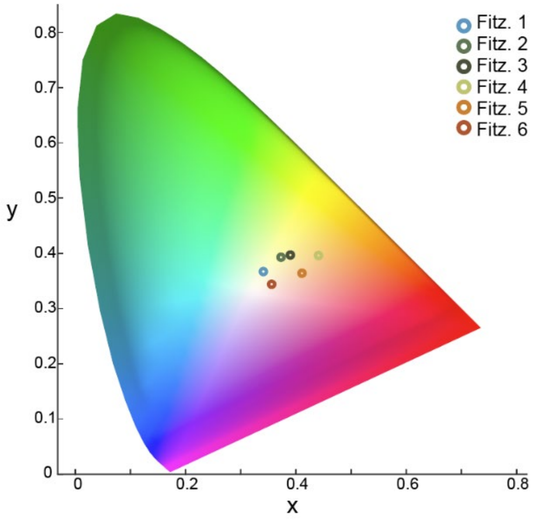

Figure 4.26 CIE coordinates of mimicked skin-tone phantoms
Fitz. 1 (0.341, 0.367), Fitz. 2 (0.373, 0.394), Fitz. 3 (0.390, 0.397), Fitz. 4 (0.441, 0.396), Fitz. 5 (0.411, 0.364), and Fitz. 6 (0.356, 0.344).

Figure 4.27 Impact of skin phototypes on biomedical optics

a, Decreased energy of 680 nm, 800 nm, and 1064 nm lasers due to light absorption by mimicked skin phototypes. The error bars represent the standard deviation of three individual samples. Photograph shows 3D-bioprinted skin phantoms with different skin phototypes (from Fitz. 1 to 6). b, μ_a and μ_s' (solid lines) values of Fitz. 1, 3, and 5 skin phantoms. The dotted lines represent the tunable range of μ_a and μ_s' by adjusting PDA content in the epidermis. c, PA image of MB dye covered by Fitz. 1, 3, and 5 skin phantoms. Yellow dotted area remained uncovered showing no decrease in the laser power. d, PA signal attenuation of MB and ICG dyes by Fitz. 1, 3, and 5 skin phantoms. The error bars represent the standard deviation of six regions of interests. e, PA image of MB dye in a 5-mm-thick phantom covered by Fitz. 1, 3, and 5 skin phantoms. f, PA signal attenuation of MB and ICG dyes at different imaging depths from 1 to 5 mm. MB and ICG dyes (10 mM) were covered by Fitz. 1, 3, and 5 skin phantoms. The error bars represent the standard deviation of six regions of interest. g, PA signal attenuation of real human blood. Human blood in the blood vessel scaffold was covered by Fitz. 1, 3, and 5 skin phantoms. Yellow-dotted area remained uncovered as a negative control. The error bar represents the standard deviation of six regions of interest. h, Fluorescence attenuation of Cy5.5 and ICG dye by mimicked skin phototypes. Insert images show that Cy5.5 and ICG dyes were covered by phantoms with different skin phototypes from Fitz. 2 (left) to the Fitz. 5 (right). i, Impact of skin phototypes on photothermal therapy. NIR-I (808 nm) and NIR-II (1064 nm) lasers were used for the test. Fitz. 0 indicates the phantom without synthetic melanin. The experiments in a, d, f, g, h, and i were repeated independently three times with similar results.

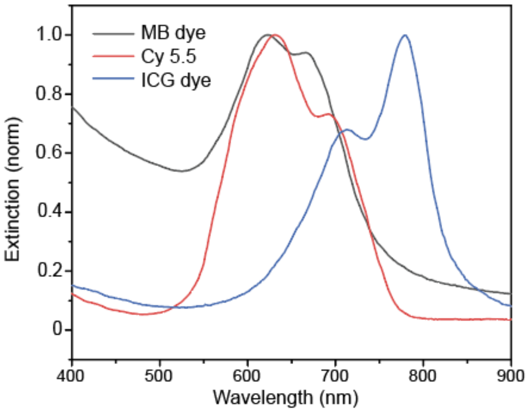

Figure 4.28 Optical spectra of MB, ICG, and Cy 5.5

MB, ICG, and Cy 5.5 dyes were used to test PA imaging and fluorescence imaging showing wavelength-dependent skin tone impact. MB and Cy 5.5 have similar absorption peaks around 680 nm while the ICG dye has an absorption peak at 800 nm.

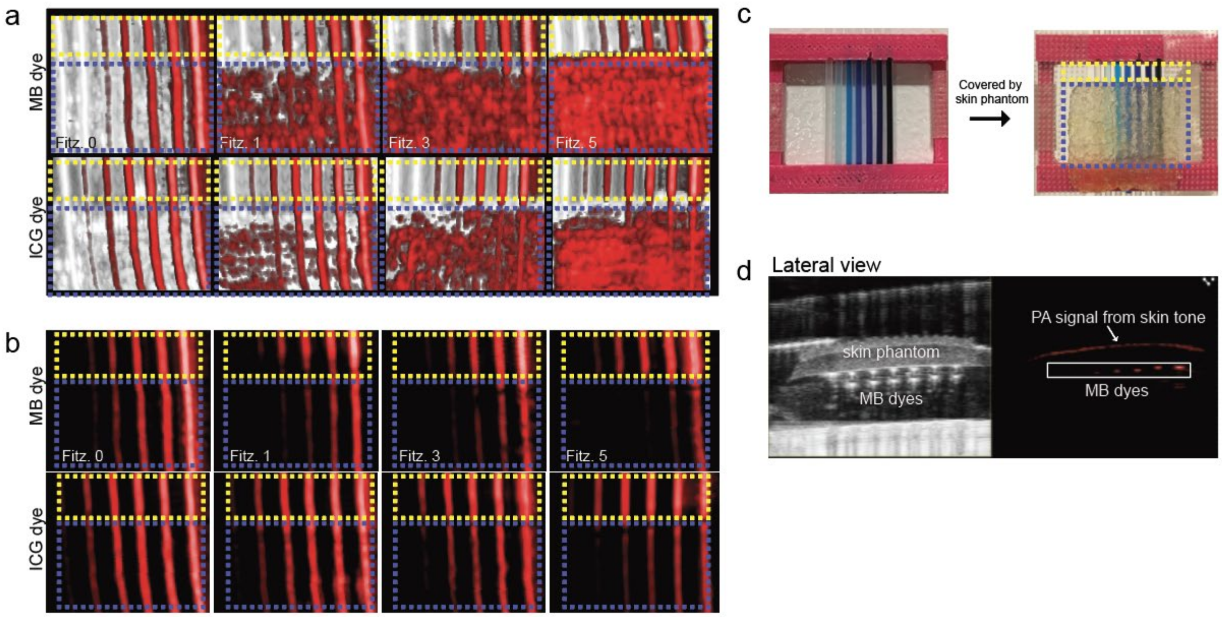

Figure 4.29 Skin tone impacts on PA imaging
a, PA image and photographs (c) in the front view when MB and ICG dyes in the tubes were covered by Fitz. 1, 3, and 5 skin phototypes. Fitz. 0 indicates the printed sample without melanin (negative control). b, PA image showed that PA signal of MB and ICG dyes attenuated under the skin phototypes. Yellow and blue dotted area means covered/uncovered area by the mimicked skin phototypes. Yellow dotted area remained uncovered on purpose to show that there was no decrease in laser power or sample degradation (*e.g.,* photobleaching). c, Photograph of sample measurement. MB dyes were injected into the polyethylene tubes and fixed within a 3D-printed holder (pink). Then, the skin phantom was placed on the polyethylene tubes for PA measurement. The air bubbles were removed using a pipette before the PA measurement. d, US/PA image of MB dyes covered by Fitz. 1 skin phototype in lateral.

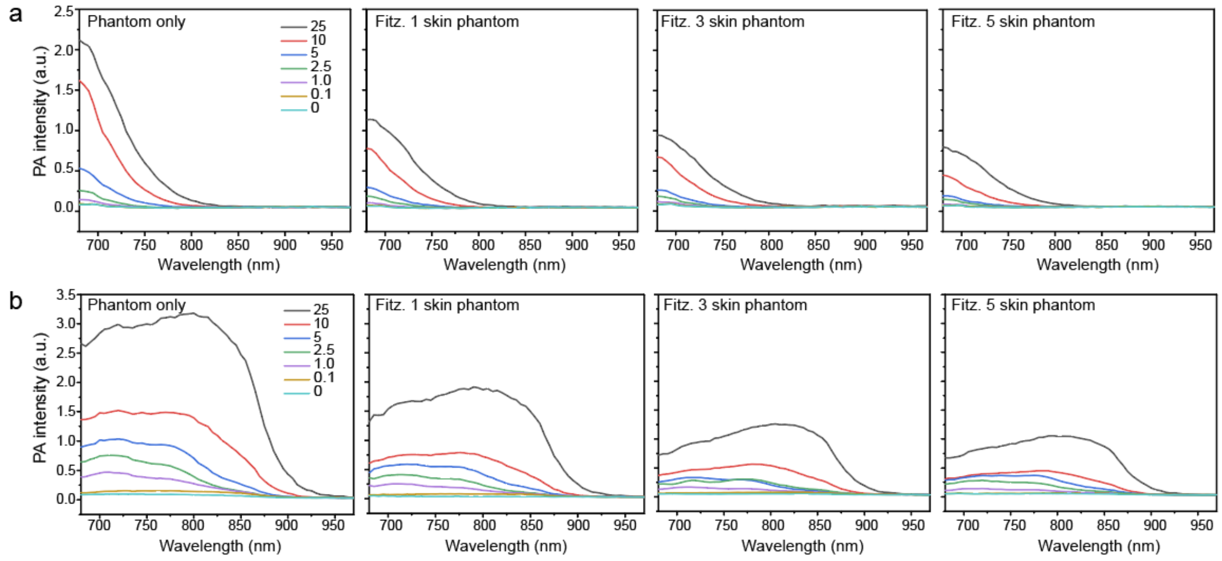

Figure 4.30 PA spectrum of the MB and ICG dyes under the mimicked skin phototypes
PA spectra of MB (a) and ICG (b) dyes under mimicked Fitz. 1, 3, and 5 skin phototypes. Different dye concentrations (*e.g.,* 0.1, 1, 2.5, 5, 10, 25 mM) were used to measure the PA spectrum from 680 to 970 nm.

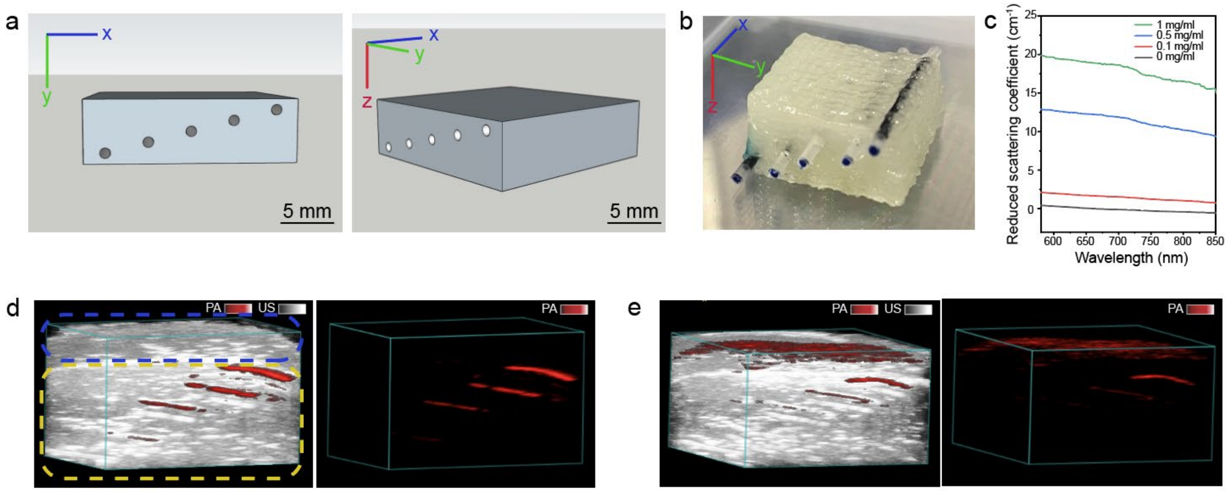

Figure 4.31 Imaging depths under mimicked skin phototypes
a, A 3D design of 5 mm thick phantom: there were five holes where each sample was injected. b, Photograph of the printed phantom using a 3D-bioprinter. MB dyes with the concentration of 10 mM were injected at heights of 1 mm apart. TiO_2 (0.5 mg/ml) was used to induce light scattering. c, Reduced scattering coefficients (μ_s') of TiO_2 at different mass concentrations: 0, 0.2, 0.5, and 1 mg/ml. The measured μ_s' values were comparable to our previous phantom study.[208] PA and US images of 5 mm thick phantom under (d) Fitz. 0 (no color) and (e) Fitz. 3 skin phototypes. The skin prototypes were attached on the top of the printed 5 mm phantom shown in (b). Blue dotted area indicates mimicked skin phototypes and yellow dotted area indicates 5 mm thick phantom.

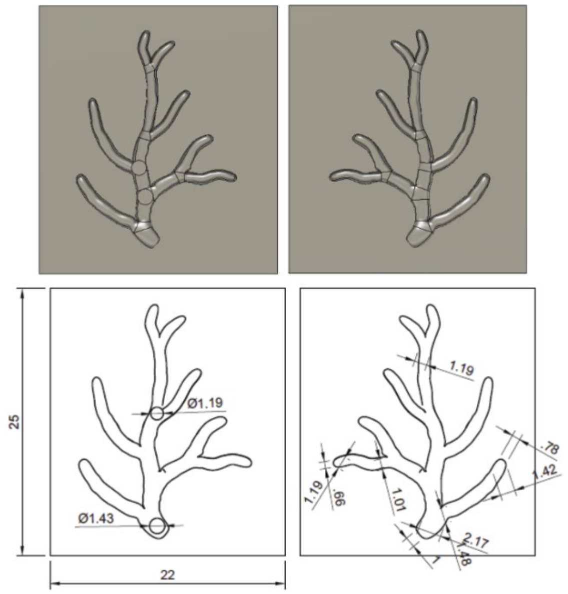

Figure 4.32 Blood vessel scaffold
Human blood vessel was scanned using a CT and MRI scanning, and the scanned images were on the NIH 3D print exchange (open source). We used a Fusion 360 software to adjust dimensions and printed a PDMS mold with the shape of blood vessel using a 3D printer.

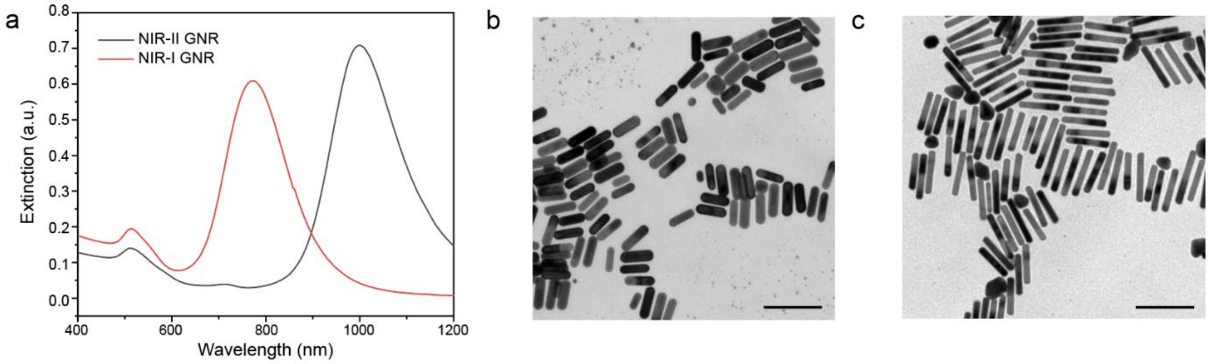

Figure 4.33 808 and 1064 nm gold nanorods
GNRs with an aspect ratio of 7.3 ± 0.6 and 3.3 ± 0.2 were synthesized using a seed-mediated method. a, UV-vis-NIR spectra showed that GNRs had longitudinal peak at 800 (NIR-I) and 1064 nm (NIR-II), respectively. TEM image of NIR-I GNR (b) and NIR-II GNR (c). The scale bars represent 100 nm.

Table 4.1 L, a, b (LAB) color values of the mimicked skin phototypes

	Fitz. 1	Fitz. 2	Fitz. 3	Fitz. 4	Fitz. 5	Fitz. 6
L	60.21	45.64	43.75	39.49	30.59	26.21
a	-0.1	1.87	6.19	4.87	4.07	2.49
b	8.97	8.83	15.83	12.47	12.63	21.08

Table 4.2 Absorption coefficient (μ_a) and reduced scattering coefficient (μ_s') of real and mimicked skin.

The μ_a and μ_s' values of real human skin (i.e., Asian) were obtained from the recent study (15 individual epidermis samples).[209] Both studies used an integrating sphere spectrophotometer with IAD method to calibrate absorption and reduced scattering coefficients.

Wavelength (nm)	Epidermis (real)		Epidermis (mimicked)	
	μ_a (mm^{-1})	μ_s' (mm^{-1})	μ_a (mm^{-1})	μ_s' (mm^{-1})
405	3.32 ± 1.51	9.95 ± 2.02	2.50 ± 0.25	5.12 ± 0.16
532	1.44 ± 0.69	7.04 ± 1.48	1.42 ± 0.13	4.49 ± 0.14
595	0.94 ± 0.53	6.02 ± 1.33	1.23 ± 0.11	4.44 ± 0.14
632	0.94 ± 0.41	5.55 ± 1.25	1.16 ± 0.10	4.37 ± 0.13
694	0.72 ± 0.29	4.89 ± 1.15	1.03 ± 0.10	4.34 ± 0.13
755	0.49 ± 0.19	4.28 ± 1.04	0.89 ± 0.09	4.19 ± 0.13
800	0.39 ± 0.15	3.98 ± 1.00	0.80 ± 0.08	3.98 ± 0.12

4.5. Conclusions

Phantom-based testing is a powerful approach to evaluate the performance of various imaging devices and judge quality of medical imaging without risks to human. Skin-mimicking phantoms have been developed for optical diagnostic modalities.[183, 210-213] One phantom used gelatin and synthetic melanin to make 0.1 mm-thick epidermal layer and characterized tunable mechanical, optical and acoustic properties.[210] However, this hydrogel-based phantom is limited to control the thickness of each layer and needs vacuum sealed container for storage. In other study, polydimethylsiloxane (PDMS) silicone and ground coffee were used to make tissue-mimicking phantom.[213] Although PDMS-based phantom provides high stability and simplicity, ground coffee is limited to mimic optical absorption of real human skin. To improve this, one recent study used synthetic melanin with PDMS and showed high stability with comparable absorption values to real human skin.[183] However, synthetic melanin used for those phantoms is a form of solid power which lacks of bio-relevant size or shape to real melanosomes. All those phantoms barely focused on different concentrations to achieve different skin pigmentation levels.

Here we developed 3D-bioprinted phantoms with synthetic melanin (i.e., PDA) as a tool to study the impact of skin phototypes on biomedical optics. We characterized the optical properties of spherical PDA in different sizes, mixtures, and clustering phases. These assemblies are biologically relevant to the variable melanosome contents in real human skin. 3D bioprinting provides high scalability, good controllability (thickness: 0.1–50 mm), and low cost compared to mold-based phantom fabrications. We used 3D bioprinting for custom phantom designs for testing various forms (*e.g.,* imaging depths or curved shapes) of medical imaging devices. GelMA-based scaffolds could serve as extracellular matrix for cell growth,[214] providing more opportunities for deciphering the role of melanosomes in tissue engineering for the future study.[215] Finally, our skin-tone mimicking phantom could benefit other biomedical optics techniques (*e.g.,* OCT, cerebral oximeter, wearable electronics).[216] Our skin phantoms are enabled by 3D bioprinting and will boost the development of biomedical optics and possibly motivate more phantom studies to correct for race-based bias in biomedical optics.

4.6. Acknowledgement

The authors wish to thank the individuals who donated their bodies and tissues for the advancement of education and research. This work was supported by National Science Foundation (#1937674 and #2149602) and National Institutes of Health (T32AR064194, and R03DE031009). This work was performed in part at San Diego Nanotechnology Infrastructure (SDNI) of University of California San Diego supported by (NSF ECCS-1542148), and by the Cellular and Molecular Medicine Electron Microscopy core facility (NIH S10 OD 023527). This work was also supported by National Science Foundation (DMR-2011924) through the UC San Diego Materials Research Science and Engineering Center (UCSD MRSEC). The authors also thanks Sunwoo Kwak for technical support for artwork, and Dr. Lingyan Shi, and Dr. Ali Hariri for helpful discussions.

Chapter 4, in part, is a reprint of the material as it appears in “3D-bioprinted phantom with human skin phototypes for biomedical optics” by Yim, Wonjun; Zhou, Jiajing; Sasi, Lekshmi; Zhao, Jiayu; Yeung, Justin; Cheng, Yong; Jin, Zhicheng; Johnson, Wade; Xu, Ming; Chavez, Jorge Palma; Fu, Lei; Qi, Baiyan; Retout, Maurice; Shah, Nisarg J.; Bae, Jinhye; Jokerst, Jesse V., Advanced Materials 2022. The dissertation author was the primary investigator and author of this paper.

CHAPTER 5. A goldilocks energy minimum: peptide-based reversible aggregation and biosensing

5.1. Abstract

Colorimetric biosensors based on gold nanoparticle (AuNP) aggregation are often challenged by matrix interference in biofluids, poor specificity, and limited utility with clinical samples. Here, we propose a peptide-driven nanoscale disassembly approach, where AuNP aggregates induced by electrostatic attractions are dissociated in response to proteolytic cleavage. Initially, citrate-coated AuNPs were assembled *via* a short cationic peptide (RRK) and characterized by experiments and simulations. The dissociation peptides were then used to reversibly dissociate the AuNP aggregates as a function of target protease detection, *i.e.,* main protease (M^{pro}), a biomarker for SARS-CoV-2. The dissociation propensity depends on peptide length, hydrophilicity, charge, and ligand architecture. Finally, our dissociation strategy provides a rapid and distinct optical signal through M^{pro} cleavage with a detection limit of 12.3 nM in saliva. Our dissociation peptide effectively dissociates plasmonic assemblies in diverse matrices including 100% human saliva, urine, plasma, and seawater, as well as other types of plasmonic nanoparticles such as silver. Our peptide-enabled dissociation platform provides a simple, matrix-insensitive, and versatile method for protease sensing.

5.2. Introduction

Colorimetric biosensor using gold nanoparticles (AuNPs) is a popular tool for *in vitro* Colorimetric biosensors using gold nanoparticles (AuNPs) are a popular tool for *in vitro* detection of various disease biomarkers (*e.g.,* proteins, enzymes, nucleic acids, and metal ions).[217-220] Colorimetry is easy, simple, affordable, and does not require a skilled operator.[221] A simple spectrophotometer and/or naked eye can be used for detection, and a relatively small amount of AuNPs can provide sufficient visible color changes due to their high molar absorption coefficients.[222]

Most research on this topic has focused on *aggregation*-based color changes facilitated by electric dipole-dipole interactions between proximal AuNPs leading to plasmonic coupling and a bathochromic shift (red to blue color shift).[223] This aggregation is governed by DLVO theory.[224] This theory suggests that AuNPs remain colloidally stable because the attractive Van der Waals (VdW) forces are balanced by the repulsive steric forces and electrostatic forces. When used for sensors, hydrogen bonding[225], DNA pairings[217, 220], antibody-antigen,[226] electrostatic[222], and hydrophobic[218] interactions can change the electrostatic repulsion, steric repulsion, or VdW attraction to induce such aggregation and thus a color change. This aggregation is nearly always irreversible because the VdW forces scale to the sixth power of separation distance. Thus, the VdW forces become insurmountably large, and the particles fall into an energy well—they are permanently aggregated.

Sensors based on this mechanism often have poor specificity and limited utility with clinical samples for several reasons. First, citrate-stabilized AuNPs are very sensitive to pH, solvent polarity, and ionic strength—all of these can cause undesired aggregation and thus require surface modifications of the particles (*e.g.,* PEGylation, BSPP).[227, 228] Second, biofluids such as plasma, serum, saliva, sweat, or urine can lead to a protein corona, thus changing the surface charge and preventing electrostatic-based plasmonic coupling.[229] Third, AuNP colloidal stability is notoriously dependent on ionic strength—physiological salt concentrations can lead to charge screening of the electrostatic repulsions thus allowing attractive VdW to predominate. Although a few studies have reported aggregation-based colorimetric assays in biofluids, they often require sample dilution or removal of the analyte from the matrix.[222, 230, 231] Finally, AuNP aggregation can amplify eventually leading to aggregates larger than 1 μm that lose colloidal stability and become colorless.[219]

To address these issues, we recently proposed colorimetric assays based on *dissociation*.[230] Here, particle aggregation was first triggered by a short cationic peptide containing arginine and lysine that induced plasmonic coupling of anionic AuNPs coated with citrate. Most importantly, this aggregation was *reversible* upon addition of steric stabilizers such as thiol-PEG molecules (HS-PEGs).[46] We then made a PEG-peptide conjugate containing a cleavage sequence specific to trypsin.[230] The first value of this approach was a remarkable insensitivity to the matrix—dispersion could even be done in seawater and bile. Second, the aggregated AuNPs were stable for months and could even be dried to completeness but could still be redissolved and used to detect proteases.

The work reported here satisfied three goals inspired by this prior work. First, we used computational methods to better understand the mechanism of this reversible aggregation. We hypothesized that the short cationic peptide has a steric bulk that maintains some separation distance between the AuNPs thus preventing runaway attractive VdW attraction. Second, we used an all-peptide strategy that is simpler and requires no PEG-peptide couplings. We demonstrated that charge, hydrophilicity, peptide length, and ligand architecture can impact on the dissociation efficiency. Finally, we construct a practical sensor that is made of the optimized dissociation domain with a biomolecular recognition element of SARS-CoV-2 main protease *i.e.,* M^{pro}.[232, 233]

After protease cleavage, released peptides successfully provided a rapid color readout of M^{pro} with a detection limit (LoD) of 12.3 nM in saliva. Furthermore, our dissociation peptide can dissociate AuNP aggregates in various matrixes including 100% human urine, plasma, and seawater, and can be applied to other types of plasmonic nanoparticles (*e.g.,* silver).

5.3. Materials and method

5.3.1. Preparation of AuNPs and AuNP aggregates

Briefly, a dried peptide powder was dissolved in phosphate buffer (20 mM, pH 8.0) and incubated with the M^{pro} at a molar ratio of 3000:1 (substrate: enzyme ratio) for 0.5h at 37 ºC. To confirm the M^{pro} cleavage site, the sample was purified using a C18 column (5 µm, 9.4×250 mm) and eluted with a flow rate of 3 mL/min over 30 min with a linear gradient from 10% to 95% to ACN in H_2O. After the purification, the molecular weight of a fragment peptide was confirmed by using ESI-MS (positive or negative mode) or/and matrix (e.g., HCCA) assisted laser desorption ionization time of flight mass spectrometry (MALDI-TOF MS, Bruker Autoflex Max) in the Molecular Mass Spectrometry Facility at UC San Diego.

To test particle dissociation in saliva and EBC condition, the desired amounts (conc, 30 µM) of the dissociation peptides (A18, Ace-CGGKKEEAVLQSGFR-Am) were incubated with M^{pro} in the 100% of saliva or EBC for 0.5h at 37 ºC. Then, the 40 µL of A18 fragment peptides in saliva or EBC were mixed with 100 µL of AuNP aggregates for colorimetric sensing. The mass peaks of the A18 peptide and fragment were also confirmed by MALDI-TOF MS examination.

5.3.2. Dissociation of AuNP aggregates using proteolysis of peptides

Briefly, a dried peptide powder was dissolved in phosphate buffer (20 mM, pH 8.0) and incubated with the M^{pro} at a molar ratio of 3000:1 (substrate: enzyme ratio) for 0.5h at 37 ºC. To confirm the M^{pro} cleavage site, the sample was purified using a C18 column (5 μm, 9.4×250 mm) and eluted with a flow rate of 3 mL/min over 30 min with a linear gradient from 10% to 95% to ACN in H_2O. After the purification, the molecular weight of a fragment peptide was confirmed by using ESI-MS (positive or negative mode) or/and matrix (e.g., HCCA) assisted laser desorption ionization time of flight mass spectrometry (MALDI-TOF MS, Bruker Autoflex Max) in the Molecular Mass Spectrometry Facility at UC San Diego.

To test particle dissociation in saliva and EBC condition, the desired amounts (conc, 30 μM) of the dissociation peptides (A18, Ace-CGGKKEEAVLQSGFR-Am) were incubated with M^{pro} in the 100% of saliva or EBC for 0.5h at 37 ºC. Then, the 40 μL of A18 fragment peptides in saliva or EBC were mixed with 100 μL of AuNP aggregates for colorimetric sensing. The mass peaks of the A18 peptide and fragment were also confirmed by MALDI-TOF MS examination.

5.3.3. Dissociation of AuNP aggregates using proteolysis of peptides

Briefly, RRK peptides (8–10 μM) was first used to trigger AuNP aggregation in distilled water. The sample was centrifuged at 1 g for 5 min to remove the supernatant. Then, the pellet was re-dispersed in 100% human saliva, plasma, urine, and seawater. After re-dispersion, the desired amounts of dissociation peptide were used to dissociate AuNPs aggregates in different matrixes. Both A11 and A12 peptides successfully dissociated the aggregated AuNPs in diverse matrixes. The experiment was performed with three replicates, and the microplate reader was used to measure spectral scanning from 300 to 900 nm before and after dissociation. The ratiometric signal ($\lambda_{520}/\lambda_{700}$) was referred as dissociation. The data was blanked to remove background signal.

5.3.4. Peptide synthesis

Peptides were synthesized based on Fmoc-SPPS (solid-phase peptide synthesis) on Rink-amide-MBHA-resin (0.55 mmol/g, 200 mg) using an automated Eclipse^{TM} peptide synthesizer (AAPPTec, Louisville, KY). Amino acids were coupled under the protection of the nitrogen with 0.2 M Fmoc-amino acid (5 *equiv*) in 3 mL DMF, 0.2 M HBTU (5 *equiv*) in 3 mL DMF, 0.4 M DIPEA (7.5 *equiv*) in 3 mL DMF, and 20% (v/v) piperidine in 2 x 4 mL DMF for each cycle of synthesis. The number of synthesis cycles are based on the sequence analysis tool established in the software tool (AAPPTec). The resulting peptides on the resin were transferred to the syringe filter (Torviq Inc), washed with two times of DMF (4 mL each) and four times of DCM (4 mL each), and dried under the vacuum condition (> 1h). N-terminal of the peptides was acetylated using the solution that contains 4 mL of DMF, 0.5 mL of Pyridine, and 0.5 mL of acetic anhydride. After then, the resulting product was washed with three times of DMF (3 mL) and three times of DCM (5 mL), and was vacuumed again to dry the sample. Lastly, the crude peptides were cleaved from the resins using a cocktail solution (5 mL) that includes 5 mL of TFA (83%), 300 µL of H_2O (5%), 300 µL of thioanisole (5%), 300 mg of phenol (5%), and 150 µL of EDDET (2%). The resins were incubated with the cocktail solution and rotated for 2 h. After the cleavage, the resin was filtered and the filtrate containing the crude peptides was precipitated using cold ethyl ether (10 mL, –20 ºC) and centrifuged three times (7,500 rpm, 2 minutes) to remove supernatants. The precipitated pellets were dried and re-suspended using 10 mL of ACN/H_2O mixtures (the percentage of ACN was controlled based on the solubility of the pellet (20–40% of CAN)). The peptides were purified by the reversed phase HPLC (Shimadzu LC-40), confirmed by the ESI-MS, and stored in the dry conditions at –20 ºC for future use.

The crude peptides were purified using a Shimadzu LC-40 HPLC system established with a LC-40D solvent delivery module, photodiode array detector SPD-M40, and degassing unit DGU-403. 2 L of ACN (or H_2O) solution containing 0.05% TFA (HPLC grade) was prepared and degassed for the HPLC purification. 2 mL of the crude peptides dissolved in ACN/H_2O mixtures (10 mL, 20% of ACN and 80% of H_2O) was injected for each cycle. C4 column (5 μm, 20×200 mm) from SHMADZU was used for the purification and eluted with a flow rate of 5 mL/min over a 30 min with a linear gradient from 10% to 95% of ACN in H_2O. The injection was monitored at 220 and 300 nm to collect the samples. The fractions which contained the target peptide confirmed by ESI-MS or/and MALDI were frozen at –80 ºC for 3 h, lyophilized, and aliquoted for future use. All the purified peptide reached a purity of at least 90%. FreezeZone Plus 2.5 freeze dry system was used for the lyophilization.

The concentration of each peptide was calibrated using a NanoDrop^{TM} One UV-vis-spectrometer (Thermo Fisher Scientific, Waltham, MA). The 31-method adapted in Nanodrop^{TM} was used to calibrate the concentration of the peptides except tryptophan and tyrosine residues. The absorption of coefficient of ε_{205} (about 75 $mL \cdot mg^{-1} \cdot cm^{-1}$) was used for the calibration. Water or alcohol was used as a blank since DMSO and ACN solutions have absorption at 205 nm which could mis-calibrate concentrations. After concentration measurement, the purified peptides were dried using a vacufuge and stored them at –20 ºC for future use.

5.3.5. Limit of detection

The limit of detection (LoD) was calibrated using the limit of blank (LoB).[234] The LoB defines the highest signal generated from a sample that includes no analyte. LoB could be calculated using the mean ($\text{mean}_{\text{blank}}$) and standard deviation (SD_{blank}) of a blank sample following equation:

$$\text{LoB} = \text{mean}_{\text{blank}} + 1.645\ (\text{SD}_{\text{blank}})$$

The LoD defines the lowest analyte concentration that could be differentiated from the LoB. LoD is calculated based on the LoB and standard deviation of the lowest concentration sample ($\text{SD}_{\text{low concentration sample}}$). Here, the LoD represents an analyte concentration that 95% of measured samples are readily distinguished from the LoB while remaining 5% can contain no analyte.

$$\text{LoD} = \text{LoB} + 1.645\ (\text{SD}_{\text{low concentration sample}})$$

Here, we used the dissociation peptide (*e.g.,* A18) and M^{pro} enzyme to measure the LoD in different conditions (PB buffer: 20 mM, pH 8.5, saliva, and EBC). The fresh M^{pro} enzyme of the described amount was mixed with the parent peptide for 0.5h at 37 ºC. The, the assay was transferred to the 96-well plate and incubate with RRK-induced gold aggregates. At least three replicates of each experiment in saliva, EBC, and PB were performed in different day, respectively.

5.3.6. Inhibitor test

GC376 inhibitor was used for the M^{pro} inhibitor assay. Briefly, the desired amounts of GC376 were pre-incubated with M^{pro} (200 nM) to reach final ratios; 1:5, 1:2, 1:1, 2:1, 5:1, and 10:1 indicate the molar ratio of inhibitor to M^{pro}. After the pre-incubation at room temperature for 15 min, the parent A18 peptide (c_{final} = 50 μM) was added and incubated for another 0.5h at 37 ºC.

Then, the inhibitor assay was transferred into a 96-well plate and incubated with 100 μL of the RRK-induced gold aggregates for the inhibitor test. The absorbance of 520 nm and 700 nm were readout in the microplate reader at 37 ºC every 1 min for 1h. The ratiometric signal ($\lambda_{520/700}$) at 1h was used for data analysis. The experiment was performed with three replicates in different conditions (PB, saliva, and EBC) to measure the average and standard deviation.

5.3.7. Colloidal stability test

The colloidal stability was tested using sodium chloride. Briefly, the peptide capped AuNPs was incubated with NaCl (0.5 to 2M) for 1h at room temperature. After the incubation, the assay was transferred into a 96-well plate, and absorbance from 300 to 900 nm was readout with the step size of 2 nm. Aggregation parameter (AP) was defined as follows:[235] AP = $(A - A_o)/A_o$, where A_o and A are the absorbance difference between 530 to 600 nm at the initial and final conditions. Here, we used absorbance difference at 530 nm and 600 nm to calibrate AP values. At least two replicates of each experiment were measured. The dissociated AuNPs by the A18 fragment was incubated in 50% Dulbecco's modified eagle medium, human saliva, urine, plasma and NaCl, respectively and the size was measured by DLS to check particle dispersion for Figure 4l.

5.3.8. Dissociation strategy using AgNPs

Briefly, 100 μL of the RRK peptides (0.1 mM) were used to aggregate AgNPs, changing the color from yellow to blue in 10 s. The dissociation peptides (*i.e.,* A18, Ace-CGGKKEEAVLQSGFR-Am) were incubated with M^{pro} at 37 ºC for 1h. After the incubation, the fragment peptide with different concentrations (from 50 μM to 200 μM) were used to dissociate AgNP aggregates. The ratiometric signal ($\lambda_{520/700}$) was readout in the microplate reader every 1min for 1h.

5.3.9. Investigation of RRK interaction on a citrate coated AuNP using MD simulation

The forcefields applied in MD simulations were based on AMBER[236] forcefield (RRK, citrate, Na^+, Cl^-), TIP3P[237] forcefield (water), and EAM/Fs potential (Au) from Ackland et. al. [238]. The pair interactions were determined by general mixing rule except the RRK|Au and citrate|Au interactions, which were constructed based on the parameterization of QM interaction energies. In MD simulations, a long-range particle-particle particle-mesh solver, Van der Waals cutoff 10Å, timesteps 1.0 fs, and SHAKE algorithm [239] for water molecules and Hydrogen atoms were adopted.

To investigate the binding phenomenon for RRK molecules toward a citrate-coated AuNP system, we performed MD simulations using LAMMPS [240] engine. The initial structure contained a 5nm-diameter Au nanoparticle, 80 citrate molecules, 240 Na^+ ions, and 4670 water molecules. A MD simulation was initiated with 500 conjugated gradient steps, followed by the canonical ensemble (NVT) to heat up a system into 298K. Afterwards, the isobaric/isothermal ensemble (NPT) was proceeded to optimize systemic density at 298K/1atm and NVT ensemble was further applied to equilibrate a system. Based on the equilibrated citrate-coated Au nanoparticle structure, furthermore, we constructed a citrate|RRK Au nanoparticle system by randomly placing 80 RRK molecules and 240 Cl^- ions around the citrate-coated Au nanoparticle and embedding it into water solvents, thereby a structure with AuNP|80 citrate|240 Na|80 RRK|240 Cl|33622 water was constructed. With the same procedure as mentioned in this section, an equilibrated AuNP|80 citrate|240 Na|80 RRK|240 Cl^- |33622 water system was obtained, demonstrating the RRK binding phenomenon.

5.3.10. Determining free energies as a function of nanoparticle distance using steered molecular dynamics simulation

SMD simulations were performed to investigate free energy values as two Au nanoparticles approached to each other. In this study, we adopted the same forcefield parameters, long-range solver, cutoff point, and SHAKE algorithm as mentioned in MD simulation (SI-Section 6.2.11) section. There were two systems performed: a system without RRK^{+3} molecules and a system with RRK^{+3} molecules, where the first system contained two 5nm-diameter Au nanoparticles, 870 $citrate^{-3}$, 2160 Na^{+}, and 29238 water, and the second system contained two 5nm-diameter Au nanoparticles, 870 $citrate^{-3}$, 2160 Na^{+}, $95RRK^{+3}$, $285Cl^{-}$, and 45542 water. Each model was initially equilibrated using the same procedure as MD simulation and further performed a 3.7ns SMD simulation to investigate free energies as a function of Au nanoparticle distance. In a SMD simulation, we adopted a harmonic restraint with a force constant 100 kcal/mol.$Å^2$, where the equilibrium value of the harmonic restraint was gradually changed from 91 Å into 55 Å, and saved free energy values as two Au nanoparticles approached to each other, thereby the free energy values at different Au nanoparticle distance were determined.

5.3.11. Investigation of RRK/Au and citrate/Au interactions using quantum mechanics

To investigate the RRK|Au and citrate|Au interaction energies, we performed QM computations using Quantum Espresso (QE)[241, 242] package. For RRK, a relatively large molecule, we investigated RRK|Au interaction energy *via* computing the R^{+} group/K^{+} group binding on an Au(001). For citrate, we investigated citrate|Au interaction energy via computing the interaction of an entire citrate molecule on an Au(001). In addition, each model contained a corresponding number of Cl^{-}/H^{+} ions to ensure a charge neutral system. QM computations were performed with ultrasoft pseudopotentials, a cell box of (16.26, 12.195, 60) in (x,y,z), and a K-point grid (5,5,1). For each configuration, a molecule was initially placed near an Au(001) slab and gradually moved far away from an Au(001). Those QM energies were further applied in determining the Van der Waals parameters of RRK|Au and citrate|Au interactions for MD simulations.

5.3.12. Free energy investigation using Metadynamics approach

To explore the molecular behavior when a molecule approaches to an Au(111) surface, we constructed systems with periodic boundaries in x, y coordinates and a finite boundary in z coordinate, and explored free energy values using Metadynamics (MTD) approach.[243] Two systems were constructed: (1) a single citrate molecule on an Au(111) slab, representing as the procedure to form a citrate-coated Au surface, and (2) a single RRK molecule on a citrate-coated Au surface, representing as the procedure for adding RRK molecules into a citrate-coated Au system. The corresponding number of $Na^+(Cl^-)$ ions were added to form a charge neutral system and the system cell size was (57.48778 Å,49.78588 Å, 150 Å) in (x, y, z). Au(111) slab position was fixed at 19 Å /31 Å (bottom/top) and the slab-slab interactions were turned off via inserting empty volume in z with a factor 2.0.

Each system was initialized using 500 steps CG minimization and further heated up into 298K using Nose-Hoover thermostat (NVT ensemble). Afterwards, 1ns NVT ensemble was adopted to equilibrate a system. In Metadynamics section, 50 ns trajectory was proceeded, and the z coordinate was measured as the center of mass of the citrate molecule in (1) system and the center of mass of the RRK molecule in (2) system, where Gaussian functions with a weight of 1.0 kcal/mol and a width 1.25 Å were deposited every 0.2ps into each system. As the results (Figure S3), a weaker peak with a relatively far distance from an Au (111) surface was found in (2) system, implying a RRK molecule interacted with citrates and bound on a citrate-coated Au surface, which reduced the charge effect on Au surfaces and further resulted in the NP aggregation phenomenon.

5.3.13. General characterizations

Transmission electron microscopy (TEM) images were obtained using a JEOL JEM-1400 Plus operating at 80 kV in the Nano3 cleanroom UCSD. TEM images were taken using an installed Gatan 4k digital camera in the machine. 2 µL of each diluted sample was dropped on the carbon grids and dried overnight for the sample preparation. The hydrodynamic size and zeta potential (i.e., surface charge) were measured using dynamic light scattering (DLS) with a Malvern Instrument Zetasizer ZS 90. 70 µL and 800 µL of the diluted sample was used for the size and zeta potential measurements. MQ water was used for the dilution. Absorbance spectra were measuring using a BioTek Synergy H1 plate reader; 120 µL of each sample was measured in 96-well plates. Absorbance was collected from 400 to 800 nm with a step size of 2 nm. The sample absorption at the desired wavelength (*e.g.,* 520 and 700) was measured every 1 min for 1–3h. After injecting the samples into a 96-well plate, a film was attached on the plate to prevent solvent evaporation. The MQ water (or PB buffer) was used as a blank. Fourier transform infrared (FTIR) data was obtained using A Bruker Tensor II FTIR spectrophotometer. The samples were dried for overnight, and the dried sample was used for the measurement. Multi-laser nanoparticle tracking analysis (M-NTA) measurement was performed using a ViewSizer 3000 (Horiba Scientific, CA, USA) to measure particle concentrations and size information.[153] 10 videos (8-bit) were recorded with a 30 fps for 10 s (*i.e.,* 300 frames for seconds), and the recorded videos were used to calibrate particle size. A quartz cuvette with a minimum sample volume of 0.8 mL was used for the measurement. 10 µL of each sample was diluted in 5 mL of DI water. The quartz cuvette and stirring bar were cleaned with DI water to minimize the background noises. Peptide synthesis and cleavage was confirmed using electrospray ionization mass spectrometry (ESI-MS) *via* the Micromass Quattro Ultima mass spectrometer in the Molecular Mass facility (MMSF) at Chemistry and Biochemistry Department at UC San Diego. The sample for ESI-MS was prepared using 50% MeOH/H_2O mixtures. 2 µL of each sample was injected into the instrument three times independently to obtain ESI-MS data. Peptide cleavage was confirmed using matrix assisted laser absorption ionization time of flight mass spectrometry (MALDI-TOF MS, Bruker Autoflex Max) in the MMSF at UC San Diego. 2 µL of each sample was mixed with 6 µL of HCCA matrix. Then, the mixture was placed on the plate and dried using a heat gun. The measurement was performed with three replicates to confirm the peptide cleavage.

5.3.14. DLVO theory

The colloidal dispersion of AuNPs have been explained by DLVO theory where van der Waals (vdW) attraction is balanced by electrostatic repulsion, separating nanoparticles due to electric double layer (EDL). When breaking this balance by chemical bonding or ionic strength, Debye length (*i.e.,* electrostatic repulsive potential) decreases, leading to plasmon couplings (i.e., aggregation).[205]

$$U_{1-2}^{DLVO} = U_{1-2}^{vdW} + U_{1-2}^{EDL}$$

$$U_{1-2}^{vdW} = -\frac{A_H}{6}\left[\frac{8R_R^2}{h(R_R+h)} + \frac{8R_R^2}{(4R_R+h)} + ln\frac{h(8R_R+h)}{(4R_R+h)^2}\right]$$

$$U_{1-2}^{EDL} = 4\pi\varepsilon\varepsilon_0 R_R[\varphi_1\varphi_2\exp(-\kappa h) - \frac{1}{4}(\varphi_1{}^2 + \varphi_2{}^2\exp(-2\kappa h)]$$

$$\kappa^{-1} = \sqrt{\frac{\varepsilon\varepsilon_0 k_B T}{2N_A I e^2}}$$

where $U_{1\text{-}2}$ is the total interaction energy between AuNP #1 and AuNP #2 in water as a function of interaction distance (h). $U_{1\text{-}2}^{vdW}$ is the vdW interaction energy and $U_{1\text{-}2}^{EDL}$ is the electrostatic interaction energy. A_H is Hamaker constant (intrinsic property) of the two interacting AuNPs. R_R is reduced particle radius, e is a unit charge (1.602×10^{-19}), φ_1 and φ_2 are surface potentials (mV) of two interacting AuNPs. N_A is Avogadro's number (6.02×10^{23} mol^{-1}), ε is dielectric constant of water (78.5), ε_0 is dielectric permittivity of a vacuum (8.854×10^{-12} C/(V·M)) and I is the ionic strength. κ^{-1} is a Debye length (mm) which represent the thickness of EDL as a result of the ionic strength and electrolytes.[205]

In conclusion, EDL energy barriers between two AuNPs could decrease when RRK peptide was introduced, inducing particle aggregation. The particle dissociation could occur likely due to the increased steric repulsion, hydrophilicity, and recovered electrostatic repulsion.

5.4. Results and discussion

5.4.1. Short cationic peptides for reversible aggregation

To induce reversible aggregation of the AuNPs, we used positively charged Arg and Lys-based peptide residues (*i.e.,* RRK). The RRK peptide could induce plasmonic coupling by electrostatic attractions between negatively charged citrate molecules and guanidine and amine groups in RRK (Figure 5.1a).[224, 244] The size of AuNPs increased upon addition of RRK peptides, as confirmed by transmission electron microscopy (TEM) and dynamic light scattering (DLS) (Figure 5.1b and Figure 5.2). UV-vis spectroscopy showed that plasmonic resonance peak (520 nm) of AuNPs red-shifted to 648 nm; by eye the sample changed color from red to blue (Figure 5.1c). Raman spectroscopy observed the appearance of C–C stretching at 984 cm^{-1} and C–N stretching at 1443 cm^{-1} from Arg residues in RRK (Figure 5.1d).[245] Lastly, R, RRK, and RRKRRK peptides (from 0.5 to 30 µM) were used to induce AuNP aggregates to study the impact of charge number on particle aggregation. The results showed that RRKRRK and RRK peptides effectively induced particle aggregation whereas AuNPs did not aggregate with just one R even at 8-fold higher concentration than RRK (Figure 5.1e). A higher positive charge number can decrease the critical coagulation concentration (CCC).[223] RRK peptide was chosen in this study because particle aggregation induced by a strong cationic peptide (*i.e.,* RRKRRK) can result in irreversible aggregation.

To further study RRK-based plasmonic coupling, we adopted both quantum mechanics (QM) computation and molecular dynamics (MD) simulation. MD simulation revealed that the surface environment of AuNP changed as a function of RRK molecules interacting with citrate-coated AuNPs (Figure 5.3). Furthermore, we computed free energies before and after adding RRK peptides into the citrate coated AuNPs *via* steered molecular dynamics (SMD) simulation. Initially the citrate-coated AuNPs were favorably dispersed due to strong electrostatic repulsions. After adding enough RRK peptides, a free energy minimum point at 87 Å was observed, which suggests a separation distance where nanoparticles were reversibly plasmonically coupled (Figure 5.1f and Figure 5.4). Lastly, Metadynamic (MTD) simulations evaluated the binding mechanism between Au (111) surface and citrate or RRK molecule, respectively (Figure 5.1g). The Z coordinates of citrate and RRK molecule are 34 Å and 39 Å, thus indicating that RRK peptides are favored to bind on the top of a citrate-coated Au (111) surface rather than replacing citrate molecules.

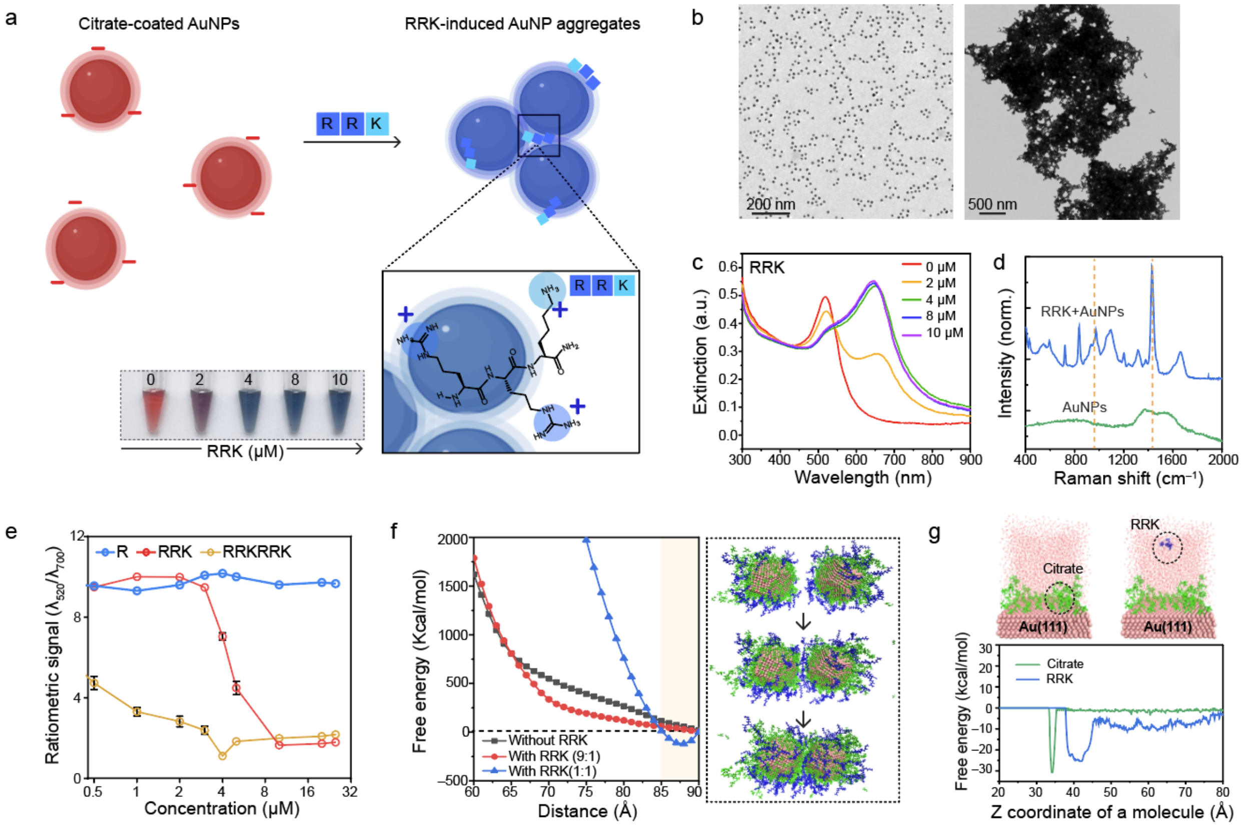

Figure 5.1 Short cationic peptides for reversible aggregation.
a, Schematic illustration of RRK-based particle aggregation. AuNPs were aggregated by electrostatic attractions between negatively charged citrate on AuNPs and positively charged RRK peptides. The inset photograph shows color change from red to blue as a function of RRK peptide (2–10 μM). b, TEM images of citrate-coated AuNPs (left) and RRK-induced AuNP aggregates (right). c, UV-vis spectrum of RRK-induced AuNP aggregates. The plasmonic resonance peak of AuNPs was red-shifted due to the plasmonic coupling. d, Raman shifts before and after adding RRK peptides into citrate-coated AuNPs. The Raman peak at 1443 cm^{-1} was attributed to the C–N stretching in Arg residue.[245] e, Ratiometric signal ($\lambda_{520}/\lambda_{700}$) of AuNPs after adding R, RRK, and RRKRRK peptides with different concentrations 0.5–32 μM, respectively. The error bars represent standard deviation of three independent samples. f, SMD simulations for free energy investigation as a function of AuNP distance at 298K and 1 atm. Energy minimum point was observed after adding RRK peptides. Black, red, and blue lines indicate a citrate to RRK molar ratios of 1:0, 9:1, and 1:1, respectively. The inset images indicate the simulation stages along a trajectory of the citrate-coated AuNPs with RRK (9:1) system. g, Metadynamics (MTD) free energy investigation for a system with 1 RRK on Au(111) surface (right) and a system with 1 citrate on Au(111) surface (left). The Z coordinate value was calculated based on the center mass of RRK and citrate molecule shown in the inset images. The upper surface of Au(111) slab was located at 31 Å. The MTD results observed no surface ligand exchange on Au(111) during the electrostatic interactions between RRK and citrate molecules.

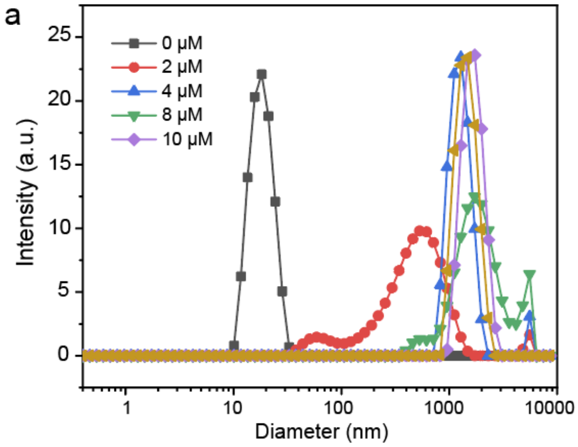

Figure 5.2 RRK-induced AuNP aggregates
RRK peptides with 2 to 10 µM were used to aggregate AuNPs. DLS data showed that the size of citrate-coated AuNPs were aggregated by the RRK peptides.

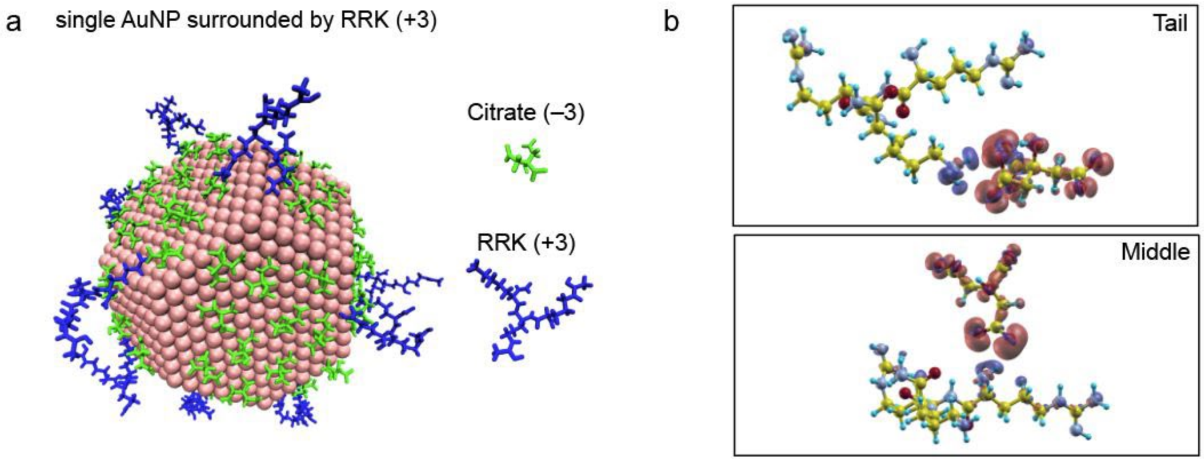

Figure 5.3 Interactions between RRK and citrate molecules
a, Molecular dynamics (MD) snapshots of a citrate-coated Au nanoparticle system after adding RRK molecules. Na ions, Cl ions, and water molecules are not shown for clarification. b, Simulated charge density indicated that molecular interactions between RRK peptides and citrate readily occurred at a tail portion rather than the middle portion due to atomic charge effects.

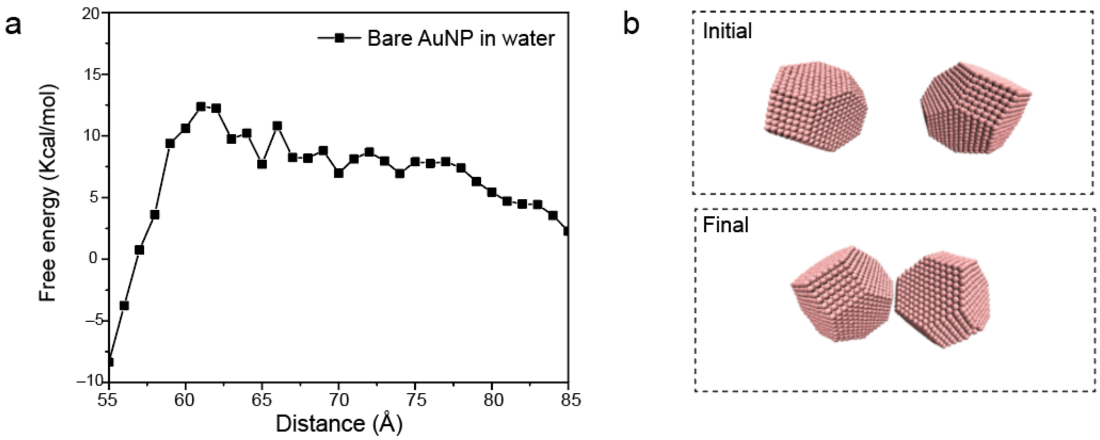

Figure 5.4 Free energy investigation as a function of AuNP distance
a, SMD simulation for a system with bare Au nanoparticles in water, where the distance indicates the distance between the center of mass of each Au nanoparticle. b, The initial and final snapshots are shown, where the water molecules are not shown for clarify.

5.4.2. Peptide-based dissociation of AuNP aggregates

Peptide-based ligands for AuNPs are of particular interest because of their structural- and chemical- versatilities that can provide high colloidal stability, functionalization, and prevention of protein adsorptions.[235, 246-248] Peptides which could provide electrostatic repulsion, steric distance, and hydrophilicity can attenuate electrostatic attractions induced by RRK, leading to reversible aggregation. We designed our dissociation peptides (*i.e.,* A1 peptide) to have three major components: charge, spacer, and anchoring groups (Figure 5.5a). First, we used Glu (E) and Lys (K) amino acids to provide steric distance and strong hydration layer.[246] Negatively charged EE residues provides electrostatic repulsion, and positively charged KK residues in the vicinity of the thiol could increase the grafting kinetics of thiols onto the citrated-coated AuNPs.[249] Second, Pro-based linker residues provide a space between charge and anchoring group, further increasing the stability of the AuNPs.[250] Lastly, Cys (C) amino acid contains a thiol side chain that binds to the surface of AuNPs *via* strong Au–S bonds.[251]

After inducing AuNP aggregates by the RRK peptides, the A1 peptides with different concentrations from 7 to 300 μM were used to dissociate AuNP aggregates. The plasmonic resonance peak of AuNP aggregates blue shifted to 520 nm after particle dissociation. (Figure 5.5b). The hydrodynamic diameter of AuNP aggregates (>1 μm) was reduced to 27 ± 0.07 nm, and the surface charge of AuNPs was – 13.4 ± 1.03 mV because of surface modification with neutral charged A1 peptides (150 μM) and residual citrates (Figure 5.5c). Particle dissociation induced color change from blue to red and a decrease in size as confirmed by time-dependent photographs, multi-laser wavelength nanoparticle tracking analysis (M-NTA), and TEM (Figure 5.5d-e and Figure 5.6). Ratiometric signal ($\lambda_{520}/\lambda_{700}$) indicated that A1 peptide (>150 μM) rapidly dissociate AuNP aggregates in 20 minutes (Figure 5.5f).

To further study the role of each amino acid in the A1 peptide, we synthesized eight peptide sequences (from A2 to A8) for control experiments (Figure 5.7). Table 5.1 includes peptide sequence, net charge, critical dissociation concentrations (CDC), and design rationale. First, we replaced Cys residue with Gly (*i.e.,* A2) to confirm the role of the anchoring group. Not surprisingly, the A2 peptide failed to dissociate AuNP aggregates due to absence of the Au-S binding (Figure 5.5g and Figure 5.8). Second, we hypothesized that negatively charged EE residues were required for particle dissociation because they provide electrostatic repulsions for citrate-coated AuNPs. To prove this, the A1 peptide without acetylation (*i.e.,* A3) and one Lys residue (*i.e.,* A4) were synthesized. The A3 and A4 peptides showed no particle dissociations, confirming that positively charged peptide could not dissociate AuNP aggregates likely due to lack of electrostatic repulsions (Figure 5.5g and Figure 5.9).

We further studied the role of Glu, Lys, and Pro amino acids in A1 peptides (Fig. 2h). For example, Pro-based spacer can provide a rigid and self-assembling monolayer (SAM) that increases the colloidal stability of AuNPs.[252] When the spacer was moved to the site between Glu and Lys residues (*i.e.,* A5), the dissociation capacity was 50% lower than A1 peptide. In addition, when the position of Glu was switched with Lys (*i.e.,* A6), particle dissociation was quenched, meaning that the position of positively charged residue is important to maintain the negatively charged electrical double layers. A1 peptide without Lys (*i.e.,* A7) decreased to 30% of the dissociation capacity likely due to the decrease in grafting kinetics of thiol-Au bonds and hydration layers.[246, 249] Lastly, the dissociated AuNPs were incubated in different concentrations (0.5 to 2 M) of NaCl to examine colloidal stability of the dissociated AuNPs (Figure 5.5i). The aggregation parameter defines the variations of absorbance ratio between 520 and 600 nm at the initial and final conditions (see Supporting information).[222, 235] The results showed that the A1 peptide-capped AuNPs showed the higher colloidal stability than citrate-coated AuNPs due to its longer peptide length, rigid SAM, and improved hydrophilicity.[235]

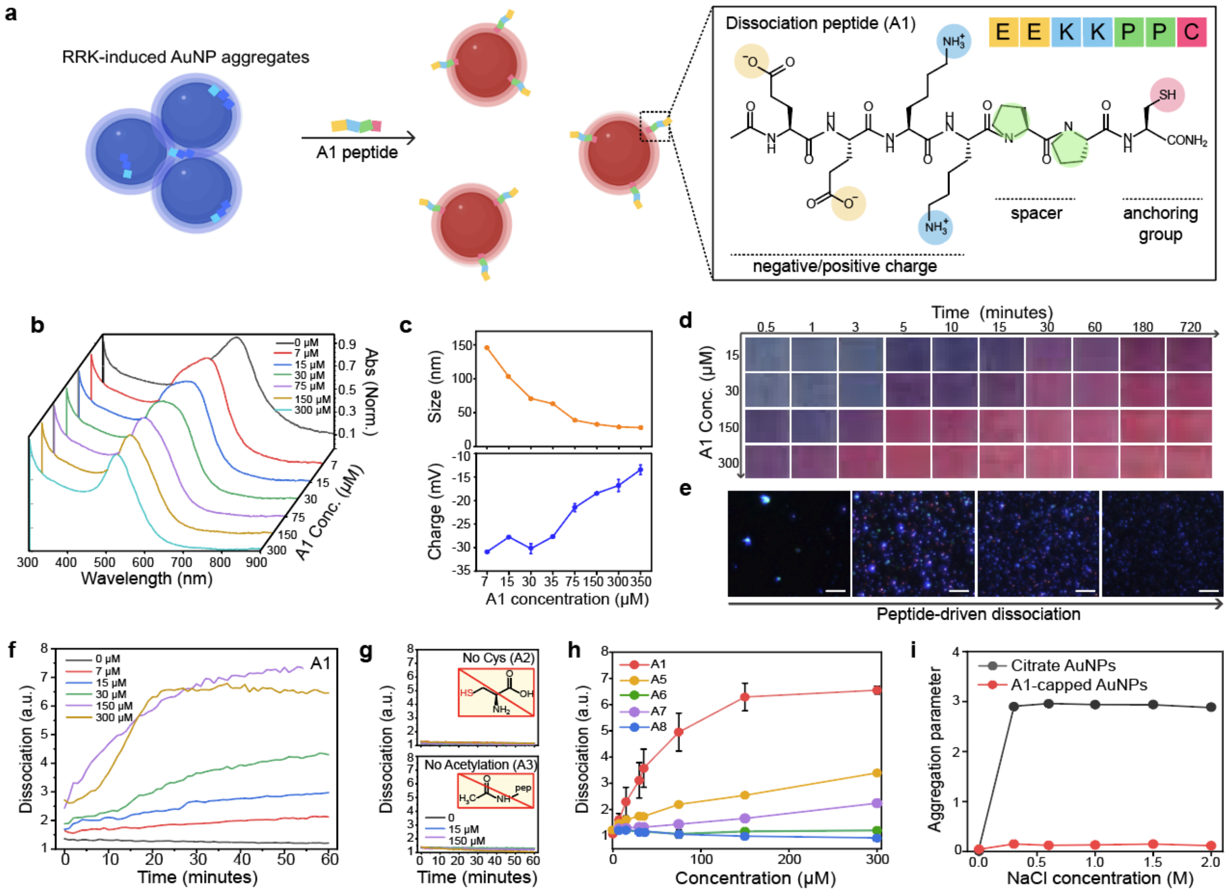

Figure 5.5 Peptide-enabled dissociation of AuNP aggregates

a, Schematic illustration of peptide-based particle dissociations. AuNP aggregates induced by RRK peptides were reversibly dissociated by the A1 peptides. The structural component of the A1 peptide contains charge, spacer, and anchoring group. b, UV-vis spectrum shows that the plasmonic resonance peak of AuNP aggregates blue-shifted upon addition of the A1 peptide (7–300 μM). c, Hydrodynamic diameter, and the surface charge after adding the A1 peptide. d, Time-dependent photographs show 150 μM of the A1 peptide requires to dissociate AuNP aggregates. x and y axis indicate time and the A1 concentration, respectively. e, Darkfield images of AuNP aggregates (left) and the dissociated AuNPs (right). The scale bar indicates 10 μm. Blue dots represent actual AuNPs dissociated by the A1 peptide. f, Time-dependent particle dissociation driven by the A1 peptide. The ratiometric signal (λ_{520}/ λ_{700}) was referred as dissociation (y axis). g, Particle dissociation was quenched without Cys (A2), and acetylation (A3). h, Dissociation capacity of the A1, A5, A6, A7 and A8 peptides. i, The dissociated AuNPs by the A1 (red) showed higher colloidal stability than citrate-coated AuNPs (black). Panel c, h and i repeated three independent times and showed similar results.

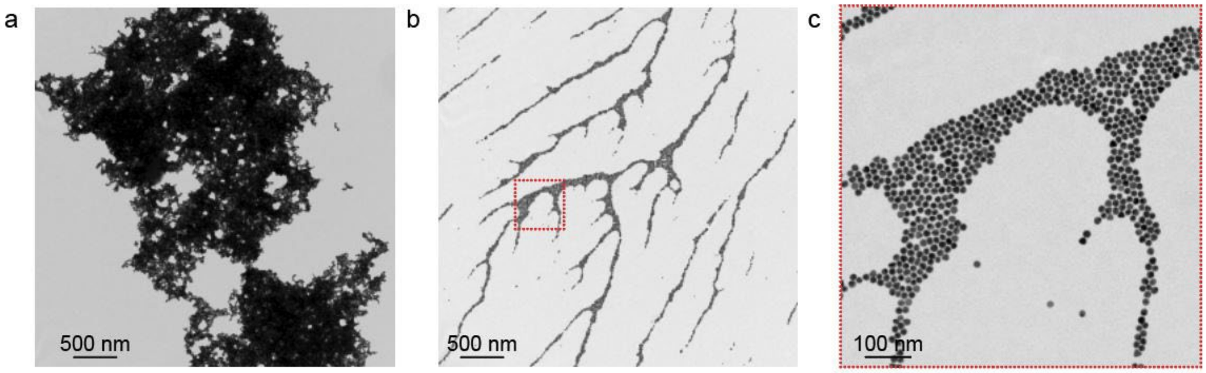

Figure 5.6 TEM images of AuNP aggregates and particle dissociations
a, AuNP aggregates induced by RRK peptides. b, After adding the dissociation peptides (A1, Ace-EEKKPPC-Am), the aggregated AuNPs were re-dispersed. c, High-magnified TEM image in the red-dotted box in panel b, 10 µM of RRK peptide was used to induce particle aggregation. 150 µM of the A1 peptide was used for particle dissociation of AuNP aggregates.

Table 5.1 A1-A8 peptides to study role of structural components in the dissociation peptide

Peptide name	Peptide sequence Ace: acetylation, Am: amide	Net Charge	M.W. (g mol^{-1})	CDC (µM)	Description
A1	Ace –EEKKPPC–Am	0	870.43	150	Dissociation peptide
A2	Ace –EEKKPP**G**–Am	0	824.44	X	Remove Cys
A3	**NH_2**–EEKKPPC–Am	+1	828.42	X	No acetylation
A4	Ace –**K**EEKKPPC–Am	+1	998.52	X	Single Lys
A5	Ace –EE**PP**KKC–Am	0	870.43	>300	Change the position of P spacer
A6	Ace –**KKEE**PPC–Am	0	870.43	X	Switch position of E and K
A7	Ace –**EE**PPC–Am	–2	614.24	>300	Glu only
A8	Ace –**KK**PPC–Am	+2	612.34	X	Lys Only

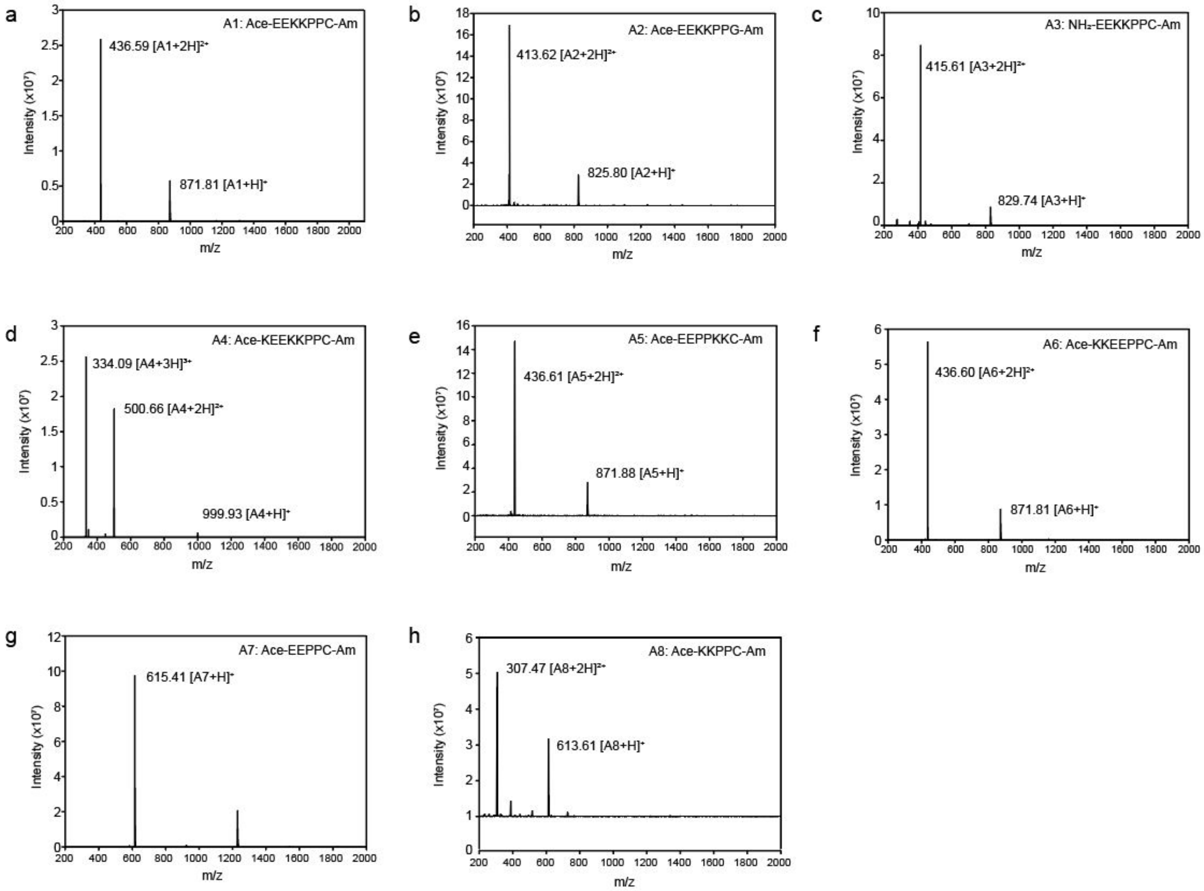

Figure 5.7 ESI-MS data of eight peptide sequences (A1–A8) to define the role of amino acid in dissociation peptide

ESI-MS data of a A1 (Ace-EEKKPPC-Am), b A2 (Ace-EEKKPPG-Am), c A3 (NH_2-EEKKPPG-Am), d A4 (Ace-KEEKKPPC-Am), e A5 (Ace-KEEPPKKC-Am), f A6 (Ace-KKEEPPC-Am), g A7 (Ace-EEPPC-Am), h A8 (Ace-KKPPC-Am).

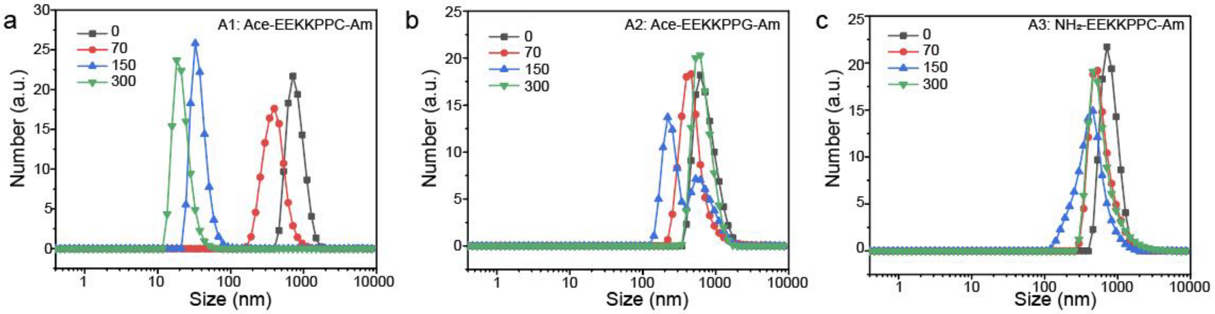

Figure 5.8 The role of cysteine and acetylation in the particle dissociation
a, A1 peptide with the concentration of 150 and 300 μM dissociated AuNP aggregates while A2 peptide (i.e., without cysteine) (b) and A3 (free amine at the N-terminus) (c) failed to dissociate AuNP aggregates. These results indicate that the cysteine residue in the C-terminus is required for Au-S binding. Acetylation is required to provide electrostatic repulsions by negatively charged Glu (E) amino acid.

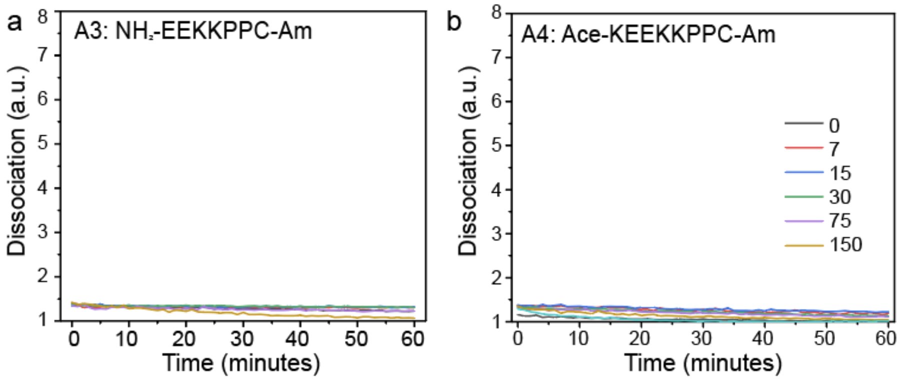

Figure 5.9 Free amine at N terminus prevents particle dissociation
To further confirm the free amine at N terminus can inversely impact on particle dissociation, we synthesized the A4 peptide which contain Lys residue at the C terminus (with acetylation). Not surprisingly, the A3 (a) and A4 (b) peptide failed to dissociate AuNP aggregates, meaning that positive charged peptides are incapable of dissociating AuNP aggregates likely due to lack of electrostatic repulsions.

5.4.3. Impact of hydrophilicity and steric bulk on particle dissociation.

Pro-, Ala-, and Gly-based spacers have different hydrophobic and hydrophilic natures, rigidity, and flexibility.[246, 253] For example, Pro residue is more hydrophobic and rigid (*i.e,* low mobility) while Gly residue is more hydrophilic and flexible. To investigate the impact of the rigidity and hydrophilicity of the peptides on the particle dissociation, we synthesized A1, A10, and A11 peptides that have different spacers: PP, AA, GG (Figure 5.10a-b and Figure 5.11). We also synthesized the peptide without a spacer (*i.e.,* A9) to confirm the impact of the spacer on particle dissociation. The results showed that the A1, A9, A10, and A11 peptides dissociated AuNP aggregates, changing color from blue to red within 10 min, respectively (Figure 5.10c-d and Figure 5.12). The A11 peptide showed the highest dissociation capacity compared to other spacers (Figure 5.10e). For example, the CDC of A11, A1, and A10 peptides were 16 μM, 40 μM, and 150 μM, respectively, indicating that higher hydrophilic and flexible spacer could enhance dissociation process. We further compared colloidal stability of the dissociated AuNPs by A1, A9, A10, and A11 peptides. The dissociated AuNPs were incubated in NaCl (from 0.5 to 2 M) for 1 h and measured variations of absorbance between 520 nm and 600 nm. The A9-capped AuNPs (*i.e.,* without spacer) showed relatively low colloidal stability compared to Pro-, Ala-, and Gly- capped AuNPs (Figure 5.10f). Pro-capped AuNPs showed a two-fold lower aggregation parameter than Gly- or Ala-capped AuNPs possibly due to their rigid structure and SAM.[246] Lastly, Fourier-transform infrared spectroscopy (FTIR) data confirmed peaks at 1600 cm^{-1} and 1400 cm^{-1} attributed to carboxyl groups in Glu amino acid (Figure 5.10g).

Next, we examined the impact of the peptide length on the particle dissociation. Gly spacer was selected because it showed the highest dissociation capacity compared to the Pro- and Ala-spacers. The A11, A12, and A13 peptides which contain two, four, and six repeated Gly amino acid were synthesized for the test (Figure 5.10b). The average peptide length of four repeated Gly (GGGG) is known around 18–20 Å.[246] The particle dissociation was improved as a function of the increased number of Gly spacer (from two to four) (Figure 5.10h and Figure 5.13). The A11 and A12 peptides dissociate AuNP aggregates with the concentration of 16 μM, respectively. However, the A13 peptide showed 25% lower dissociation capacity than the A12 peptides at the same peptide concentration (30 μM). These results revealed that the particle dissociation relies on the peptide length: the spacer length until 20 Å improved particle dissociation while over 20 Å could inversely impact the dissociation capacity likely due to steric hinderance caused by the large size of the spacer.[230]

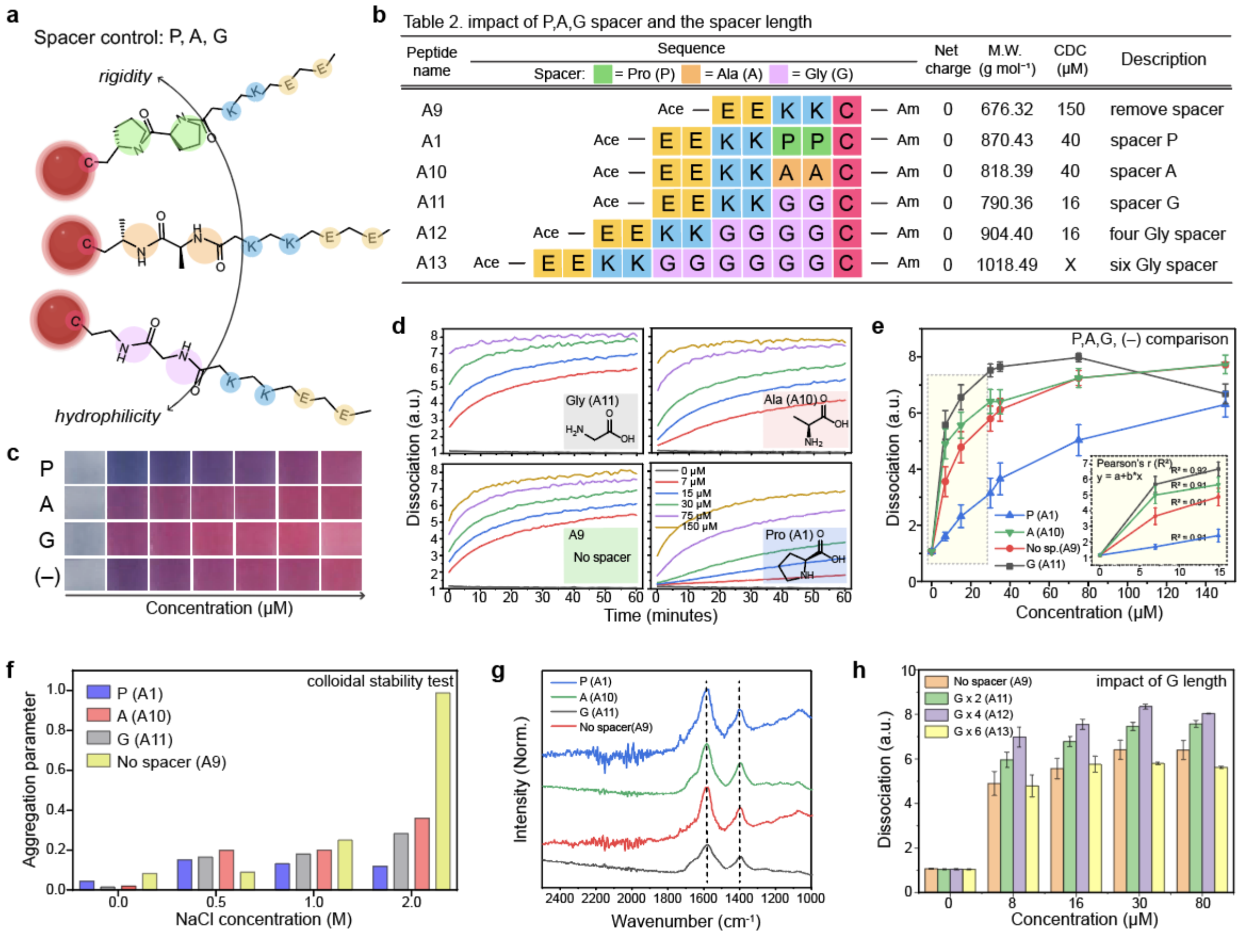

Table 2. impact of P,A,G spacer and the spacer length

Spacer: 🟩 = Pro (P) 🟧 = Ala (A) 🟪 = Gly (G)

Peptide name	Sequence	Net charge	M.W. (g mol⁻¹)	CDC (μM)	Description
A9	Ace — E E K K C — Am	0	676.32	150	remove spacer
A1	Ace — E E K K P P C — Am	0	870.43	40	spacer P
A10	Ace — E E K K A A C — Am	0	818.39	40	spacer A
A11	Ace — E E K K G G C — Am	0	790.36	16	spacer G
A12	Ace — E E K K G G G G C — Am	0	904.40	16	four Gly spacer
A13	Ace — E E K K G G G G G G C — Am	0	1018.49	X	six Gly spacer

Figure 5.10 Impact of hydrophilicity and steric bulk on particle dissociation.
a, Different Pro-, Ala-, Gly- spacers have different nature of rigidity and hydrophilicity which can impact on the dissociation capacity. Table 2 in (b) describes peptide sequences that are designed to investigate the impact of spacers. c, Photographs of the dissociated AuNPs by the PP, AA, GG spacers and without spacer (–) as a negative control. d, Time-dependent particle dissociations driven by the A1, A9, A10, and A11 peptides, respectively. e, Gly spacer showed the higher dissociation capacity than the Pro- and Ala- spacers. f, Aggregation parameter of the dissociated AuNPs driven by the A1, A9, A10, and A11 peptides. The results showed that the peptide with spacer can provide higher colloidal stability for AuNPs than the peptide without spacer. g, FTIR data of the dissociated AuNPs by the A1, A9, A10, and A11 peptides. The peaks at 1400 cm^{-1} and 1600 cm^{-1} were attributed to carboxyl group in Glu amino acid. h, Impact of the spacer length on the particle dissociation. Increasing the length of the spacer (from two to four) improved dissociation capacity while the spacer with six Glu (i.e., A13) showed lower dissociation capacity than A12 peptide. The panel e, f, and h repeated three independent times and showed similar results.

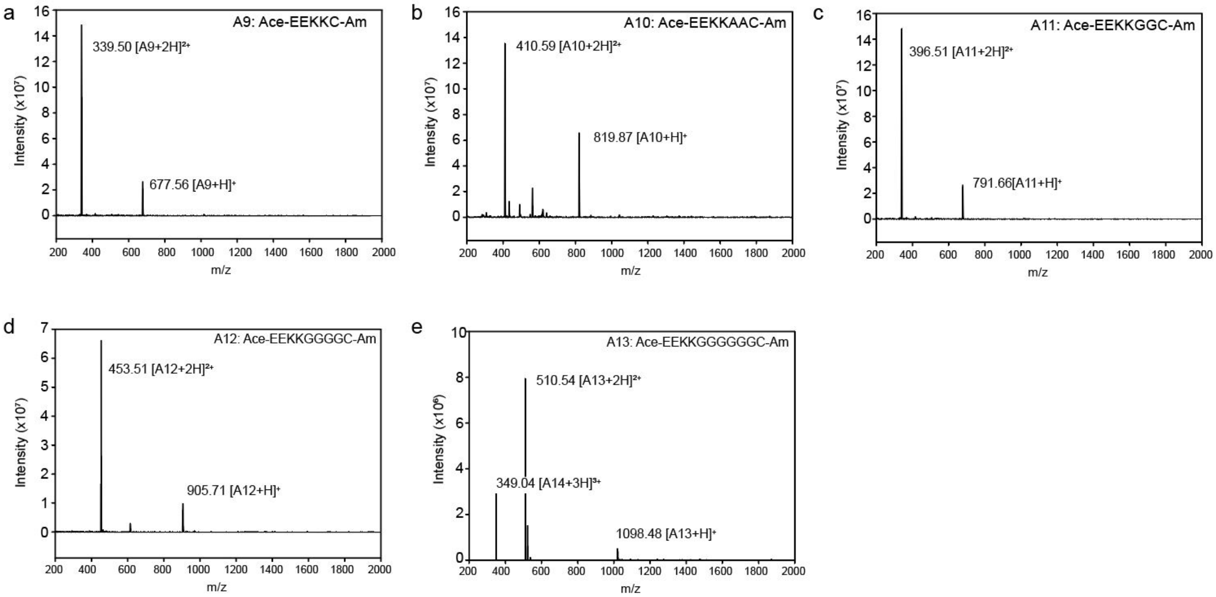

Figure 5.11 ESI-MS data A9–A13 peptides
ESI-MS data of a A9 (Ace-EEKKC-Am), b A10 (Ace-EEKKAAG-Am), c A11 (Ace-EEKKGGC-Am), d A12 (Ace-EEKKGGGGC-Am), e A13 (Ace-EEKKGGGGGGC-Am).

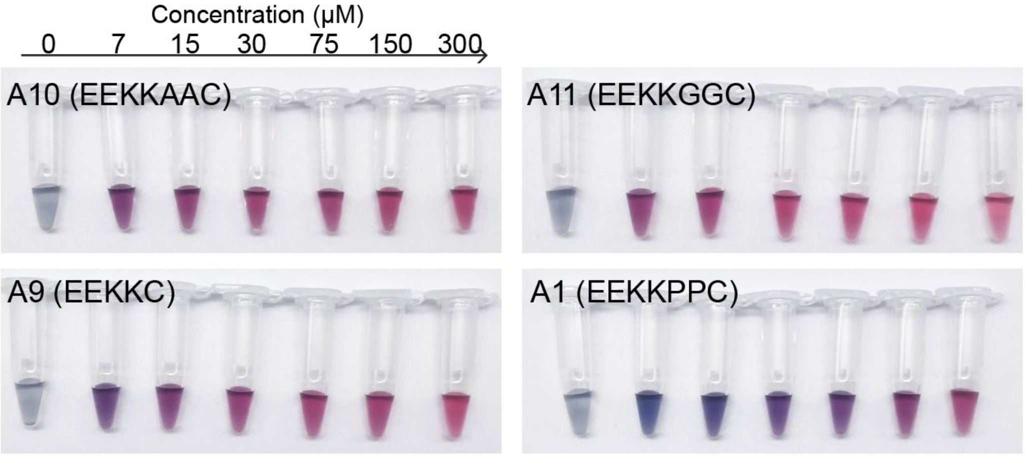

Figure 5.12 Photographs of the dissociated AuNPs by A1, A9, A10, A11 peptides
AuNP aggregates were dissociated using A1 (Ace-EEKKPPC-Am), A9 (Ace-EEKKC-Am), A10 (Ace-EEKKAAC-Am), A11 (Ace-EEKKGGC-Am). The color changed from blue to red due to the particle dissociation.

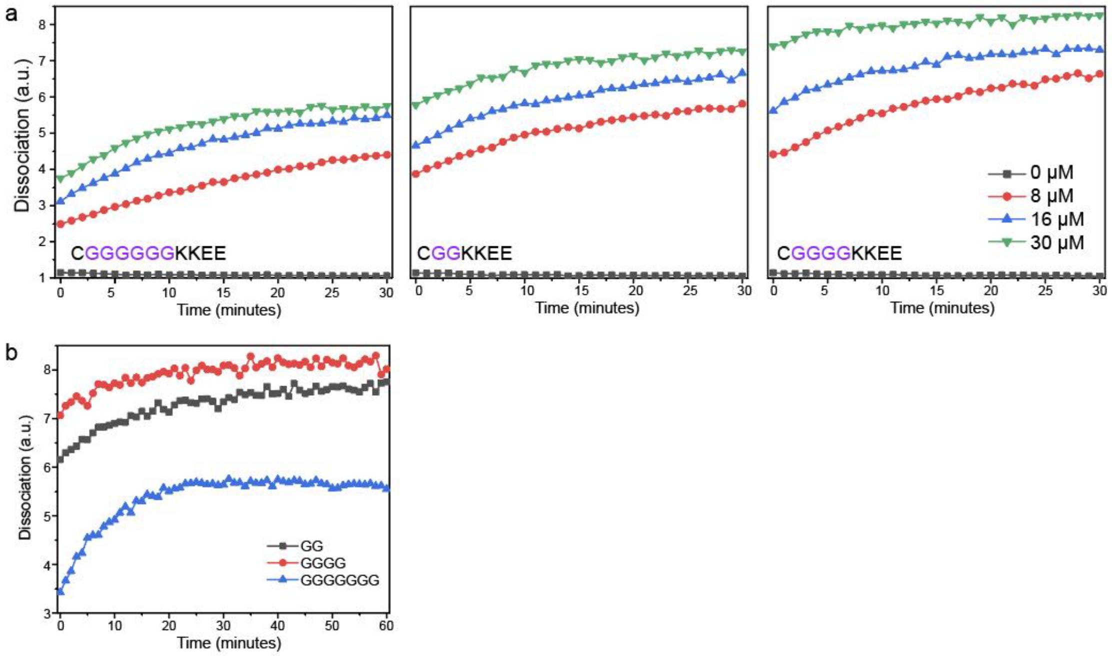

Figure 5.13 Impact of spacer lengths on the particle dissociation
a, Time-dependent particle dissociations using A11 (Ace-EEKKGGC-Am), A12 (Ace-EEKKGGGGC-Am), and A13 (Ace-EEKKGGGGGGC-Am) peptides. The results showed that spacer length can impact the dissociation capacity of the peptide. b, The particle dissociation was attenuated likely due to the increased steric hinderance by length.

5.4.4. Protease detection with dissociation peptide

We then applied our dissociation strategy for M^{pro} detection.[232, 233] We used the A18 peptide which contains three major structural components: dissociation domain (CGGKKEE at the N terminus), cleavage site (AVLQ↓SGF), and one Arg at the C terminus for dissociation shielding according to the A4 peptides (Figure 5.14a). The A18 fragments released by M^{pro} in PB buffer dissociated AuNP aggregates, changing color from blue to red while the A18 peptides without M^{pro} showed no color changes and became transparent due to the colloidal settlement (Figure 5.14b). Matrix assisted laser absorption ionization time of flight mass spectrometry (MALDI-TOF MS) data confirmed the mass peaks of the A18 fragments (CGGKKEEAVLQ: 1203.84) which is a result of the M^{pro} proteolysis (Figure 5.14c). After M^{pro} incubation (200 nM) for 1 h, the A18 fragments with different concentrations from 8 to 80 μM were used for the dissociation. The result showed that at least 40 μM of the A18 peptide (CDC) was required to dissociate AuNP aggregates, and the dissociation quickly occurred within 10 min (Figure 5.14d). The plasmonic resonance peak of AuNP aggregates blue shifted to 520 nm which was an absorption peak of pristine AuNPs. (Figure 5.14e). The size of AuNP aggregates was reduced to 26 ± 0.30 nm, and the surface charge was –27 ± 0.95 mV as a function of the released A18 fragments by M^{pro} cleavage (Figure 5.14f).

Next, we synthesized four different peptide sequences to study the impact of the fragments (*e.g.,* SGF or AVLQ), charge density, and the location of Cys residue on the particle dissociation (Figure 5.14g and Figure 5.15). M^{pro} cleavage requires an AVLQ↓SGF site (M^{pro} cleaves after Arg), and the two different fragments (*e.g.,* AVLQ or SGF) could impact on the dissociation capacity of the peptide. To decide the location of the dissociation domain, we synthesized a dissociation domain with AVLQ (*i.e.,* A15) and SGF (*i.e.,* A14), respectively. The A15 peptide showed higher dissociation capacity than the A14 peptide, indicating that adding the dissociation domain at the N-terminus is a better approach than adding at the C-terminus (Figure 5.14h and Figure 5.16). In addition, the A17 peptide which has lower charge components decreased the dissociation capacity, and the location of the Cys amino acid can impact particle dissociation. For example, the Cys at the N terminus showed 5-fold higher dissociation capacity than the peptide with Cys in the middle as Cys in the middle gives less passivation of AuNPs, thus preventing particle dissociation.[246] In conclusion, we placed our dissociation domain (*i.e.,* CGGKKEE) at the N terminus to efficiently activate particle dissociation by M^{pro} proteolysis.

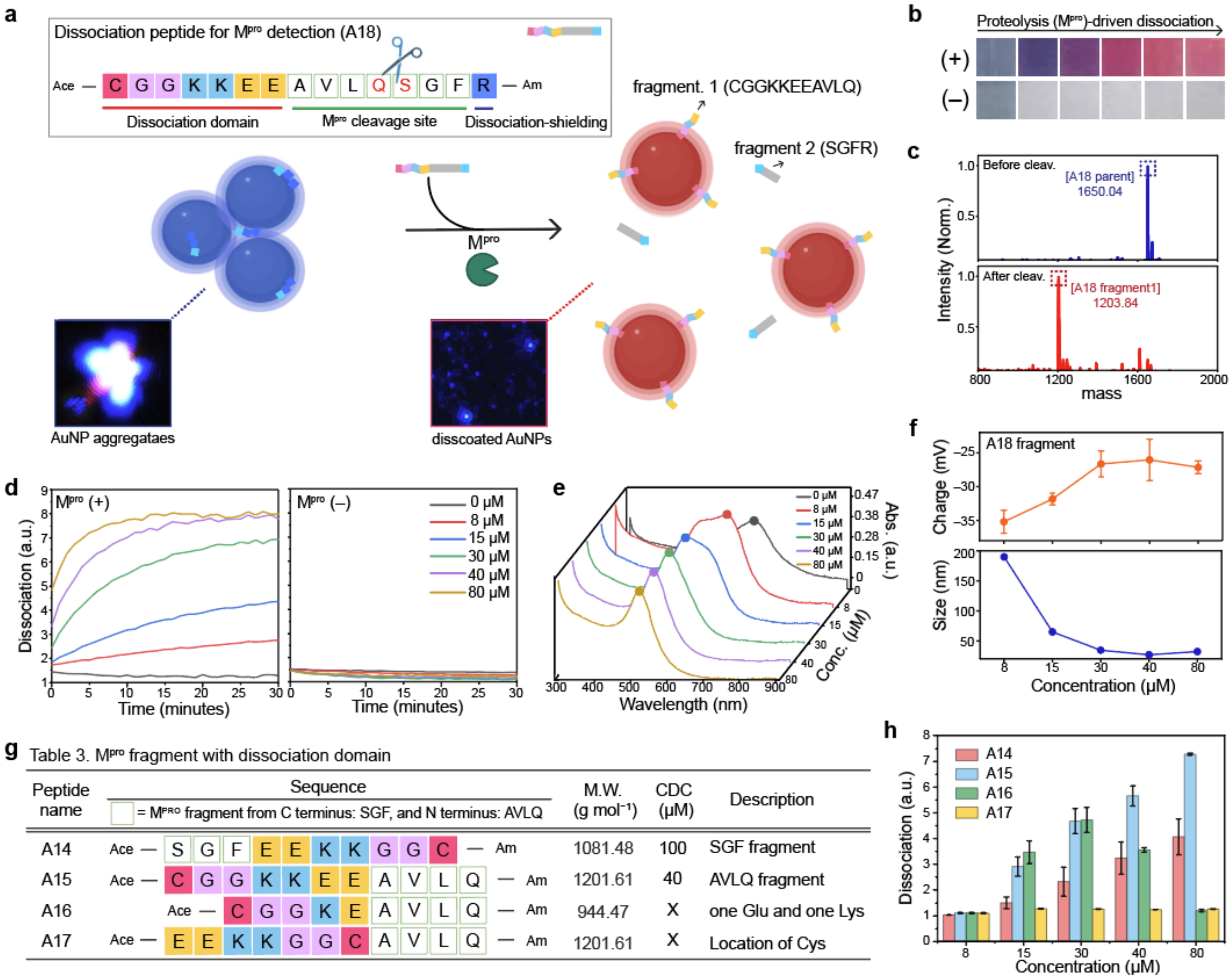

Table 3. Mpro fragment with dissociation domain

Peptide name	Sequence ☐ = MPRO fragment from C terminus: SGF, and N terminus: AVLQ	M.W. (g mol⁻¹)	CDC (μM)	Description
A14	Ace — S G F E E K K G G C — Am	1081.48	100	SGF fragment
A15	Ace — C G G K K E E A V L Q — Am	1201.61	40	AVLQ fragment
A16	Ace — C G G K E A V L Q — Am	944.47	X	one Glu and one Lys
A17	Ace — E E K K G G C A V L Q — Am	1201.61	X	Location of Cys

Figure 5.14 M^{pro} detection using dissociation strategy

a, Schematic illustrates that M^{pro} cleavage releases dissociation domains, changing the color from blue to red. Our dissociation peptide (*i.e.,* A18) consists of three parts: dissociation domain (CGGKKEE), cleavage site (AVLQ↓SGF), and dissociation shielding site (R). The inset images are before and after particle dissociation obtained by darkfield microscopy. Blue dots indicate actual AuNP aggregates (left) and the dissociated AuNPs (right). The particles are scattered in the distilled water. b, Color changes with (+) and without (–) M^{pro} in PB buffer. The released A18 fragment (CGGKKEEAVLQ) dissociated AuNP aggregates, changing the color from blue to red. c, MALDI-TOF MS data before and after M^{pro} cleavage, confirming the mass peaks of the A18 parent and its fragment. d, Time-dependent particle dissociation by the A18 fragments (from 8 to 80 μM). The results showed that at least 40 μM of the A18 fragment was required for particle dissociations. e, UV-vis spectrum before (black) and after particle dissociation by the A18 fragments. f, Changes in the size and surface charge after the dissociation induced by M^{pro} cleavage. Table 3 in (g) describes peptide sequences that are designed to confirm the best location and order of the dissociation domain for M^{pro} detection. h, Particle dissociations driven by the A14, A15, A16, and A17 peptides. The results show that the dissociation domain located at C-terminus showed the highest dissociation capacity. In addition, the thiol group at the tail showed higher dissociation affinity than thiol group in the middle. The panel f, and h repeated three independent times and showed similar results.

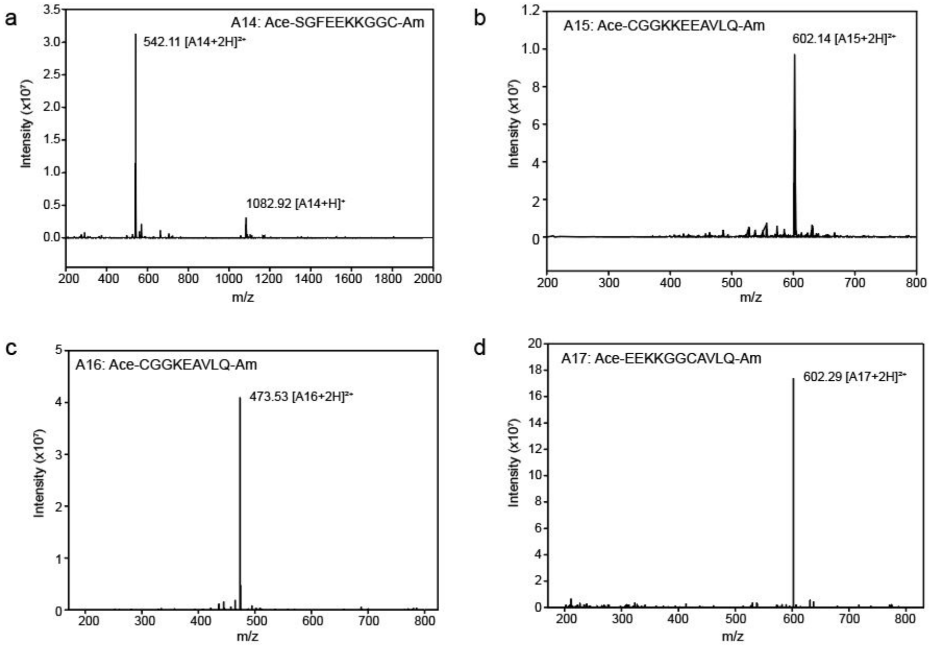

Figure 5.15 ESI-MS data of A14–A17 peptides

ESI-MS data of a A14 (Ace-SGFEEKKGGC-Am), b A15 (Ace- CGGKKEEAVLQ-Am), c A16 (Ace-CGGKEAVLQ-Am), and d A17 (Ace- EEKKGGCAVLQ-Am).

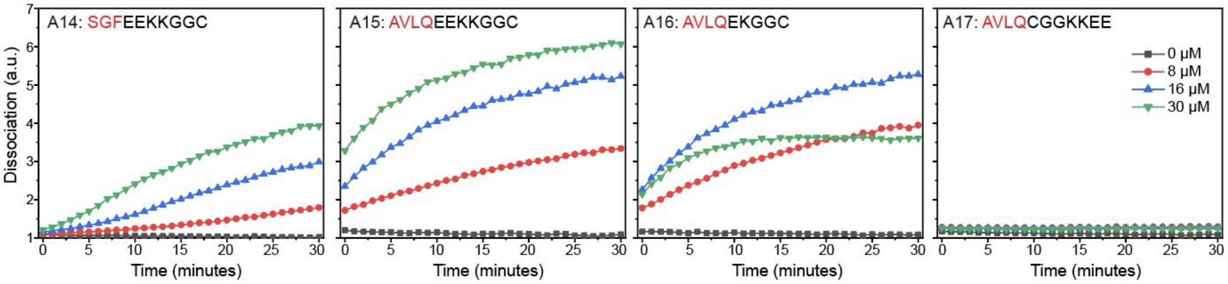

Figure 5.16 Impact of the fragment sequence, length, and the location of cysteine on the particle dissociation

Time-dependent particle dissociations using the A14, A15, A16, and A17 peptides. M^{pro} fragments (which are SGF and AVLQ) could attenuate the dissociation efficiency. The SGF fragment more reduced the dissociation efficiency than AVLQ fragment likely due to strong hydrophobicity of Phe (F) amino acid. It is also notable that the location of Cys is important to dissociate AuNP aggregates. For example, the Cys at the N-terminus (i.e., A15) dissociated AuNP aggregates while the Cys in the middle (i.e., A17) failed to dissociate AuNP aggregates. This is likely due to the fact that ligand architecture could impact on grafting density of peptide on AuNPs. The Cys in the middle could have less passivation layer which prevents particle dissociation.[246]

5.4.5. Matrix-insensitive M^{pro} detection

Our dissociation strategy offers a matrix-insensitive target detection because the dissociation mechanism is less interrupted by operating mediums (*e.g.,* proteins, ions) compared to aggregation-based biosensors.[230] Since SARS-CoV-2-infected patients might release viral proteases to respiratory fluids,[254] our A18 peptides were examined to dissociate AuNP aggregates in saliva or EBC (Figure 5.17a). We performed a stepwise assay by first incubating the A18 peptide with different M^{pro} concentrations (0.3 to 47 nM) for 30 min at 37 C°. Then, AuNP aggregates were added as a readout for 1 h. Figure 5.17b showed that the A18 fragments cleaved by M^{pro} in saliva or EBC dissociated AuNP aggregates within 10 min. Figure 5.17c plots the ratiometric signal (λ_{520}/ λ_{700}) against different M^{pro} concentrations (from 0.6 to 150 nM), showing that higher M^{pro} concentrations quickly activated particle dissociation than at lower concentrations. The LoD for M^{pro} was determined to be 12.3 nM in saliva, 16.7 nM in the EBC, and 16.4 nM in PB buffer, respectively. The CDC of the A18 fragment was 40 μM. When the concentration of the A18 fragment was above CDC, the color turned to red. Otherwise, the color became transparent due to colloidal settlement in saliva or EBC (Figure 5.18).

To prevent non-desired particle dissociation, a positively charged domain was placed at the C terminus for dissociation-screening: one R in A18 and no R in A19 as a negative control (Table 4 in Figure 5.17 and Figure 5.19). In the absence of M^{pro}, A19 peptide over 50 μM can cause non-desired particle dissociation while A18 peptide showed no false positives (Figure 5.17d and Figure 5.20). We further confirmed that the release of SGFR fragments during M^{pro} proteolysis had negligible impact on the dissociation process (Figure 5.17e and Figure 5.21**)**. We conducted a specificity test for M^{pro} using several related proteins such as hemoglobin (hg), inactivated M^{pro} (incubated at 60 C° for 3h), thrombin (thr), bovine serum albumin (BSA), human saliva, and α-amylase (amal). Figure 5.17f shows that only the positive control (*i.e.,* 200 nM M^{pro}) produced a prominent optical signal due to the release of the dissociation peptide by proteolytic cleavage (Figure 5.22). To define the enzymatic role in the protease in the colorimetric assays, a competitive inhibitor (GC376) for M^{pro} was used for the test. M^{pro} (200 nM) was incubated with increasing molarity of GC376 (i.e., 0 – 2 μM) in different operating mediums such as saliva, EBC, and PB buffer for 10 min prior to adding the A18 substrates. Fig. 5g indicates that particle dissociation was prevented by the addition of inhibitors (from 400 nM to 2 μM) due to the formation of M^{pro}–GC376 complexes (Figure 5.23–24).

Next, we applied our dissociation strategy on silver nanoparticles (AgNPs, 20 nm in size) because AgNPs offer a higher order of extinction coefficient compared to AuNPs.[255] As expected, the release of the A18 fragments by M^{pro} cleavage could dissociate AgNP aggregates, changing color from blue to yellow (Figure 5.17h and Figure 5.25). Our dissociation strategy can also improve colloidal stability of plasmonic nanoparticles. After the particle dissociation, the A18-capped AuNPs maintained high colloidal stability in extreme conditions such as Dulbecco's modified eagle medium (DMEM), human plasma, saliva, human urine, and NaCl (from 0.5 to 2M) (Figure 5.17i**)**. Lastly, our dissociation strategy is less affected by matrix interference. We replaced the sample matrix with 100% human plasma, urine, saliva, and seawater after RRK-based AuNPs aggregation. After adding dissociation peptides, reversible aggregation still occurred, leading to a blue-shift of the plasmonic resonance peak; this in turn changes color from blue to red in 100% human plasma, urine, saliva, and seawater (Figure 5.17j-k and Figure 5.26). These results emphasize that our peptide-based dissociation strategy provides a simple and versatile approach for reversible aggregation of plasmonic assemblies, offering a new mechanism for designing a matrix-insensitive plasmonic biosensor.

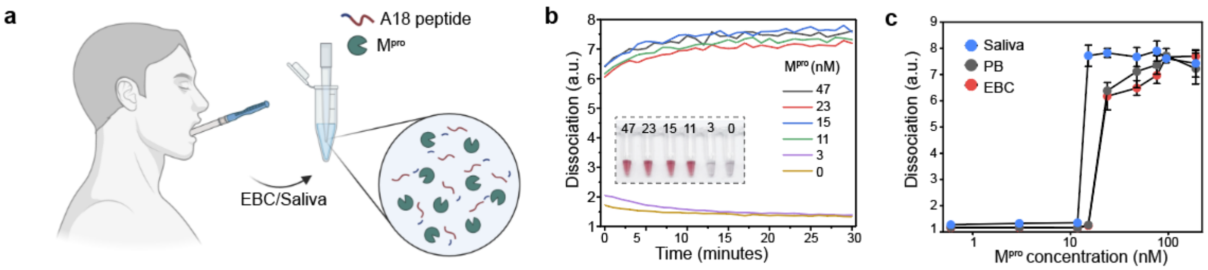

Table 4. M^{pro} target sequence

Peptide name	Sequence	M.W. (g mol⁻¹)	CDC (μM)	Net Charge	Description
	☐ = M^{pro} cleavage sequence (cleavage site: after Q)				
A18	Ace — C G G K K E E A V L Q S G F R — Am	1648.83	40	+1	R for dissociation-screening
A19	Ace — C G G K K E E A V L Q S G F — Am	1492.72	X	+0	Removed dissociation-screening (false positive)

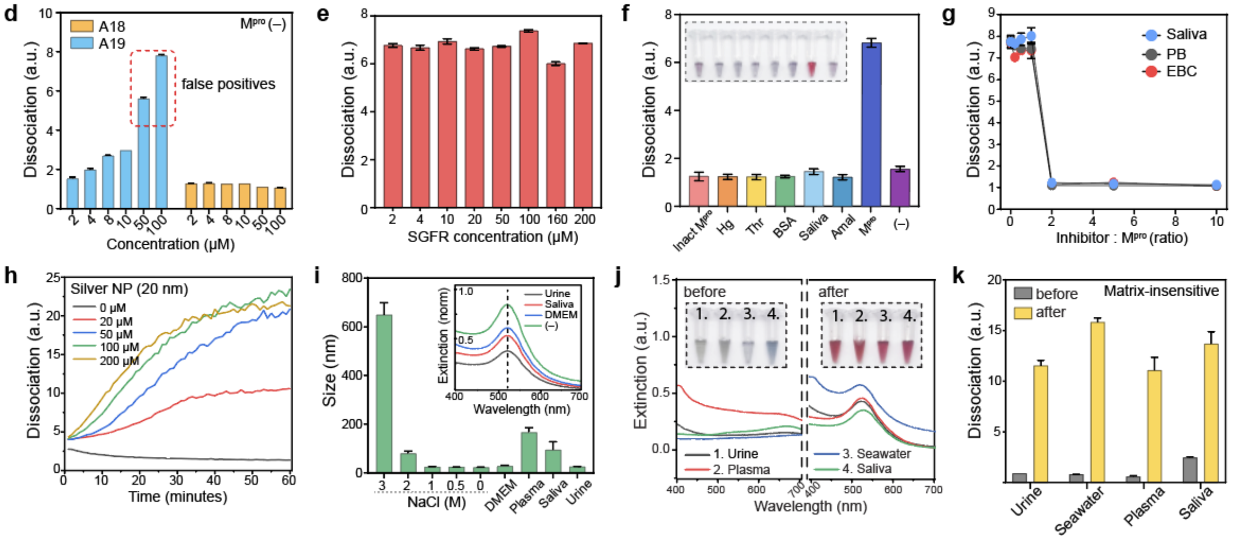

Figure 5.17 Matrix-insensitive M^{pro} detection

a, Schematic illustration of a matrix insensitive M^{pro} detection. The released A18 fragment by M^{pro} cleavage was used for colorimetric biosensing in saliva or EBC. b, Time-dependent M^{pro} detection from 0 to 47 nM in saliva. The inset photograph shows that our dissociation strategy can provide a clear readout of positive M^{pro} sample above 11 nM in saliva. c, Detection limits of M^{pro} in saliva, EBC, and PB buffer, respectively. Table 4 describes peptide sequences that are designed to verify the role of dissociation screening domain. d, One Arg at the C-terminus can prevent false positives. False positives occurred in A19 when the peptide concentration was over 50 µM while A18 showed no false positive in the absence of M^{pro}. e, A18 fragment from C terminus (*i.e.*, SGFR) had negligible impact on the dissociation process. f, Specificity test using multiple different biological essays (*e.g.,* inactivated M^{pro} (inact M^{pro}), hemoglobin (Hg), Thrombin (Thr), BSA, Saliva, Amalyase (Amal)). g, GC376 inhibitor assay test in saliva, EBC, and PB buffer, respectively. h, The released A18 fragments by M^{pro} cleavage can dissociate other types of plasmonic assemblies such as AgNP aggregates. i, After particle dissociation, the A18-capping AuNPs maintained high colloidal stability in different biological (*e.g.,* urine, saliva, plasma, DMEM) and extreme condition (*e.g.,* 2M NaCl). j, The plasmonic resonance peaks of the AuNP aggregates blue-shifted after particle dissociation in 100% of 1. human urine, 2. plasma, 3. seawater, and 4. saliva. The inset photographs show before (left) and after (right) adding dissociation peptides. k, Ratiometric signal (λ_{520}/ λ_{700}) of the dissociated AuNPs in diverse matrixes, indicating that our dissociation strategy is less affected by sample matrix. The panel c, d, e, f, g, i, j, and k repeated three independent times and showed similar results.

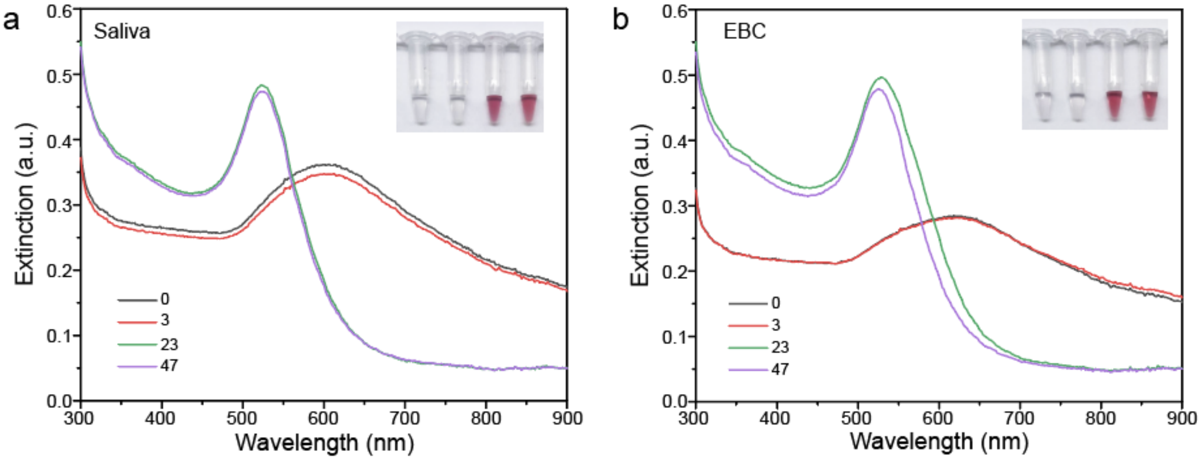

Figure 5.18 Dissociation strategy applied in saliva and EBC
M^{pro} cleaved the dissociation peptides (*i.e.,* A18, Ace-CGGKKEEAVLQSGFR-Am) in saliva (a), EBC (b), and the fragments dissociated AuNPs, changing color to reddish. The UV-vis spectrum showed the dissociated AuNPs with the different M^{pro} concentrations.

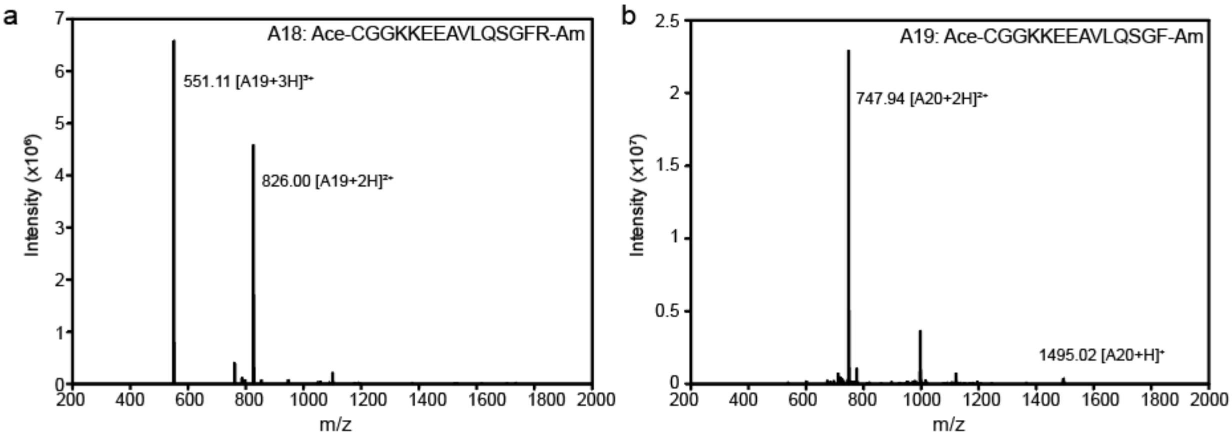

Figure 5.19 ESI-MS data of A18–19 peptides
ESI-MS data of (**a**) A18 (Ace-CGGKKEEAVLQSGFR-Am). **b,** A19 (Ace-CGGKKEEAVLQSGF-Am).

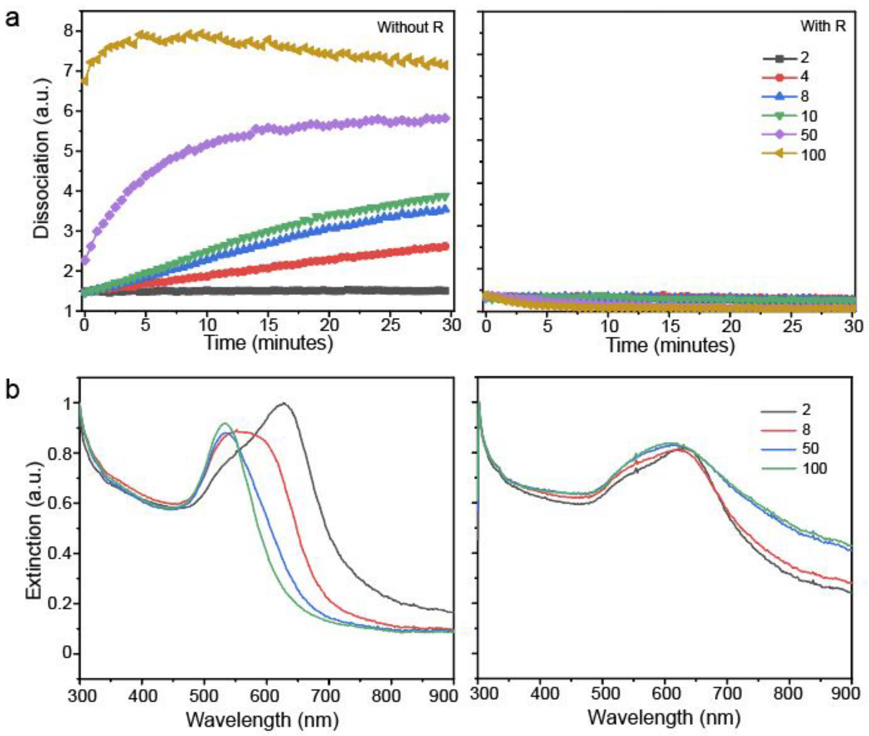

Figure 5.20 Arg residue at the C terminus for charge-screening

To prevent false positive, the dissociation peptide was charge-screened using Arg at the C terminus. AuNP aggregates were incubated with the different concentrations (from 2 to 100 μM) of A18 (with R) and A19 (without R) peptides. **a,** Time-dependent particle dissociations and their UV-vis spectrum (**b**). The results showed that the A19 peptide dissociated AuNP aggregates without M^{pro} (i.e., false positive) while A18 peptide which included Arg residue prevents the false positive.

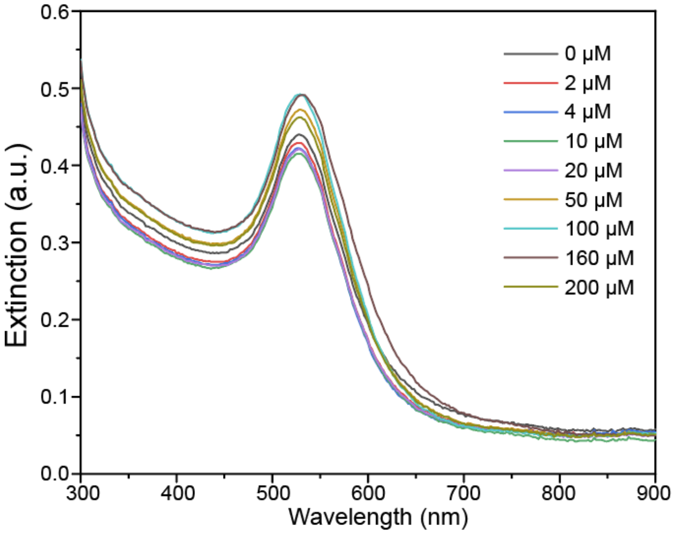

Figure 5.21 Impact of the SGFR fragment on particle dissociation
After M^{pro} cleavage, the A18 fragments (*i.e.,* CGGKKEEAVLQ) dissociated AuNP aggregates. SGFR showed negligible impact on particle dissociation. UV-vis spectrum showed that the dissociated AuNPs by the A18 fragments maintained high colloidal stability in the presence of SGFR fragments from 2 to 200 µM.

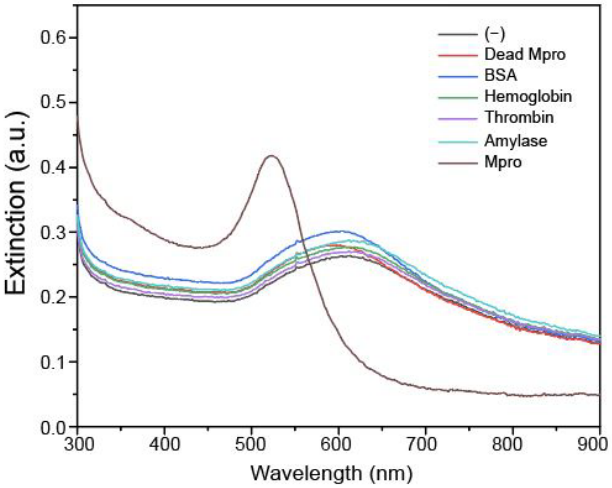

Figure 5.22 UV-vis spectrum of the specificity test
The inactive M^{pro} (incubated 60 ºC for 3h), BSA, hemoglobin, thrombin, α-amylase, saliva and M^{pro} were incubated with the dissociation peptide (*i.e.,* A18) for 1h at 37 ºC. After then, AuNP aggregates were used for the specificity test. The UV-vis spectrum showed that only M^{pro} dissociated AuNP aggregates due to the release of the dissociation peptides while other enzymes and proteins could not induce the particle dissociations.

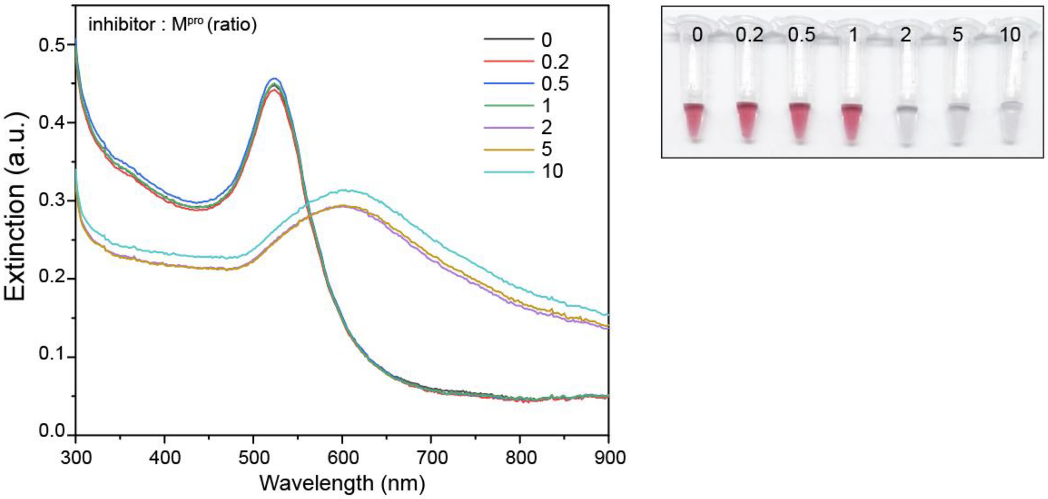

Figure 5.23 UV-vis spectrum of the inhibition test
The GC376 inhibitor was incubated with M^{pro} for the inhibition test. The 0, 0.2, 0.5, 1, 2, 5, and 10 represent the ratio between inhibitor to M^{pro} (200 nM). The results showed that GC376 inhibited M^{pro} proteolytic activity, preventing the particle dissociation.

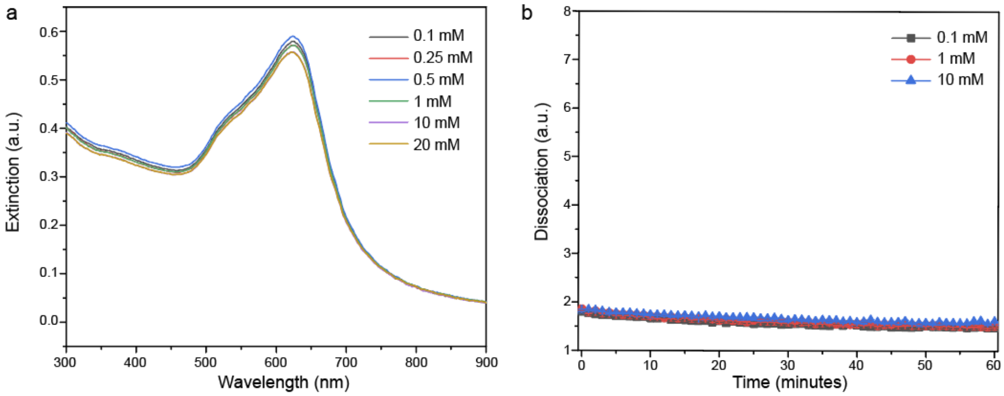

Figure 5.24 GC376 inhibitor with AuNP aggregates
The GC376 inhibitor (from 0.1 to 20 mM) was incubated with AuNP aggregates. UV-vis spectrum (a) and time-dependent particle dissociation (b) showed that the inhibitor itself had no impact on the particle dissociation.

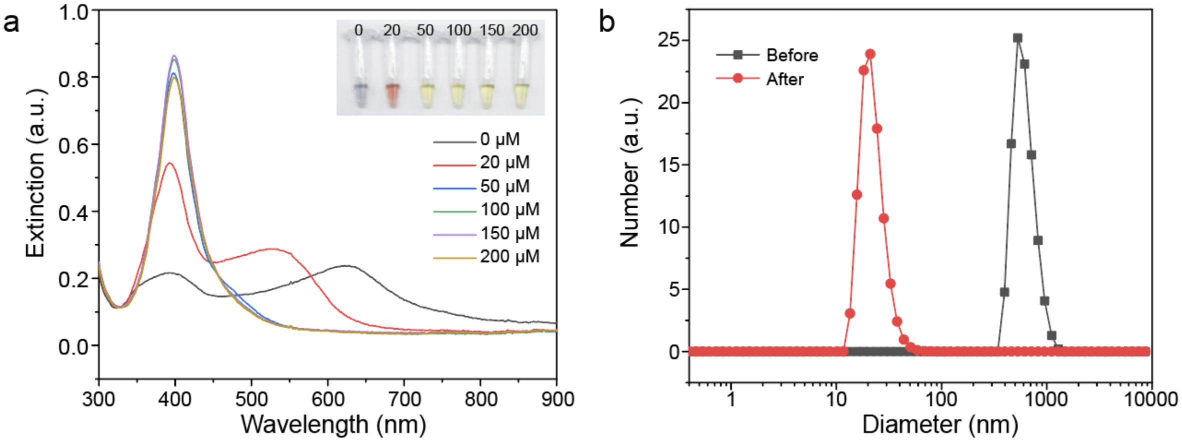

Figure 5.25 Dissociation strategy using 20 nm AgNPs
a, UV-vis spectrum and (b) DLS data of the dissociated Ag aggregates using the dissociation peptides. These results showed that our dissociation strategy could be applied using AgNPs which provide more broad absorption shift (from blue to yellow).

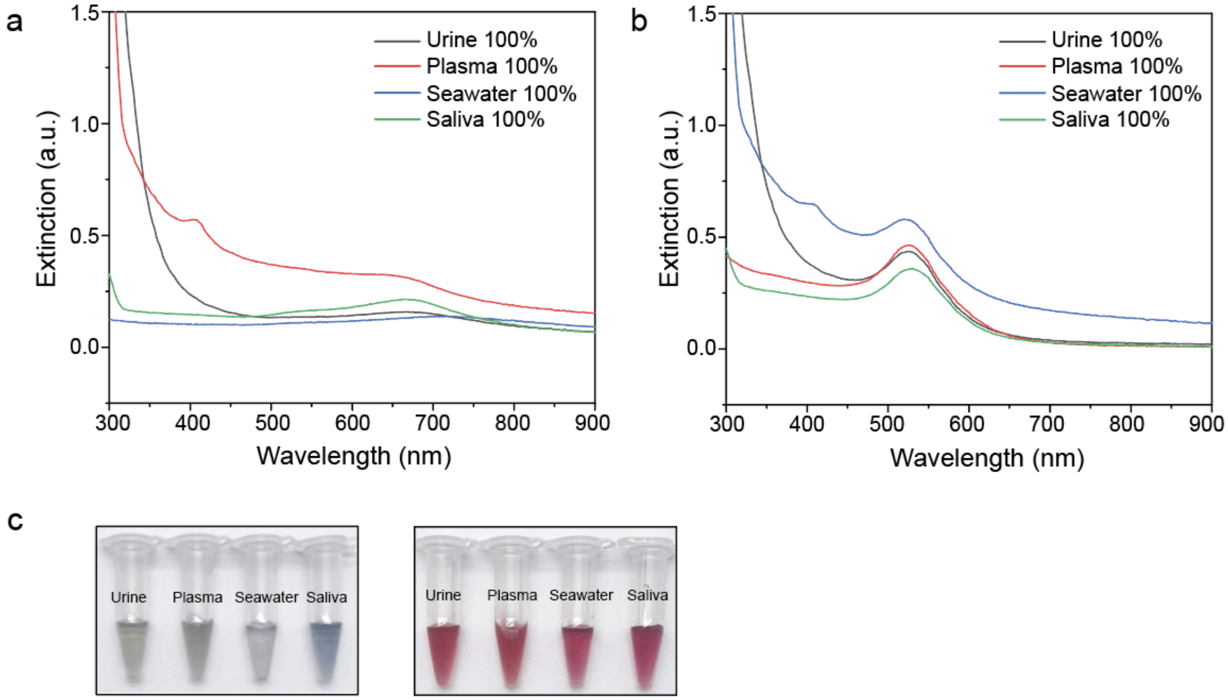

Figure 5.26 Particle dissociation in 100% human urine, plasma, seawater, and saliva
UV-vis spectrum of AuNP aggregates (a) and the dissociated AuNPs (b) after adding dissociation peptide (*i.e,* A11) in 100% human urine, plasma, seawater, and saliva. c, Photographs show that our dissociation peptide can re-disperse AuNP aggregates, offering color changes from blue to red in diverse matrixes.

5.5. Conclusions

In summary, we developed peptide-driven dissociation of plasmonic assemblies as a response to M^{pro} detection of SARS-CoV-2. This strategy eliminated the need for surface modifications of AuNPs and complex couplings (*e.g.,* PEG-peptide) for protease sensing. Both computational and experimental methods were used to understand reversible aggregation by a short cationic RRK peptide. Using 19 different peptide sequences, we verified that the dissociation capacity relies on hydrophilicity, charge density, ligand architecture, and steric distance. After incorporating the dissociation domain with an M^{pro} cleavage site, a colorimetric assay using UV-vis spectroscopy was tested to confirm the reproducibility and applicability of our platform for M^{pro} detection.

With optimized peptide sequence, our dissociation strategy successfully produced a distinct optical signal as a function of the released peptides by M^{pro} cleavage with a detection limit of 12.3 nM in saliva. The dissociation-screening site at C terminus enhances proteolytic cleavage (around 3-fold)[256] and prevents false positives. Inhibitor assay and specificity test further confirmed the critical role of M^{pro} in dissociation process, showing no non-specific activation. The dissociated AuNPs maintained high colloidal stability in extreme conditions, and our dissociation strategy can be applied to other types of plasmonic materials such as silver. We further demonstrated that our dissociation strategy can be less interrupted by matrixes such as human plasma, urine, and seawater. This peptide-driven dissociation strategy holds significant promise in various fields such as colloidal science, biochemistry, and plasmonic biosensors with diverse applications ranging from disease diagnosis and drug detection to environmental monitoring.

5.6. Acknowledgement

This work was supported by the National Institute of Health (#1R21AI157957 and #1R01DE031114). This work was performed in part at San Diego Nanotechnology Infrastructure (SDNI) of University of California San Diego supported by (NSF ECCS-1542148), and by the Cellular and Molecular Medicine Electron Microscopy core facility (NIH S10 OD 023527). This work was performed in part at the San Diego Nanotechnology Infrastructure (SDNI) of UCSD which is supported by the National Science Foundation (Grant ECCS-2025752). The author acknowledges start-up funds from UCSD, Sloan Research Fellowship, and ENLACE mentoring program supported by Dr. Graeve. The author also acknowledges Biorender for supporting artwork design.

Chapter 5, in part is currently being prepared for submission for publication of the material. “Peptide-driven dissociation of plasmonic couplings for protease detection” by Yim, Wonjun; Retout, Maurice; Chen, Amanda A.; Ling, Chuxuan; Amer, Lubna; Jin, Zhicheng; Chang, Yu-ci; Chavez, Saul; Barrios, Karen; Lam, Benjamin; Li, Zhi; Zhou, Jiajing; Shi, Lingyan; Pascal, Tod A.; Jokerst, Jesse V., The dissertation author was the primary researcher and author of this material.

REFERENCES

1. Xu, M.; Wang, L. V., Photoacoustic imaging in biomedicine. *Rev. of Sci. Instrum.* **2006,** *77* (4), 041101.
2. Mallidi, S.; Luke, G. P.; Emelianov, S., Photoacoustic imaging in cancer detection, diagnosis, and treatment guidance. *Trends Biotechnol.* **2011,** *29* (5), 213-221.
3. Cheng, M. H. Y.; Mo, Y.; Zheng, G., Nano versus molecular: optical imaging approaches to detect and monitor tumor hypoxia. *Adv. Healthc. Mater.* **2020**, 2001549.
4. Huang, J.; Pu, K., Activatable molecular probes for second near-infrared fluorescence, chemiluminescence, and photoacoustic Imaging. *Angew. Chem.* **2020,** *132*, 11813-11827.
5. Moore, C.; Chen, F.; Wang, J.; Jokerst, J. V., Listening for the therapeutic window: advances in drug delivery utilizing photoacoustic imaging. *Adv. Drug Deliv. Rev.* **2019,** *144*, 78-89.
6. Mishra, K.; Fuenzalida-Werner, J. P.; Ntziachristos, V.; Stiel, A. C., Photocontrollable proteins for optoacoustic imaging. *Anal. Chem.* **2019,** *91*, 5470-5477.
7. Jeevarathinam, A. S.; Lemaster, J. E.; Chen, F.; Zhao, E.; Jokerst, J. V., Photoacoustic imaging quantifies drug release from nanocarriers via redox chemistry of dye-labeled cargo. *Angew. Chem. Int. Ed.* **2020,** *59* (12), 4678-4683.
8. Chen, F.; Zhao, E. R.; Hableel, G.; Hu, T.; Kim, T.; Li, J.; Gonzalez-Pech, N. I.; Cheng, D. J.; Lemaster, J. E.; Xie, Y., Increasing the efficacy of stem cell therapy via triple-function inorganic nanoparticles. *ACS nano* **2019,** *13* (6), 6605-6617.
9. Pu, K.; Shuhendler, A. J.; Jokerst, J. V.; Mei, J.; Gambhir, S. S.; Bao, Z.; Rao, J., Semiconducting polymer nanoparticles as photoacoustic molecular imaging probes in living mice. *Nat. Nanotechnol.* **2014,** *9* (3), 233-239.
10. Weber, J.; Beard, P. C.; Bohndiek, S. E., Contrast agents for molecular photoacoustic imaging. *Nat. Methods* **2016,** *13* (8), 639-650.
11. Dreaden, E. C.; Alkilany, A. M.; Huang, X.; Murphy, C. J.; El-Sayed, M. A., The golden age: gold nanoparticles for biomedicine. *Chem. Soc. Rev.* **2012,** *41* (7), 2740-2779.
12. Liu, Y.; He, J.; Yang, K.; Yi, C.; Liu, Y.; Nie, L.; Khashab, N. M.; Chen, X.; Nie, Z., Folding up of gold nanoparticle strings into plasmonic vesicles for enhanced photoacoustic imaging. *Angew. Chem. Int. Ed.* **2015,** *54* (52), 15809-15812.

13. Mantri, Y.; Jokerst, J. V., Engineering plasmonic nanoparticles for enhanced photoacoustic imaging. *ACS Nano* **2020,** *14* (8), 9408-9422.

14. Jain, P. K., Gold nanoparticles for physics, chemistry, and biology. edited by catherine louis and olivier pluchery. *Angew. Chem. Int. Ed.* **2014,** *53* (5), 1197-1197.

15. Chen, Y.-S.; Zhao, Y.; Yoon, S. J.; Gambhir, S. S.; Emelianov, S., Miniature gold nanorods for photoacoustic molecular imaging in the second near-infrared optical window. *Nat. Nanotechnol.* **2019,** *14* (5), 465-472.

16. SoRelle, E. D.; Liba, O.; Hussain, Z.; Gambhir, M.; de la Zerda, A., Biofunctionalization of large gold nanorods realizes ultrahigh-sensitivity optical imaging agents. *Langmuir* **2015,** *31* (45), 12339-12347.

17. Busbee, B. D.; Obare, S. O.; Murphy, C. J., An improved synthesis of high-aspect-ratio gold nanorods. *Adv. Mater.* **2003,** *15* (5), 414-416.

18. Mantri, Y.; Davidi, B.; Lemaster, J. E.; Hariri, A.; Jokerst, J. V., Iodide-doped precious metal nanoparticles: measuring oxidative stress in vivo via photoacoustic imaging. *Nanoscale* **2020,** *12* (19), 10511-10520.

19. Jiang, Y.; Upputuri, P. K.; Xie, C.; Zeng, Z.; Sharma, A.; Zhen, X.; Li, J.; Huang, J.; Pramanik, M.; Pu, K., Metabolizable semiconducting polymer nanoparticles for second near-infrared photoacoustic imaging. *Adv. Mater.* **2019,** *31* (11), 1808166.

20. Ma, L.; Huang, S.; He, S.; Wang, Z.; Cheng, Z., Polydopamine-coated Downconversion Nanoparticle as an Efficient Dual-Modal Near-Infrared-II Fluorescence and Photoacoustic Contrast Agent for Non-Invasive Visualization of Gastrointestinal Tract In Vivo. *Biosens and Bioelectron* **2020,** *151*, 112000.

21. Liu, Y.; Liu, H.; Yan, H.; Liu, Y.; Zhang, J.; Shan, W.; Lai, P.; Li, H.; Ren, L.; Li, Z., Aggregation-Induced Absorption Enhancement for Deep Near-Infrared II Photoacoustic Imaging of Brain Gliomas In Vivo. *Adv. Sci.* **2019,** *6*, 1801615.

22. Chen, R.; Huang, S.; Lin, T.; Ma, H.; Shan, W.; Duan, F.; Lv, J.; Zhang, J.; Ren, L.; Nie, L., Photoacoustic Molecular Imaging-Escorted Adipose Photodynamic–Browning Synergy for Fighting Obesity with Virus-like Complexes. *Nat. Nanotechnol.* **2021**, 1–11.

23. Antaris, A. L.; Chen, H.; Cheng, K.; Sun, Y.; Hong, G.; Qu, C.; Diao, S.; Deng, Z.; Hu, X.; Zhang, B., A small-molecule dye for NIR-II imaging. *Nat. Mater.* **2016,** *15* (2), 235-242.

24. Jiang, Y.; Zhao, X.; Huang, J.; Li, J.; Upputuri, P. K.; Sun, H.; Han, X.; Pramanik, M.; Miao, Y.; Duan, H., Transformable hybrid semiconducting polymer nanozyme for second near-infrared photothermal ferrotherapy. *Nat. Commun.* **2020,** *11* (1), 1-13.

25. Ding, X.; Liow, C. H.; Zhang, M.; Huang, R.; Li, C.; Shen, H.; Liu, M.; Zou, Y.; Gao, N.; Zhang, Z., Surface plasmon resonance enhanced light absorption and photothermal therapy in the second near-infrared window. *J. Am. Chem. Soc.* **2014,** *136* (44), 15684-15693.

26. Chang, S.-S.; Shih, C.-W.; Chen, C.-D.; Lai, W.-C.; Wang, C. C., The shape transition of gold nanorods. *Langmuir* **1999,** *15* (3), 701-709.

27. Link, S.; Wang, Z. L.; El-Sayed, M. A., How does a gold nanorod melt? *J. Phys. Chem. B* **2000,** *104* (33), 7867-7870.

28. Link, S.; Burda, C.; Nikoobakht, B.; El-Sayed, M. A., Laser-induced shape changes of colloidal gold nanorods using femtosecond and nanosecond laser pulses. *J. Phys. Chem. B* **2000,** *104* (26), 6152-6163.

29. Albrecht, W.; Deng, T.-S.; Goris, B.; van Huis, M. A.; Bals, S.; van Blaaderen, A., Single particle deformation and analysis of silica-coated gold nanorods before and after femtosecond laser pulse excitation. *Nano Lett.* **2016,** *16* (3), 1818-1825.

30. Chen, L.-C.; Wei, C.-W.; Souris, J. S.; Cheng, S.-H.; Chen, C.-T.; Yang, C.-S.; Li, P.-C.; Lo, L.-W., Enhanced photoacoustic stability of gold nanorods by silica matrix confinement. *J. Biomed. Opt.* **2010,** *15* (1), 016010.

31. Bae, C.; Lee, J.; Yao, L.; Park, S.; Lee, Y.; Lee, J.; Chen, Q.; Kim, J., Mechanistic insight into gold nanorod transformation in nanoscale confinement of ZIF-8. *Nano Res.* **2020,** *14* (1), 66-73.

32. Qi, C.; Fu, L.-H.; Xu, H.; Wang, T.-F.; Lin, J.; Huang, P., Melanin/polydopamine-based nanomaterials for biomedical applications. *Sci. China Chem.* **2019,** *62* (2), 162-188.

33. Lee, H.; Dellatore, S. M.; Miller, W. M.; Messersmith, P. B., Mussel-inspired surface chemistry for multifunctional coatings. *Science* **2007,** *318* (5849), 426-430.

34. Battistella, C.; McCallum, N. C.; Vanthournout, B.; Forman, C. J.; Ni, Q. Z.; La Clair, J. J.; Burkart, M. D.; Shawkey, M. D.; Gianneschi, N. C., Bioinspired chemoenzymatic route to artificial melanin for hair pigmentation. *Chem. Mater.* **2020,** *32* (21), 9201-9210.

35. Schanze, K. S.; Lee, H.; Messersmith, P. B., Ten years of polydopamine: current status and future directions. *ACS Appl. Mater. Interfaces* **2018,** *10* (9).

36. Wu, D.; Zhou, J.; Creyer, M. N.; Yim, W.; Chen, Z.; Messersmith, P. B.; Jokerst, J. V., Phenolic-Enabled Nanotechnology: Versatile Particle Engineering for Biomedicine. *Chem. Soc. Rev.* **2021**.

37. Zhou, J.; Lin, Z.; Ju, Y.; Rahim, M. A.; Richardson, J. J.; Caruso, F., Polyphenol-Mediated Assembly for Particle Engineering. *Acc. Chem. Res.* **2020,** *53*, 1269–1278.

38. Zhou, J.; Jiang, Y.; Hou, S.; Upputuri, P. K.; Wu, D.; Li, J.; Wang, P.; Zhen, X.; Pramanik, M.; Pu, K., Compact plasmonic blackbody for cancer theranosis in the near-infrared II window. *ACS nano* **2018,** *12* (3), 2643-2651.

39. Hong, S.; Kim, K. Y.; Wook, H. J.; Park, S. Y.; Lee, K. D.; Lee, D. Y.; Lee, H., Attenuation of the In Vivo Toxicity of Biomaterials by Polydopamine Surface Modification. *Nanomedicine* **2011,** *6*, 793–801.

40. Ryu, J.; Ku, S. H.; Lee, H.; Park, C. B., Mussel-Inspired Polydopamine Coating as a Universal Route to Hydroxyapatite Crystallization. *Adv. Funct. Mater.* **2010,** *20*, 2132–2139.

41. Huang, W.; Chen, R.; Peng, Y.; Duan, F.; Huang, Y.; Guo, W.; Chen, X.; Nie, L., In vivo Quantitative Photoacoustic Diagnosis of Gastric and Intestinal Dysfunctions with a Broad pH-Responsive Sensor. *ACS Nano* **2019,** *13*, 9561–9570.

42. Zhou, J.; Xiong, Q.; Ma, J.; Ren, J.; Messersmith, P. B.; Chen, P.; Duan, H., Polydopamine-enabled approach toward tailored plasmonic nanogapped nanoparticles: from nanogap engineering to multifunctionality. *ACS nano* **2016,** *10* (12), 11066-11075.

43. Kim, T.; Zhang, Q.; Li, J.; Zhang, L.; Jokerst, J. V., A Gold/Silver Hybrid Nanoparticle for Treatment and Photoacoustic Imaging of Bacterial Infection. *ACS Nano* **2018,** *12*, 5615–5625.

44. Schneider, C. A.; Rasband, W. S.; Eliceiri, K. W., NIH Image to ImageJ: 25 years of image analysis. *Nat. Methods* **2012,** *9* (7), 671-675.

45. de Gennes, P., Conformations of polymers attached to an interface. *Macromolecules* **1980,** *13* (5), 1069-1075.

46. Jokerst, J. V.; Lobovkina, T.; Zare, R. N.; Gambhir, S. S., Nanoparticle PEGylation for imaging and therapy. *Nanomedicine* **2011,** *6* (4), 715-728.

47. Lemaster, J. E.; Jeevarathinam, A. S.; Kumar, A.; Chandrasekar, B.; Chen, F.; Jokerst, J. V., Synthesis of ultrasmall synthetic melanin nanoparticles by UV irradiation in acidic and neutral conditions. *ACS Appl. Bio Mater.* **2019,** *2* (10), 4667-4674.

48. Zhang, L.; Su, H.; Cai, J.; Cheng, D.; Ma, Y.; Zhang, J.; Zhou, C.; Liu, S.; Shi, H.; Zhang, Y., A multifunctional platform for tumor angiogenesis-targeted chemo-thermal therapy using polydopamine-coated gold nanorods. *ACS nano* **2016,** *10* (11), 10404-10417.

49. Lemaster, J. E.; Wang, Z.; Hariri, A.; Chen, F.; Hu, Z.; Huang, Y.; Barback, C. V.; Cochran, R.; Gianneschi, N. C.; Jokerst, J. V., Gadolinium doping enhances the photoacoustic signal of synthetic melanin nanoparticles: a dual modality contrast agent for stem cell imaging. *Chem. Mater.* **2018,** *31* (1), 251-259.

50. Zmerli, I.; Michel, J.-P.; Makky, A., Bioinspired polydopamine nanoparticles: synthesis, nanomechanical properties, and efficient PEGylation strategy. *J. Mater. Chem. B* **2020,** *8* (20), 4489-4504.

51. Wang, S.; Fu, L.; Xin, J.; Wang, S.; Yao, C.; Zhang, Z.; Wang, J., Photoacoustic response induced by nanoparticle-mediated photothermal bubbles beyond the thermal expansion for potential theranostics. *J. Biomed. Opt.* **2018,** *23* (12), 125002.

52. Zhang, C.; Wu, B.-H.; Du, Y.; Ma, M.-Q.; Xu, Z.-K., Mussel-inspired polydopamine coatings for large-scale and angle-independent structural colors. *J. Mater. Chem. C* **2017,** *5* (16), 3898-3902.

53. Shi, Y.; Qin, H.; Yang, S.; Xing, D., Thermally confined shell coating amplifies the photoacoustic conversion efficiency of nanoprobes. *Nano Res.* **2016,** *9* (12), 3644-3655.

54. Repenko, T.; Rix, A.; Nedilko, A.; Rose, J.; Hermann, A.; Vinokur, R.; Moli, S.; Cao-Milàn, R.; Mayer, M.; von Plessen, G., Strong photoacoustic signal enhancement by coating gold nanoparticles with melanin for biomedical imaging. *Adv. Funct. Mater.* **2018,** *28* (7), 1705607.

55. Swinehart, D. F., The beer-lambert law. *J. Chem. Educ.* **1962,** *39* (7), 333-335.

56. Gandhi, S. R.; Bernstein, R. B., Influence of the focal length of the laser beam focusing lens on MPI yield. *Chem. Phys.* **1986,** *105* (3), 423-434.

57. Centi, S.; Cavigli, L.; Borri, C.; Milanesi, A.; Banchelli, M.; Chioccioli, S.; Khlebtsov, B. N.; Khlebtsov, N. G.; Matteini, P.; Bogani, P., Small thiols stabilize the shape of gold nanorods. *J. Phys. Chem. C* **2020,** *124* (20), 11132-11140.

58. Postma, A.; Yan, Y.; Wang, Y.; Zelikin, A. N.; Tjipto, E.; Caruso, F., Self-polymerization of dopamine as a versatile and robust technique to prepare polymer capsules. *Chem. Mater.* **2009,** *21* (14), 3042-3044.

59. Zhou, J.; Lin, Z.; Penna, M.; Pan, S.; Ju, Y.; Li, S.; Han, Y.; Chen, J.; Lin, G.; Richardson, J. J., Particle Engineering Enabled by Polyphenol-Mediated Supramolecular Networks. *Nat. Commun.* **2020,** *11*, 1–8.

60. Zou, R.; Zhang, Q.; Zhao, Q.; Peng, F.; Wang, H.; Yu, H.; Yang, J., Thermal stability of gold nanorods in an aqueous solution. *Colloids Surf. A Physicochem. Eng. Asp.* **2010,** *372* (1-3), 177-181.

61. Huang, Z.; Raciti, D.; Yu, S.; Zhang, L.; Deng, L.; He, J.; Liu, Y.; Khashab, N. M.; Wang, C.; Gong, J., Synthesis of platinum nanotubes and nanorings via simultaneous metal alloying and etching. *J. Am. Chem. Soc.* **2016,** *138* (20), 6332-6335.

62. Li, W.; Hu, J.; Wang, J.; Tang, W.; Yang, W.; Liu, Y.; Li, R.; Liu, H., Polydopamine-Mediated Polypyrrole/Doxorubicin Nanocomplex for Chemotherapy-Enhanced Photothermal Therapy in Both NIR-I and NIR-II Biowindows against Tumor Cells. *J. Appl. Polym. Sci.* **2020,** *137*, 49239.

63. Zhao, P.; Jin, Z.; Chen, Q.; Yang, T.; Chen, D.; Meng, J.; Lu, X.; Gu, Z.; He, Q., Local generation of hydrogen for enhanced photothermal therapy. *Nat. Commun.* **2018,** *9* (1), 1-12.

64. Li, Q.; Li, S.; He, S.; Chen, W.; Cheng, P.; Zhang, Y.; Miao, Q.; Pu, K., An activatable polymeric reporter for near-infrared fluorescent and photoacoustic imaging of invasive cancer. *Angew. Chem.* **2020,** *132* (18), 7084-7089.

65. Zhou, J.; Jokerst, J. V., Photoacoustic imaging with fiber optic technology: A review. *Photoacoustics* **2020**, 100211.

66. Borum, R. M.; Jokerst, J. V., Hybridizing clinical translatability with enzyme-free DNA signal amplifiers: recent advances in nucleic acid detection and imaging. *Biomater. Sci.* **2020**.

67. Jeevarathinam, A. S.; Lemaster, J. E.; Chen, F.; Zhao, E.; Jokerst, J. V., Photoacoustic imaging quantifies drug release from nanocarriers via redox chemistry of dye-labeled cargo. *Angew. Chem. Inter. Edi.* **2020,** *59* (12), 4678-4683.

68. Liu, S.; Pan, X.; Liu, H., Two-dimensional nanomaterials for photothermal therapy. *Angew. Chem.* **2020,** *132* (15), 5943-5953.

69. Jung, H. S.; Verwilst, P.; Sharma, A.; Shin, J.; Sessler, J. L.; Kim, J. S., Organic molecule-based photothermal agents: an expanding photothermal therapy universe. *Chem. Soc. Rev.* **2018,** *47* (7), 2280-2297.

70. Day, E. S.; Morton, J. G.; West, J. L., Nanoparticles for thermal cancer therapy. *J. Biomech. Eng.* **2009,** *131* (7).

71. Li, J.; Yu, X.; Jiang, Y.; He, S.; Zhang, Y.; Luo, Y.; Pu, K., Second near-infrared photothermal semiconducting polymer nanoadjuvant for enhanced cancer immunotherapy. *Adv. Mater.* **2021,** *33* (4), 2003458.

72. Xu, M.; Yim, W.; Zhou, J.; Zhou, J.; Jin, Z.; Moore, C.; Borum, R.; Jorns, A.; Jokersta, J. V., The Application of Organic Nanomaterials for Bioimaging, Drug Delivery, and Therapy: Spanning Various Domains. *IEEE Nanotechnol. Mag.* **2021**.

73. Chitgupi, U.; Nyayapathi, N.; Kim, J.; Wang, D.; Sun, B.; Li, C.; Carter, K.; Huang, W. C.; Kim, C.; Xia, J., Surfactant-stripped micelles for NIR-II photoacoustic imaging through 12 cm of breast tissue and whole human breasts. *Adv. Mater.* **2019,** *31* (40), 1902279.

74. Xu, C.; Pu, K., Second near-infrared photothermal materials for combinational nanotheranostics. *Chem. Soc. Rev.* **2021**.

75. Jiang, Y.; Huang, J.; Xu, C.; Pu, K., Activatable polymer nanoagonist for second near-infrared photothermal immunotherapy of cancer. *Nat. Commun.* **2021,** *12* (1), 1-14.

76. Chen, Y.-S.; Zhao, Y.; Yoon, S. J.; Gambhir, S. S.; Emelianov, S., Miniature Gold Nanorods for Photoacoustic Molecular Imaging in the Second Near-Infrared Optical Window. *Nat. Nanotech.* **2019,** *14* (5), 465-472.

77. Kaneti, Y. V.; Chen, C.; Liu, M.; Wang, X.; Yang, J. L.; Taylor, R. A.; Jiang, X.; Yu, A., Carbon-coated gold nanorods: a facile route to biocompatible materials for photothermal applications. *ACS Appl. Mater. Interfaces* **2015,** *7* (46), 25658-25668.

78. Zhao, Y.-Q.; Sun, Y.; Zhang, Y.; Ding, X.; Zhao, N.; Yu, B.; Zhao, H.; Duan, S.; Xu, F.-J., Well-defined gold nanorod/polymer hybrid coating with inherent antifouling and photothermal bactericidal properties for treating an infected hernia. *ACS Nano* **2020,** *14* (2), 2265-2275.

79. Zhang, Z.; Wang, L.; Wang, J.; Jiang, X.; Li, X.; Hu, Z.; Ji, Y.; Wu, X.; Chen, C., Mesoporous silica-coated gold nanorods as a light-mediated multifunctional theranostic platform for cancer treatment. *Adv. Mater.* **2012,** *24* (11), 1418-1423.

80. Zhou, J.; Lin, Z.; Penna, M.; Pan, S.; Ju, Y.; Li, S.; Han, Y.; Chen, J.; Lin, G.; Richardson, J. J., Particle Engineering Enabled by Polyphenol-Mediated Supramolecular Networks. *Nat. Commun.* **2020,** *11* (1), 1-8.

81. Del Caño, R.; Gisbert-González, J. M.; González-Rodríguez, J.; Sánchez-Obrero, G.; Madueño, R.; Blázquez, M.; Pineda, T., Effective replacement of cetyltrimethylammonium bromide (CTAB) by mercaptoalkanoic acids on gold nanorod (AuNR) surfaces in aqueous solutions. *Nanoscale* **2020,** *12* (2), 658-668.

82. Shi, X.; Perry, H. L.; Wilton-Ely, J. D., Strategies for the functionalisation of gold nanorods to reduce toxicity and aid clinical translation. *Nanotheranostics* **2021,** *5* (2), 155.

83. Wang, L.; Li, D.; Hao, Y.; Niu, M.; Hu, Y.; Zhao, H.; Chang, J.; Zhang, Z.; Zhang, Y., Gold nanorod–based poly (lactic-co-glycolic acid) with manganese dioxide core–shell structured multifunctional nanoplatform for cancer theranostic applications. *Int. J. Nanomed.* **2017,** *12*, 3059.

84. Siwicka, Z. E.; Son, F. A.; Battistella, C.; Moore, M. H.; Korpanty, J.; McCallum, N. C.; Wang, Z.; Johnson, B. J.; Farha, O. K.; Gianneschi, N. C., Synthetic porous melanin. *J. Am.. Chem. Soc.* **2021,** *143* (8), 3094-3103.

85. Yim, W.; Zhou, J.; Mantri, Y.; Creyer, M. N.; Moore, C. A.; Jokerst, J. V., Gold nanorod–melanin hybrids for enhanced and prolonged photoacoustic imaging in the near-infrared-II window. *ACS. Appl. Mater. Interfaces* **2021**.

86. Perrault, S. D.; Walkey, C.; Jennings, T.; Fischer, H. C.; Chan, W. C., Mediating tumor targeting efficiency of nanoparticles through design. *Nano Lett.* **2009,** *9* (5), 1909-1915.

87. Northfelt, D. W.; Dezube, B. J.; Thommes, J. A.; Miller, B. J.; Fischl, M. A.; Friedman-Kien, A.; Kaplan, L. D.; Du Mond, C.; Mamelok, R. D.; Henry, D. H., Pegylated-liposomal doxorubicin versus doxorubicin, bleomycin, and vincristine in the treatment of AIDS-related Kaposi's sarcoma: results of a randomized phase III clinical trial. *J. Clin. Oncol.* **1998,** *16* (7), 2445-2451.

88. Gradishar, W. J.; Tjulandin, S.; Davidson, N.; Shaw, H.; Desai, N.; Bhar, P.; Hawkins, M.; O'Shaughnessy, J., Phase III trial of nanoparticle albumin-bound paclitaxel compared with polyethylated castor oil–based paclitaxel in women with breast cancer. *J. Clin. Oncol.* **2005,** *23* (31), 7794-7803.

89. Huo, S.; Ma, H.; Huang, K.; Liu, J.; Wei, T.; Jin, S.; Zhang, J.; He, S.; Liang, X.-J., Superior penetration and retention behavior of 50 nm gold nanoparticles in tumors. *Cancer Res.* **2013,** *73* (1), 319-330.

90. Tang, L.; Fan, T. M.; Borst, L. B.; Cheng, J., Synthesis and biological response of size-specific, monodisperse drug–silica nanoconjugates. *ACS Nano* **2012,** *6* (5), 3954-3966.

91. Tang, L.; Gabrielson, N. P.; Uckun, F. M.; Fan, T. M.; Cheng, J., Size-dependent tumor penetration and in vivo efficacy of monodisperse drug–silica nanoconjugates. *Mol. Pharm.* **2013,** *10* (3), 883-892.

92. Murphy, C. J.; Sau, T. K.; Gole, A. M.; Orendorff, C. J.; Gao, J.; Gou, L.; Hunyadi, S. E.; Li, T., Anisotropic metal nanoparticles: synthesis, assembly, and optical applications. *J. Phys. Chem. B* **2005,** *109* (29), 13857-13870.

93. Schindelin, J.; Arganda-Carreras, I.; Frise, E.; Kaynig, V.; Longair, M.; Pietzsch, T.; Preibisch, S.; Rueden, C.; Saalfeld, S.; Schmid, B., Fiji: an open-source platform for biological-image analysis. *Nat. Methods* **2012,** *9* (7), 676-682.

94. Vigderman, L.; Zubarev, E. R., High-yield synthesis of gold nanorods with longitudinal SPR peak greater than 1200 nm using hydroquinone as a reducing agent. *Chem. Mater.* **2013,** *25* (8), 1450-1457.

95. Jana, N. R.; Gearheart, L.; Murphy, C. J., Seed-mediated growth approach for shape-controlled synthesis of spheroidal and rod-like gold nanoparticles using a surfactant template. *Adv. Mater.* **2001,** *13* (18), 1389-1393.

96. Liebscher, J. r.; Mrówczyński, R.; Scheidt, H. A.; Filip, C.; Hădade, N. D.; Turcu, R.; Bende, A.; Beck, S., Structure of polydopamine: a never-ending story? *Langmuir* **2013,** *29* (33), 10539-10548.

97. Jin, Z.; Sugiyama, Y.; Zhang, C.; Palui, G.; Xin, Y.; Du, L.; Wang, S.; Dridi, N.; Mattoussi, H., Rapid Photoligation of Gold Nanocolloids with Lipoic Acid-Based Ligands. *Chem. Mater.* **2020,** *32* (17), 7469-7483.

98. Nguyen, S. C.; Zhang, Q.; Manthiram, K.; Ye, X.; Lomont, J. P.; Harris, C. B.; Weller, H.; Alivisatos, A. P., Study of heat transfer dynamics from gold nanorods to the environment via time-resolved infrared spectroscopy. *ACS Nano* **2016,** *10* (2), 2144-2151.

99. Chen, Y. S.; Frey, W.; Aglyamov, S.; Emelianov, S., Environment-dependent generation of photoacoustic waves from plasmonic nanoparticles. *Small* **2012,** *8* (1), 47-52.

100. Huang, X.; Neretina, S.; El-Sayed, M. A., Gold nanorods: from synthesis and properties to biological and biomedical applications. *Adv. Mater.* **2009,** *21* (48), 4880-4910.

101. Mei, Z.; Gao, D.; Hu, D.; Zhou, H.; Ma, T.; Huang, L.; Liu, X.; Zheng, R.; Zheng, H.; Zhao, P., Activatable NIR-II photoacoustic imaging and photochemical synergistic therapy of MRSA infections using miniature Au/Ag nanorods. *Biomaterials* **2020,** *251*, 120092.

102. Deng, X.; Liang, S.; Cai, X.; Huang, S.; Cheng, Z.; Shi, Y.; Pang, M.; Ma, P. a.; Lin, J., Yolk–shell structured Au nanostar@ metal–organic framework for synergistic chemo-photothermal therapy in the second near-infrared window. *Nano lett.* **2019,** *19* (10), 6772-6780.

103. Francis, C. W., Prophylaxis for Thromboembolism in Hospitalized Medical Patients. *N. Engl. J. Med.* **2007,** *356* (14), 1438-1444.

104. Weitz, J. I., Low-Molecular-Weight Heparins. *N. Engl. J. Med.* **1997,** *337* (10), 688-698.

105. Mackman, N., Triggers, Targets and Treatments for Thrombosis. *Nature* **2008,** *451* (7181), 914-918.

106. Li, W.; Johnson, D. J.; Esmon, C. T.; Huntington, J. A., Structure of the Antithrombin–Thrombin–Heparin Ternary Complex Reveals the Antithrombotic Mechanism of Heparin. *Nat. Struct. Mol.* **2004,** *11* (9), 857-862.

107. Chen, I. Y.; Matsa, E.; Wu, J. C., Induced Pluripotent Stem Cells: At the Heart of Cardiovascular Precision Medicine. *Nat. Rev. Cardiol.* **2016,** *13* (6), 333-349.

108. Kaushal, R.; Bates, D. W.; Landrigan, C.; McKenna, K. J.; Clapp, M. D.; Federico, F.; Goldmann, D. A., Medication Errors and Adverse Drug Events in Pediatric Inpatients. *Jama* **2001,** *285* (16), 2114-2120.

109. Monagle, P.; Studdert, D. M.; Newall, F., Infant Deaths Due to Heparin Overdose: Time for a Concerted Action on Prevention. *J. Paediatr. Child Health* **2012,** *48* (5), 380-381.

110. Dix, D.; Andrew, M.; Marzinotto, V.; Charpentier, K.; Bridge, S.; Monagle, P.; deVeber, G.; Leaker, M.; Chan, A. K.; Massicotte, M. P., The Use of Low Molecular Weight Heparin in Pediatric Patients: A Prospective Cohort Study. *J. Pediatr.* **2000,** *136* (4), 439-445.

111. Arimura, J.; Poole, R. L.; Jeng, M.; Rhine, W.; Sharek, P., Neonatal Heparin Overdose—A Multidisciplinary Team Approach to Medication Error Prevention. *J. Pediatr. Pharmacol. Ther.* **2008,** *13* (2), 96-98.

112. Despotis, G.; Summerfield, A.; Joist, J.; Goodnough, L.; Santoro, S.; Spitznagel, E.; Cox, J. L.; Lappas, D., Comparison of Activated Coagulation Time and Whole Blood Heparin

Measurements with Laboratory Plasma Anti-Xa Heparin Concentration in Patients Having Cardiac Operations. *J. Thorac. Cardiovasc. Surg.* **1994,** *108* (6), 1076-1082.

113. Vandiver, J. W.; Vondracek, T. G., Antifactor Xa Levels *versus* Activated Partial Thromboplastin Time for Monitoring Unfractionated Heparin. *Pharmacotherapy: J. Human Pharmacology and Drug Therapy* **2012,** *32* (6), 546-558.

114. Vera-Aguilera, J.; Yousef, H.; Beltran-Melgarejo, D.; Teng, T. H.; Jan, R.; Mok, M.; Vera-Aguilera, C.; Moreno-Aguilera, E., Clinical Scenarios for Discordant Anti-Xa. *Adv. Hematol.* **2016,** *2016*.

115. Murray, D. J.; Brosnahan, W. J.; Pennell, B.; Kapalanski, D.; Weiler, J. M.; Olson, J., Heparin Detection by the Activated Coagulation Time: A Comparison of the Sensitivity of Coagulation Tests and Heparin Assays. *J. Cardiothorac. Vasc. Anesth.* **1997,** *11* (1), 24-28.

116. Gertler, R.; Wiesner, G.; Tassani-Prell, P.; Braun, S.-L.; Martin, K., Are the Point-of-Care Diagnostics Multiplate and ROTEM Valid in the Setting of High Concentrations of Heparin and Its Reversal with Protamine? *J, Cardiothorac Vasc. Anesth.* **2011,** *25* (6), 981-986.

117. Ma, S.-d.; Chen, Y.-l.; Feng, J.; Liu, J.-j.; Zuo, X.-w.; Chen, X.-g., One-Step Synthesis of Water-Dispersible and Biocompatible Silicon Nanoparticles for Selective Heparin Sensing and Cell Imaging. *Anal. Chem.* **2016,** *88* (21), 10474-10481.

118. Li, S.; Huang, P.; Wu, F., Highly Selective and Sensitive Detection of Heparin Based on Competition-Modulated Assembly and Disassembly of Fluorescent Gold Nanoclusters. *New J. Chem.* **2017,** *41* (2), 717-723.

119. Liu, Z.; Ma, Q.; Wang, X.; Lin, Z.; Zhang, H.; Liu, L.; Su, X., A Novel Fluorescent Nanosensor for Detection of Heparin and Heparinase Based on CuInS2 Quantum Dots. *Biosen. Bioelectron.* **2014,** *54*, 617-622.

120. Li, Y.; Sun, H.; Shi, F.; Cai, N.; Lu, L.; Su, X., Multi-Positively Charged Dendrimeric Nanoparticles Induced Fluorescence Quenching of Graphene Quantum Dots for Heparin and Chondroitin Sulfate Detection. *Biosen. Bioelectron.* **2015,** *74*, 284-290.

121. Zhu, D.; Ye, J.; Hu, Y.; Wen, H. M.; Kang, A.; Tang, Y.-P.; Chen, J.; Shan, C. X.; Cui, X. B., Specific Enrichment Combined with Highly Efficient Solid-Phase Tagging for the Sensitive Detection of Heparin Based on Boronic Acid-Functionalized Mesoporous Silica Nanospheres. *Chem. Commun.* **2016,** *52* (79), 11779-11782.

122. Xu, M.; Wang, L. V., Photoacoustic Imaging in Biomedicine. *Rev. Sci. Instrum.* **2006,** *77* (4), 041101.

123. Hu, L.; Liao, H.; Feng, L.; Wang, M.; Fu, W., Accelerating the Peroxidase-Like Activity of Gold Nanoclusters at Neutral pH for Colorimetric Detection of Heparin and Heparinase Activity. *Anal. Chem.* **2018,** *90* (10), 6247-6252.

124. Qu, F.; Liu, Y.; Lao, H.; Wang, Y.; You, J., Colorimetric Detection of Heparin with High Sensitivity Based on the Aggregation of Gold Nanoparticles Induced by Polymer Nanoparticles. *New J. Chem.* **2017,** *41* (19), 10592-10597.

125. Bamrungsap, S.; Cherngsuwanwong, J.; Srisurat, P.; Chonirat, J.; Sangsing, N.; Wiriyachaiporn, N., Visual Colorimetric Sensing System Based on the Self-Assembly of Gold Nanorods and Graphene Oxide for Heparin Detection Using a Polycationic Polymer as a Molecular Probe. *Anal. Methods* **2019,** *11* (10), 1387-1392.

126. Yoshimi, Y.; Sato, K.; Ohshima, M.; Piletska, E., Application of the 'Gate Effect'of a Molecularly Imprinted Polymer Grafted on an Electrode for the Real-Time Sensing of Heparin in Blood. *Analyst* **2013,** *138* (17), 5121-5128.

127. Tan, L.; Yao, S.; Xie, Q., Electrochemical Determination of Heparin Using Methylene Blue Probe and Study on Competition of Ba2+ with Methylene Blue for Binding Heparin. *Talanta* **2007,** *71* (2), 827-832.
128. Tian, L.; Zhao, H.; Zhao, Z.; Zhai, J.; Zhang, Z., A Facile Voltammetric Method for Detection of Heparin in Plasma Based on the Polyethylenimine Modified Electrode. *Anal. Methods* **2019,** *11* (10), 1324-1330.
129. Wang, J.; Chen, F.; Arconada-Alvarez, S. J.; Hartanto, J.; Yap, L.-P.; Park, R.; Wang, F.; Vorobyova, I.; Dagliyan, G.; Conti, P. S., A Nanoscale Tool for Photoacoustic-Based Measurements of Clotting Time and Therapeutic Drug Monitoring of Heparin. *Nano Lett.* **2016,** *16* (10), 6265-6271.
130. Chitgupi, U.; Nyayapathi, N.; Kim, J.; Wang, D.; Sun, B.; Li, C.; Carter, K.; Huang, W. C.; Kim, C.; Xia, J.; Lovell, J. F., Surfactant-Stripped Micelles for NIR-II Photoacoustic Imaging Through 12 cm of Breast Tissue and Whole Human Breasts. *Adv. Mater.* **2019,** *31* (40), 1902279.
131. Jeevarathinam, A. S.; Pai, N.; Huang, K.; Hariri, A.; Wang, J.; Bai, Y.; Wang, L.; Hancock, T.; Keys, S.; Penny, W., A Cellulose-Based Photoacoustic Sensor to Measure Heparin Concentration and Activity in Human Blood Samples. *Biosens. Bioelectron.* **2019,** *126*, 831-837.
132. Feng, G.; Zhang, G.-Q.; Ding, D., Design of Superior Phototheranostic Agents Guided by Jablonski Diagrams. *Chem. Soc. Rev.* **2020,** *49* (22), 8179-8234.
133. Ou, H.; Dai, S.; Liu, R.; Ding, D., Manipulating the Intramolecular Motion of AIEgens for Boosted Biomedical Applications. *Sci. China Chem.* **2019,** *62*, 929-932.
134. Chen, Y.-S.; Yoon, S. J.; Frey, W.; Dockery, M.; Emelianov, S., Dynamic Contrast-Enhanced Photoacoustic Imaging Using Photothermal Stimuli-Responsive Composite Nanomodulators. *Nat. Commun.* **2017,** *8* (1), 1-10.
135. Lyu, Y.; Fang, Y.; Miao, Q.; Zhen, X.; Ding, D.; Pu, K., Intraparticle Molecular Orbital Engineering of Semiconducting Polymer Nanoparticles as Amplified Theranostics for *in Vivo* Photoacoustic Imaging and Photothermal Therapy. *ACS Nano* **2016,** *10* (4), 4472-4481.
136. Kang, J.; Kim, D.; Wang, J.; Han, Y.; Zuidema, J. M.; Hariri, A.; Park, J. H.; Jokerst, J. V.; Sailor, M. J., Enhanced Performance of a Molecular Photoacoustic Imaging Agent by Encapsulation in Mesoporous Silicon Nanoparticles. *Adv. Mater.* **2018,** *30* (27), 1800512.
137. Qin, H.; Zhou, T.; Yang, S.; Xing, D., Fluorescence Quenching Nanoprobes Dedicated to *in Vivo* Photoacoustic Imaging and High-Efficient Tumor Therapy in Deep-Seated Tissue. *Small* **2015,** *11* (22), 2675-2686.
138. Brkovic, N.; Zhang, L.; Peters, J. N.; Kleine-Doepke, S.; Parak, W. J.; Zhu, D., Quantitative Assessment of Endosomal Escape of Various Endocytosed Polymer-Encapsulated Molecular Cargos upon Photothermal Heating. *Small* **2020,** *16* (46), 2003639.
139. Siwicka, Z. E.; Son, F. A.; Battistella, C.; Moore, M. H.; Korpanty, J.; McCallum, N. C.; Wang, Z.; Johnson, B. J.; Farha, O. K.; Gianneschi, N. C., Synthetic Porous Melanin. *J. Am. Chem. Soc.* **2021,** *143* (8), 3094-3103.
140. Jokerst, J.; Zhou, J.; Xu, M.; Jin, Z.; Borum, R.; Avakyan, N.; Cheng, Y.; Yim, W.; He, T.; Zhou, J., Versatile Polymer Nanocapsules *via* Redox Competition. *Angew. Chem. Int. Ed.* **2021**.
141. Yim, W.; Borum, R. M.; Zhou, J.; Mantri, Y.; Wu, Z.; Zhou, J.; Jin, Z.; Creyer, M.; Jokerst, J. V., Ultrasmall Gold Nanorod-Polydopamine Hybrids for Enhanced Photoacoustic Imaging and Photothermal Therapy in Second Near-Infrared Window. *Nanotheranostics* **2022,** *6* (1), 79-90.

142. Wang, J.; Jeevarathinam, A. S.; Humphries, K.; Jhunjhunwala, A.; Chen, F.; Hariri, A.; Miller III, B. R.; Jokerst, J. V., A Mechanistic Investigation of Methylene Blue and Heparin Interactions and Their Photoacoustic Enhancement. *Bioconjug. Chem.* **2018,** *29* (11), 3768-3775.
143. Kuttel, M. M.; Ståhle, J.; Widmalm, G., CarbBuilder: Software for Building Molecular Models of Complex Oligo-and Polysaccharide Structures. *J. Comput. Chem.* **2016,** (37), 2098-2105.
144. Chen, C.-T.; Martin-Martinez, F. J.; Jung, G. S.; Buehler, M. J., Polydopamine and Eumelanin Molecular Structures Investigated with *ab Initio* Calculations. *Chem. Sci.* **2017,** *8* (2), 1631-1641.
145. Trucks, G.; Frisch, M.; Schlegel, H.; Scuseria, G.; Robb, M.; Cheeseman, J.; Scalmani, G.; Barone, V.; Petersson, G.; Nakatsuji, H. *Gaussian 16* Revision B. 01; Gaussian Inc: Wallingford, CT, 2016.
146. Schmidt, J.; Polik, W. *WebMO Enterprise*, version 13.0; WebMO LLC: Holland, MI, USA, 2013.
147. Case, D. A.; Berryman, J.; Betz, R.; Cerutti, D.; Cheatham Iii, T.; Darden, T.; Duke, R.; Giese, T.; Gohlke, H.; Goetz, A. *AMBER 2015*, University of California: San Francisco, 2015.
148. Maier, J. A.; Martinez, C.; Kasavajhala, K.; Wickstrom, L.; Hauser, K. E.; Simmerling, C., ff14SB: Improving the Accuracy of Protein Side Chain and Backbone Parameters from ff99SB. *J. Chem. Theory Comput.* **2015,** *11* (8), 3696-3713.
149. Wang, J.; Wolf, R. M.; Caldwell, J. W.; Kollman, P. A.; Case, D. A., Development and Testing of a General Amber Force Field. *J. Comput. Chem.* **2004,** *25* (9), 1157-1174.
150. Humphrey, W.; Dalke, A.; Schulten, K., VMD: Visual Molecular Dynamics. *J. Molecul. Graphics* **1996,** *14* (1), 33-38.
151. Roe, D. R.; Cheatham III, T. E., PTRAJ and CPPTRAJ: Software for Processing and Analysis of Molecular Dynamics Trajectory Data. *J. Chem. Theory Comput.* **2013,** *9* (7), 3084-3095.
152. Armbruster, D. A.; Pry, T., Limit of Blank, Limit of Detection and Limit of Quantitation. *Clin. Biochem. Rev.* **2008,** *29* (Suppl 1), S49.
153. McElfresh, C.; Harrington, T.; Vecchio, K. S., Application of a Novel New Multispectral Nanoparticle Tracking Technique. *Meas. Sci. Technol.* **2018,** *29* (6), 065002.
154. Liu, C.-Y.; Huang, C.-J., Functionalization of Polydopamine *via* the Aza-Michael Reaction for Antimicrobial Interfaces. *Langmuir* **2016,** *32* (19), 5019-5028.
155. Cao, W.; Zhou, X.; McCallum, N. C.; Hu, Z.; Ni, Q. Z.; Kapoor, U.; Heil, C. M.; Cay, K. S.; Zand, T.; Mantanona, A. J., Unraveling the Structure and Function of Melanin Through Synthesis. *J. Am. Chem. Soc.* **2021,** *143* (7), 2622-2637.
156. Yim, W.; Zhou, J.; Mantri, Y.; Creyer, M. N.; Moore, C. A.; Jokerst, J. V., Gold Nanorod–Melanin Hybrids for Enhanced and Prolonged Photoacoustic Imaging in the Near-Infrared-II Window. *ACS Appl. Mater. & Interfaces* **2021**.
157. Jokerst, J. V.; Lobovkina, T.; Zare, R. N.; Gambhir, S. S., Nanoparticle PEGylation for Imaging and Therapy. *Nanomed.* **2011,** *6* (4), 715-728.
158. Delparastan, P.; Malollari, K. G.; Lee, H.; Messersmith, P. B., Direct Evidence for the Polymeric Nature of Polydopamine. *Angew. Chem. Int. Ed.* **2019,** *58* (4), 1077-1082.
159. Han, Y.; Lin, Z.; Zhou, J.; Yun, G.; Guo, R.; Richardson, J. J.; Caruso, F., Polyphenol-Mediated Assembly of Proteins for Engineering Functional Materials. *Angew. Chem. Int. Ed.* **2020,** *132* (36), 15748-15755.
160. Jaques, L., Protamine—Antagonist to Heparin. *Can. Med. Assoc. J.* **1973,** *108* (10), 1291.

161. De Waele, J. J.; Van Cauwenberghe, S.; Hoste, E.; Benoit, D.; Colardyn, F., The Use of the Activated Clotting Time for Monitoring Heparin Therapy in Critically Ill Patients. *Intensive Care Med.* **2003,** *29* (2), 325-328.

162. Bromfield, S. M.; Barnard, A.; Posocco, P.; Fermeglia, M.; Pricl, S.; Smith, D. K., Mallard Blue: A High-Affinity Selective Heparin Sensor That Operates in Highly Competitive Media. *J. Am. Chem. Soc.* **2013,** *135* (8), 2911-2914.

163. Zhou, J.; Yim, W.; Zhou, J.; Jin, Z.; Xu, M.; Mantri, Y.; He, T.; Cheng, Y.; Fu, L.; Wu, Z., A Fiber Optic Photoacoustic Sensor for Real-Time Heparin Monitoring. *Biosens. Bioelectron.* **2021**, 113692.

164. Dyring-Andersen, B.; Løvendorf, M. B.; Coscia, F.; Santos, A.; Møller, L. B. P.; Colaço, A. R.; Niu, L.; Bzorek, M.; Doll, S.; Andersen, J. L., Spatially and cell-type resolved quantitative proteomic atlas of healthy human skin. *Nat. Commun.* **2020,** *11* (1), 1-14.

165. Natarajan, V. T.; Ganju, P.; Ramkumar, A.; Grover, R.; Gokhale, R. S., Multifaceted pathways protect human skin from UV radiation. *Nat. Chem. Biol.* **2014,** *10* (7), 542-551.

166. Lechler, T.; Fuchs, E., Asymmetric cell divisions promote stratification and differentiation of mammalian skin. *Nature* **2005,** *437* (7056), 275-280.

167. Bowden, G. T., Prevention of non-melanoma skin cancer by targeting ultraviolet-B-light signalling. *Nat. Rev. Cancer* **2004,** *4* (1), 23-35.

168. Bald, T.; Quast, T.; Landsberg, J.; Rogava, M.; Glodde, N.; Lopez-Ramos, D.; Kohlmeyer, J.; Riesenberg, S.; Van Den Boorn-Konijnenberg, D.; Hömig-Hölzel, C., Ultraviolet-radiation-induced inflammation promotes angiotropism and metastasis in melanoma. *Nature* **2014,** *507* (7490), 109-113.

169. Epstein, J. H., Photocarcinogenesis, skin cancer, and aging. *J. Am. Acad. Dermatol.* **1983,** *9* (4), 487-502.

170. Eller, M. S.; Yaar, M.; Gilchrest, B. A., DNA damage and melanogenesis. *Nature* **1994,** *372* (6505), 413-414.

171. Wicks, N. L.; Chan, J. W.; Najera, J. A.; Ciriello, J. M.; Oancea, E., UVA phototransduction drives early melanin synthesis in human melanocytes. *Curr. Biol.* **2011,** *21* (22), 1906-1911.

172. Thong, H. Y.; Jee, S. H.; Sun, C. C.; Boissy, R., The patterns of melanosome distribution in keratinocytes of human skin as one determining factor of skin colour. *Bri. J. Dermatol.* **2003,** *149* (3), 498-505.

173. Jacques, S. L., Origins of tissue optical properties in the UVA, visible, and NIR regions. *OSA TOPS on advances in optical imaging and photon migration* **1996,** *2*, 364-369.

174. Ou-Yang, H.; Stamatas, G.; Kollias, N., Spectral responses of melanin to ultraviolet A irradiation. *J. Invest. Dermatol.* **2004,** *122* (2), 492-496.

175. Jacques, S. L., Optical properties of biological tissues: a review. *Phys. Med. Biol.* **2013,** *58* (11), R37.

176. Sjoding, M. W.; Dickson, R. P.; Iwashyna, T. J.; Gay, S. E.; Valley, T. S., Racial bias in pulse oximetry measurement. *N. Engl. J. Med.* **2020,** *383* (25), 2477-2478.

177. O'Rese, J. K.; Girkin, C. A.; Budenz, D. L.; Durbin, M. K.; Feuer, W. J.; Group, C. O. N. D. S., Effect of race, age, and axial length on optic nerve head parameters and retinal nerve fiber layer thickness measured by Cirrus HD-OCT. *Arch. Ophthalmol.* **2012,** *130* (3), 312-318.

178. Bent, B.; Goldstein, B. A.; Kibbe, W. A.; Dunn, J. P., Investigating sources of inaccuracy in wearable optical heart rate sensors. *NPJ Digit. Med.* **2020,** *3* (1), 1-9.

179. Ray, I.; Liaqat, D.; Gabel, M.; de Lara, E., Skin tone, confidence, and data quality of heart rate sensing in WearOS smartwatches. *Proc. IEEE* **2021**, 213-219.
180. Li, X.; Dinish, U.; Aguirre, J.; Bi, R.; Dev, K.; Attia, A. B. E.; Nitkunanantharajah, S.; Lim, Q. H.; Schwarz, M.; Yew, Y. W., Optoacoustic mesoscopy analysis and quantitative estimation of specific imaging metrics in Fitzpatrick skin phototypes II to V. *J. Biophotonics* **2019,** *12* (9), e201800442.
181. Rennie, M. Y.; Dunham, D.; Lindvere-Teene, L.; Raizman, R.; Hill, R.; Linden, R., Understanding real-time fluorescence signals from bacteria and wound tissues observed with the MolecuLight i: XTM. *Diagnostics* **2019,** *9* (1), 22.
182. Joensen, J.; Demmink, J. H.; Johnson, M. I.; Iversen, V. V.; Lopes-Martins, R. Á. B.; Bjordal, J. M., The thermal effects of therapeutic lasers with 810 and 904 nm wavelengths on human skin. *Photomed. Laser Surg.* **2011,** *29* (3), 145-153.
183. Afshari, A.; Saager, R. B.; Burgos, D.; Vogt, W. C.; Wang, J.; Mendoza, G.; Weininger, S.; Sung, K.-B.; Durkin, A. J.; Pfefer, T. J., Evaluation of the robustness of cerebral oximetry to variations in skin pigmentation using a tissue-simulating phantom. *Biomed. Opt. Express* **2022,** *13* (5), 2909-2928.
184. Saager, R. B.; Quach, A.; Rowland, R. A.; Baldado, M. L.; Durkin, A. J., Low-cost tissue simulating phantoms with adjustable wavelength-dependent scattering properties in the visible and infrared ranges. *J. Biomed. Opt.* **2016,** *21* (6), 067001.
185. Roberts, W. E., Skin type classification systems old and new. *Dermatol. Clin.* **2009,** *27* (4), 529-533.
186. Mantri, Y.; Jokerst, J. V., Impact of skin tone on photoacoustic oximetry and tools to minimize bias. *Biomed. Opt. Express* **2022,** *13* (2), 875-887.
187. Yim, W.; Takemura, K.; Zhou, J.; Zhou, J.; Jin, Z.; Borum, R. M.; Xu, M.; Cheng, Y.; He, T.; Penny, W., Enhanced photoacoustic detection of heparin in whole blood via melanin nanocapsules carrying molecular agents. *ACS Nano* **2021**.
188. Hurbain, I.; Romao, M.; Sextius, P.; Bourreau, E.; Marchal, C.; Bernerd, F.; Duval, C.; Raposo, G., Melanosome distribution in keratinocytes in different skin types: melanosome clusters are not degradative organelles. *J. Invest. Dermatol.* **2018,** *138* (3), 647-656.
189. Nichol, J. W.; Koshy, S. T.; Bae, H.; Hwang, C. M.; Yamanlar, S.; Khademhosseini, A., Cell-laden microengineered gelatin methacrylate hydrogels. *Biomaterials* **2010,** *31* (21), 5536-5544.
190. Barros, N. R.; Kim, H.-J.; Gouidie, M. J.; Lee, K.; Bandaru, P.; Banton, E. A.; Sarikhani, E.; Sun, W.; Zhang, S.; Cho, H.-J., Biofabrication of endothelial cell, dermal fibroblast, and multilayered keratinocyte layers for skin tissue engineering. *Biofabrication* **2021,** *13* (3), 035030.
191. Yim, W.; Zhou, J.; Mantri, Y.; Creyer, M. N.; Moore, C. A.; Jokerst, J. V., Gold nanorod–melanin hybrids for enhanced and prolonged photoacoustic imaging in the near-infrared-II window. *ACS Appl. Mater. Interfaces* **2021,** *13* (13), 14974-14984.
192. Hoch, E.; Hirth, T.; Tovar, G. E.; Borchers, K., Chemical tailoring of gelatin to adjust its chemical and physical properties for functional bioprinting. *J. Mater. Chem. B* **2013,** *1* (41), 5675-5685.
193. Gottlieb, H. E.; Kotlyar, V.; Nudelman, A., NMR chemical shifts of common laboratory solvents as trace impurities. *J. Org. Chem.* **1997,** *62* (21), 7512-7515.
194. Prahl, S. A.; van Gemert, M. J.; Welch, A. J., Determining the optical properties of turbid media by using the adding–doubling method. *Appl. Opt.* **1993,** *32* (4), 559-568.
195. Riley, P. A., Melanin. *Int. J. Biochem. Cell Biol.* **1997,** *29* (11), 1235-1239.

196. Pralea, I.-E.; Moldovan, R.-C.; Petrache, A.-M.; Ilieș, M.; Hegheș, S.-C.; Ielciu, I.; Nicoară, R.; Moldovan, M.; Ene, M.; Radu, M., From extraction to advanced analytical methods: The challenges of melanin analysis. *Int. J. Mol. Sci.* **2019,** *20* (16), 3943.
197. Battistella, C.; McCallum, N. C.; Gnanasekaran, K.; Zhou, X.; Caponetti, V.; Montalti, M.; Gianneschi, N. C., Mimicking natural human hair pigmentation with synthetic melanin. *ACS Cent. Sci.* **2020,** *6* (7), 1179-1188.
198. Wu, D.; Zhou, J.; Creyer, M. N.; Yim, W.; Chen, Z.; Messersmith, P. B.; Jokerst, J. V., Phenolic-enabled nanotechnology: versatile particle engineering for biomedicine. *Chem. Soc. Rev.* **2021,** *50* (7), 4432-4483.
199. Patel, K.; Singh, N.; Yadav, J.; Nayak, J. M.; Sahoo, S. K.; Lata, J.; Chand, D.; Kumar, S.; Kumar, R., Polydopamine films change their physicochemical and antimicrobial properties with a change in reaction conditions. *Phys. Chem. Chem. Phys.* **2018,** *20* (8), 5744-5755.
200. Kollias, N.; Baqer, A. H., Absorption mechanisms of human melanin in the visible, 400–720 nm. *J. Invest. Dermatol.* **1987,** *89* (4), 384-388.
201. Wang, B.-X.; Zhou, L.-P.; Peng, X.-F., Surface and size effects on the specific heat capacity of nanoparticles. *Int. J. Thermophys.* **2006,** *27* (1), 139-151.
202. Ejima, H.; Richardson, J. J.; Liang, K.; Best, J. P.; van Koeverden, M. P.; Such, G. K.; Cui, J.; Caruso, F., One-step assembly of coordination complexes for versatile film and particle engineering. *Science* **2013,** *341* (6142), 154-157.
203. Fan, Z.; Sun, L.; Huang, Y.; Wang, Y.; Zhang, M., Bioinspired fluorescent dipeptide nanoparticles for targeted cancer cell imaging and real-time monitoring of drug release. *Nat. Nanotech.* **2016,** *11* (4), 388-394.
204. Ju, K.-Y.; Kang, J.; Pyo, J.; Lim, J.; Chang, J. H.; Lee, J.-K., pH-Induced aggregated melanin nanoparticles for photoacoustic signal amplification. *Nanoscale* **2016,** *8* (30), 14448-14456.
205. Zhang, W., Nanoparticle aggregation: principles and modeling. *Nanomater.* **2014**, 19-43.
206. Branchet, M.; Boisnic, S.; Frances, C.; Robert, A., Skin thickness changes in normal aging skin. *Gerontology* **1990,** *36* (1), 28-35.
207. Boissy, R. E., Melanosome transfer to and translocation in the keratinocyte. *Exp. Dermatol,* **2003,** *12*, 5-12.
208. Hariri, A.; Palma-Chavez, J.; Wear, K. A.; Pfefer, T. J.; Jokerst, J. V.; Vogt, W. C., Polyacrylamide hydrogel phantoms for performance evaluation of multispectral photoacoustic imaging systems. *Photoacoustics* **2021,** *22*, 100245.
209. Shimojo, Y.; Nishimura, T.; Hazama, H.; Ozawa, T.; Awazu, K., Measurement of absorption and reduced scattering coefficients in Asian human epidermis, dermis, and subcutaneous fat tissues in the 400-to 1100-nm wavelength range for optical penetration depth and energy deposition analysis. *J. Biomed. Opt.* **2020,** *25* (4), 045002.
210. Chen, A. I.; Balter, M. L.; Chen, M. I.; Gross, D.; Alam, S. K.; Maguire, T. J.; Yarmush, M. L., Multilayered tissue mimicking skin and vessel phantoms with tunable mechanical, optical, and acoustic properties. *Med. Phys.* **2016,** *43* (6Part1), 3117-3131.
211. Saager, R. B.; Cuccia, D. J.; Durkin, A. J., Determination of optical properties of turbid media spanning visible and near-infrared regimes via spatially modulated quantitative spectroscopy. *J. Biomed. Opt.* **2010,** *15* (1), 017012.
212. Soyemi, O. O.; Landry, M. R.; Yang, Y.; Idwasi, P. O.; Soller, B. R., Skin color correction for tissue spectroscopy: demonstration of a novel approach with tissue-mimicking phantoms. *Appl. Spectrosc.* **2005,** *59* (2), 237-244.

213. Saager, R. B.; Kondru, C.; Au, K.; Sry, K.; Ayers, F.; Durkin, A. J. In *Multilayer silicone phantoms for the evaluation of quantitative optical techniques in skin imaging*, Design and performance validation of phantoms used in conjunction with optical measurement of tissue II, Proc. SPIE: 2010; pp 40-47.

214. Lee, J.; Manoharan, V.; Cheung, L.; Lee, S.; Cha, B.-H.; Newman, P.; Farzad, R.; Mehrotra, S.; Zhang, K.; Khan, F., Nanoparticle-based hybrid scaffolds for deciphering the role of multimodal cues in cardiac tissue engineering. *ACS nano* **2019,** *13* (11), 12525-12539.

215. Gaharwar, A. K.; Singh, I.; Khademhosseini, A., Engineered biomaterials for in situ tissue regeneration. *Nat. Rev. Mater.* **2020,** *5* (9), 686-705.

216. Yang, J. C.; Mun, J.; Kwon, S. Y.; Park, S.; Bao, Z.; Park, S., Electronic skin: recent progress and future prospects for skin-attachable devices for health monitoring, robotics, and prosthetics. *Adv. Mater.* **2019,** *31* (48), 1904765.

217. Liu, J.; Lu, Y., A colorimetric lead biosensor using DNAzyme-directed assembly of gold nanoparticles. *Journal of the American Chemical Society* **2003,** *125* (22), 6642-6643.

218. Jin, Z.; Li, Y.; Li, K.; Zhou, J.; Yeung, J.; Ling, C.; Yim, W.; He, T.; Cheng, Y.; Xu, M., Peptide Amphiphile Mediated Co-assembly for Nanoplasmonic Sensing. *Angewandte Chemie* **2023,** *135* (4), e202214394.

219. Guo, L.; Xu, Y.; Ferhan, A. R.; Chen, G.; Kim, D.-H., Oriented gold nanoparticle aggregation for colorimetric sensors with surprisingly high analytical figures of merit. *Journal of the American Chemical Society* **2013,** *135* (33), 12338-12345.

220. Liu, J.; Lu, Y., Accelerated color change of gold nanoparticles assembled by DNAzymes for simple and fast colorimetric Pb2+ detection. *Journal of the American Chemical Society* **2004,** *126* (39), 12298-12305.

221. Ghosh, S. K.; Pal, T., Interparticle coupling effect on the surface plasmon resonance of gold nanoparticles: from theory to applications. *Chemical reviews* **2007,** *107* (11), 4797-4862.

222. Jin, Z.; Mantri, Y.; Retout, M.; Cheng, Y.; Zhou, J.; Jorns, A.; Fajtova, P.; Yim, W.; Moore, C.; Xu, M., A Charge-Switchable Zwitterionic Peptide for Rapid Detection of SARS-CoV-2 Main Protease. *Angewandte Chemie International Edition* **2022,** *61* (9), e202112995.

223. Jokerst, J. V.; Chang, Y.-C.; Jin, Z.; Li, K.; Zhou, J.; Yim, W.; Yeung, J.; Cheng, Y.; Retout, M.; Creyer, M. N., Peptide valence-induced breaks in plasmonic coupling. *Chemical Science* **2023**.

224. Kim, T.; Lee, K.; Gong, M.-s.; Joo, S.-W., Control of gold nanoparticle aggregates by manipulation of interparticle interaction. *Langmuir* **2005,** *21* (21), 9524-9528.

225. Lin, S. Y.; Wu, S. H.; Chen, C. h., A simple strategy for prompt visual sensing by gold nanoparticles: general applications of interparticle hydrogen bonds. *Angewandte Chemie International Edition* **2006,** *45* (30), 4948-4951.

226. Zhang, L.; Mazouzi, Y.; Salmain, M.; Liedberg, B.; Boujday, S., Antibody-gold nanoparticle bioconjugates for biosensors: synthesis, characterization and selected applications. *Biosensors and Bioelectronics* **2020,** *165*, 112370.

227. Wang, Y.; Quinsaat, J. E. Q.; Ono, T.; Maeki, M.; Tokeshi, M.; Isono, T.; Tajima, K.; Satoh, T.; Sato, S.-i.; Miura, Y., Enhanced dispersion stability of gold nanoparticles by the physisorption of cyclic poly (ethylene glycol). *Nature communications* **2020,** *11* (1), 6089.

228. Yim, W.; Takemura, K.; Zhou, J.; Zhou, J.; Jin, Z.; Borum, R. M.; Xu, M.; Cheng, Y.; He, T.; Penny, W., Enhanced Photoacoustic Detection of Heparin in Whole Blood via Melanin Nanocapsules Carrying Molecular Agents. *ACS nano* **2021,** *16* (1), 683-693.

229. Cedervall, T.; Lynch, I.; Lindman, S.; Berggård, T.; Thulin, E.; Nilsson, H.; Dawson, K. A.; Linse, S., Understanding the nanoparticle–protein corona using methods to quantify exchange rates and affinities of proteins for nanoparticles. *Proceedings of the National Academy of Sciences* **2007,** *104* (7), 2050-2055.
230. Retout, M.; Jin, Z.; Tsujimoto, J.; Mantri, Y.; Borum, R.; Creyer, M. N.; Yim, W.; He, T.; Chang, Y.-C.; Jokerst, J. V., Di-Arginine Additives for Dissociation of Gold Nanoparticle Aggregates: A Matrix-Insensitive Approach with Applications in Protease Detection. *ACS Applied Materials & Interfaces* **2022,** *14* (46), 52553-52565.
231. Liang, X.; Wei, H.; Cui, Z.; Deng, J.; Zhang, Z.; You, X.; Zhang, X.-E., Colorimetric detection of melamine in complex matrices based on cysteamine-modified gold nanoparticles. *Analyst* **2011,** *136* (1), 179-183.
232. Jin, Z.; Du, X.; Xu, Y.; Deng, Y.; Liu, M.; Zhao, Y.; Zhang, B.; Li, X.; Zhang, L.; Peng, C., Structure of Mpro from SARS-CoV-2 and discovery of its inhibitors. *Nature* **2020,** *582* (7811), 289-293.
233. Owen, D. R.; Allerton, C. M.; Anderson, A. S.; Aschenbrenner, L.; Avery, M.; Berritt, S.; Boras, B.; Cardin, R. D.; Carlo, A.; Coffman, K. J., An oral SARS-CoV-2 Mpro inhibitor clinical candidate for the treatment of COVID-19. *Science* **2021,** *374* (6575), 1586-1593.
234. Armbruster, D. A.; Pry, T., Limit of blank, limit of detection and limit of quantitation. *The clinical biochemist reviews* **2008,** *29* (Suppl 1), S49.
235. Lévy, R.; Thanh, N. T.; Doty, R. C.; Hussain, I.; Nichols, R. J.; Schiffrin, D. J.; Brust, M.; Fernig, D. G., Rational and combinatorial design of peptide capping ligands for gold nanoparticles. *Journal of the American Chemical Society* **2004,** *126* (32), 10076-10084.
236. Salomon-Ferrer, R.; Case, D. A.; Walker, R. C., An overview of the Amber biomolecular simulation package. *Wiley Interdisciplinary Reviews: Computational Molecular Science* **2013,** *3* (2), 198-210.
237. Mark, P.; Nilsson, L., Structure and dynamics of the TIP3P, SPC, and SPC/E water models at 298 K. *Journal of Physical Chemistry A* **2001,** *105* (43), 9954-9960.
238. Ackland, G. J.; Tichy, G.; Vitek, V.; Finnis, M. W., Simple N-body potentials for the noble metals and nickel. *Philosophical Magazine A* **1987,** *56* (6), 735-756.
239. Ryckaert, J.-P.; Ciccotti, G.; Berendsen, H. J. C., Numerical integration of the cartesian equations of motion of a system with constraints: molecular dynamics of n-alkanes. *Journal of computational physics* **1977,** *23* (3), 327-341.
240. Plimpton, S., Fast Parallel Algorithms for Short-Range Molecular Dynamics. *Journal of Computational Physics* **1995,** *117*, 1-19.
241. Giannozzi, P.; Baroni, S.; Bonini, N.; Calandra, M.; Car, R.; Cavazzoni, C.; Ceresoli, D.; Chiarotti, G. L.; Cococcioni, M.; Dabo, I.; Corso, A. D.; Gironcoli, S. d.; Fabris, S.; Fratesi, G.; Gebauer, R.; Gerstmann, U.; Gougoussis, C.; Kokalj, A.; Lazzeri, M.; Martin-Samos, L.; Marzari, N.; Mauri, F.; Mazzarello, R.; Paolini, S.; Pasquarello, A.; Paulatto, L.; Sbraccia, C.; Scandolo, S.; Sclauzero, G.; Seitsonen, A. P.; Smogunov, A.; Umari, P.; Wentzcovitch, R. M., QUANTUM ESPRESSO: a modular and open-source software project for quantum simulations of materials. *Journal of Physics: Condensed Matter* **2009,** *21*, 395502.
242. Giannozzi, P.; Andreussi, O.; Brumme, T.; Bunau, O.; Nardelli, M. B.; Calandra, M.; Car, R.; Cavazzoni, C.; Ceresoli, D.; Cococcioni, M.; Colonna, N.; Carnimeo, I.; Corso, A. D.; Gironcoli, S. d.; Delugas, P.; Jr, R. A. D.; Ferretti, A.; Floris, A.; Fratesi, G.; Fugallo, G.; Gebauer, R.; Gerstmann, U.; Giustino, F.; Gorni, T.; Jia, J.; Kawamura, M.; Ko, H.-Y.; Kokalj, A.; Küçükbenli, E.; Lazzeri, M.; Marsili, M.; Marzari, N.; Mauri, F.; Nguyen, N. L.; Nguyen,

H.-V.; Otero-de-la-Roza, A.; Paulatto, L.; Poncé, S.; Rocca, D.; Sabatini, R.; Santra, B.; Schlipf, M.; Seitsonen, A. P.; Smogunov, A.; Timrov, I.; Thonhauser, T.; Umari, P.; Vast, N.; Wu, X.; Baroni, S., Advanced capabilities for materials modelling with Quantum ESPRESSO. *J. Phys.: Condens. Matter* **2017,** *29*, 465901.

243. Mahinthichaichan, P.; Vo, Q. N.; Ellis, C. R.; Shen, J., Kinetics and Mechanism of Fentanyl Dissociation from the μ-Opioid Receptor. *American Chemical Society* **2021,** *1*, 2208-2215.

244. Yim, W.; Zhou, J.; Sasi, L.; Zhao, J.; Yeung, J.; Cheng, Y.; Jin, Z.; Johnson, W.; Xu, M.; Palma-Chavez, J., 3D-Bioprinted Phantom with Human Skin Phototypes for Biomedical Optics. *Advanced Materials* **2023,** *35* (3), 2206385.

245. Zhu, G.; Zhu, X.; Fan, Q.; Wan, X., Raman spectra of amino acids and their aqueous solutions. *Spectrochimica Acta Part A: Molecular and Biomolecular Spectroscopy* **2011,** *78* (3), 1187-1195.

246. Nowinski, A. K.; Sun, F.; White, A. D.; Keefe, A. J.; Jiang, S., Sequence, structure, and function of peptide self-assembled monolayers. *Journal of the American Chemical Society* **2012,** *134* (13), 6000-6005.

247. Mokashi-Punekar, S.; Walsh, T. R.; Rosi, N. L., Tuning the structure and chiroptical properties of gold nanoparticle single helices via peptide sequence variation. *Journal of the American Chemical Society* **2019,** *141* (39), 15710-15716.

248. Liu, X.; Zhang, Q.; Knoll, W.; Liedberg, B.; Wang, Y., Rational design of functional peptide–gold hybrid nanomaterials for molecular interactions. *Advanced Materials* **2020,** *32* (37), 2000866.

249. Olmedo, I.; Araya, E.; Sanz, F.; Medina, E.; Arbiol, J.; Toledo, P.; Alvarez-Lueje, A.; Giralt, E.; Kogan, M. J., How changes in the sequence of the peptide CLPFFD-NH2 can modify the conjugation and stability of gold nanoparticles and their affinity for β-amyloid fibrils. *Bioconjugate chemistry* **2008,** *19* (6), 1154-1163.

250. Jin, Z.; Ling, C.; Li, Y.; Zhou, J.; Li, K.; Yim, W.; Yeung, J.; Chang, Y.-C.; He, T.; Cheng, Y., Spacer Matters: All-Peptide-Based Ligand for Promoting Interfacial Proteolysis and Plasmonic Coupling. *Nano Letters* **2022,** *22* (22), 8932-8940.

251. Yim, W.; Zhou, J.; Mantri, Y.; Creyer, M. N.; Moore, C. A.; Jokerst, J. V., Gold nanorod–melanin hybrids for enhanced and prolonged photoacoustic imaging in the near-infrared-II window. *ACS applied materials & interfaces* **2021,** *13* (13), 14974-14984.

252. Chen, S.; Cao, Z.; Jiang, S., Ultra-low fouling peptide surfaces derived from natural amino acids. *Biomaterials* **2009,** *30* (29), 5892-5896.

253. YináYi, M., An AM1 and PM3 molecular orbital and self-consistent reaction-field study of the aqueous solvation of glycine, alanine and proline in their neutral and zwitterionic forms. *Journal of the Chemical Society, Perkin Transactions 2* **1991,** (4), 531-537.

254. Huang, N.; Pérez, P.; Kato, T.; Mikami, Y.; Okuda, K.; Gilmore, R. C.; Conde, C. D.; Gasmi, B.; Stein, S.; Beach, M., SARS-CoV-2 infection of the oral cavity and saliva. *Nature medicine* **2021,** *27* (5), 892-903.

255. Retout, M.; Gosselin, B.; Mattiuzzi, A.; Ternad, I.; Jabin, I.; Bruylants, G., Peptide-Conjugated Silver Nanoparticles for the Colorimetric Detection of the Oncoprotein Mdm2 in Human Serum. *ChemPlusChem* **2022,** *87* (4), e202100450.

256. SHAN, Y. F.; XU, G. J., Study on substrate specificity at subsites for severe acute respiratory syndrome coronavirus 3CL protease. *Acta biochimica et biophysica Sinica* **2005,** *37* (12), 807-813.